Atomistic description of transport at the molecular scale

Miriam del Valle

Memoria presentada para optar al grado de Doctor en
Ciencias Físicas por la Universidad Autónoma de Madrid
bajo la dirección de Dr. Carlos Tejedor
y codirección de Dr. Gianaurelio Cuniberti

Octubre 2006

Contents

Resumen

Esta tesis está dedicada a la investigación de las propiedades de transporte de diversos sistemas de baja dimensionalidad. En concreto, se ha realizado un estudio de las propiedades de transporte de grafeno (sistema bidimensional), de nanotubos de carbono o de oro (sistemas quasi-unidimensionales), o los fulerenos de carbono (sistema de dimensión cero). En la investigación de las propiedades de estructura electrónica de estos materiales se han empleado diversas técnicas, desde métodos ab-initio o de primeros principios hasta aproximaciones del tipo de ligaduras fuertes. Combinadas con métodos para el estudio de propiedades de transporte en el esquema de Landauer y con la ayuda que ofrece el formalismo de las funciones de Green, constituyen una valiosa herramienta para investigar propiedades de transporte en sistemas de dimensiones moleculares, permitiendo una determinación atómica de las estructuras.

Los resultados obtenidos en estos estudios se pueden dividir en cuatro grupos:
(i) estudio de las propiedades vibracionales de fulerenos, publicado en Physics of Semiconductors 2002, (ISBN:0750309245) con el título "Electromodulation of charge transfer and vibrational properties of C_{60} on surfaces",
(ii) análisis de las propiedades de conductancia de un sistema de tres terminales con nanotubos de carbono como elemento constituyente, donde los defectos estructurales dan lugar a resonancias de tipo Fano, que pueden ser empleadas para controlar el transporte en estas uniones como se muestra en el trabajo "Defective transport properties of three-terminal carbon nanotube junctions" [1],
(iii) estudio sobre los nanotubos de oro con la obtención de una fórmula analítica que permite comprobar el comportamiento de la conductancia al variar el helicidad o el diámetro de estos tubos, publicado bajo el título "Scaling of the conductance in gold nanotubes" [2],
(iv) examen del transporte a través de una molécula biestable, el azobenceno, conectada a nanotubos de carbono de diferentes quiralidades que se expone en el trabajo "Tuning the conductance of a molecular switch" [3].

Introduction

The success of the current information technology originates from the advances in the fabrication of silicon based devices. Such accelerated technological development was a driving factor for most scientific achievements in mesoscopic physics which is the fundamental understanding of electron dynamics in the reduced dimensions.

Lithographic techniques allow for the very-large-scale integration of electronic devices. They are nevertheless constrained by optical resolution limits which will necessarily hinder the miniaturization trend forseen by Moore's law when arriving at feature sizes in the nanometer scale. Bottom-up electronics, *i.e.* the possibility to assemble electronic devices using the self-assemble capabilities of functional molecular building blocks, proposes itself as a post-silicon solution to the end-of-the-roadmap for semiconductor technologies. Still, understanding the behavior of *single molecule* quantum transport is a condition towards this ambitious goal of molecular electronics [4].

Electron transport through a single molecule device relies on exotic quantum effects of electrons confined in low-dimensional systems. A deep understanding of this problem was developed during the last two decades within the mesoscopic physics at the sub-micron scale. Indeed, classical "solid state physics" does allow for an accurate description of electron dynamics in *bulk* crystalline materials in the three physical dimensions (3D). But it was the possibility to confine electrons at the interface of semiconducting heterostructures in the so-called *two-dimensional electron gas* (2D), or further in *quantum wires* (1D) or even in *quantum dots* (0D) that allowed to test truly quantum mechanical phenomena via optical and transport low temperature experiments. Additionally, beyond a mere test of quantum mechanics, new quantum phenomena were discovered in such electronically confined systems; one for all, the quantum Hall effect, indeed awarded two times with the prestigious Nobel prize [5, 6, 7, 8].

Semiconducting heterostructures represent, though the first, only one of the possible materials for investigating electronic dynamics in low dimensions.

As a matter of fact, in a parallel development of chemical and physical sciences, new materials for electronics have been posed to the attention of the scientific community. The so-called carbon family plays a prominent role among these classes of new electronic materials. The two forms of known carbon solids (diamond and graphite) were complemented by the discovery of the controlled synthesis of fullerenes [9], carbon nanotubes [10], and single graphene layers [11], to follow the historical development. Graphene (2D), carbon nanotubes (1D), small organic molecules and fullerenes (0D) are nowadays under an intense investigation not only because they represent the ultimate *atomistic* limit of quantum confinement but also because of the new phenomenology related to their lattice topology. As an example, π electrons in graphene and nanotubes display at low energies Dirac-like (massless) electronic dispersion relations [12, 13], reflected for instance in the relativistic Landau levels of graphene in an external magnetic fields and in the expected spin-charge separation effect in carbon nanotubes under a bias voltage. Such effects which, for the low energy physics, can be easily understood within a continuum, field theoretical approach have to be complemented by an atomistic description of electron dynamics that allow us to access the full electron spectrum.

This thesis aims at merging, within the study of molecular systems, theoretical tools typical of mesoscopic physics and an atomistic determination of the electronic structure. The *Leitmotiv* of our investigations is the calculation of quantum transport observables at the molecular scale.

Quantum conductances of the order of $2e^2/h$ characteristic of a single molecule or a single nanotube with a typical lateral dimension of at most 1 nm, are at best understood, in contrast to classical dissipative conduction in the bulk state, as an electron wave diffraction problem. As already realized in 1957 by Rolf Landauer [14] the conductance of a phase coherent system is proportional to the quantum mechanical transmission. The latter can be calculated within the formalism of the Green functions.

Finite size effects such as for example surface states in carbon nanotubes, are captured only by an atomistic description of the molecular device. The Density Functional Theory based on Tight Binding (DFTB) approach adopted in this thesis attempts to combine the accuracy of an *ab initio* description with a relatively modest numerical demand.

All in all, these theoretical tools are important instruments for calculation of quantum transport characteristics in systems where charging and inelastic effects could be neglected. They are applied in this thesis to understand the transport properties of different molecular scale devices.

The outline of this thesis is organized as follows:

Electronic structure	Chapter 1 presents an illustration of the different instruments that will be needed throughout this thesis for the determination and characterization of the electronic structure of nanoscopic systems. Both density functional theory and tight-binding approaches are treated and references are given for an extension of this introduction in electronic structure methods.
Quantum transport	In Chapter 2 an overview of the tools used in this work is given which allow for the charge transport calculations in the equilibrium regime. Together with Chapter 1 completes the description of the methods applied in the studies described bellow.
Carbon-based materials	The characteristics of carbon-based systems are exposed in Chapter 3. These materials, comprising fullerenes, carbon nanotubes and graphene layers, constitute the major part of the systems studied in this thesis. Examples of transport observables for carbon-based systems are also given.
Carbon nanotube junctions	Chapter 4 will be devoted to the study of transport properties through different three-terminal carbon nanotube junctions, where two terminals are used for charge transport which is modified by applying a gate voltage on the third arm. A discussion of an addition control of the transport through these systems is also enclosed.
Electromodulation of C_{60}	In Chapter 5 a study based on density-functional theory calculations is presented on the modulation of charge transfer to a C_{60} molecule, placed onto a graphene substrate, due to an external applied electric field.
Gold Nanotubes	Chapter 6 will be centered on the analysis of transport through gold nanotubes, where a model of the systems allows to prediction of conductance values through an analytical formula.

Molecular junctions

Finally, Chapter 7 analyzes the conduction properties of a single molecule of azobenzene attached to nanoscopic metallic electrodes. A study of the switching capacity of this bistable molecule, together with the properties of the contact to the electrodes is presented in detail.

Chapter 1

Electronic structure calculations

This chapter presents an overview of some of the theory and methods to calculate the electronic structure of solids and molecules, which constitute the fundamentals for understanding the properties of matter. Nevertheless such a task poses problems of such a great complexity that approximations are needed to deal with them. A good control of these approximations is thus essential to understand the obtained results.

1.1 Solving the Schrödinger equation

Describing systems at the atomic level requires the use of quantum mechanics. To describe these systems solutions to the many-body Schrödinger equation for isolated systems in time-indepedent fields (see *e.g.* [15]) are therefore needed, which determine the wavefunction of the system:

$$\mathcal{H}\left(\mathbf{r},\mathbf{R}\right)\Phi\left(\mathbf{r},\mathbf{R}\right)=E\Phi\left(\mathbf{r},\mathbf{R}\right) \tag{1.1}$$

where $\mathcal{H}$ is the time-independent Hamiltonian operator for a system of N_e electrons and N_i nuclei, or more properly ions, described by position vectors $\mathbf{r}$ and $\mathbf{R}$, respectively. Φ is the spatial part of the solution to the more general time-dependent Schrödinger equation,

$$\mathrm{i}\hbar\frac{\partial}{\partial t}\Upsilon\left(\mathbf{r},\mathbf{R},t\right)=\mathcal{H}\Upsilon\left(\mathbf{r},\mathbf{R},t\right). \tag{1.2}$$

But, since the problems that we will consider in the following are described by a time-independent Hamiltonian $\mathcal{H}$, a separation of time and space variables

can be made. This separation Ansatz, $\Upsilon(\mathbf{r},\mathbf{R},t) = \Phi(\mathbf{r},\mathbf{R})\,\chi(t)$, yields for time-independent Hamiltonians a trivial time evolution, leaving the problem of solving the time-independent Schrödinger equation, Eq. (1.1).

The complete Hamiltonian $\mathcal{H}(\mathbf{r},\mathbf{R})$ can be written as:

$$\begin{aligned}\mathcal{H} &= \sum_{\alpha}\frac{\mathbf{p}_\alpha^2}{2M_\alpha} + \frac{1}{2}\sum_{\alpha,\beta}\frac{Z_\alpha Z_\beta e^2}{|\mathbf{R}_\alpha - \mathbf{R}_\beta|} + \sum_{i}\frac{\mathbf{p}_i^2}{2m} + \frac{1}{2}\sum_{i,j}\frac{e^2}{|\mathbf{r}_i - \mathbf{r}_j|} - \sum_{\alpha,i}\frac{Z_\alpha e^2}{|\mathbf{R}_\alpha - \mathbf{r}_i|} \\ &= T_{\mathrm{i}}(\mathbf{R}) + V_{\mathrm{ii}}(\mathbf{R}) + T_{\mathrm{e}}(\mathbf{r}) + V_{\mathrm{ee}}(\mathbf{r}) + V_{\mathrm{ie}}(\mathbf{r},\mathbf{R})\end{aligned} \tag{1.3}$$

where the different terms in which it has been decomposed are respectively:

- T_{i}: ionic kinetic energy operator,
- V_{ii}: ion-ion coulomb repulsive potential energy operator,
- T_{e}: kinetic energy operator of the electrons,
- V_{ee}: coulomb repulsion between electrons,
- V_{ie}: electron-ion coulomb interaction, which is the only attractive term.

M_α is the mass of the nuclei, m that of the electron, and $\mathbf{p}_\alpha$ and $\mathbf{p}_i$ are the ionic and electronic momentum operators. Z_α denotes the nuclear charge of the corresponding atom, $\mathbf{r} = (\mathbf{r}_1,\ldots,\mathbf{r}_{N_e})$ and $\mathbf{R} = (\mathbf{R}_1,\ldots,\mathbf{R}_{N_i})$. Greek character indices are used for ionic degrees of freedom and latin indices sum over the electronic degrees of freedom. For the rest of this chapter, atomic units will be adopted, where $m = 1$, $e = 1$, $\hbar = 1$, which will simplify the expressions.

To solve such a complex problem some approximations have to be introduced.

1.1.1 The Born-Oppenheimer approximation

Nuclei are considerably heavier than electrons and move therefore slower. Hence, to a good approximation, the electrons in a molecule can be considered to be moving in the field of fixed nuclei, so that the dynamic evolution of electrons and nuclei can then be decoupled. In this way, the Hamiltonian describing the motion of the electrons can be written as

$$\mathcal{H}_{\mathrm{a}} = \sum_{i}\frac{\mathbf{p}_i^2}{2} + \frac{1}{2}\sum_{i,j}\frac{1}{|\mathbf{r}_i - \mathbf{r}_j|} - \sum_{\alpha,i}\frac{Z_\alpha}{|\mathbf{R}_\alpha - \mathbf{r}_i|} \tag{1.4}$$

where the first two terms in Eq. (1.3) can be taken as constants. This adiabatic Hamiltonian $\mathcal{H}_a$ thus depends explicitly only on the electronic coordinates and the dependence on the nuclear coordinates is just parametric: $\mathcal{H}_a(\mathbf{r};\mathbf{R})$.

From now on, the problem to be concerned with is the solution of the following equation:

$$\mathcal{H}_a(\mathbf{r};\mathbf{R})\,\Psi(\mathbf{r};\mathbf{R}) = E_a\Psi(\mathbf{r};\mathbf{R})\,. \tag{1.5}$$

Its solution Ψ is the normalized wavefunction for the electrons. Due to the fermionic character of electrons Ψ must be antisymmetric with respect to the interchange of the coordinate $\mathbf{r}$ of any two electrons:

$$\Psi(\mathbf{r}_1,...,\mathbf{r}_i,...,\mathbf{r}_j,...,\mathbf{r}_{N_e}) = -\Psi(\mathbf{r}_1,...,\mathbf{r}_j,...,\mathbf{r}_i,...,\mathbf{r}_{N_e})\,. \tag{1.6}$$

This requirement, known as the *antisymmetry principle*, is a consequence of the familiar Pauli exclusion principle.

On the other hand, the nuclei will move on a potential energy surface obtained by solving the electronic problem and will be described following the classical physics laws. The Schrödinger equation for the ions in the Born-Oppenheimer approximation is therefore

$$\left[\sum_\alpha \frac{\mathbf{p}_\alpha^2}{2M_\alpha} + \frac{1}{2}\sum_{\alpha,\beta}\frac{Z_\alpha Z_\beta}{|\mathbf{R}_\alpha - \mathbf{R}_\beta|} + E_a(\mathbf{R})\right]\phi(\mathbf{R}) = E\phi(\mathbf{R})\,. \tag{1.7}$$

The total wavefunction is then written as the product of the nuclear and electronic parts:

$$\Phi(\mathbf{r},\mathbf{R}) = \Psi(\mathbf{r};\mathbf{R})\,\phi(\mathbf{R})\,. \tag{1.8}$$

Within the Born-Oppenheimer approximation, for a given set of nuclear positions the ion-electron interaction can be included in an external potential for the electrons. The Hamiltonian of a system of N_e interacting electrons in an external potential $V_{\text{ext}}(\mathbf{r})$ can be expressed as $H = T + U + V_{\text{ext}}$. T and U are the electronic kinetic energy and the electronic interaction potential energy, respectively, and will depend only on the electronic properties ("universal"), whereas V_{ext} is a characteristic of the particular system.

In density functional theory (DFT), on the other hand, the electronic properties of the system will be considered as functionals of the electronic density distribution of the ground state energy. The fundamental variable is then $n(\mathbf{r})$ instead of the electronic wavefunction $\Psi(\{\mathbf{r}\})$, as we will see in Sec. 1.3. But let us first have an overview of a wavefunction based method: the tight-binding formalism.

1.2 Tight-binding

The tight-binding (TB) method provides quite satisfying descriptions of the electronic structure and bonding properties and at the same time provides an intuitive picture which allows for a better understanding of the fundamental features of electronic bands. It has been largely used in the physics community, for these reasons and for its efficiency in simulations and calculations with a large number of atoms. For a more complete and clear introduction to the tight binding approximation we refer the reader to standard books of solid state physics [16, 17]. A simplified form of the tight-binding is known in the chemical community as the Hückel model [18, 19, 20, 21].

In this approximation the wave function is expanded in a linear combination of fixed energy-independent orbitals, each associated to a specific atom in the molecule or crystal. This working hypothesis, called linear combination of atomic orbitals, makes sense if the full Hamiltonian resembles that of a single atom in its vicinity. An appropriate choice for these localized basis functions is a set of atomic-like functions centered on the atom sites. On each site the basis functions can be written as a product of radial functions and spherical harmonics,

$$\chi(\mathbf{r}) \rightarrow \chi_{n\ell m} = \chi_{n\ell}(|\mathbf{r}|)\, Y_{\ell m}(\mathbf{r}), \tag{1.9}$$

where n indicates different functions with the same angular momentum (labelled by $\{\ell, m\}$). The matrix elements of the Hamiltonian matrix between two orbitals of the localized basis $\mathcal{H}_{\chi\chi'}$ can be divided into one-, two- and three-center terms. One-center terms are those where both orbitals as well as the potential energy operator of the Hamiltonian are centered on the same site. In two-center terms, the orbitals are centered on different sites and the potential is on one of the two. And for the three-center terms, the orbitals and the potential are all centered on different sites. The overlap matrix elements can only have one-center terms if both orbitals are on the same side or two-center terms otherwise. The semi-empirical tight-binding approaches involves only up to two-center terms with matrix elements expressed in a parameterized form. Using the crystal symmetries the number of parameters needed to describe a solid can be considerably reduced, as can be seen in the valuable tables given by Papaconstantopoulos [22].

Slater and Koster [23, 24] (SK) developed a widely used approach, by approximating the Hamiltonian matrix elements with the two-center form. The values of the matrix elements may be derived approximately or fitted to experimental data or accurate theoretical calculations. In this approach all

matrix elements have the same symmetry as of two atoms in free space. The choice of the SK parameters depends often on the properties one is interested in.

1.3 The density functional theory

Many reviews and books have been written about density functional theory (DFT) methods and algorithms [25, 26, 27, 28, 29, 30, 31], so that in this section just a short description of the theorems that gave birth to DFT will be given.

The first density functional theory of quantum systems is the method proposed in 1927 independently by Thomas [32] and Fermi [33], and extended by Dirac [34] to include exchange among the electrons. This method, though including too hard approximations, showed the appeal of a density functional theory, since it is remarkably simpler to deal with one equation for the density than with the full many-body Schrödinger equation with $3N_e$ degrees of freedom.

The modern formulation of density functional theory begins with the publication in 1964 of two important theorems by Hohenberg and Kohn [35, 30], which constitute the formal basis of a density functional theory as an exact theory of correlated many-body systems. The formulation applies to any system of interacting particles in an external potential $V(\mathbf{r})$.

Theorem 1 *For any system of interacting particles in an external potential* $V(\mathbf{r})$*, this potential* $V(\mathbf{r})$ *is determined uniquely, except for a constant, being a unique function of the ground state particle density* $n_0(\mathbf{r})$*.*

As a consequence, the complete Hamiltonian of the system is fully determined by $n_0(\mathbf{r})$, and therefore also the many body wavefunction for the ground state. The use of this theorem an the central point of DFT is to transfer every functional dependence on V into a functional dependence on n by substituting the single-valued $V[n]$.

Theorem 2 *A universal functional for the energy* $E[n(\mathbf{r})]$ *in terms of the density* $n(\mathbf{r})$ *can be defined for any external potential* $V(\mathbf{r})$*. The exact ground state energy of the system is the global minimum of this functional and the density* $n(\mathbf{r})$ *that minimizes the functional is the exact ground state density* $n_0(\mathbf{r})$*.*

The electronic ground state energy of the system can be obtained by minimizing the functional of the density with the constraint of constant number of particles.

$$\begin{aligned} &\delta\left\{E\left[n\right]-\mu\left[\int n\left(\mathbf{r}\right)\mathrm{d}\mathbf{r}-N_e\right]\right\}=0 \\ &\left.\frac{\delta E\left[n\right]}{\delta n\left(\mathbf{r}\right)}\right|_{n=n_0}=\mu \end{aligned} \tag{1.10}$$

where δ indicates the functional derivative of E, defined as $\delta F[n] = F[n+\delta n] - F[n]$ and $\delta F[n]/\delta n(\mathbf{r}) = \lim_{\eta\to 0^+}\left\{F[n(\mathbf{r}')+\eta A_0\delta(\mathbf{r}-\mathbf{r}')]-F[n(\mathbf{r}')]\right\}/(\eta A_0)$, assuring A_0 for the correct dimensions [28]. The Lagrange multiplier, μ, acts as the chemical potential of the system.

No guidance whatsoever was given by Hohenberg and Kohn for constructing the energy functionals explicitly. Nevertheless, their variational principle is general and rigorously based on quantum theory. The generality of DFT has been emphasized by many extensions as the work of Mermin [36] in 1965 to include finite temperature canonical and grand canonical ensembles, or the alternative definitions of Levy and Lieb [37, 38, 39].

1.3.1 Kohn-Sham equations

The real break-through in density functional theory came from the Ansatz made by Kohn and Sham [40] in 1965, which made possible the application of the previous theorems by the development of useful independent particle approaches. They proposed to replace the many body interacting electron system with a different *auxiliary independent particle system*, assuming that the ground state density of the original interacting system is equal to that of a non-interacting system of particles. This automatically leads to independent particle equations that are in principle exactly soluble with all the complexity of the many-body terms incorporated into an exchange-correlation functional of the density $E_{\mathrm{xc}}[n]$.

The set of Kohn-Sham (KS) equations for the auxiliary system of N_e non-interacting electrons are:

$$\left\{-\frac{1}{2}\nabla^2+v_{\mathrm{ext}}(\mathbf{r})+v_{\mathrm{H}}\left(\mathbf{r}\right)+v_{\mathrm{xc}}\left(\left[n\right];\mathbf{r}\right)\right\}\psi_i=\epsilon_i\psi_i \tag{1.11}$$

with

$$v_{\mathrm{H}}\left(\mathbf{r}\right)=\frac{\delta E_H}{\delta n\left(\mathbf{r}\right)}=\int\frac{n\left(\mathbf{r}'\right)}{\left|\mathbf{r}-\mathbf{r}'\right|}\mathrm{d}\mathbf{r}' \tag{1.12}$$

being the Hartree potential, which can be evaluated either by direct integration or by solving the equivalent differential Poisson equation,

$$\nabla^2 v_{\mathrm{H}}(\mathbf{r}) = -4\pi n(\mathbf{r}). \tag{1.13}$$

v_{xc} is the exchange-correlation potential, which is formally defined as

$$v_{\mathrm{xc}}([n];\mathbf{r}) = \frac{\delta E_{\mathrm{xc}}[n]}{\delta n(\mathbf{r})}. \tag{1.14}$$

The density of the auxiliary system is defined in terms of the Kohn-Sham wavefunctions by summing over occupied states:

$$n(\mathbf{r}) = \sum_{i}^{occ} |\psi_i(\mathbf{r})|^2. \tag{1.15}$$

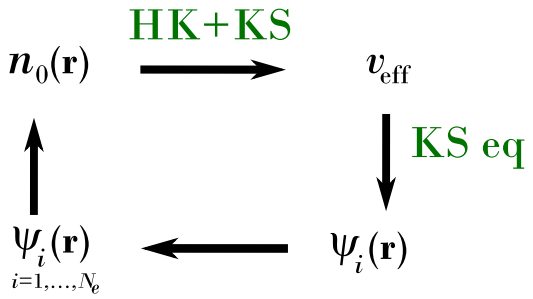

Figure 1.1: Schematic illustration of the self-consistent procedure to obtain the final total energy of the system. The solution of Eq. (1.11) produces the wavefunctions ψ_i to obtain the electronic density from Eq. (1.15), which is used to define the effective potential in Eq. (1.11), applying Hohenberg-Kohn theorem to the non-interacting problem (Kohn-Sham). An initial guess of the density od states must be made to start the process. This self-consistency cycle is repeated until the tolerance imposed on the difference η_n between the input and output density is reached: $\int \mathbf{dr} \left| n^{out} - n^{in} \right| < \eta_n$. The convergence criterium can be equivalently imposed on the difference of total energies. Finally, the solution obtained for the independent particle Kohn-Sham problem determines all properties of the full many-body system.

These equations correspond to the Schrödinger equation of a particle in an effective potential that has a functional dependence on n and results of the

external potential, the Hartree electronic interaction and the exchange and correlation potential:

$$v_{\text{eff}}(\mathbf{r}) = v_{\text{ext}}(\mathbf{r}) + v_{\text{H}}(\mathbf{r}) + v_{\text{xc}}(\mathbf{r}), \tag{1.16}$$

which must be found self-consistently, as illustrated in Fig. 1.1. The KS equations are independent of any approximation to the functional $E_{\text{xc}}[n]$, and they would lead to the exact ground state density if the exact form of $E_{\text{xc}}[n]$ was known. The accuracy is thus only limited by the approximations made in this exchange-correlation functional.

The Kohn-Sham Hamiltonian eigenvalues ϵ_i do not represent the excitation energies of the interacting many-body system. Only the highest eigenvalue associated to an occupied state in a finite system can be directly interpreted as being minus the ionization energy. Originally ϵ_i's are introduced as the Lagrange multipliers of the KS variational equations that ensure the orthonormality of the non-interacting particle wavefunctions. However, they allow to express the total energy of the ground state as:

$$\begin{aligned} E &= -\sum_{i}^{occ} \int \psi_i^*(\mathbf{r}) \frac{\nabla^2}{2} \psi_i(\mathbf{r})\, \mathrm{d}\mathbf{r} + \int v_{\text{ext}}(\mathbf{r}) n(\mathbf{r}) \mathrm{d}\mathbf{r} + E_{\text{H}} + E_{\text{xc}} \\ &= \sum_i n_i \epsilon_i + E_{\text{xc}}[n(\mathbf{r})] - \int v_{\text{xc}}(\mathbf{r}) n(\mathbf{r}) \mathrm{d}\mathbf{r} - \frac{1}{2} \int \frac{n(\mathbf{r}) n(\mathbf{r}')}{|\mathbf{r} - \mathbf{r}'|} \mathrm{d}\mathbf{r}\, \mathrm{d}\mathbf{r}' \end{aligned} \tag{1.17}$$

where usually $E_{\text{BS}} = \sum_i n_i \epsilon_i$ is defined as the band structure energy. The eigenvalue ϵ_i describes the first-order change of the total energy with respect to small changes of the orbital occupation number n_i. This relation is known as Janaks theorem [41]. A non rigorous interpretation of this equation associates ϵ_i with the energy levels occupied by the interacting electrons whereas the remaining terms are corrections to the energy due to the double counting of the electron-electron interaction included in E_{BS}. When performing geometry optimization or nuclear dynamics the repulsive Coulomb term corresponding to ion-ion interactions must be added to the total energy given by Eq. (1.17):

$$E_{\text{ii}} = \frac{1}{2} \sum_{\alpha,\beta} \frac{Z_\alpha Z_\beta}{|\mathbf{R}_\alpha - \mathbf{R}_\beta|}. \tag{1.18}$$

In order to solve the KS equations (1.11) it is necessary to reduce the problem to a finite number of variables. Except in the so-called real-space scheme, where functions are sampled in a real-space mesh (see for instance Ref. [42]),

this is done by expanding the unknown $\psi_i(\mathbf{r})$ in terms of known basis functions, χ_μ, as $\psi_i(\mathbf{r}) = \sum_\mu c_{\mu i}\chi_\mu(\mathbf{r})$.

Depending on the type of basis functions used in the expansion, two popular choices exist: plane waves and localized orbital methods. Plane waves are the simplest representation in the description of the wavefunctions. They are eigenfunctions of the Schrödinger equation with constant potential, and therefore they are natural basis for the description of bands in the nearly free electron approximation. They provide a simple derivation of the Bloch theorem when the Schrödinger equation is solved accounting for periodic boundary conditions with the crystal symmetry. On the other hand, localized orbital methods, usually referred as linear combination of atomic orbitals (LCAO) use basis functions that reproduce the essence of the atomic-like features of atoms in solids and molecules.

A further approximation usually taken is to introduce so-called pseudopotentials that describe the effect of the core electrons in the internal region of the atoms but leave everything unchanged outside this core region defined through a cutoff radius. These fictitious potentials describe the screening effects of the core electrons on the nuclear potentials and also the oscillatory behavior in the wavefunctions of the valence electrons around the core region that comes from the orthogonality of these wavefunctions with those of the core electrons. The description of these oscillations through the pseudopotentials saves high computational costs that would be required to describe them with an all-electron calculation (many more basis functions or real space grid points would be needed). A pseudopotential is usually generated in an atomic calculation and then used to compute the properties of valence electrons in molecules and solids.

1.3.2 Exchange and correlation

One key point in the success of the Kohn-Sham approach is that, though being the exchange and correlation functional ($E_{\mathrm{xc}}[n]$) unknown, it can be reasonably approximated by a local or nearly local functional of the density, by the explicit separation of the independent particle kinetic energy and long-range Hartree terms. That is, the exchange and correlation functional can be written as

$$E_{\mathrm{xc}}[n] = \int n(\mathbf{r})\varepsilon_{\mathrm{xc}}\left([n(\mathbf{r})]\,,\mathbf{r}\right)\mathrm{d}\mathbf{r}, \tag{1.19}$$

with $\varepsilon_{\mathrm{xc}}\left([n(\mathbf{r})]\,,\mathbf{r}\right)$ being the exchange and correlation energy density per electron at point $\mathbf{r}$.

Even though the exact form of $E_{xc}[n]$ has to be very complex, a lot of progress has been made with remarkable simple approximations. Perhaps the most relevant ones are the local density approximation and the generalized-gradient approximation, which we will shortly comment here. In the local density approximation (LDA), $E_{xc}[n]$ is an integral of the exchange-correlation energy over all space, in which the ε_{xc} is assumed to be the same as in an homogeneous electron gas with that density ($\varepsilon_{xc}^{LDA} = \varepsilon_{xc}^{hom}$):

$$E_{xc}^{LDA}[n] = \int n(\mathbf{r}) \varepsilon_{xc}^{LDA}(n(\mathbf{r}))\, \mathbf{dr}. \tag{1.20}$$

This approximation is expected to be best when $n(\mathbf{r})$ is smooth, *i.e.*, for solids close to the homogeneous electron gas. Though it also seems to work for inhomogeneous cases, such as molecular systems where the density has to go continuously to zero outside the atom, for some systems the generalized-gradient approximation (GGA) proves to be a better one. However, the validity of the local approximation must be checked with experimental results for the given system.

The generic formulation of the GGA approximation to $E_{xc}[n]$ is:

$$E_{xc}^{GGA}[n] = \int n(\mathbf{r}) \varepsilon_{xc}^{GGA}(n(\mathbf{r}), |\nabla n(\mathbf{r})|)\, \mathbf{dr}, \tag{1.21}$$

which is the first step beyond the local approximation, including not only a dependence on the local density but also on gradients of the density, allowing to take into account the variations of the electronic density that characterize very inhomogeneous systems. A gradient expansion approximation was even already suggested in the original paper of Kohn and Sham.

To preserve the desired properties in GGA the exchange-correlation energy is expressed as (see *i.e.* [43]):

$$E_{xc}^{GGA} = \int n(\mathbf{r}) \varepsilon_{xc}^{hom}(n(\mathbf{r}))\, F_{xc}(n(\mathbf{r}), |\nabla n(\mathbf{r})|)\, \mathbf{dr} \tag{1.22}$$

where the dimensionless function F_{xc} is required to satisfy a series of formal conditions related to the exchange and correlation hole.

1.4 Computational length scales

We can generally assign a length scale to any solid scale computational technique, which constitutes a measurement of the applicability range of the

method. Primarily this length is dependent on the scaling properties of the computational scheme, but other factors such as the optimization of numerical libraries or the availability of parallelization techniques play an important role. The assignment of such a length is not a precise task but it helps in order to have a quick comparison factor to evaluate different techniques.

Density functional theory scales in typical calculations as N^3, though as it will be seen in Sec. 1.5, order-N methods are already available. A large number of codes implementing this scheme of electronic structure calculations exit nowadays, and typical systems studied with these codes consist of hundreds and even thousand atoms. The length characterizing DFT methods can be estimated to be of around 10^2 Å.

Tight-binding calculations on the other hand, based on the fact that a relative small set of parameters is needed to express the Hamiltonian and these parameters are then calculated or fitted from experiments, but in general this process is not a self-consistent one. For these reason this computational scheme can be used to study large scale systems. The characteristic length associated with this method is therefore much larger than the previous one and can be set to be of circa 10^6 Å.

1.5 The SIESTA method

The DFT code *SIESTA* (Spanish Initiative for Electronic Simulations with Thousands of Atoms) is a flexible LCAO method based on the use of numerical atomic orbitals of finite support to expand the electron wavefunctions [44, 45]. The choice of a localized basis is made since they allow the construction of the Hamiltonian and overlap matrices in $\mathcal{O}(N)$ operations. It is an "ab initio" (or "from first principles") methodology as there are no free parameters in the calculations.

Exchange and correlation are treated within Kohn-Sham DFT, either with the local spin density or with generalized gradient approximations. Standard norm-conserving pseudopotentials [46]in their fully nonlocal form [47] are used, usually adopting the Troullier-Martins parametrization [48], but other parametrizations can be given by the code user.

As already mentioned, SIESTA is based on a flexible LCAO basis set, with essentially $\mathcal{O}(N)$ scaling. These orbitals are localized, *i.e.* defined to be zero beyond a specified cutoff radius. This condition assures the sparsity of the Hamiltonian and overlap matrices, a necessary requirement for the $\mathcal{O}(N)$ scaling. Within the cutoff radius, the basis orbitals are given by the product

of a spherical harmonic times a radial function as in Eq. (1.9), where there will be several orbitals with the same angular dependence, but different radial dependence, which is conventionally called a "multiple-ζ" basis. The radial functions are defined by a cubic spline interpolation from the values given on a fine radial grid. The generation of the basis set, like that of the pseudopotential, is to a large extent up to the user and independent of the SIESTA method itself. Nevertheless automatic procedures are included based in the numerical atomic orbitals originally proposed by Sankey and Niklewski [49], which are implemented also in other codes such as FIREBALL [50]. Soft confining potentials for the radial Schrödinger equation for the corresponding orbital instead of hard ones are implemented in SIESTA as proposed by Junquera *et al.* [51].

The basis functions and the electron density are projected on a real-space grid, in order to calculate the Hartree and exchange-correlation potentials and matrix elements, with a number of operations that scales linearly with the size of the system. Some terms of the Hamiltonian and overlap matrix elements are calculated in a real space grid and others in the Fourier space. The simplest ones to calculate in $\mathcal{O}(N)$ operations are those involving two-centre integrals between overlapping orbitals, because each orbital overlaps only with a small number of other orbitals, independent of the system size, as well as the two-centre integrals of the Hamiltonian, which are the terms involving the kinetic energy operator. All of these are calculated in Fourier space, using convolution techniques, and stored as a product of spherical harmonics times numerical radial functions, interpolated in a fine radial grid.

To evaluation of $n(\mathbf{r})$ is an $\mathcal{O}(N)$ operation as for a given point $\mathbf{r}$, only a few orbitals are nonzero and contribute to the sum in Eq. (1.15). From $n(\mathbf{r})$ the Hartree potential $v_{\mathrm{H}}$is calculated using fast Fourier transforms. The exchange and correlation potential v_{xc} is computed in LDA or GGA approximations, the latter using finite difference derivatives. The total effective potential v_{eff} is calculated by adding the local pseudopotentials of all the atoms to $v_{\mathrm{H}} + v_{\mathrm{xc}}$. Since both v_{H} and the local part of the pseudopotentials have long range parts with opposite signs, the electrostatic potential created by a reference density (the sum of the electron densities of the free atoms) is subtracted to each of them. Finally the matrix elements $\langle \chi_\mu | V_{eff} | \chi_\nu \rangle$ are calculated by direct integration in the grid points. Also here, the effort of this step has $\mathcal{O}(N)$ scaling, since the number of nonzero orbitals at each grid point is independent of the system size.

The evaluation of the total energy, atomic forces, and stress tensor, proceeds simultaneously to that of the Hamiltonian matrix elements, using the last density matrix available during the self consistency process.

Once the Hamiltonian and overlap matrices have been calculated, a new density matrix is obtained either by: (*i*) solving the generalized eigenvalue problem by conventional $\mathcal{O}(N^3)$ methods of linear algebra, or (*ii*) using the $\mathcal{O}(N)$ orbital minimization method of Kim *et al.* [52, 53], for which a modified energy functional is used, whose minimization produces orthogonal wavefunctions and the same energy and density as the Kohn-Sham energy functional, without the need for an explicit orthogonalization.

The reader is referred to the cited literature for a deeper knowledge of the characteristics of this widely used method.

1.6 The density functional based tight-binding (DFTB) method

One appropriate approach to calculate extended systems with reasonable computational costs is the self-consistent, nonorthogonal density functional based tight-binding (DFTB) scheme developed by Porezag *et al.* [54], in which the Hamiltonian and overlap matrix elements are tabulated beforehand on the basis of self-consistent DFT-LDA linear combination of atomic orbitals LCAO calculations, retaining only two-center contributions to the Hamiltonian matrix elements. The procedure for the determination of the desired matrix elements is well-defined and does not involve any fitting. This method is an extension of the tight-binding formalism described in Sec. 1.2 and is a good compromise between the sophisticated but much more computationally expensive *ab initio* or first principles techniques and the simple empirical potentials, which lack transferability (*e.g.* [55]).

The original formulation of DFTB was given by Seifert, Eschrig and Bieger [56, 57] around 1985, applying the formalism of optimized linear combination of atomic orbitals (O-LCAO) as introduced by Eschrig and Bergert for band structure calculations [58]. In this approximation, the Kohn-Sham orbitals ψ_i of the system, solutions of Eq. (1.11), are expanded in terms of atom-centered localized basis functions φ_ν:

$$\psi_i(\mathbf{r}) = \sum_{\nu}^{M} c_{\nu i}\varphi_\nu(\mathbf{r} - \mathbf{R}_\alpha^\nu) \tag{1.23}$$

where M is the total number of basis functions and $\mathbf{R}_\alpha^\nu$ the center of the function φ_ν. As a result of the expansion, the Kohn-Sham equations, Eq. (1.11),

are transformed into a set of algebraic equations:

$$\begin{aligned} &\sum_{\nu=1}^{M} \left(\mathcal{H}_{\mu\nu} - \epsilon_i \mathcal{S}_{\mu\nu}\right) c_{\nu i} = 0 \quad \forall \mu, i \\ &\mathcal{H}_{\mu\nu} = \left\langle \varphi_\mu \right| \mathcal{H} \left| \varphi_\nu \right\rangle, \; \mathcal{S}_{\mu\nu} = \left\langle \varphi_\mu \right| \left. \varphi_\nu \right\rangle \end{aligned} \tag{1.24}$$

The first step (i) is thus the creation of the wavefunctions to expand the Kohn-Sham orbitals as in Eq. (1.23), then (ii) the Hamiltonian and overlap matrix elements of Eq. (1.24) must be calculated. With the definition of the Hamiltonian the band structure energy E_{BS} can be obtained as seen in Eq. (1.17). The corrections terms in this equation can be approximated by a short-range repulsive potential [59, 60, 61], which here is assumed to be a pair potential:

$$E \approx E_{\mathrm{BS}} + \sum_{\alpha}^{N_i} \sum_{\beta>\alpha}^{N_i} V_{\mathrm{rep}} \left(\left| \mathbf{R}_\alpha - \mathbf{R}_\beta \right| \right) \tag{1.25}$$

The last step (iii) is to determine the repulsive contributions V_{rep}.

(i) Creation of (spin-unpolarized and spherically symmetric) pseudoatomic wavefunctions

The Kohn-Sham orbitals of free atoms do not represent a very efficient basis for condensed systems. Therefore Eschrig *et al.* [58] suggested to improve them introducing an optimized set of pseudoatomic orbitals, which can be obtained by solving self-consistently a modified Kohn-Sham equation for an isolated atom, with an effective one-particle potential v_{eff} approximated by

$$v_{\mathrm{eff}}^{\mathrm{psat}} \simeq V^{\mathrm{psat}} \left(|\mathbf{r}| \right) + \left(\frac{|\mathbf{r}|}{r_0} \right)^n . \tag{1.26}$$

The last term forces the electrons to avoid areas far away from the nucleus, thus resulting in wavefunctions that are more short-range (contracted) in comparison to those of the free atom, and solving in this way many numerical difficulties. For small molecules though the contraction of the wavefunction may also be omitted. The potential V^{psat} deviates from that of the free spin-unpolarized and spherically symmetric atom in such a way that

$$\sum_{\alpha}^{N_i} v_{\mathrm{eff}}^{\mathrm{psat}} \left(|\mathbf{r} - \mathbf{R}_\alpha| \right) \approx v_{\mathrm{eff}}^{\mathrm{wholeKSsystem}} \tag{1.27}$$

The parameters n and r_0 to be fitted for every atom type are also chosen in such that this condition is fulfilled. The exchange and correlation potential included in V^{psat} (free atom potential) is expressed in terms of the local density approximation as parameterized by Perdew and Zunger [62].

(ii) Calculation of the matrix elements

The eigenfunction solutions of the Kohn-Sham equation with effective potential $v_{\text{eff}}^{\text{wholeKSsystem}}$ as described in Eq. (1.27) and Eq. (1.26), $\varphi_\nu^{\text{psat}}$, are then used as a basis set for the LCAO treatment of the whole non-interacting system. In DFTB only valence orbitals are considered, that is, it restricts to a minimal basis description.

The overlap matrix elements which are at most two-center terms are calculated directly. For the Hamiltonian matrix elements only two-center Hamiltonian matrix elements are treated, and consistently with the previously made approximations for v_{eff}, several contributions have to be neglected, approximating the integral as

$$\mathcal{H}_{A\mu\,B\nu} = \begin{cases} \varepsilon_{A\mu} \text{ (free atom)} & \text{if } \mu = \nu \text{ and } A = B \\ \left\langle \varphi_\mu^A \left| T + V_A^{\text{psat}} + V_B^{\text{psat}} \right| \varphi_\nu^B \right\rangle & \text{if } \mu \neq \nu \\ 0 & \text{otherwise} \end{cases} \tag{1.28}$$

The indices A and B indicate the atom on which the wavefunctions and the potentials are centered and μ and ν the basis orbital. Since the diagonal elements of the Hamiltonian are determined by the eigenvalues of the free atom, the correct limit for large distances is guaranteed.

Due to the fact that all matrix elements depend only on interatomic distances, they need to be calculated only once for each pair of atom types and can be stored as a function of the interatomic distance. Matrix elements corresponding to any given interatomic distance may be easily obtained by interpolating between the stored values.

(iii) Determination of the repulsive potential

The short-range repulsive potential V_{rep} is the difference between the band structure energy E_{BS} and the total energy resulting from a self-consistent LDA calculation:

$$E_{\text{rep}} = E_{\text{LDA}}^{sc} - E_{\text{BS}} \tag{1.29}$$

V_{rep} is then obtained by a fitting procedure, where the following Ansatz is made for the potential:

$$V_{\text{rep}} = \begin{cases} \sum_{n=2}^{5} d_n \left(R_c - R\right)^n & \text{for } R < R_c \\ 0 & \text{otherwise} \end{cases} \tag{1.30}$$

This Ansatz guarantees that V_{rep} vanishes for $R \geq R_c$. The polynomial expansion goes usually up to polynomials of order 5, but the range of n can be varied. The two adjustable parameters d_n and R_c are determined by fitting the vibrational frequency and equilibrium distance of the corresponding diatomic molecules.

To improve the description of systems with a substantial amount of transferred charge, a second-order expansion of the Kohn-Sham total energy, Eq. (1.17), with respect to charge density fluctuations is made [63]. The second-order term in the expansion can be approximated by

$$E_2 \approx \frac{1}{2} \sum_{A}^{N_i} \sum_{B}^{N_i} \gamma_{AB} \left(q_A - q_A^0\right) \left(q_B - q_B^0\right) \tag{1.31}$$

where the sums run over the system ions, q^0 is the charge of the neutral atom and where

$$\gamma_{AB} = \frac{1}{\sqrt{\left|\mathbf{R}_A - \mathbf{R}_B\right|^2 + \frac{1}{4}\left(\frac{1}{U_A} + \frac{1}{U_B}\right)^2}} \tag{1.32}$$

with U being the difference of the experimental ionization energy and electron affinity. It is frequently called chemical hardness and can be determined for each atom type from a self-consistent LDA calculation as the second derivative of the total energy with respect to the atomic charge:

$$U = \left.\frac{\partial^2 E^{\text{at}}}{\partial q^2}\right|_{q=q^0} \tag{1.33}$$

The expression of Eq. (1.31) guarantees the correct limit for $|\mathbf{R}_A - \mathbf{R}_B| = 0$ and a smooth transition to Coulomb-like behavior as $|\mathbf{R}_A - \mathbf{R}_B|$ increases. The DFTB total energy described by Eq. (1.25) is then extended to become:

$$E \approx E_{\text{BS}} + \sum_{\alpha}^{N_i} \sum_{\beta>\alpha}^{N_i} V_{\text{rep}}\left(\left|\mathbf{R}_\alpha - \mathbf{R}_\beta\right|\right) + \frac{1}{2} \sum_{A}^{N_i} \sum_{B}^{N_i} \gamma_{AB} \left(q_A - q_A^0\right) \left(q_B - q_B^0\right).$$

(1.34)

Besides the usual short-range repulsive terms the final approximate Kohn-Sham energy additionally includes a Coulomb interaction between charge fluctuations.

The eigenvalue problem of Eq. (1.24) is modified then accordingly, yielding the expression

$$\sum_{\nu=1}^{M} \left(\tilde{\mathcal{H}}_{\mu\nu} - \epsilon_i \mathcal{S}_{\mu\nu}\right) c_{\nu i} = 0, \tag{1.35}$$

where the Hamiltonian matrix elements $\tilde{\mathcal{H}}_{\mu\nu}$ differ from those given in Eq. (1.30) as

$$\tilde{\mathcal{H}}_{\mu\nu} = \mathcal{H}_{\mu\nu} + \frac{1}{2}\mathcal{S}_{\mu\nu} \sum_{D}^{N_i} (\gamma_{AD} + \gamma_{BD}) \left(q_D - q_D^0\right), \quad \text{with } \mu \in A,\, \nu \in B. \tag{1.36}$$

To derive this expression, Mulliken charges have been used to define the atomic charges:

$$q_A = \frac{1}{2} \sum_{i}^{occ} n_i \sum_{\mu \in A} \sum_{\nu} \left(c_{\mu i}^* c_{\nu i} \mathcal{S}_{\mu\nu} + c_{\nu i}^* c_{\mu i} \mathcal{S}_{\nu\mu}\right). \tag{1.37}$$

Note that Hamiltonian matrix elements $\tilde{\mathcal{H}}_{\mu\nu}$ depend now on the charges and therefore on the expansion coefficients $c_{\nu i}$ themselves, so that the problem needs to be solved self-consistently. Nevertheless, such a DFTB calculation is still at least two orders of magnitude faster than a full-potential self-consistent LDA calculation.

This method together with the quantum transport calculation techniques described in Chapter 2 are applied in Chapter 7 in the implementation "gDFTB" [64, 65] which has been successfully applied in transport problems in molecular systems.

Chapter 2

Coherent quantum transport calculations

In this chapter, we will give a brief introduction to the theory of transport in systems ranging from the mesoscopic to the molecular scale. Mesoscopic conductors are much larger than objects like atoms, but smaller than macroscopic ("ohmic") conductors like ordinary metal wires. We will start presenting the classification of transport due to the correlation between the size of the conductor and the characteristic transport lengths. Then, we will introduce the Landauer approach to transport in mesoscopic systems and the linking between the Landauer formula and the Green functions.

2.1 Transport classification: Characteristic lengths

The transport behavior of a conductor is usually classified by the interplay between its length L and the characteristic transport lengths. We will next discuss the relevant lengths connected to the motion of the electrons in a material (see Ref. [66, 67]).

2.1.1 Fermi wavelength (λ_F)

An important quantity is the wave length of the conducting electrons. As the current is effectively carried by a small fraction of the total electrons, those

with energies close to the Fermi energy. We can thus write

$$\lambda_F = \frac{2\pi}{k_F} = \frac{2\pi\hbar}{m v_F}, \tag{2.1}$$

where k_F is the Fermi wavenumber, v_F is the Fermi velocity, and m is the effective mass which incorporates the effects of the lattice potential.

In typical metals such as copper and silver λ_F is of the order of few Ångstroms, while in semiconductor heterostructures, in a two-dimensional electron gas, it can reach considerable values of about $\lambda_F \sim 400\,\text{Å}$ (see Sec. 2.1.6).

2.1.2 System size (H, W, L)

The ratio between the size of the system at hand and the Fermi wavelength of the conduction electrons in it, determines the relevant physics of the device. For simplicity, consider a system as sketched in Fig. 2.1, confined in all three spacial directions in a box of dimensions (H, W, L). As schematically drawn we will on the following assume $H < W < L$.

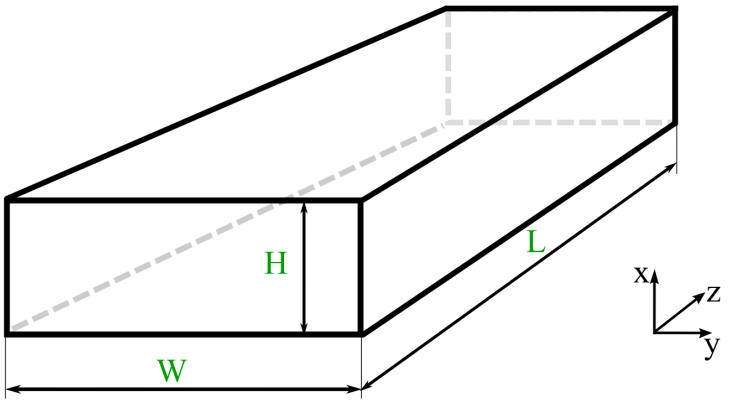

Figure 2.1: Box defining the characteristic dimensions of a finite system, of length L, width W, and height H.

The relation between the Fermi wavelength and H, W, and L allows us to defined the dimensionality of the system. In particular, we can identify the different classes of devices simply with the help of the inequalities shown in Table 2.1.

The energy of the confined electron in this box would be

$$E\left(n_x, n_y, n_z\right) = \frac{\hbar^2}{2m}\left[\left(\frac{\pi n_x}{H}\right)^2 + \left(\frac{\pi n_y}{W}\right)^2 + \left(\frac{\pi n_z}{L}\right)^2\right], \tag{2.2}$$

Condition	Dimensionality	Examples
$\lambda_F \ll H$	3D	bulk crystals
$\lambda_F \sim H$	quasi-2D	thin films
$H < \lambda_F \ll W$	2D	MOSFET, graphene near E_F
$W \sim \lambda_F < L$	quasi-1D	quantum wires
$W < \lambda_F < L$	1D	CNTs near E_F
$L < \lambda_F$	0D	quantum dots

Table 2.1: Rough classification of finite systems according to their dimensionality.

with n_x, n_y, n_z integer quantum numbers identifying the electronic state. If for instance $W \ll \lambda_F$, energy levels with different n_y will be very far apart and only that with the lowest n_y will be occupied. That is, the y direction is frozen and we have practically a one-dimensional system if still $L > \lambda_F$.

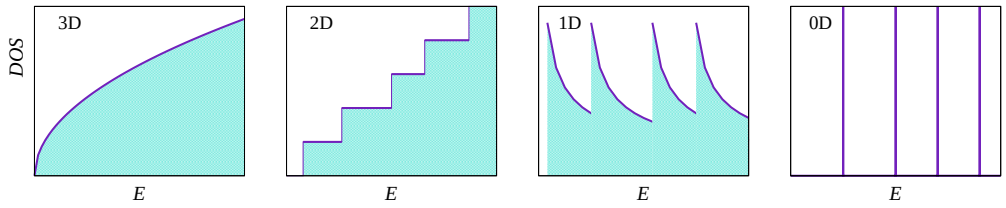

Figure 2.2: Density of states (DOS) as characteristic of non-interacting electrons in three to zero dimensions.

If, according to the Table 2.1, the system can be classified as three-dimensional (3D), Eq. (2.2) can be rewritten introducing continuous variables as

$$E\left(k_x, k_y, k_z\right) = \frac{\hbar^2}{2m}\left(k_x^2 + k_y^2 + k_z^2\right), \tag{2.3}$$

since the energy spectrum is continuous. The corresponding density of states N is thus

$$N\left(E\right) = \sum_{\mathbf{k}\,\sigma} \delta\left(E - \frac{\hbar^2|\mathbf{k}|^2}{2m}\right) = \frac{V}{\pi^2\hbar^3}\sqrt{2m^3E}, \tag{2.4}$$

where $\mathbf{k} = \left(k_x, k_y, k_z\right)$, σ runs over the two possible spin states and $V = H \times W \times L$ is the bulk volume. The typical square root shape of the density of states of such a bulk system can be seen in Fig. 2.2.

In the case of a two-dimensional system, where the electron motion in one direction is quantized into discrete electric subbands but has an unlimited two-dimensional k-space, the dispersion relation reads

$$E(\mathbf{k}) = \frac{\hbar^2}{2m}\left(k_y^2 + k_z^2\right) + \frac{\hbar^2}{2m}\left(\frac{\pi n_x}{H}\right)^2 = \frac{\hbar^2}{2m}\left(k_y^2 + k_z^2\right) + E_{n_x}, \quad (2.5)$$

and the corresponding density of states shows therefore a step-like behavior as observed in Fig. 2.2:

$$N(E) = \sum_{\mathbf{k}\sigma} \delta\left(E - \frac{\hbar^2|\mathbf{k}|^2}{2m} - E_{n_x}\right) = \frac{Sm}{\pi\hbar^2}\sum_{n_x}\Theta\left(E - E_{n_x}\right), \quad (2.6)$$

with the area $S = W \times L$ and Θ being the Heaviside function.

For a one-dimensional system, the energy spectrum corresponds to

$$E(\mathbf{k}) = \frac{\hbar^2 k_z^2}{2m} + \frac{\hbar^2}{2m}\left[\left(\frac{\pi n_x}{H}\right)^2 + \left(\frac{\pi n_y}{W}\right)^2\right] = \frac{\hbar^2 k_z^2}{2m} + E_{n_x} + E_{n_y}, \quad (2.7)$$

from which square root divergences in the density of states are obtained:

$$N(E) = \sum_{\mathbf{k}\sigma} \delta\left(E - \frac{\hbar^2 k_z^2}{2m} - E_{n_x} - E_{n_y}\right) = \frac{L}{\pi\hbar}\sum_{n_x n_y}\frac{\sqrt{2m}}{\sqrt{E - E_{n_x} - E_{n_y}}}. \quad (2.8)$$

This characteristic behavior of one-dimensional systems (Fig. 2.2) will later on be observed in the nanotube-systems studied.

If an additional confinement is imposed on the electron motion, so that it has restrictions in all three dimensions, one comes back to the zero-dimensional box with a dispersion relation given by Eq. (2.2). The energy spectrum is hence built by discrete levels, and the density of states is composed by series of delta-function peaks as

$$N(E) = \sum_{n_x n_y n_z} \delta\left(E - E_{n_x} - E_{n_y} - E_{n_z}\right). \quad (2.9)$$

2.1.3 Elastic mean free path (ℓ_m)

An electron moving in a real crystal, *i.e.* with impurities, lattice vibrations and other electrons, experiences collisions which change its state. We define the time between two scattering processes which lead to a change in the electron momentum as the momentum relaxation time τ_m. The time between

any two scattering processes is the collision time τ_c. The relation between these two characteristic time scales is given by

$$\frac{1}{\tau_c} \longrightarrow \frac{1}{\tau_m}\alpha_m, \qquad \text{with} \quad 0 \leq \alpha_m \leq 1, \tag{2.10}$$

the factor α_m describing the efficiency by which an individual collision changes the momentum of the electron. If the electron has been scattered only by a small angle, the momentum loss, and therefore α_m, is very small so that the momentum relaxation time is much longer than the collision time.

The momentum change is given by scattering processes which do not change the electron energy, usually scattering to impurities or interfaces. Since the electron energy is conserved, the phase of the wave function is also conserved.

The length corresponding to the momentum relaxation time is the mean free path ℓ_m. The mean free path is the average distance an electron can travel before its initial momentum has been destroyed. It is given by the relation

$$\ell_m = v_F \, \tau_m. \tag{2.11}$$

2.1.4 Phase relaxation length (ℓ_φ)

In analogy to the expression for τ_m, Eq. (2.10), we can relate a phase relaxation time τ_φ to τ_c through a factor α_φ describing the efficiency by which a collision changes the energy and therefore the phase of the electron:

$$\frac{1}{\tau_c} \longrightarrow \frac{1}{\tau_\varphi}\alpha_\varphi, \qquad \text{with} \quad 0 \leq \alpha_\varphi \leq 1. \tag{2.12}$$

The phase relaxation length ℓ_φ, or phase coherent length, denotes the average distance an electron can travel with a well defined phase. Since changes in the phase information affect the ability of the electron waves to interfere, we will not expect interference effects for lengths exceeding ℓ_φ. Examples of scattering events changing the energy of the electrons are scattering to lattice vibrations, electron-electron scattering, or more generally the interaction with a dynamic scatterer with some kind of degree of freedom with which the electron exchanges energy. That is, rigid scatterers do not contribute to phase relaxation; only fluctuating scatterers are phase-randomizing. At low temperatures the dominant source of phase relaxation is the electron-electron scattering, which nevertheless tends to zero with the temperature as the exclusion principle suppresses the states an electron can scatter into.

Since not all the scattering events are inelastic, generally $\ell_\varphi > \ell_m$. Though, if the phase relaxation time is of the same order of the momentum relaxation time, that is $\tau_\varphi \sim \tau_m$, we get the following relation between τ_φ and ℓ_φ:

$$\ell_\varphi = v_F \tau_\varphi. \tag{2.13}$$

If the momentum relaxation time is much shorter than the phase relaxation time, $\tau_\varphi \gg \tau_m$, the trajectory of an electron over a phase relaxation time can be seen as sum of short trajectories of length $\sim \ell_m$. In this case, the relation between the phase relaxation length and the phase relaxation time is given by

$$\ell_\varphi^2 = D\tau_\varphi, \tag{2.14}$$

with $D = v_F^2 \tau_m / 2$ being the diffusion constant. This result is obtained since we average over all directions, as the trajectories after the scattering event are directed randomly:

$$\ell_\varphi^2 = \frac{\tau_\varphi}{\tau_m} \ell_m^2 \left\langle \cos^2\theta \right\rangle \quad \text{where} \quad \left\langle \cos^2\theta \right\rangle \equiv \int_{-\pi}^{\pi} \frac{d\theta}{2\pi} \cos^2\theta = \frac{1}{2}. \tag{2.15}$$

Summarizing: elastic scattering, for example to static impurities or interfaces, conserves the energy of the electron and therefore the phase, but changes the momentum, so that $\alpha_m \neq 0$ but $\alpha_\varphi = 0$. Electron-electron scattering changes the energy of the electron but does not affect ℓ_m. Since any momentum lost by one electron is picked up by another, there is no change in the net momentum, so $\alpha_m = 0$ but $\alpha_\varphi \neq 0$. Inelastic scattering, for example to lattice vibrations (phonons) or impurities with an internal degree of freedom, which allows them to change the state, lead to a change of both the energy and the momentum, $\alpha_m \neq 0$, $\alpha_\varphi \neq 0$.

2.1.5 Transport classification

For a sample of length L we can distinguish between several transport regimes, depending on the relation between L and the characteristic transport lengths [68].

We speak of *ballistic transport* if $L < \ell_m$, of *diffusive transport* if $L > \ell_m$ (see Fig. 2.3), of *phase coherent transport* if $L < \ell_\varphi$, and of *phase incoherent transport* if $L > \ell_\varphi$. Classical conductors, which show *ohmic transport* behavior, are both in the diffusive and phase incoherent transport regime,

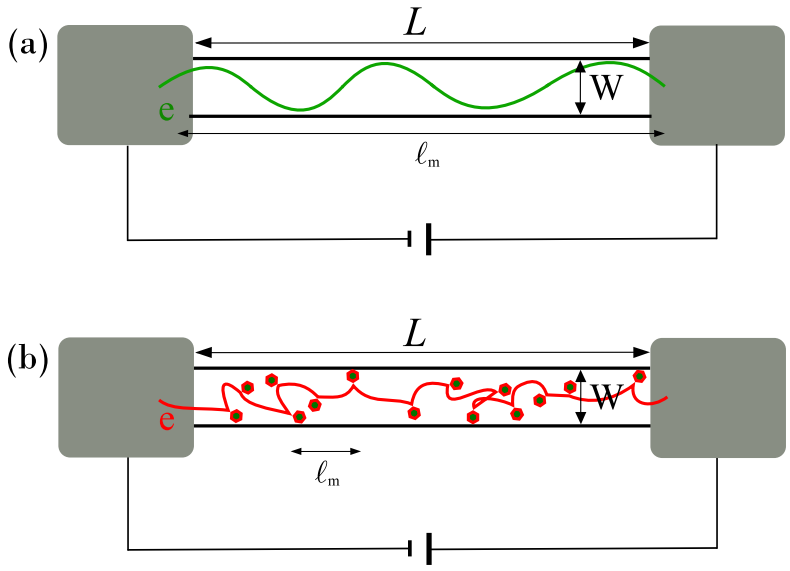

Figure 2.3: Schematic illustration of the difference between a (a) ballistic and a (b) diffusive conductor, where many scattering events can take place during transport through it.

$L \gg \ell_m, \ell_\varphi, \lambda_F$. Usually one refers to a sample as a ballistic conductor (with effectively no scattering) when the sample shows both ballistic and phase coherent transport behavior, $L \ll \ell_m, \ell_\varphi$. In this case the energy is not dissipated as resistance in the device and the current can be calculated using the Landauer formalism (see Sec. 2.2). In analogy it is usually referred to a diffusive conductor when $L \gg \ell_m, \ell_\varphi$. In this case ℓ_φ is rather short and quantum interference is averaged out. The transport is then described by Boltzmann equations, which govern the evolution of the electron momentum distribution [69]. These facts are summarized in Table 2.2.

$L < \ell_m$	ballistic	$L \gg \ell_m$	diffusive
$L < \ell_\varphi$	phase coherent	$L \gg \ell_\varphi$	incoherent
$L < \lambda_F$	size quantization	$L \gg \lambda_F$	no size quantization

Table 2.2: Classification of transport regimes. The left column shows those features that might be present in mesoscopic devices, whereas the characteristics shown in the right column are all present in so-called conventional devices.

The classification of the different transport regimes is not to be taken as completely rigorous, and there are for instance devices where the electrons behave ballistically at low temperature and diffusively at high temperatures. These are difficult situations as some hybrid descriptions crossing different transport regimes are needed.

Theoretical works predicted the possibility of ballistic transport in metallic SWCNTs [70, 71]. By now, this prediction has been confirmed by different experiments, revealing ballistic transport with mean free paths and phase coherent lengths of order of microns, both for SWCNTs and commensurate MWCNTs, even at room temperature [72, 73, 74, 75, 76]. It has been also shown that transport through CNTs is strongly dependent on the purity of the sample and on the transparency of the contacts [77].

2.1.6 Length scales

Let us make some estimations of the order of magnitude of the quantities described in the previous sections. We first make a rough calculation of the Fermi wavenumber k_F, assuming a parabolic dispersion relation characteristic of a free electron gas:

$$E = \frac{\hbar^2 k^2}{2m}, \tag{2.16}$$

measured from the bottom of the subband (set as the zero of energies). For a two-dimensional gas the density of states per unit area is given by Eq. (2.6) or it can be equivalently calculated as the energy derivative of the number of possible states

$$N(E) = \frac{1}{S}\frac{d}{dE}\left[2\frac{\pi k^2}{4\pi^2/S}\right] = \frac{m}{\pi\hbar^2}, \tag{2.17}$$

with S being the area of the conductor, πk^2 the area enclosed by the circle in the momentum space with radius $k(E)$, and $4\pi^2/S$ the area of an individual state, as the k vectors take quantized values due to the finite dimensions of the sample.

The equilibrium electron density n is obtained by integration of the previously introduced $N(E)$ with a weight given by the Fermi distribution function $f(E) = [1 + \exp[(E - E_F)/k_B T]]^{-1}$, where E_F and k_B are the Fermi energy and the Boltzmann constant respectively. For low enough temperatures, the

Fermi distribution is very accurately described by a simple step function: $f(E) \approx \Theta(E_F - E)$. Thus

$$n = \int N(E) f(E) \, dE = \frac{m}{\pi\hbar^2} E_F. \tag{2.18}$$

Applying once more the parabolic dispersion relation we obtain the estimation of k_F as follows:

$$k_F = \sqrt{2mE_F/\hbar^2} = \sqrt{2\pi n} \tag{2.19}$$

For an electron density in a sample of $5 \times 10^{11}\,\mathrm{cm}^{-2}$, we can estimate a value for λ_F (see Eq. (2.1)) of $\lambda_F \approx 354\,\text{Å}$. Moreover the Fermi wavelength is extremely sensitive on dimensionality since

$$n \propto \begin{cases} k_F^3 & (3D), \\ k_F^2 & (2D), \\ k_F & (1D). \end{cases} \tag{2.20}$$

For the density value given above, the $(2D)$ Fermi velocity is $\sim 293\,\mathrm{km/s}$ for an effective mass $m = 0.07 m_e$, that is, approximately two orders of magnitude smaller than the free electron mass. Assuming a momentum relaxation time of $100\,\mathrm{ps}$, the mean free path, Eq. (2.11), has a value of $\ell_m \approx 29.3\,\mu\mathrm{m}$. This quantity depends strongly on the metallicity and purity of the material, and it could also be as small as of the order of a few atomic planes, that is a few Å. Since not all scattering events are inelastic, generally $\ell_\varphi > \ell_m$, an estimated value could be one order of magnitude greater than ℓ_m, but its value also depends strongly on the sample and the temperature.

It is important to compare these length scales with the range of applicability of modern quantum mechanical methods (see Sec. 1.4).

2.2 Landauer approach to quantum transport

The Landauer approach [14, 78] has proved to be a very useful tool in describing the transport in mesoscopic systems, by expressing the current through a conductor in terms of the probability of an electron to be transmitted through it, that is, the transmission probability.

Landauer related the linear response conductance to the transmission probability. Later this formalism was extended to multiterminal devices and magnetic fields, being called the Landauer-Büttiker approach.

2.2.1 Conductance of a ballistic conductor

Let us consider a ($2D$) ballistic conductor smoothly connected to two bulk contacts, that is, where electrons can be fed to and absorbed from the conductor without any scattering (see Fig. 2.4). The contacts have chemical potentials μ_1 (left lead) and μ_2 (right lead), with $\mu_1 - \mu_2 \to 0^+$. Let us assume that the applied voltage generating this chemical potential difference drops entirely across the conductor, that is, the leads are infinitely more conducting than the central region. For simplicity we will assume zero temperature, so that Pauli exclusion principle prevents electrons with an energy outside the window $\mu_1 > E > \mu_2$ to flow through the system.

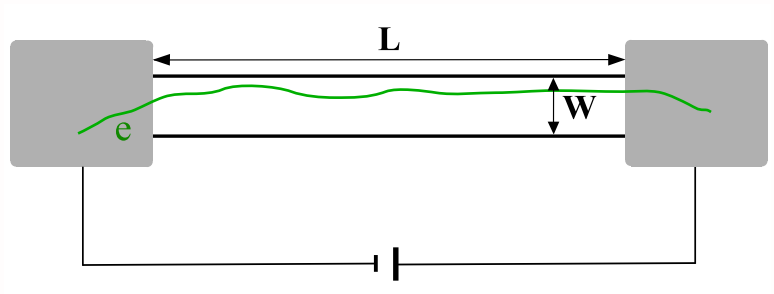

Figure 2.4: Schematic description of a ballistic device with a ballistic conductor between two bulk contacts at different external chemical potentials when applying a bias voltage. W is the width of the conductor, and L its length.

Classically the conductance is given by

$$G^{\text{tot}} = \sigma \frac{W}{L}, \tag{2.21}$$

where the conductivity σ is a material constant, W and L are respectively the width and the length of the conductor. Assuming the validity of this ohmic scaling relation, we would expect the conductance to grow indefinitely by decreasing the length of the conductor. Yet experiments reveal an upper limit $G_{\text{C}}^{\text{tot}}$ of the conductance for conductor lengths much smaller than the mean free path, $L \ll \ell_{\text{m}}$. This is quite surprising, since a ballistic conductor should have zero resistance, as there is no scattering in the transmission process.

This conductance limit is actually due to the interfaces between the conductor and the leads: The current is carried in the contacts by infinitely many transverse modes, while in the conductor only a few independent conducting modes are available. In this sense the classical result is not completely lost

also at the mesoscopic level: The resistance of a ballistic conductor measured on the conductor itself is zero, but in series with two contact resistances (see for example Imry).

For the moment we assume that the number of modes in the energy window $[\mu_2, \mu_1]$ are energy independent, $M(E) = M$, consistent with the fact that $\mu_1 - \mu_2 \to 0^+$. This requires a redistribution of the current at the interface, from many modes in the contacts to the few in the conductor, which leads to the observed *contact resistance* $\left(G_C^{\text{tot}}\right)^{-1}$.

In order to calculate G_C^{tot}, let us consider a conductor with only one conducting mode. The number of electronic states per mode in the energy window $[\mu_2, \mu_1]$ is

$$N_S = \frac{dn}{dE}(\mu_1 - \mu_2), \tag{2.22}$$

where $\frac{dn}{dE}$ is the density of states. The current carried by a single electronic state is

$$I_S = e\frac{1}{L}v_k, \tag{2.23}$$

with the group velocity $v_k = \frac{1}{\hbar}\frac{\partial E}{\partial k}$. The current carried by a mode is the product between the current carried by a state and the number of states:

$$I_M = e\frac{v_k}{L}\left(\frac{dn}{dE}\right)(\mu_1 - \mu_2). \tag{2.24}$$

Writing the density of states in terms of group velocity:

$$\frac{dn}{dE} = \frac{\partial n}{\partial k}\frac{\partial k}{\partial E} = \frac{L}{2\pi}\frac{1}{\hbar v_k} = \frac{L}{h v_k}, \tag{2.25}$$

the current becomes

$$I_M = \frac{e}{h}(\mu_1 - \mu_2). \tag{2.26}$$

$\frac{dn}{dE}|_F \times v_F$ is just an integer proportional to the number of bands crossing the projection of the Fermi surface on the plane perpendicular to the direction of the transport [79].

Since the number of modes is energy independent, the total current for a conductor with more than one conducting mode is obtained by multiplying the current per mode by the number of modes M:

$$I = M I_M = \frac{e}{h}M(\mu_1 - \mu_2). \tag{2.27}$$

Considering the bias voltage through the chemical potential difference

$$eΔV = Δμ, \tag{2.28}$$

we can express the conductance of the system as

$$G_C^{tot} = \frac{2e^2}{h} M = G_0^{tot} M, \tag{2.29}$$

with the factor 2 due to the spin degeneracy, and G_0^{tot} being the conductance quantum:

$$G_0^{tot} = \frac{2e^2}{h} \approx \frac{1}{12.9\,\mathrm{k\Omega}} \approx 77.5\,\mu\mathrm{S}. \tag{2.30}$$

The contact resistance of a single-moded ballistic conductor is thus $\sim 13\,\mathrm{k\Omega}$, which is certainly not negligible, but which becomes very small for wide conductors with thousands of modes. As the number of modes is proportional to the width W, (actually to the ratio W/λ_F) as we decrease its size, Eq. (2.29) means that the conductance goes down in discrete steps of height $2e^2/h$: The conductance is quantized in units of G_0^{tot}, independently of the nature of the conductor and of its length (see for instance the experiments described in Ref. [80, 81]).

2.2.2 Landauer formula

Finally, let us consider the case of a conductor with M modes, having a scattering region as displayed in Fig. 2.5. Let us call the ballistic parts of the conductor, to the left and right of the scattering region, left and right lead respectively. We define $\mathcal{T}_{ij}$ as the probability of an electron of being transmitted from the j^{th} channel of the left lead in the i^{th} channel in the right lead. Therefore we get for the conductance associated to the j^{th} channel

$$G_j^{tot} = \frac{2e^2}{h} \sum_i \mathcal{T}_{ij}, \tag{2.31}$$

with the sum running over all final states. The total conductance is then

$$G^{tot} = \frac{2e^2}{h} \sum_{ij} \mathcal{T}_{ij}. \tag{2.32}$$

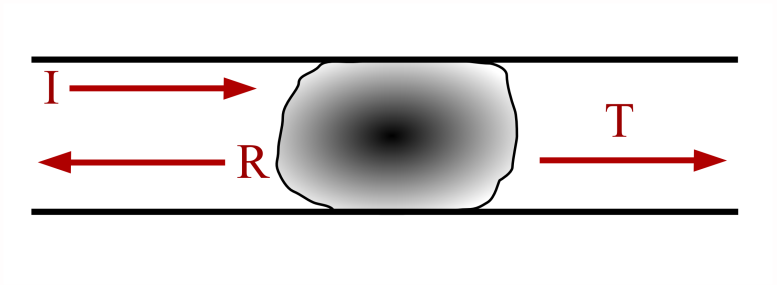

Figure 2.5: Schematic description of a ballistic conductor with a scattering region (shaded area). $\mathcal{T}$ and $\mathcal{R}$ are respectively the transmission and reflection probabilities for the incident electron I, corresponding to the scattering potential.

This is the multi-channel generalization of the Landauer formula, giving the connection between the transport and scattering properties of a device. We can write the *Landauer formula* also in terms of the average probability $\mathcal{T}$ that an electron injected in the left lead will transmit to the right lead:

$$G^{\text{tot}} = \frac{2e^2}{h} M\mathcal{T}, \tag{2.33}$$

which takes into account the contact resistance as well as the resistance rising from the presence of scatterers. For a ballistic conductor $\mathcal{T} = 1$ for all modes, whereas its value is reduced by the possible scattering processes.

Note that in general $\mathcal{T} = \mathcal{T}(E)$ is energy dependent and since we are considering $\mu_1 - \mu_2 \to 0^+$, then the relevant $\mathcal{T}$ is that calculated at the Fermi level $\mathcal{T}(E_{\text{F}})$.

2.3 Transmission calculation

With the Landauer formula we can calculate the conductance if the transmission is known. Next, we will introduce the calculation of the transmission function using the scattering matrix ($\mathcal{S}$-matrix) and Green functions.

2.3.1 Transmission function and the $\mathcal{S}$-matrix

A coherent conductor can be characterized at each energy by an $\mathcal{S}$-matrix relating the outgoing wave amplitudes to the incoming wave amplitudes at the different leads:

$$\psi^{\text{OUT}} = \mathcal{S}\psi^{\text{IN}}. \tag{2.34}$$

The dimension of the $\mathcal{S}$-matrix is $M_{\mathrm{T}}(E)$, which is the total number of modes in the leads, obtained by summing the number of modes in each lead $M_p(E)$:

$$M_{\mathrm{T}}(E) = \sum_p M_p(E). \tag{2.35}$$

The transmission between the mode j in the lead q and the mode i in the lead p can be expressed in terms of the elements of the $\mathcal{S}$-matrix as

$$\mathcal{T}_{ij} = |\mathcal{S}_{ij}|^2. \tag{2.36}$$

This relation follows from the definition of the quantum mechanical transmission, as the ratio between the amplitude of the outgoing wave and the amplitude of the incoming wave. For the transmission between the lead q and p we obtain:

$$\mathcal{T}_{pq} = \sum_{i\in p}\sum_{j\in q}\mathcal{T}_{ij}. \tag{2.37}$$

The $\mathcal{S}$-matrix is a unitary matrix, fact that ensures current conservation [66].

If we are dealing with an incoherent conductor (or just a large one), the problem of transport through it can be tackled by dividing it into segments where the transport is coherent, computing the $\mathcal{S}$-matrices for these segments and combining them to a composite $\mathcal{S}$-matrix, which can be done incoherently. For details of the know-how of this combination process we refer to the literature [66].

2.3.2 Green functions

Green functions constitute a very useful tool in the perturbation theory for describing the response at any point (inside or outside the conductor) due to an excitation at any other, and can include effects of interactions. For non-interacting transport, they can be viewed as generalized $\mathcal{S}$-matrices, which are limited to the description of the response at one lead due to the excitation at another lead.

Consider the response function $\Psi(x)$ related to an excitation $f(x)$ by a differential operator $\mathcal{D}$:

$$\mathcal{D}\Psi(x) = f(x). \tag{2.38}$$

The general solution for this inhomogeneous differential equation is

$$\Psi(x) = \Psi_0(x) + \int \mathrm{d}x' \mathcal{G}(x,x') f(x'), \tag{2.39}$$

with the Green function $\mathcal{G}$ defined through

$$\mathcal{D}\mathcal{G}\left(x,x'\right)=\delta\left(x-x'\right) \quad \Longrightarrow \quad \mathcal{G}=\mathcal{D}^{-1}. \tag{2.40}$$

To obtain solutions for $\mathcal{G}$, we need to specify boundary conditions, as the inverse of a differential operator is not uniquely defined.

Let us consider now the simple case of an infinite one dimensional wire with a constant potential energy ϵ_0. We can write Eq. (2.38) in terms of the Hamiltonian operator:

$$[E-\mathcal{H}]\Psi\left(x\right)=f\left(x\right) \quad \text{with} \quad \mathcal{H}=-\frac{\hbar^2}{2m}\frac{\partial^2}{\partial x^2}+\epsilon_0, \tag{2.41}$$

where Ψ is the wave function and f an excitation. Hence the Green function is given by

$$\mathcal{G}=\left[E-\epsilon_0+\frac{\hbar^2}{2m}\frac{\partial^2}{\partial x^2}\right]^{-1}, \tag{2.42}$$

that is

$$\left(E-\epsilon_0+\frac{\hbar^2}{2m}\frac{\partial^2}{\partial x^2}\right)\mathcal{G}\left(x,x'\right)=\delta\left(x-x'\right), \tag{2.43}$$

which is similar to the Schrödinger equation

$$\left(E-\epsilon_0+\frac{\hbar^2}{2m}\frac{\partial^2}{\partial x^2}\right)\Psi\left(x\right)=0, \tag{2.44}$$

except for $\delta\left(x-x'\right)$. Considering this similarity, one can think of the Green function $\mathcal{G}\left(x,x'\right)$ as the wave function at x resulting from an unity excitation at x'. When an excitation occurs at x', one expects two waves with the amplitudes A^+ and A^-, moving outwards from x' (see Fig. 2.6, left). We can write

$$\begin{array}{lll}\mathcal{G}\left(x,x'\right)=A^+\exp\left[ik\left(x-x'\right)\right] & \text{for} & x>x' \\ \mathcal{G}\left(x,x'\right)=A^-\exp\left[-ik\left(x-x'\right)\right] & \text{for} & x<x'\end{array} \tag{2.45}$$

with $k=\left[2m\left(E-\epsilon_0\right)\right]^{1/2}/\hbar$. For any A^+, A^-, these solutions satisfy Eq. (2.43) for $x\neq x'$. The values of A^+ and A^- are obtained by considering the boundary conditions for $x=x'$:

$$\begin{aligned}&\left[\mathcal{G}\left(x,x'\right)\right]_{x=x'^+}=\left[\mathcal{G}\left(x,x'\right)\right]_{x=x'^-} \\ &\left[\frac{\partial\mathcal{G}\left(x,x'\right)}{\partial x}\right]_{x=x'^+}-\left[\frac{\partial\mathcal{G}\left(x,x'\right)}{\partial x}\right]_{x=x'^-}=\frac{2m}{\hbar}.\end{aligned} \tag{2.46}$$

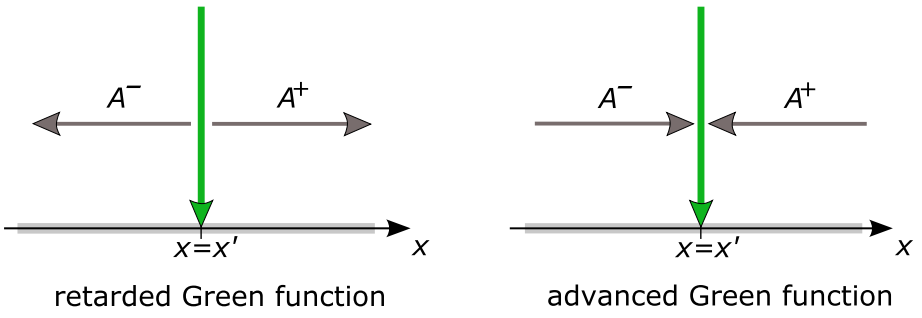

Figure 2.6: Retarded and advanced Green functions for an infinite one dimensional wire with a unit excitation taking place at $x = x'$.

We obtain for the wave amplitudes

$$A^+ = A^- = -\frac{\mathrm{i}}{\hbar v} \quad \text{where} \quad v = \frac{\hbar k}{m}. \tag{2.47}$$

Hence one of the solutions satisfying Eq. (2.43) is the so-called *retarded Green function*:

$$\mathcal{G}^{\mathrm{r}}\left(x, x'\right) = -\frac{\mathrm{i}}{\hbar v} \exp\left[\mathrm{i}k|x - x'|\right], \tag{2.48}$$

which corresponds to outgoing waves that originate at the point of excitation (see Fig. 2.6, left).

There is also another solution of Eq. (2.43): the so-called *advanced Green function* given by

$$\mathcal{G}^{\mathrm{a}}\left(x, x'\right) = +\frac{\mathrm{i}}{\hbar v} \exp\left[-\mathrm{i}k|x - x'|\right], \tag{2.49}$$

and corresponding to incoming waves that disappear at the point of excitation (see Fig. 2.6, right).

The infinitesimal η

A way to incorporate the boundary conditions directly into Eq. (2.43) is the addition of an infinitesimal imaginary part to the energy:

$$\left(E - \epsilon_0 + \frac{\hbar^2}{2m}\frac{\partial^2}{\partial x^2} + \mathrm{i}\eta\right) \mathcal{G}^{\mathrm{r}}\left(x, x'\right) = \delta\left(x - x'\right), \tag{2.50}$$

for $\eta > 0$. The only suitable solution to this equation is the retarded Green function, since the solution must be bounded and the imaginary part makes the advanced Green function divergent as it introduces a positive imaginary component to the wavenumber k. By virtue of the same argument, the advanced Green function is the only adequate solution to the equation

$$\left(E - \epsilon_0 + \frac{\hbar^2}{2m}\frac{\partial^2}{\partial x^2} - \mathrm{i}\eta\right) \mathcal{G}^{\mathrm{a}}\left(x, x'\right) = \delta\left(x - x'\right). \tag{2.51}$$

In general, the retarded and the advanced Green functions are then defined as

$$\mathcal{G}^{\mathrm{r}} = \left[E - \mathcal{H} + \mathrm{i}\eta\right]^{-1}, \tag{2.52}$$

$$\mathcal{G}^{\mathrm{a}} = \left[E - \mathcal{H} - \mathrm{i}\eta\right]^{-1}, \tag{2.53}$$

where $\eta \to 0^+$. It is important to noticed that the advanced Green function is the hermitian conjugate of the retarded Green function:

$$\mathcal{G}^{\mathrm{a}} = \mathcal{G}^{\mathrm{r}\dagger}. \tag{2.54}$$

From hereon, if it is not explicitly mentioned, we will refer to the retarded Green function generally as the "Green function".

Green functions and $\mathcal{S}$-matrix

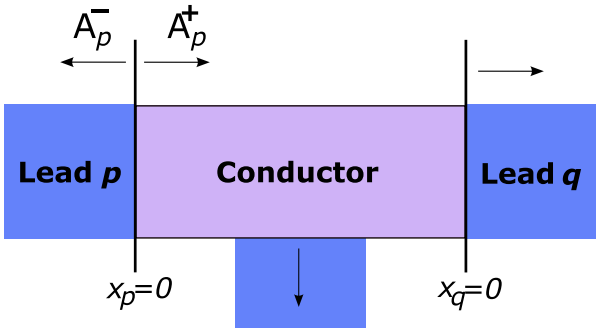

Figure 2.7: A unit excitation in lead p generates two waves, the wave with the amplitude A_p^- moving away from the conductor, the one with the amplitude A_p^+ being partially transmitted to each of the other leads.

Next we will relate the Green functions and the $\mathcal{S}$-matrix. Let us consider a conductor connected to a set of one-moded leads (Fig. 2.7). The points $x_p =$

0 and $x_q = 0$ denote the interfaces between the lead p and the conductor and between the lead q and the conductor respectively. $\mathcal{G}_{qp}$ is the Green function between these interfaces, $x_p = 0$ and $x_q = 0$. A unit excitation at $x_p = 0$ will give rise to two waves, one with the amplitude A_p^- propagating away from the conductor and one with the amplitude A_p^+ propagating through the conductor and being partially transmitted to each of the leads.

We can write the Green function in terms of the wave amplitudes and of the scattering matrix as

$$\mathcal{G}_{qp} = \delta_{qp} A_p^- + \mathcal{S}_{qp} \sqrt{v_p / v_q} A_p^+. \tag{2.55}$$

The square-root factor on the second term of the right-hand side comes from the fact that the plane-waves used for the definition of the scattering matrix are normalized to unit flux by dividing by the square-root of their group velocities, which makes the $\mathcal{S}$-matrix unitary.

Using the values of the wave amplitudes given in Eq. (2.47) we obtain the desired equation expressing the $\mathcal{S}$-matrix in terms of the Green function:

$$\mathcal{S}_{qp} = -\delta_{qp} + \mathrm{i}\hbar \sqrt{v_q v_p}\, \mathcal{G}_{qp}, \tag{2.56}$$

with $v_{p,q} = \hbar k_{p,q} / m$.

By now we have all relations we need to calculate the transmission and therefore the conductance, but still we have to obtain the Green function by the (numerical) inversion of the matrix $\left[E - \mathcal{H} + \mathrm{i}\eta\right]$, as seen in Eq. (2.52). Yet the Hamiltonian of the system has infinite extent in real space, as we are dealing with an open system, so the explicit manipulation of the Green function is impossible. To solve this problem, we have to partition the Green function of the system into manageable parts.

2.3.3 Transmission and Green functions

Consider the system as consisting of a left lead, a conductor and a right lead (see Fig. 2.8). We can write the Hamiltonian of the system

$$\mathcal{H} = \begin{pmatrix} \mathcal{H}_{\mathrm{L}} & \mathcal{H}_{\mathrm{LC}} & 0 \\ \mathcal{H}_{\mathrm{LC}}^\dagger & \mathcal{H}_{\mathrm{C}} & \mathcal{H}_{\mathrm{RC}}^\dagger \\ 0 & \mathcal{H}_{\mathrm{RC}} & \mathcal{H}_{\mathrm{R}} \end{pmatrix} \tag{2.57}$$

where $\mathcal{H}_{\mathrm{L,R}}$ and $\mathcal{H}_{\mathrm{C}}$ are the Hamiltonians of the leads and of the conductor, respectively. $\mathcal{H}_{\mathrm{LC}}$ is the coupling Hamiltonian between the left lead and the

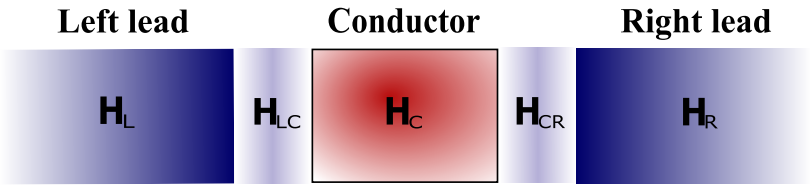

Figure 2.8: Setup of a system of a conductor sandwiched between two leads that stretch out to infinity.

conductor; $\mathcal{H}_{RC}$ the coupling Hamiltonian between the right lead and the conductor. We assume that the coupling integrals between both leads are zero as they lie sufficiently apart. Hence we can write Eq. (2.52), partitioning the Green function into submatrices as follows:

$$\begin{pmatrix} \mathcal{G}_L & \mathcal{G}_{LC} & \mathcal{G}_{LR} \\ \mathcal{G}_{CL} & \mathcal{G}_C & \mathcal{G}_{CR} \\ \mathcal{G}_{RL} & \mathcal{G}_{RC} & \mathcal{G}_R \end{pmatrix} \cdot \begin{pmatrix} \varepsilon - \mathcal{H}_L & -\mathcal{H}_{LC} & 0 \\ -\mathcal{H}_{LC}^\dagger & \varepsilon - \mathcal{H}_C & -\mathcal{H}_{RC}^\dagger \\ 0 & -\mathcal{H}_{RC} & \varepsilon - \mathcal{H}_R \end{pmatrix} = \mathbb{1} \tag{2.58}$$

with $\varepsilon = (E + i\eta)\,\mathbb{1}$. The Green functions corresponding to the isolated leads and conductor, respectively are:

$$\begin{aligned} g_L &= (\varepsilon - \mathcal{H}_L)^{-1} \text{ for the left lead,} \\ g_R &= (\varepsilon - \mathcal{H}_R)^{-1} \text{ for the right lead,} \\ g_C &= (\varepsilon - \mathcal{H}_C)^{-1} \text{ for the conductor.} \end{aligned}$$

Our interest is to obtain the effective Green function of the conductor $\mathcal{G}_C = (\varepsilon - \mathcal{H}_{eff})^{-1}$, *i.e.* the Green function corresponding to the conductor with attached leads, including them effectively in the conductor region. From Eq. (2.58) we can extract the following set of equations:

$$\mathcal{G}_{CL}\,(\varepsilon - \mathcal{H}_L) - \mathcal{G}_C \mathcal{H}_{LC}^\dagger = 0 \tag{2.59}$$

$$-\mathcal{G}_{CL}\mathcal{H}_{LC} + \mathcal{G}_C\,(\varepsilon - \mathcal{H}_C) - \mathcal{G}_{CR}\mathcal{H}_{RC} = \mathbb{1} \tag{2.60}$$

$$-\mathcal{G}_C \mathcal{H}_{RC}^\dagger + \mathcal{G}_{CR}\,(\varepsilon - \mathcal{H}_R) = 0 \tag{2.61}$$

from which we derive the expression of $\mathcal{G}_C$ we are interested in, by substituting in Eq. (2.60) $\mathcal{G}_{CL}$ and $\mathcal{G}_{CR}$ (obtained from Eq. (2.59) and Eq. (2.61) respectively). Hence we obtain for the effective Green function of the conductor:

$$\begin{aligned} \mathcal{G}_C = (\varepsilon - \mathcal{H}_{eff})^{-1} &= \left(\varepsilon - \mathcal{H}_C - \mathcal{H}_{RC}^\dagger\, g_R\, \mathcal{H}_{RC} - \mathcal{H}_{LC}^\dagger\, g_L\, \mathcal{H}_{LC}\right)^{-1} \\ &= (\varepsilon - \mathcal{H}_C - \Sigma_R - \Sigma_L)^{-1}, \end{aligned} \tag{2.62}$$

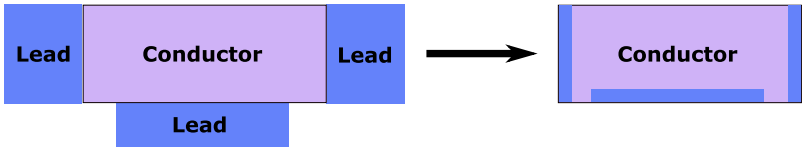

Figure 2.9: Schematic representation of the replacement of the original infinite open system with an equivalent finite one due to the inclusion of the self-energy terms.

where we define $\Sigma_{\mathrm{R}} \equiv \mathcal{H}_{\mathrm{RC}}^{\dagger}\, g_{\mathrm{R}}\, \mathcal{H}_{\mathrm{RC}}$ and $\Sigma_{\mathrm{L}} \equiv \mathcal{H}_{\mathrm{LC}}^{\dagger}\, g_{\mathrm{L}}\, \mathcal{H}_{\mathrm{LC}}$ as the *self-energy terms* due to the leads. They can be seen as effective Hamiltonians arising from the interaction of the conductor with the leads, describing *exactly* the effect of the leads on the conductor. Their effect is schematically depicted in Fig. 2.9.

In general, Eq. (2.62) can be extended to include any number of different leads. As long as the leads are independent from each other, their effects are additive:

$$\mathcal{G}_{\mathrm{C}} = \left(\varepsilon - \mathcal{H}_{\mathrm{C}} - \sum_{p} \Sigma_{p}\right)^{-1}. \tag{2.63}$$

In the Eq. (2.62), all matrices are finite except for the Green functions of the isolated leads g_{L} and g_{R}. In Sec. A.1 of Appendix A, several methods to calculate these quantities are discussed.

Once we have calculated the Green function, we can use it to obtain the elements of the $\mathcal{S}$-matrix with Eq. (2.56), from which the transmission can be calculated using Eq. (2.36). The transmission can then be expressed in a very compact form as [66, 82]:

$$\mathcal{T}_{LR}(E) = \mathrm{Tr}[\Gamma_{\mathrm{L}} \mathcal{G}_{\mathrm{C}}^{\mathrm{r}} \Gamma_{\mathrm{R}} \mathcal{G}_{\mathrm{C}}^{\mathrm{a}}]. \tag{2.64}$$

known as the Fisher-Lee relation. The terms $\Gamma_{\mathrm{L}} = \mathrm{i}[\Sigma_{\mathrm{L}} - \Sigma_{\mathrm{L}}^{\dagger}]$ and $\Gamma_{\mathrm{R}} = \mathrm{i}[\Sigma_{\mathrm{R}} - \Sigma_{\mathrm{R}}^{\dagger}]$ are the injection rates, describing the strength of the coupling of the leads to the conductor.

The coupling strength $\Gamma = \mathrm{i}[\Sigma - \Sigma^{\dagger}]$ is not zero as generally the self-energy terms are not Hermitian. Therefore the effective Hamiltonian $\left(\mathcal{H}_{\mathrm{C}} + \sum_{p} \Sigma_{p}\right)$ is also not Hermitian. This implies that the eigenvalues of the problem described by this Hamiltonian will be in general complex eigenenergies, which

we could write as

$$\epsilon_\alpha = \epsilon_\alpha^0 - \Delta_\alpha - \mathrm{i}\frac{\gamma_\alpha}{2}, \tag{2.65}$$

where ϵ_α^0 is the corresponding αth eigenvalue of the problem of the associated isolated system (without leads) described by the Hamiltonian $\mathcal{H}_\mathrm{C}$, and $-\Delta_\alpha - \mathrm{i}\gamma_\alpha/2$ come from the inclusion of the self-energy terms. The time dependence of an eigenstate with eigenvalue ϵ_α is

$$\exp\left[-\mathrm{i}\frac{\epsilon_\alpha}{\hbar}t\right] = \exp\left[-\mathrm{i}\frac{\epsilon_\alpha^0 - \Delta_\alpha}{\hbar}t\right]\cdot\exp\left[-\frac{\gamma_\alpha}{2\hbar}t\right]. \tag{2.66}$$

Δ_α represents a shift in the energy due to the modification of the dynamics of an electron in the conductor by the interaction with the leads and γ_α reflects the fact that an electron injected anywhere in the conductor will eventually disappear in one of the leads. $\hbar/\gamma_\alpha$ represents then the average time or lifetime of an electron remaining in state α before going into one lead. Hence γ_α broadens the peaks of the eigenenergies ϵ_α^0. The complex eigenvalues coming from the coupling to the leads also make the previously introduced infinitesimal part η unnecessary for the calculation of the Green functions.

Density of States

For the spectral density of states (DOS) we can write:

$$N(E) = -\frac{1}{\pi}\mathrm{Im}\ \left[\mathrm{Tr}\,\mathcal{G}_\mathrm{C}(E)\right], \tag{2.67}$$

and the local density of states is given by the diagonal elements of the green function

$$N(\mathbf{r}, E) = -\frac{1}{\pi}\mathrm{Im}\ \left[\mathcal{G}_\mathrm{C}(\mathbf{r}, \mathbf{r}; E)\right]. \tag{2.68}$$

Chapter 3

Carbon-based materials

The interest on carbon-based materials has experienced an incredible boom in the last decades. Mainly to the fact that new forms of carbon materials have been discovered, as fullerenes and carbon nanotubes, but also because recently new properties of the well-known graphite have been brought to light. The beauty of these materials is always a center of attraction for physicists and comes from the richness that is hidden in their simplicity. For theoreticians, their simplicity seems even more striking, as for carbon nanotubes for instance, all their important properties can be extracted already from tight-binding calculations for the π electrons.

3.1 The carbon family

Carbon is the sixth element of the periodic table, having six electrons that occupy the atomic orbitals: $1s^2$, $2s^2$, and $2p^2$. That is, we have four valence electrons in the $2s^2 2p^2$ orbitals, much more weakly bounded that the core electrons. The richness of the carbon family comes actually from the fact that the wave functions of these valence orbitals can mix with each other in different ways, giving rise to different occupation-probability distributions. The *hybridization*, that is, this mixing of atomic orbitals on the same atom, occurs always so as to enhance the binding energy of the C atom with its neighboring atoms, forming so-called σ bonds. This model was first developed by Linus Pauling in 1931 [83] to explain the observed shapes and bond orders in molecules and has become an effective heuristic approach widely used for understanding organic chemistry. The remaining p orbitals, which are perpendicular to the σ bonds, may also bond to other neighboring C atoms,

forming the relatively weak π bonds. We will denote as sp^n hybridization the linear combination of a single $2s$ electron with $n = 1, 2, 3$ $2p$ electrons. In sp^n hybridization, $(n+1)$ σ bonds per C atom are formed, which make the skeleton of the structure, while $4-(n+1)$ electrons are in π orbitals, which as we will see are the most important ones for determining the transport properties.

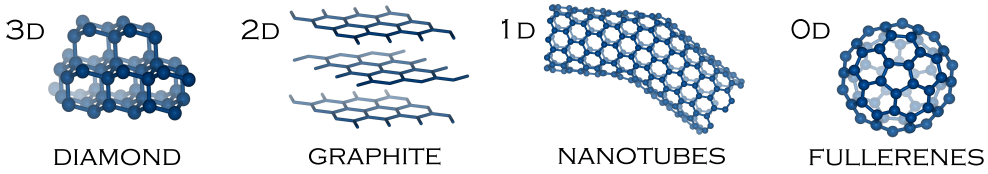

Figure 3.1: Allotropic forms of carbon: due to the different hybridization of its atomic orbitals, the carbon atom displays many possible configurations of its electronic states, which give rise to different types of binding combinations and thus to different materials.

Apart from the two well-known allotropes of carbon, diamond and graphite, carbon appears in other forms, from which the most significant are those of fullerenes and nanotubes (see Fig. 3.1). We can even speak from different dimensionality of these forms. The diamond has a three-dimensional structure consisting of two interpenetrating face-centered cubic Bravais lattices, displaced by the vector $(a/4, a/4, a/4)$, a being the cube side of approximately 3.57 Å. The graphite, though actually three-dimensional, can be considered of lower dimensionality as it is formed by the stacking of planar layers, thus of dimension two, joined between them by the much weaker π bonds. Carbon nanotubes and fullerenes can be thought of as quasi-one-dimensional and quasi-zero-dimensional compounds respectively.

The sp^3 hybridization is the one characterizing the crystal structure of diamond, with all electrons distributed between the four σ bonds, which built up a tetragonal bonding to four nearest neighbors (see Fig. 3.4). The four tetrahedral directions of these bonds determine the three-dimensional structure. As for molecules, an example of sp^3 hybridization is the organic molecule methane (CH_4).

The sp hybridization (see Fig. 3.2) forms two covalent bonds and two weaker π bonds. The structure is defined by the single axis where the σ bonds align, making thus at most polymeric forms of linear chains. Such a polymeric chain is the one of carbynes ($[\cdots - \mathrm{C} \equiv \mathrm{C} - \cdots]_n$), and the simplest example is the acetylene (HC≡CH).

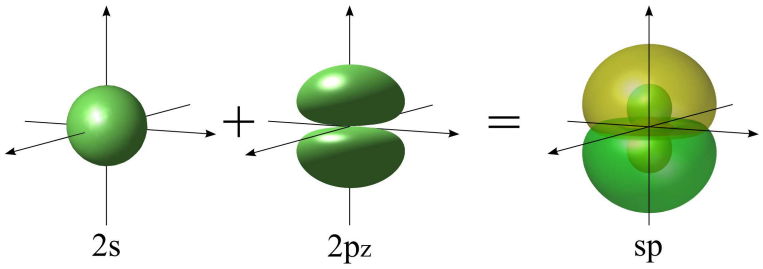

Figure 3.2: A linear combination of a $2s$ orbital and a $2p$ orbital yields two sp orbitals and determines a linear configuration of the sigma bonds they will form.

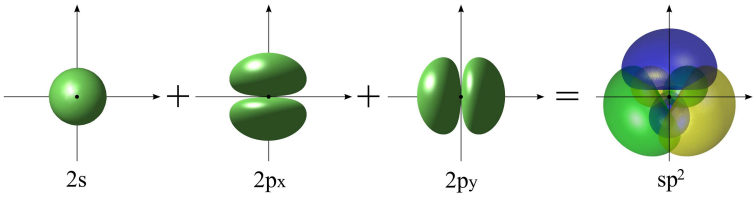

Figure 3.3: The three sp^2 orbitals are obtained by combining the $2s$ orbitals and two of the $2p$ orbitals, and they rearrange in a planar trigonal configuration, each one rotated $120°$ relative to the other. The leftover p orbitals remains perpendicular to this plane.

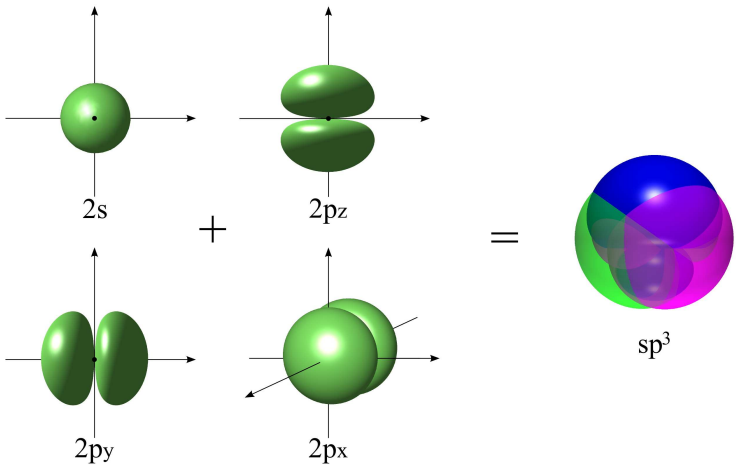

Figure 3.4: All three $2p$ orbitals and the $2s$ orbital mix to give four sp^3 hybrid orbitals. Each is equal to the others but they are rotated by $109.5°$ relative one other, building a tetrahedral. On the right, the resulting four sp^3 hybrids are shown superimposed.

The carbon compounds we are interested in, display actually sp^2 hybridization, as pictured in Fig. 3.3. Here the $2s$ orbital and two $2p$ orbitals are combined to give three σ orbitals with large amplitude in the direction of the three nearest-neighbor atoms. These bonded atoms are situated on the same plane and are distributed symmetrically around the central atom. This binding geometry is at the base of the zigzag structure of *trans*-polyacetylene, and of the honeycomb lattice of the two-dimensional graphite.

3.2 Graphene

3.2.1 Geometric structure of graphene

As already mentioned, graphite is a three-dimensional (3D) layered crystal composed by planar sheets of carbon atoms arrange in a honeycomb lattice. The two-dimensional (2D) sheets of graphite (also referred to as graphene layers) are stacked usually in an AB alternation. The interaction between them is relatively weak, as the interlayer spacing of $3.35\,\text{Å}$ is much larger than the carbon-carbon bond length $a_{\text{C-C}} = 1.42\,\text{Å}$ in the hexagonal rings, which are held together through σ bonds.

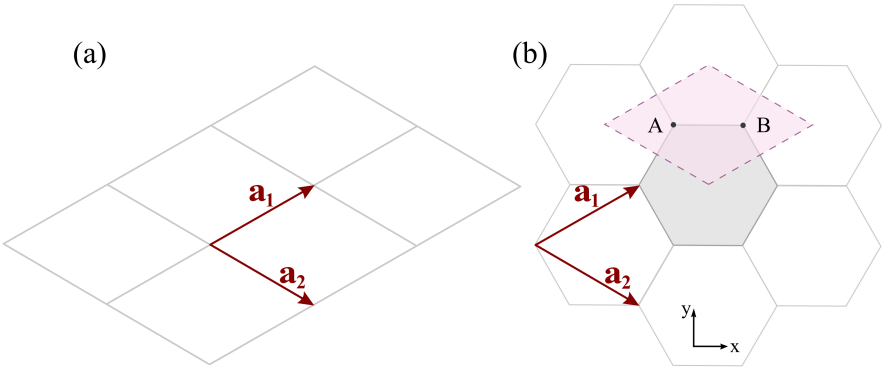

Figure 3.5: (a) The 2D triangular lattice, which is the Bravais lattice underlying the honeycomb network of the graphene. (b) The graphene is a triangular lattice with a two-atom basis (atom A and atom B). The dotted lines indicate one possible choice of unit cell, whereas the gray shaded hexagon represents the Wigner-Seitz unit cell. The chosen choice of translational vectors $\mathbf{a}_1$ and $\mathbf{a}_2$ which expand the Bravais lattice, is shown in this figure and is described by Eq. (3.1).

In order to describe the geometry of graphene, we start considering the 2D hexagonal Bravais lattice, which consists of atoms ordered in a triangular

pattern in the plane as illustrated in Fig. 3.5 (a), but with a basis containing two inequivalent atoms, called A and B, as shown in Fig. 3.5 (b). Its structure is thus defined by the lattice vectors:

$$\mathbf{a}_1 = \left(\frac{\sqrt{3}}{2}a, \frac{a}{2}\right), \quad \mathbf{a}_2 = \left(\frac{\sqrt{3}}{2}a, -\frac{a}{2}\right), \tag{3.1}$$

with the lattice constant $a = |\mathbf{a}_1| = |\mathbf{a}_2| = \sqrt{3}\,1.42 = 2.46$ Å. This is just a particular choice of vectors forming an angle of 60°, but any other valid choice will yield the same results. There are then several possibilities to choose a unit cell, the dotted lines in Fig. 3.5 (b) indicate one in real space which has the shape of a rhombus and is defined by the lattice vectors of Eq. (3.1). The reciprocal lattice of both the hexagonal lattice and of graphene is again hexagonal but rotated by 90° respectively to the real space one and with a different lattice constant, which now is $b = 4\pi/\sqrt{3}a$. The reciprocal lattice vectors fulfill the condition $\mathbf{a}_i \cdot \mathbf{b}_j = 2\pi\delta_{ij}$ and can be written as

$$\mathbf{b}_1 = \left(\frac{2\pi}{\sqrt{3}a}, \frac{2\pi}{a}\right), \quad \mathbf{b}_2 = \left(\frac{2\pi}{\sqrt{3}a}, -\frac{2\pi}{a}\right). \tag{3.2}$$

Figure 3.6 shows the reciprocal lattice vectors pointing at the reciprocal

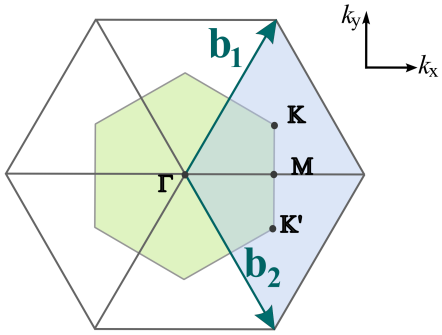

Figure 3.6: The reciprocal lattice of graphene is a two-dimensional hexagonal lattice. The shaded area represent two possible unite cells of this lattice, being the hexagonal one the symmetrical first Brillouin zone.

lattice points, while the shaded hexagon indicates the Brillouin zone. The whole system has once more a six-fold rotational symmetry, which means that rotations by 60° do not change the lattice. Γ, K (there are actually two inequivalent K points: K and K') and M are high-symmetry-points and are situated respectively at the center, the corner, and the center of the edge of

the Brillouin zone, and it is usual to calculate the dispersion relations along the lines connecting this three points. These points are given by:

$$\Gamma = (0,0)\,,\ \ \mathrm{M} = \left(\frac{2\pi}{\sqrt{3}a},0\right),\ \ \mathrm{K} = \left(\frac{2\pi}{\sqrt{3}a},\frac{2\pi}{3a}\right),\ \ \mathrm{K}' = \left(\frac{2\pi}{\sqrt{3}a},-\frac{2\pi}{3a}\right). \tag{3.3}$$

3.2.2 Dispersion relation of graphene

We will derive now the graphene band structure in the tight-binding approximation as was first done by P. R. Wallace [84] in 1947, assuming that the graphene plane is infinite in its two dimensions.

Each atom of the graphene has three σ electrons forming the bonds to the nearest neighbors and contributes with one π electron (its fourth electron) to the valence band. The bands corresponding to the σ electrons correspond to localized σ molecular orbitals and lie much lower in energy from the Fermi level and can be in a first approximation neglected [85]. Within the tight binding approximation, the π electron is localized at the atomic site and has a normalized wave function $\chi(\mathbf{r})$. The total wave function can be written as a linear combination

$$\psi = \phi_A + \lambda\phi_B, \tag{3.4}$$

where

$$\phi_A = \frac{1}{\sqrt{N}}\sum_A e^{i\mathbf{k}\cdot\mathbf{R}^A}\chi\left(\mathbf{r}-\mathbf{R}^A\right),\ \ \phi_B = \frac{1}{\sqrt{N}}\sum_B e^{i\mathbf{k}\cdot\mathbf{R}^B}\chi\left(\mathbf{r}-\mathbf{R}^B\right) \tag{3.5}$$

are the Bloch wave functions of the A and the B electrons respectively and λ is a combination coefficient which we will eliminate later. The value of N in the normalization factor is the number of unit cells in the system. Now having the Schrödinger equation $\mathcal{H}\psi = E\psi$, we multiply it by ϕ_A^* and integrate and do the same with ϕ_B^* to get the following equations:

$$\begin{aligned} \mathcal{H}_{AA} + \lambda\mathcal{H}_{AB} &= E\mathcal{S}_{AA} + \lambda E\mathcal{S}_{AB}, \\ \mathcal{H}_{BA} + \lambda\mathcal{H}_{BB} &= E\mathcal{S}_{BA} + \lambda E\mathcal{S}_{BB}, \end{aligned} \tag{3.6}$$

where $\mathcal{H}_{AA} = \int \phi_A^*\mathcal{H}\phi_A$, $\mathcal{H}_{BB} = \int \phi_B^*\mathcal{H}\phi_B$, $\mathcal{H}_{AB} = \int \phi_A^*\mathcal{H}\phi_B$, $\mathcal{H}_{BA} = \int \phi_B^*\mathcal{H}\phi_A$, and the overlap matrix elements are $\mathcal{S}_{AA} = \int \phi_A^*\phi_A$, $\mathcal{S}_{BB} = \int \phi_B^*\phi_B$, $\mathcal{S}_{AB} = \int \phi_A^*\phi_B$, and $\mathcal{S}_{BA} = \int \phi_B^*\phi_A$.

We can now eliminate λ from Eq. (3.6) using the secular equation, assuring a non-trivial solution:

$$\begin{vmatrix} \mathcal{H}_{AA} - E\mathcal{S}_{AA} & \mathcal{H}_{AB} - E\mathcal{S}_{AB} \\ \mathcal{H}_{BA} - E\mathcal{S}_{BA} & \mathcal{H}_{BB} - E\mathcal{S}_{BB} \end{vmatrix} = 0, \tag{3.7}$$

that is

$$\begin{aligned} \left(1 - |\mathcal{S}_{AB}|^2\right) E^2 + \left(\mathcal{S}_{AB}\mathcal{H}^*_{AB} + \mathcal{S}^*_{AB}\mathcal{H}_{AB} - \mathcal{H}_{AA} - \mathcal{H}_{BB}\right) E \\ + \mathcal{H}_{AA}\mathcal{H}_{BB} - |\mathcal{H}_{AB}|^2 = 0, \end{aligned} \tag{3.8}$$

as $\mathcal{H}_{BA} = \mathcal{H}^*_{AB}$, $\mathcal{S}_{BA} = \mathcal{H}^*_{AB}$ and we neglect overlap integrals between neighboring orbitals of atoms of the same kind, *i.e.*,

$$\begin{aligned} \mathcal{S}_{AA} &= \left\langle \phi_A \middle| \phi_A \right\rangle \\ &= \frac{1}{N} \sum_{\mathbf{R}^A} \sum_{\mathbf{R}'^A} e^{i\mathbf{k}\left(\mathbf{R}'^A - \mathbf{R}^A\right)} \left\langle \chi_A\left(\mathbf{r} - \mathbf{R}^A\right) \middle| \chi_A\left(\mathbf{r} - \mathbf{R}'^A\right) \right\rangle \\ &= \frac{1}{N} \sum_{\mathbf{R}^A} \left\{ \left\langle \chi_A\left(\mathbf{r} - \mathbf{R}^A\right) \middle| \chi_A\left(\mathbf{r} - \mathbf{R}^A\right) \right\rangle \right. \\ &\quad \left. + \sum_{\mathbf{R}'^A \neq \mathbf{R}^A} e^{i\mathbf{k}\left(\mathbf{R}'^A - \mathbf{R}^A\right)} \left\langle \chi_A\left(\mathbf{r} - \mathbf{R}^A\right) \middle| \chi_A\left(\mathbf{r} - \mathbf{R}'^A\right) \right\rangle \right\} \\ &\cong \left\langle \chi_A\left(\mathbf{r} - \mathbf{R}^A\right) \middle| \chi_A\left(\mathbf{r} - \mathbf{R}^A\right) \right\rangle = 1 \end{aligned} \tag{3.9}$$

and equivalently for B-type atoms $\mathcal{S}_{BB} \cong 1$.

If we further assume that the overlap integral between neighboring π orbitals of any type is negligible, *i.e.*, $\left\langle \chi\left(\mathbf{r} - \mathbf{R}_A\right) \middle| \chi\left(\mathbf{r} - \mathbf{R}_B\right) \right\rangle \cong 0$ so that $\mathcal{S}_{AB} \cong 0$, then Eq. (3.8) simplifies greatly to yield the following expression for the bands:

$$E = \frac{1}{2}\left\{ \mathcal{H}_{AA} + \mathcal{H}_{BB} \pm \sqrt{\left(\mathcal{H}_{AA} - \mathcal{H}_{BB}\right)^2 + 4\left|\mathcal{H}_{AB}\right|^2} \right\}. \tag{3.10}$$

Since atoms A and B are identical, $\mathcal{H}_{AA} = \mathcal{H}_{BB}$, so that we finally get

$$E = \mathcal{H}_{AA} \pm \left|\mathcal{H}_{AB}\right|. \tag{3.11}$$

We have now just to calculate the matrix elements $\mathcal{H}_{AA}$ and $\mathcal{H}_{AB}$. Figure (3.7) shows the six nearest neighbors of type A and the three nearest

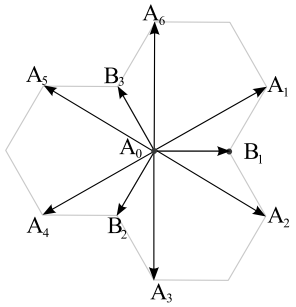

Figure 3.7: Nearest A and B neighbors of an A atom in graphene.

neighbors of type B to a central A atom. The vectors connecting these neighbors to the central atom are given by

$$\begin{aligned}
&\mathbf{R}_1^A - \mathbf{R}_0^A = \left(\tfrac{\sqrt{3}}{2}a, \tfrac{a}{2}\right), \quad \mathbf{R}_2^A - \mathbf{R}_0^A = \left(\tfrac{\sqrt{3}}{2}a, -\tfrac{a}{2}\right), \quad \mathbf{R}_3^A - \mathbf{R}_0^A = (0, -a), \\
&\mathbf{R}_4^A - \mathbf{R}_0^A = \left(-\tfrac{\sqrt{3}}{2}a, -\tfrac{a}{2}\right), \quad \mathbf{R}_5^A - \mathbf{R}_0^A = \left(-\tfrac{\sqrt{3}}{2}a, \tfrac{a}{2}\right), \quad \mathbf{R}_6^A - \mathbf{R}_0^A = (0, a),
\end{aligned} \tag{3.12}$$

for the atoms of the same kind. For the three neighboring B atoms they are given by

$$\mathbf{R}_1^B - \mathbf{R}_0^A = \left(\tfrac{a}{\sqrt{3}}, 0\right), \quad \mathbf{R}_2^B - \mathbf{R}_0^A = \left(-\tfrac{a}{2\sqrt{3}}, -\tfrac{a}{2}\right), \quad \mathbf{R}_3^B - \mathbf{R}_0^A = \left(-\tfrac{a}{2\sqrt{3}}, \tfrac{a}{2}\right). \tag{3.13}$$

The Hamiltonian element $\mathcal{H}_{AA}$ is, as seen before, defined by the expression

$$\begin{aligned}
\mathcal{H}_{AA} &= \langle \phi_A | \mathcal{H} | \phi_A \rangle \\
&= \frac{1}{N} \sum_{\mathbf{R}^A} \sum_{\mathbf{R}'^A} e^{i\mathbf{k}\left(\mathbf{R}'^A - \mathbf{R}^A\right)} \left\langle \chi_A\left(\mathbf{r} - \mathbf{R}^A\right) | \mathcal{H} | \chi_A\left(\mathbf{r} - \mathbf{R}'^A\right) \right\rangle
\end{aligned} \tag{3.14}$$

and if we consider just first A-neighbor interactions we can write it as

$$\mathcal{H}_{AA} = \frac{1}{N} \sum_{\mathbf{R}_0^A} \sum_{j=0}^{6} e^{i\mathbf{k}\left(\mathbf{R}_j^A - \mathbf{R}_0^A\right)} \int d\mathbf{r} \chi^*\left(\mathbf{r} - \mathbf{R}_0^A\right) \mathcal{H} \chi\left(\mathbf{r} - \mathbf{R}_j^A\right), \tag{3.15}$$

which can be expressed in a more compact form, considering the positions of the neighboring atoms, Eq. (3.12), and taking into account that in Eq. (3.15) two types of integrals appear, namely a nearest A-neighbor integral, which we will call γ', and a self integral which we will denote

with $\varepsilon_0 = \int \mathrm{d}\mathbf{r}\chi^*(\mathbf{r})\,\mathcal{H}\chi(\mathbf{r})$. In general, the integrals $\int \mathrm{d}\mathbf{r}\chi_i^*(\mathbf{r})\,\mathcal{H}\chi_i(\mathbf{r})$ are called the Coulomb integrals and represent the energies of an atomic orbital χ_i. $\int \mathrm{d}\mathbf{r}\chi_i^*(\mathbf{r})\,\mathcal{H}\chi_j(\mathbf{r}')$ with $i \neq j$, are known as resonance integrals or transfer integrals and express the energy of an electron moving under the influence of two different nuclei, hence giving a measure of the bonding energy.

The resulting expression takes the form:

$$\mathcal{H}_{AA} = \varepsilon_0 + 2\gamma' \left[\cos\left(ak_y\right) + 2\cos\left(\frac{a\sqrt{3}}{2}k_y\right)\cos\left(\frac{a}{2}k_y\right)\right]. \tag{3.16}$$

In a similar way we can calculate the value of $\mathcal{H}_{AB}$, now taking into account the nearest B-neighbors of A described in Eq. (3.13):

$$\mathcal{H}_{AB} = \frac{1}{N}\sum_{\mathbf{R}_0^A}\sum_{j=1}^{3} e^{\mathrm{i}\mathbf{k}\left(\mathbf{R}_j^B - \mathbf{R}_0^A\right)} \int \mathrm{d}\mathbf{r}\chi^*\left(\mathbf{r} - \mathbf{R}_0^A\right)\mathcal{H}\chi\left(\mathbf{r} - \mathbf{R}_j^B\right), \tag{3.17}$$

that is,

$$\mathcal{H}_{AB} = \gamma\left[e^{\mathrm{i}\frac{a}{\sqrt{3}}k_x} + 2e^{-\mathrm{i}\frac{a}{2\sqrt{3}}k_x}\cos\left(\frac{a}{2}k_y\right)\right], \tag{3.18}$$

where γ is the A-B nearest neighbor transfer integral or hopping parameter.

As $\gamma' \ll \gamma$, we can restrict ourselves to strictly nearest neighbors of the honeycomb network (that is, to B nearest neighbors for a central A atom and viceversa) and obtain the dispersion relation in this approximation by substituting Eq. (3.16) and Eq. (3.18) in Eq. (3.11):

$$E = \varepsilon_0 \pm \gamma\sqrt{1 + 4\cos\left(\frac{a}{2}k_y\right)\cos\left(\frac{a\sqrt{3}}{2}k_x\right) + 4\cos^2\left(\frac{a}{2}k_y\right)}. \tag{3.19}$$

The band structure within the approximations made is plotted in Fig. 3.8. As we have consider the $2p_z$ atomic orbitals of the lattice carbon atoms, from their interaction with adjacent atoms a bonding π-band and an anti-bonding π^*-band are formed. The two different signs in Eq. (3.19) represent the π- and π^*-bands. The degenerate points where the bonding and anti-bonding bands touch are the six corners of the hexagonal first Brillouin zone. This can be better seen in the left plot of Fig. 3.9, where it is clear that these points where the bands touch correspond to the K and K' points sketched in Fig. 3.6. Towards these points the dispersion relation shows a linear behavior,

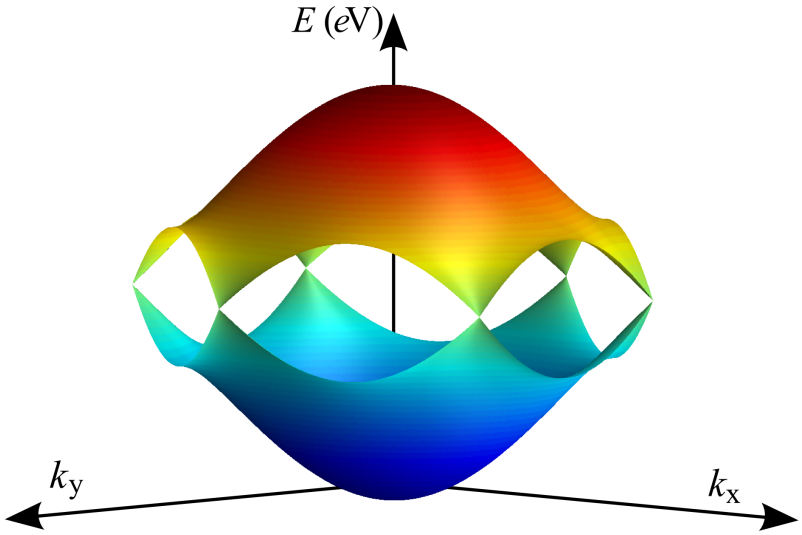

Figure 3.8: Dispersion relation of the graphene sheet for the **k** of the first Brillouin zone. The two bands are degenerate at the six Fermi points. Graphene has therefore no gap, though real graphite is a metal as the bands overlap by $\sim 40meV$ due to the interaction of the graphene planes. The whole band structure is shifted by ε_0 and rescale by the hopping parameter γ. For this figure the parameters chosen are $\varepsilon_0 = 0$ and $\gamma = -2.66\,eV$, a value typically used in the carbon literature.

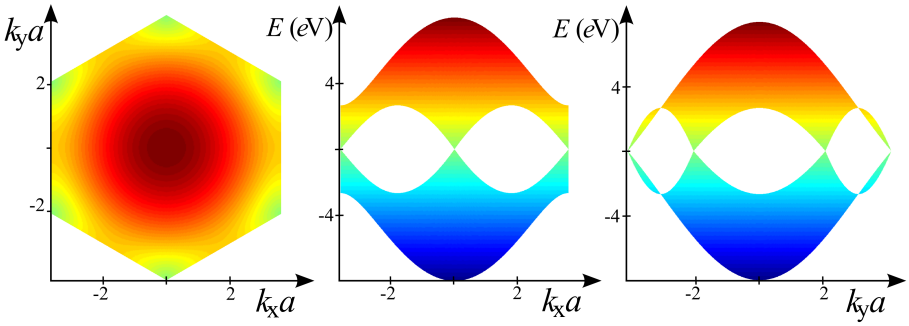

Figure 3.9: The band structure of graphene as shown in Fig. 3.8 is seen here with more detail and clarity by projecting it on the planes perpendicular to the three axis.

whereas in the vicinity of the Γ point it is parabolically shaped. Since there is only one π electron per atom, at $T = 0K$ the first band (the π-band) is complete occupy and the anti-bonding band is completely empty. The six

points where the bands touch constitute then by definition the Fermi surface, or rather the Fermi points. We are dealing thus with an unusual situation of a gap-less semiconductor. The existence of a zero-gap at the K-points comes from the requirement of identity of A-type and B-type atoms. If we break this requirement and impose different onsite energies to these two types of atoms in each unit cell, a gap opens destroying the semi-metallic character of graphene as seen in Fig. 3.10(b).

On the left hand-side of Fig. 3.10 we can observe how the inclusion of a nonzero overlap integral between orbitals of nearest neighbor atoms changes the dispersion relation breaking the electron-hole symmetry seen in Fig. 3.8. Namely if we do not neglect the overlap integral between just nearest neighboring atomic orbitals, then

$$\begin{aligned} \mathcal{S}_{AB} &= \left\langle \phi_A \middle| \phi_B \right\rangle \\ &= \frac{1}{N} \sum_{\mathbf{R}_0^A} \sum_{j=1}^{3} e^{\mathrm{i}\mathbf{k}\left(\mathbf{R}_j^B - \mathbf{R}_0^A\right)} \int \mathrm{d}\mathbf{r} \chi^* \left(\mathbf{r} - \mathbf{R}_0^A\right) \chi \left(\mathbf{r} - \mathbf{R}_j^B\right) \\ &= s \left[e^{\mathrm{i}\frac{a}{\sqrt{3}}k_x} + 2e^{-\mathrm{i}\frac{a}{2\sqrt{3}}k_x} \cos\left(\frac{a}{2}k_y\right) \right]. \end{aligned} \tag{3.20}$$

And from Eq. (3.8) we obtain the following expression for the π bands:

$$E = \frac{\varepsilon_0 \pm \gamma \sqrt{1 + 4\cos\left(\frac{a}{2}k_y\right)\cos\left(\frac{a\sqrt{3}}{2}k_x\right) + 4\cos^2\left(\frac{a}{2}k_y\right)}}{1 \pm s\sqrt{1 + 4\cos\left(\frac{a}{2}k_y\right)\cos\left(\frac{a\sqrt{3}}{2}k_x\right) + 4\cos^2\left(\frac{a}{2}k_y\right)}}. \tag{3.21}$$

Around the Fermi points the band structure can be expanded for small δk. Instead of expanding the cosine functions in Eq. (3.19), let us for the sake of simplicity expand the exponential functions in Eq. (3.18) which we then substitute in Eq. (3.11). That is, we start from the following expression for the dispersion relation

$$E = \pm \left| \gamma \left[e^{\mathrm{i}\frac{a}{\sqrt{3}}k_x} + e^{-\mathrm{i}\frac{a}{2\sqrt{3}}k_x} \left(e^{\mathrm{i}\frac{a}{2}k_y} + e^{-\mathrm{i}\frac{a}{2}k_y} \right) \right] \right|, \tag{3.22}$$

where we have set $\varepsilon_0 = 0$, which is setting the zero of energy at the Fermi energy. We will expand the exponential functions around a K point as $\exp(x + \delta x) \cong \exp(x) + \delta x \exp(x)$ for small values of δx, neglecting second and higher order terms in δx. That is, we consider then a momentum like

$$\mathbf{k} = \mathrm{K} + \delta\mathbf{k} = \left(\frac{2\pi}{\sqrt{3}a} + \alpha, \frac{2\pi}{3a} + \beta \right), \quad \text{for } \alpha, \beta \ll 1. \tag{3.23}$$

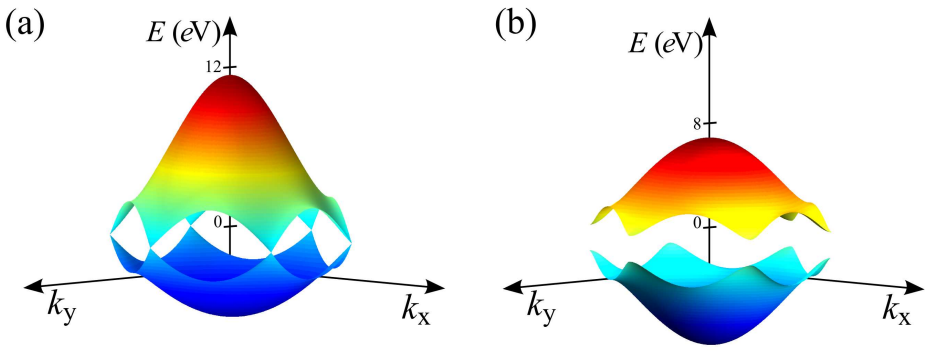

Figure 3.10: The bands of a graphene sheet for a π orbital calculation are shown here for the same hopping integral γ as in Fig. 3.8 but including a non-zero overlap integral between nearest neighbors in (a) of value $s = 0.12$. On the right (b), no overlap is included but an asymmetry of the onsite energies of the A and B atoms is introduced, opening a gap in the system.

The dispersion relation becomes then

$$\begin{aligned} E &= \pm|\gamma| \cdot \left| e^{\mathrm{i}\frac{2\pi}{3}} \left(1 + \mathrm{i}\frac{a}{\sqrt{3}}\alpha\right) + \left(e^{-\mathrm{i}\frac{\pi}{3}} - \mathrm{i}\frac{a}{2\sqrt{3}}\alpha e^{-\mathrm{i}\frac{\pi}{3}}\right)\left(1 - \frac{a\sqrt{3}}{2}\beta\right)\right| \\ &= \pm|\gamma| \cdot \left| \mathrm{i}\frac{a}{2\sqrt{3}}\alpha\left(2e^{\mathrm{i}\frac{2\pi}{3}} - e^{-\mathrm{i}\frac{\pi}{3}}\right) - \frac{a\sqrt{3}}{2}\beta e^{-\mathrm{i}\frac{\pi}{3}}\right| \\ &= \pm|\gamma| \cdot \left| -\frac{a\sqrt{3}}{2}e^{-\mathrm{i}\frac{\pi}{3}}(\beta + \mathrm{i}\alpha)\right| = \pm|\gamma|\frac{a\sqrt{3}}{2}|\delta\mathbf{k}| \end{aligned} \tag{3.24}$$

Around the Fermi points the bands are described by the linear dispersion relation

$$E(\mathbf{k}) = \pm v(\hbar|\delta\mathbf{k}|), \tag{3.25}$$

with $v = \gamma\frac{a\sqrt{3}}{2\hbar}$. This linear dispersion relation allows an exact treatment of low-energy electronic excitations described in terms of Dirac fermions [86].

3.3 Carbon nanotubes

The existence of carbon nanotubes was first hypothesized by Smalley and Dresselhaus [87] at the beginning of 1990s, after the successful production

of fullerenes. They were postulated as elongated forms of the C_{60} molecule, and some of its symmetry-based properties were predicted. In 1991 their formation in substantial quantities was first observed by Iijima *et al.* [10] using an arc-discharge evaporation method and transmission electron microscopy (TEM) for the observation of the resulting fullerene soot. This report definitely boosted the work on carbon nanotubes. Nevertheless these structures had been observed much before [88], actually back to 1952 [89], though in this work as well in later ones (*e.g.* [90]) the focus was not set in these tubes. Just two years after Iijima's report, it was possible to obtain much thinner tubes consisting of one single shell [91, 92]. Since then an incredible amount of work has been done to investigate the properties of these fascinating materials, efforts coming both from experimental as theoretical studies. There are numerous reviews and books in the literature which will complete the description given here (see for instance [85, 93, 94, 95, 96, 97]).

3.3.1 Geometric structure of carbon nanotubes

A single-wall carbon nanotube (SWCNT) is built by a single graphite layer rolled up into a seamless hollow cylinder with a typical diameter of 0.7-1.5 nm. Its structure is macroscopic along the tube axis, but of atomic dimensions in its circumference, building a quasi-one-dimensional system. We will see that the geometry of the graphene lattice is transferable, with some adaptations, to carbon nanotubes. Carbon nanotubes usually appear in a concentric configuration. A carbon nanotube (CNT) consisting of several concentric cylinders is called a multi-wall carbon nanotube (MWCNT).

Carbon nanotubes differing in diameter and chirality are obtained by wrapping up the graphene sheet in different ways (see Fig. 3.11). The resulting types of carbon nanotubes can be distinguished not only by their geometrical structure but also by several important physical properties like the electronic band structure and the spatial symmetry group.

Depending on the winding of hexagons along the tube, one talks of nanotubes of different chiralities. A slight change in chirality can transform a metallic tube into a large-gap semiconductor. SWCNTs have thus metallic or semiconducting properties depending on their chirality, due to quantization of electron waves along the circumference of the tube [99, 100, 101]. We can classify the carbon nanotubes in two categories: chiral and achiral nanotubes. The first ones have a spiral symmetry while the second ones are completely symmetric around the nanotube axis. There are only two types of achiral nanotubes: armchair and zigzag CNTs, which receive their names due to the

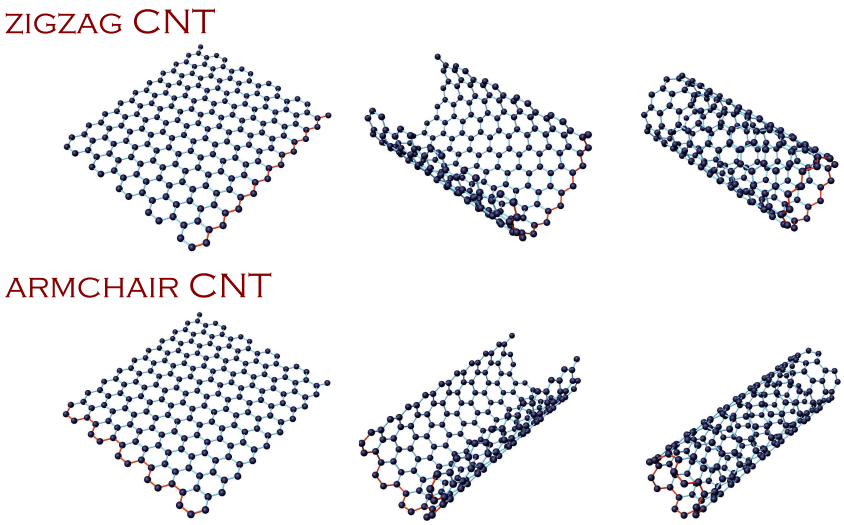

Figure 3.11: This figure illustrates how carbon nanotubes can be actually obtained by wrapping up a sheet of graphene. Depending on the axis we choose for folding up the graphene piece, we will obtain nanotubes of different chiralities. Here both a zigzag (top) and an armchair (bottom) nanotubes are shown [taken from Ref. [98]].

shape of the cross section along the circumference. In Fig. 3.12 an armchair, a zigzag and a chiral CNT are shown. It can be clearly seen in this figure that in the achiral tubes the winding of hexagons runs parallel to the tube axis, while in the chiral tube it builds an spiral.

Because the microscopic structure of carbon nanotubes is derived from that of graphene, carbon nanotubes are usually labeled in terms of the graphene lattice vectors given by Eq. (3.1). The unit cell of a CNT is defined on the graphene layer through the so-called chiral vector and the translational vector.

Chiral vector C

The chiral vector uniquely determines the *whole* microscopic and geometric structure of a particular nanotube and provides its classification in different categories. $\mathbf{C}$ is a circumferential vector and is defined in terms of the unit vectors of graphene:

$$\mathbf{C} = n\mathbf{a}_1 + m\mathbf{a}_2 = (n, m), \tag{3.26}$$

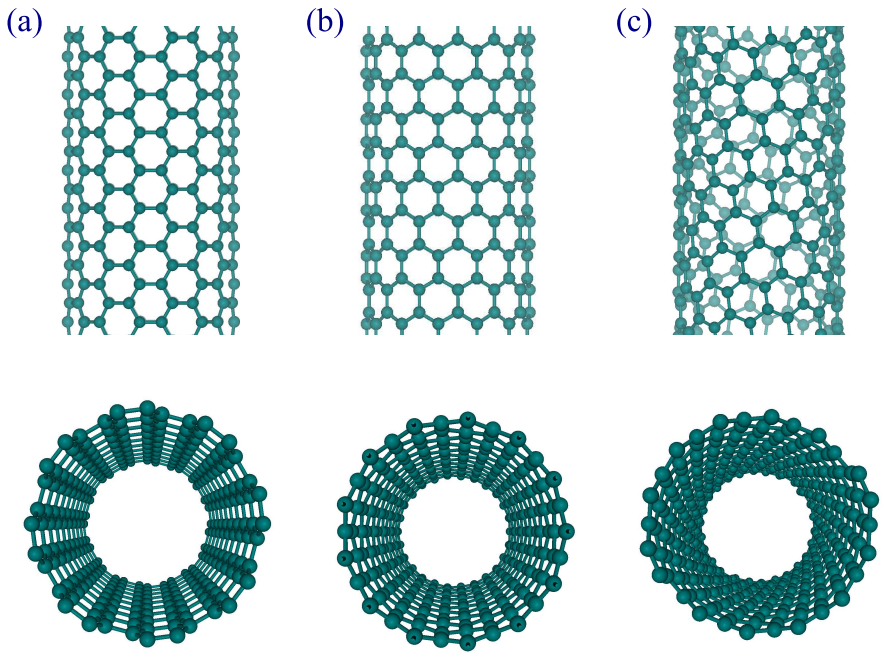

Figure 3.12: Lateral and front sight of three CNTs: two achiral ones (an armchair and a zigzag nanotube), where the mirror image has an identical structure to the original one, and one chiral tube, where the mirror image cannot be superposed to the primary one. The tubes are chosen so as to have similar diameters and are respectively (a) a (8,8) CNT, (b) a (13,0) CNT, and (c) a (12,2) CNT.

where n and m are integers. The symmetry of the hexagonal lattice allows to restrict the choice of n and m, so that the $\mathbf{C}$ lies within a wedge comprising one twelfth of the Bravais lattice (see Fig. 3.13). For any other CNT we can find an equivalent one in this region. Hence we will use the convention of values of (n, m) such that $0 \leq m \leq n$, and $n > 0$.

As $\mathbf{C}$ rolls up to build the circumference of the CNT, the tube diameter can be easily calculated from the length of the chiral vector:

$$d = \frac{|\mathbf{C}|}{\pi} = \frac{a}{\pi}\sqrt{n^2 + m^2 + nm}, \tag{3.27}$$

where $\mathbf{a}_1 \cdot \mathbf{a}_1 = \mathbf{a}_2 \cdot \mathbf{a}_2 = a^2$ and $\mathbf{a}_1 \cdot \mathbf{a}_2 = a^2/2$, as $\mathbf{a}_1$ and $\mathbf{a}_2$ are not orthogonal. Figure 3.13 shows the unrolled honeycomb lattice with the graphene unit vectors $\mathbf{a}_1$ and $\mathbf{a}_2$ and an example of chiral and translational vector,

which will be described below. The dotted arrows indicate the directions the **C** should have in order to obtain zigzag or armchair nanotubes.

The chiral vector **C** also settles the tilt angle of the hexagons with respect to the tube axis, the so-called chiral angle θ, which is defined as the angle between **C** and $\mathbf{a}_1$, that is:

$$\cos\theta = \frac{\mathbf{C}\cdot\mathbf{a}_1}{|\mathbf{C}|\,|\mathbf{a}_1|} = \frac{2n+m}{2\sqrt{n^2+m^2+nm}}. \tag{3.28}$$

As explained before the symmetry of the lattice, allows to keep the choice of θ between 0 and $\pi/6$, without loosing generality, where 0 is the special case of a zigzag and $\pi/6$ of an armchair nanotube. CNTs with a θ between these two angles are chiral as already mentioned, *i.e.*, they produce a mirror image of their structure upon exchange of n and m. Table 3.1 summarizes these facts.

Translational vector T

The translational vector is perpendicular to the chiral vector, running thus along the tube axis. Its length gives then the periodicity of the nanotube structure along the axis direction. We can write **T** in terms of two integers t_1 and t_2:

$$\mathbf{T} = t_1\mathbf{a}_1 + t_2\mathbf{a}_2 = (t_1, t_2). \tag{3.29}$$

t_1 and t_2 are chosen in such a way as to fulfill the requirement $\mathbf{C}\cdot\mathbf{T} = 0$, given by the definition of **T**. They must therefore fulfill: $(2n+m)\,t_1 = -(2m+n)\,t_2$. After imposing the smallest length to **T** to reach an equivalent lattice atom (see Fig. 3.13), so as to build with **C** the unit cell, we obtain

$$t_1 = \frac{2m+n}{d_R}, \qquad t_2 = -\frac{2n+m}{d_R} \tag{3.30}$$

where d_R is the greatest common divisor of $2m+n$ and $2n+m$.

The translational period $|\mathbf{T}|$ is strongly dependent on the chirality of the tube, in fact armchair nanotubes have the shortest unit cells with less number

Type	**C**	θ
armchair	(n,n)	$\pi/6$
zigzag	$(n,0)$	0
chiral	(n,m)	$0 < \lvert\theta\rvert < \pi/6$

Table 3.1: Properties of achiral and chiral nanotubes.

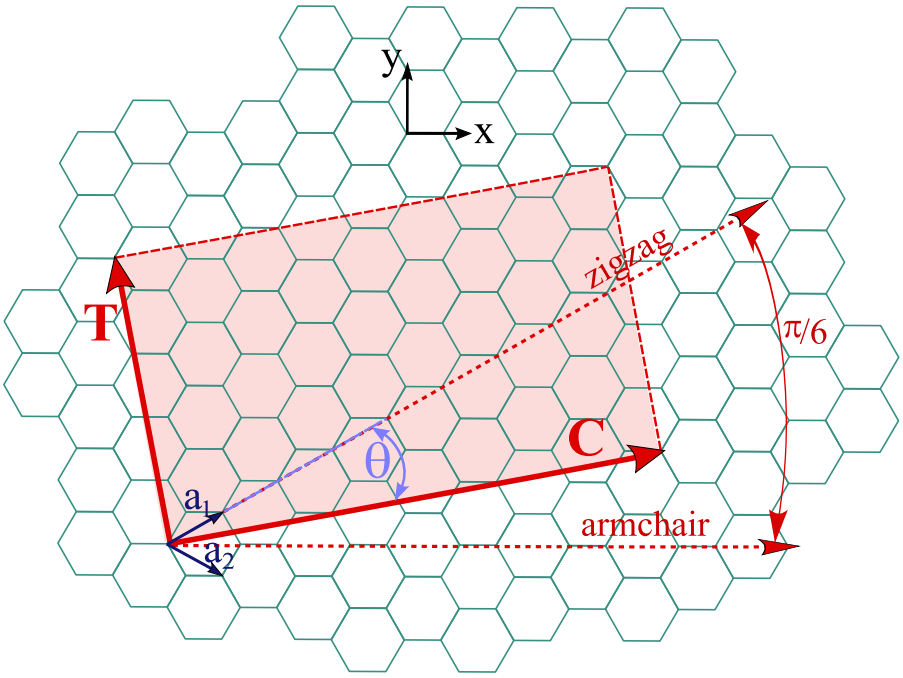

Figure 3.13: The chiral vector **C** and the translational vector **T** are shown on the graphene honeycomb lattice. The example sketched corresponds to the CNT characterized by **C** =(6,3). Together with its translational vector, given in this case then by **T**=(4,-5), it builds the rectangular unit cell of the CNT (shaded area). θ is the chiral vector described in the text, which takes values between 0 and $\pi/6$ covering all non equivalent CNTs.

of atoms and chiral tubes can have very long unit cells comprising a large number of atoms. It can be calculated to be $|\mathbf{T}| = a\sqrt{3}\sqrt{n^2+m^2+nm}/d_R$.

The area of the rectangular unit cell of a nanotube is $|\mathbf{C}\times\mathbf{T}|$, so that we can calculate the number N of graphene hexagons per unit cell by dividing it by the hexagon area:

$$N = \frac{|\mathbf{C}\times\mathbf{T}|}{|\mathbf{a}_1\times\mathbf{a}_2|} = \frac{2(n^2+m^2+nm)}{d_R}. \tag{3.31}$$

Since the graphene unit cell contains two atoms, the number of atoms per unit cell is $2N$. Hence there will be N pairs of bonding π and anti-bonding π^* electronic energy bands for the one-orbital tight-binding approximation. For the nanotubes presented in Fig. 3.12, the number of atoms per unit cell increases from left to right, being 32 for the armchair (8,8) CNT, 52 for the zigzag (13,0) CNT, and for the chiral (12,2) CNT of similar radius this

number increases up to 344.

3.3.2 Brillouin zone and dispersion relation of carbon nanotubes

was

The unit cell in real space of a SWCNT is defined, as already mentioned, by the lattice vectors **C** and **T**. The reciprocal lattice vectors have to be perpendicular to the unit vectors in real space, therefore we obtain one in the direction of the tube axis, defined as $\mathbf{K}_2$, and one that points along the circumference, $\mathbf{K}_1$. We can calculate them through the relations

$$\begin{aligned} \mathbf{C}\cdot\mathbf{K}_1 &= 2\pi, \quad & \mathbf{T}\cdot\mathbf{K}_1 &= 0, \\ \mathbf{C}\cdot\mathbf{K}_2 &= 0, \quad & \mathbf{T}\cdot\mathbf{K}_2 &= 2\pi \end{aligned} \tag{3.32}$$

and obtain using Eq. (3.30-3.31):

$$\mathbf{K}_1 = \frac{1}{N}(-t_2\mathbf{b}_1 + t_1\mathbf{b}_2), \quad \mathbf{K}_2 = \frac{1}{N}(m\mathbf{b}_1 - n\mathbf{b}_2) \tag{3.33}$$

where $\mathbf{b}_1$ and $\mathbf{b}_2$ are the reciprocal lattice vectors of graphene (see Fig. 3.6). The lengths of these vectors are respectively

$$\begin{aligned} |\mathbf{K}_1| &= \frac{4\pi}{aNd_R}\sqrt{n^2+m^2+nm} = \frac{2\pi}{|\mathbf{C}|} \quad \text{and} \\ |\mathbf{K}_2| &= \frac{4\pi}{\sqrt{3}aN}\sqrt{n^2+m^2+nm} = \frac{2\pi}{|\mathbf{T}|}, \end{aligned} \tag{3.34}$$

and they define the unit cell of the reciprocal lattice, as can be seen in the example of Fig. 3.14.

The vector $\mathbf{K}_1$ is naturally discretized by the periodic boundary condition of the circumferential direction of the nanotube, while $\mathbf{K}_2$ depends on the boundary condition at the nanotube edges. That is, while the density of allowed quantum mechanical states in the circumferential direction will be very limited, the number of states in axial direction may be very high. In case of an infinitely long nanotube the vector $\mathbf{K}_2$ is continuous. Considering that, due to the boundary conditions along the circumference, the spacing of allowed **k**'s is $2\pi/|\mathbf{C}|$, that is, that the spacing of allowed **k**'s in the direction of $\mathbf{K}_1$ equals the length of the Brillouin zone (BZ) in this was direction, it follows that the BZ of a CNT is actually a line in the momentum space defined by $\mathbf{K}_2$. The dispersion relation can be then calculated for the **k**

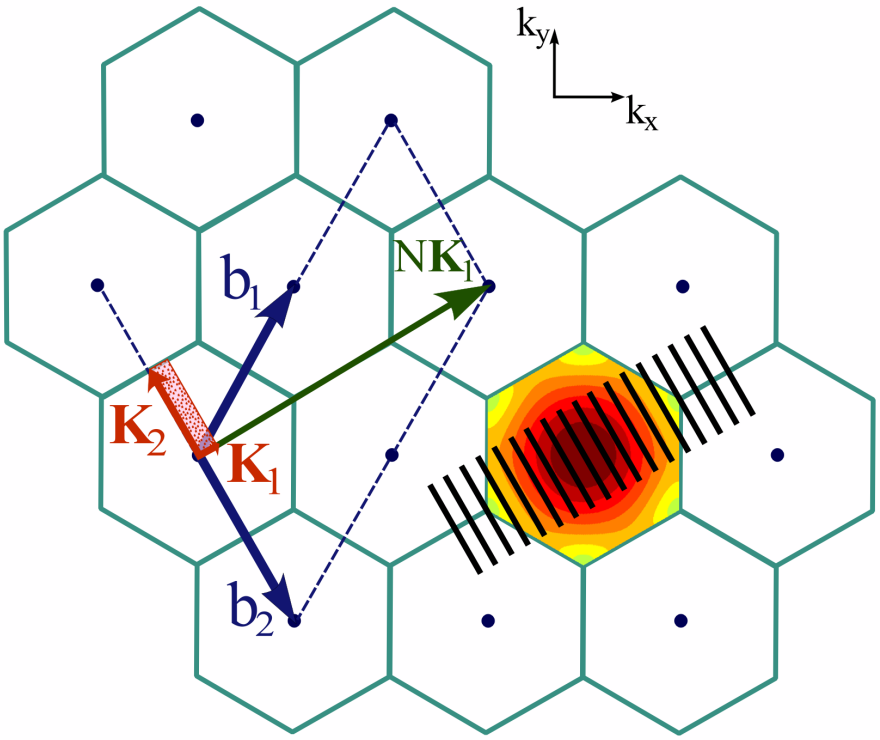

Figure 3.14: The Brillouin zone of a (9,0) CNT on the underlying reciprocal lattice of a graphene layer, with translational vectors $\mathbf{b}_1$ and $\mathbf{b}_2$. The reciprocal lattice vectors of the CNT are given by $\mathbf{K}_1$ and $\mathbf{K}_2$, which build the Brillouin zone (BZ) in the momentum space (dotted shaded area). The extended BZ in the graphene reciprocal lattice consists of N lines parallel to $\mathbf{K}_2$, the reciprocal lattice vector along the tube axis, separated by a distance $|\mathbf{K}_1|$. These discrete set of allowed values defined the bands of the nanotube as cuts of the dispersion relation for graphene (here projected into its BZ). The lines lying outside the first BZ of graphene can be always mapped back into it with the corresponding lattice vectors. In this case, the (9,0) CNT shows a metallic behavior as these lines go through the corners of the hexagonal graphene BZ, the K points.

vectors belonging to this line, as has been done for the graphene in Sec. 3.2.2, obtaining the bands for the CNT. This calculation could nevertheless involve quite big matrices even in a one-orbital approximation, as in general the number of atoms in the unit cell in real space of a CNT may be quite large, $2N$ as given by Eq. (3.31). Knowing the dispersion relation of graphene, it is however much more convenient to extract the information needed from it, exploiting their structural relation. We can then expand the BZ of the CNT by translating it by $\alpha\,\mathbf{K}_1$ with $\alpha = 0, \ldots, N-1$, as $N\,\mathbf{K}_1 = -t_2\mathbf{b}_1 + t_1\mathbf{b}_2$ is

already a reciprocal vector of two-dimensional graphite, and thus equivalent to the one we started from –for $\alpha = 1, ..., N-1$ none of the $N-1$ vectors $\alpha \mathbf{K}_1$ are reciprocal lattice vectors of graphene, because t_1 and t_2 have no common divisor as seen in Eq. (3.30)–. Hence, N lines compose the BZ of the CNT in this extended zone scheme, which give rise to $2N$ one-dimensional bands, obtained simply by substituting these allowed $\mathbf{k}$ vectors in the expression of the dispersion relation of graphene as given in Eq. (3.19). Figure 3.16 shows the bands for several CNTs.

The extended one-dimensional Brillouin zone of carbon nanotubes is therefore a cut through the Brillouin zone of graphene and consists of N lines parallel to the axis direction of length $2\pi/|\mathbf{T}|$, as illustrated in Fig. 3.14. The number of lines increases with increasing diameter, while the distance between them decreases. The allowed states are given by

$$\mathbf{k} = \alpha \mathbf{K}_1 + \beta \frac{\mathbf{K}_2}{|\mathbf{K}_2|} \quad \text{with} \quad \alpha = 0, ..., N-1, \quad -\frac{\pi}{|\mathbf{T}|} \leq \beta \leq \frac{\pi}{|\mathbf{T}|}. \tag{3.35}$$

If one of these lines goes through a K point, the nanotube is metallic, otherwise it is semiconducting.

Equivalently, the values of allowed $\mathbf{k}$ can be derived by imposing directly the boundary conditions: quantum mechanically, these boundary conditions define allowed modes (1D states) with wave vectors along the circumferential direction obeying the following quantization requirement:

$$\mathbf{C} \cdot \mathbf{k} = 2\pi\alpha \quad \Rightarrow \quad \mathbf{k} = \alpha \mathbf{K}_1. \tag{3.36}$$

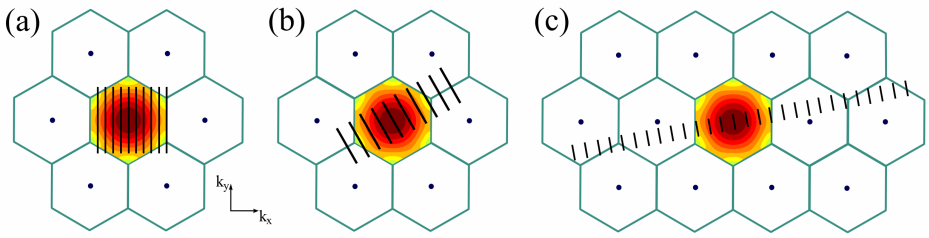

Figure 3.15: Projection of the allowed states of several CNTs onto the first Brillouin zone of graphene. Armchair CNTs as the (5,5) CNT in (a) show a metallic behavior, as it allowed momenta include the corners of the hexagon. Zigzag CNTs might show a metallic as well as a semiconducting behavior. In Fig. 3.14 a metallic zigzag NT was shown, in (b) the resulting BZ for the (5,0) CNT represents an example of semiconducting CNTs. In (c) the BZ of the chiral (4,2) CNT is sketched, consisting of 28 lines parallel to $\mathbf{K}_2 = (2/28\,\mathbf{b}_1 - 4/28\,\mathbf{b}_2)$.

Let us consider for instance an armchair CNT. The translational vectors for the real and reciprocal lattice are respectively

$$\begin{aligned} &\mathbf{C} = (n,n), \quad \mathbf{T} = (1,-1), \quad \text{and} \\ &\mathbf{K}_1 = \tfrac{1}{2n}\left(\mathbf{b}_1 + \mathbf{b}_2\right) = \tfrac{2\pi}{\sqrt{3}na} k_x, \quad \mathbf{K}_2 = \tfrac{1}{2}\left(\mathbf{b}_1 - \mathbf{b}_2\right) = \tfrac{2\pi}{a} k_y. \end{aligned} \tag{3.37}$$

Thus the lines building the BZ are parallel to the k_y axis (see Fig. 3.15 (a)) and obviously, the K points are allowed states for CNTs of this chirality.

For a zigzag CNT, the corresponding translational vectors are then:

$$\begin{aligned} &\mathbf{C} = (n,0), \quad \mathbf{T} = (1,-2), \quad \text{and} \\ &\mathbf{K}_1 = \tfrac{1}{2n}\left(2\mathbf{b}_1 + \mathbf{b}_2\right), \quad \mathbf{K}_2 = -\tfrac{1}{2}\mathbf{b}_2. \end{aligned} \tag{3.38}$$

which correspond to BZ lines parallel to vector $\mathbf{b}_2$ (see Fig. 3.15 (b)). The condition for the CNT to be metallic, that is, for the line to include a K point, as $\mathrm{K} = \left(2\pi/\sqrt{3}a, 2\pi/3a\right) = \left(2\mathbf{b}_1 + \mathbf{b}_2\right)/3$, is that $\alpha/2n = 1/3$. Thus for $(n,0)$ CNTs where n is a multiple of 3, a metallic behavior will be seen.

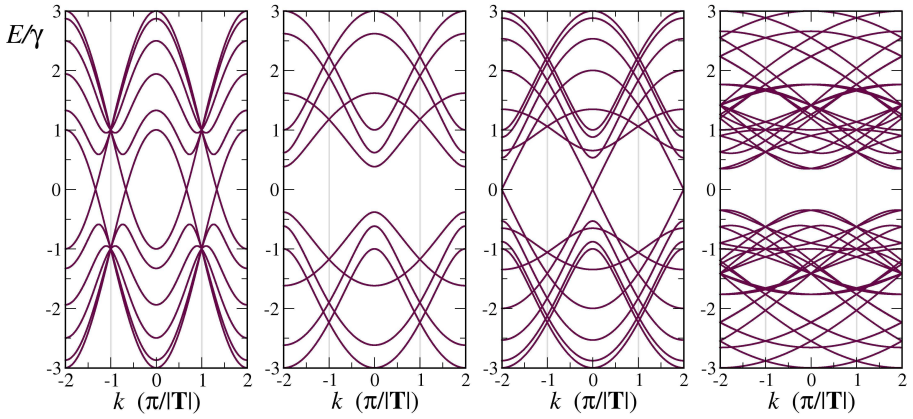

Figure 3.16: Band structure of (a) a (5,5) CNT, (b) a (5,0) CNT, (c) a (9,0) CNT, and (d) a (4,2) CNT. The bands are cross sections of the bands of graphene (see Fig. 3.8). k represents here the momentum of the electron along the tube axis, which in general is a combination of k_x and k_y components. If the cutting lines pass through a K point, the one-dimensional energy bands have a zero energy gap. Otherwise they will have a finite gap. It can be observed that tubes fulfilling $n - m = 3q$, for any integer q, are metallic.

For a general (n,m) CNT, the condition to have allowed K points in the bands can be written as

$$\alpha\mathbf{K}_1 + \beta\mathbf{K}_2 = \frac{1}{3}\left(2\mathbf{b}_1 + \mathbf{b}_2\right) \tag{3.39}$$

which is fulfilled for

$$\alpha = \frac{2n+m}{3} \quad \text{and} \quad \beta = \frac{m}{d_R}. \tag{3.40}$$

Then the general condition for metallic nanotubes is that $2n+m$ (or equivalently $n-m$) is a multiple of 3. As a consequence, one third of all CNT types are metallic for a statistic distribution of chiralities.

The band structure of carbon nanotubes can be also calculated without referring to the one of graphene. It is for this case less convenient, but we will nevertheless introduce it here because is a more general procedure and can be applied to any periodic structure, as for instance, double-walled nanotubes. Since CNTs are periodic systems, the system can be sliced into repeating unit cells as seen in Fig. 3.17. We will considered here a system periodic in one of its spatial dimensions, which we will take as being the x axis direction. The tube Hamiltonian has therefore the form

$$\mathcal{H} = \begin{pmatrix} \ddots & \ddots & \ddots & & & \\ & \mathcal{H}_1^\dagger & \mathcal{H}_0 & \mathcal{H}_1 & & 0 \\ & & \mathcal{H}_1^\dagger & \mathcal{H}_0 & \mathcal{H}_1 & \\ & 0 & & \mathcal{H}_1^\dagger & \mathcal{H}_0 & \mathcal{H}_1 \\ & & & & \ddots & \ddots & \ddots \end{pmatrix}, \tag{3.41}$$

where $\mathcal{H}_0$ and $\mathcal{H}_1$ are the unit cell Hamiltonian and the Hamiltonian for the coupling between two neighboring unit cells, respectively.

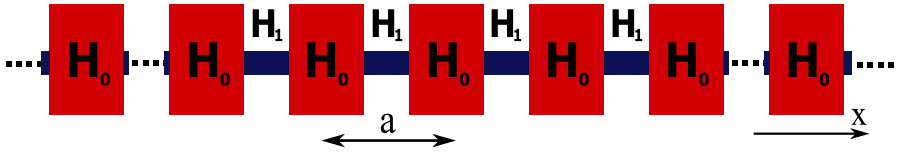

Figure 3.17: Simplified picture of a system periodic in one dimension. The system can be divided into equivalent parts, translated one from another by integer multiples of the period a. It is convenient to choose this periodic slices as small as possible. Therefore one usually takes the unit cell of the system as the repetition unit, being a the lattice constant in that direction. $\mathcal{H}_0$ is the Hamiltonian describing one of these slices in which the system is divided. $\mathcal{H}_1$ is the Hamiltonian coupling two neighboring slices. No coupling beyond first neighbor layers is considered here.

According to Bloch theorem, for a periodic Hamiltonian the wavefunction of the system can be written as a modulated plane wave with a with a modulation function containing the periodicity of the Hamiltonian. By separating

the wavefunction in its spatial directions and using Bloch Ansatz for the periodic one, we can write the wavefunction as

$$\Psi(\mathbf{k},\mathbf{r}) = e^{ik_x x}\chi(x)\xi(k_y,k_z;y,z) \tag{3.42}$$

And substituting it into Schrödinger equation, Eq. (1.1), we obtain the following equation by taking into account the structure of our Hamiltonian given in Eq. (3.41):

$$\begin{aligned}&\Big[\mathcal{H}_1^\dagger e^{ik_x(n-1)a}\chi\left((n-1)a\right) + \mathcal{H}_0 e^{ik_x na}\chi\left(na\right)\\ &+\mathcal{H}_1 e^{ik_x(n+1)a}\chi\left((n+1)a\right)\Big]\,\xi = Ee^{ik_x na}\chi\left(na\right)\xi.\end{aligned} \tag{3.43}$$

Taking into account the periodicity of the modulation function χ, it is straightforward to see that the band structure $E(k_x)$ for an infinite nanotube can be calculated by solving the eigenvalue problem of the effective Hamiltonian

$$\mathcal{H}_{\text{eff}} = \mathcal{H}_0 + \mathcal{H}_1 e^{ik_x a} + \mathcal{H}_1^\dagger e^{-ik_x a}. \tag{3.44}$$

It can be observed that $\mathcal{H}_{\text{eff}}$ is an hermitian operator.

3.4 C_{60}: the bucky-ball

The C_{60} molecule is part of a large family of cage-like carbon clusters known as fullerenes (see Fig. 3.1), which were named after the architect Richard Buckminster Fuller, who was responsible for the design of the first geodesic domes. For this same reason the C_{60} is also called the bucky-ball.

C_{60} is a soccer-ball shaped molecule, built up of fused pentagons and hexagons. The pentagons, absent in graphite and diamond, provide the characteristic curvatures. The I_h-symmetrical (icosahedral) C_{60} is the most abundant fullerene obtained by usual preparation. Since its discovery in 1985 [103] it has attracted a lot of interest worldwide (see for instance Ref. [104, 105, 106, 107, 108]). This is due to the great number of applications of this material and the progress that has been accomplished in the experimental field, especially after the invention of techniques for the production and isolation of bulk quantities of fullerenes (fullerites) in 1990 [109, 110, 111]. Particularly they have recently been subject of extensive study because of their superconducting properties [112].

Fullerenes can be understood as formed from a graphitic layer, having though a hybridization a bit different from that of graphite, as the curvature induces

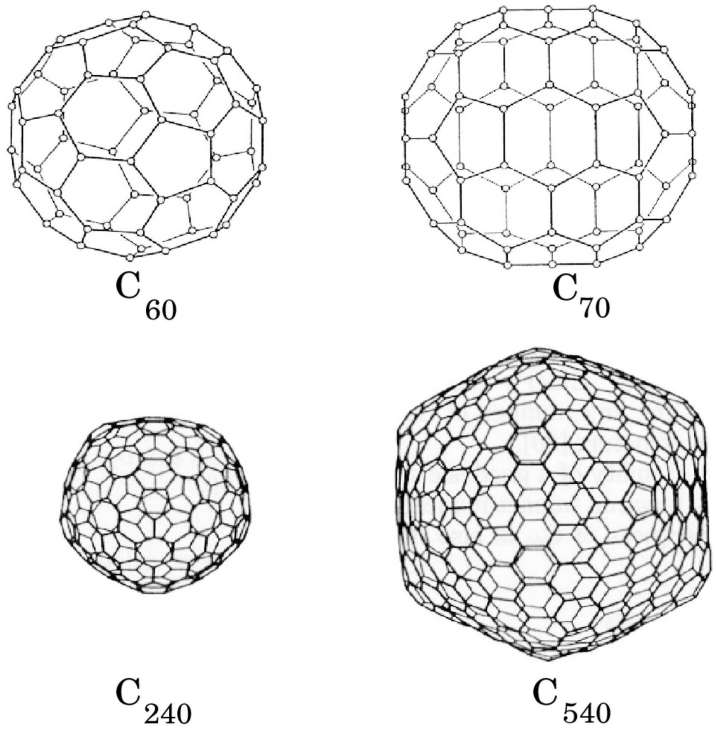

Figure 3.18: Some examples of fullerenes. C_{60}, being the simplest among them, has a more homogeneous distribution of curvature. For bigger fullerenes the curvature effect around the twelve pentagons is much more clearly seen [taken from Ref. [102]].

some mixture with sp^3 hybridization. We could referred to it as a $sp^{2+\delta}$ hybridization with $0 < \delta < 1$. We will discuss more about fullerenes and particularly about the bucky-ball in Chapter 5.

3.5 Carbon nanostructures as model systems for quantum transport

Let us apply now the methods presented up to here in this and in the previous chapters. As model systems we will considered graphene ribbons and carbon nanotubes, both systems which attract a lot of interest as they are now available for experimental investigations, they are characterized by a simple structure and nevertheless they present a whole range of interesting quantum

phenomena.

3.5.1 Transport in an infinite carbon nanotube

The transport properties of perfect infinite CNTs are expected to be characterized by their ballistic behavior, so that conduction occurs through well-separated channels with a transmission probability per conducting channel of 1. As shown in Eq. (3.25) for graphene, for metallic CNTs the dispersion relation around the Fermi points is linear. Furthermore, at these points the energy separation between the bands was crossing the Fermi level and those next in energy is of the order of electron volts, as depicted in Fig. 3.19. This large spacing in energy prevents interband scattering even at room temperature. The transport is thus constrained to a single one-dimensional mode.

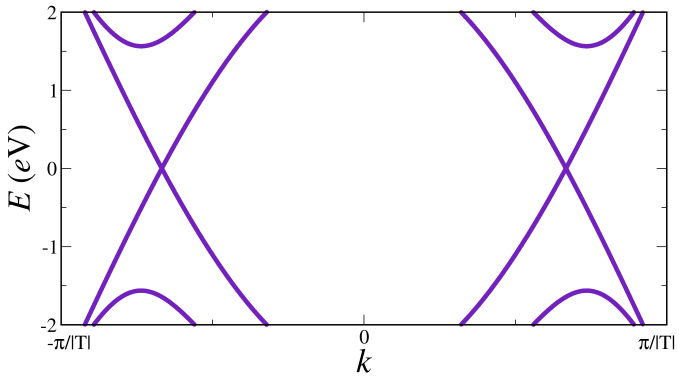

Figure 3.19: One-dimensional dispersion spectrum of a (5,5) CNT around the Fermi energy (set at zero). The linear behavior of the bands around the both Fermi points can be observed as well as the separation in energy of the next lying bands.

As there are subbands with positive and negative slope at both Fermi points, for an ideal, scattering-free CNT one expects a conductance around the Fermi energy of

$$G^{\text{tot}} = 2\frac{2e^2}{h} = \frac{4e^2}{h}, \tag{3.45}$$

that is, of two conductance quanta, according to Landauer formula, Eq. (2.33).

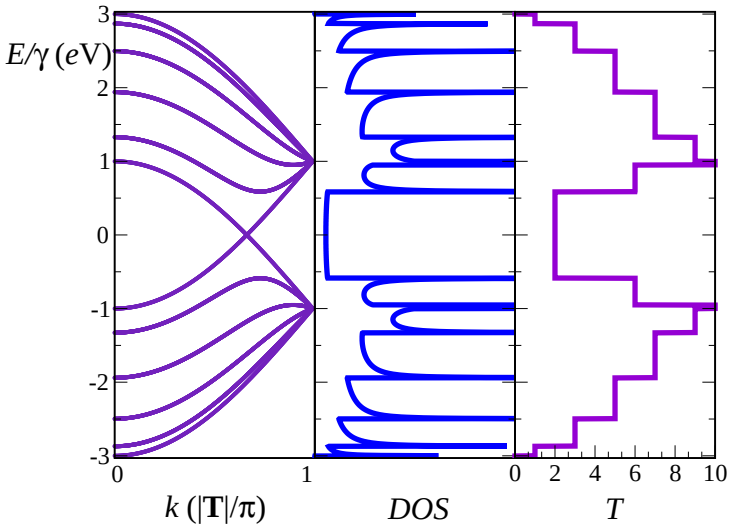

Figure 3.20: Band structure, density of states and transmission from left to right for an infinite zigzag (5,5) SWCNT.

Fig. 3.20 and Fig. 3.21 show the band structure, density of states and transmission for an infinite armchair and zigzag SWCNT respectively.

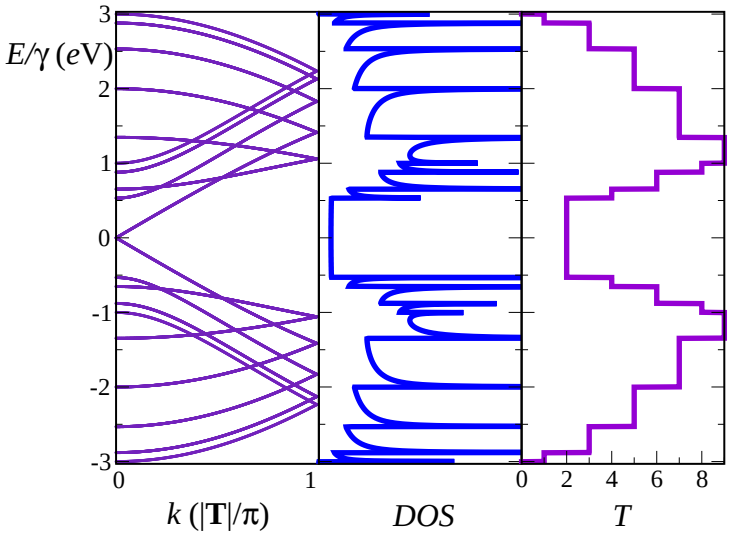

Figure 3.21: Band structure, density of states and transmission from left to right for an infinite zigzag (9,0) SWCNT.

The band structure has been calculated according to the Bloch theorem as introduced in Sec. 3.3.2. Note that for SWCNTs the bonding and antibonding states are symmetric.

For the calculation of the transmission of the infinite single wall CNTs, we used the formalisms introduced in Chapter 2, through the Fisher-Lee relation contained in Eq. (2.64). Also from the dressed Green function, Eq. (2.62), we obtain the density of states, as shown in Sec. 2.3.3.

The DOS of CNTs is characterized by a series of van-Hove singularities (VHS) corresponding to extrema in the energy dispersion. The peak form of the VHS is characteristic for one dimensional systems as seen in Sec. 2.1.2. At the Fermi energy, as both examples correspond to metallic nanotubes, they show a finite DOS, while the DOS of semiconducting nanotubes has a value of zero. The shape of the DOS has been experimentally confirmed by scanning tunnel microscope (STM) measurements [94].

In the transmission plots we see the expected steps as a function of the energy. According to the Landauer theory for ballistic transport seen in Sec. 2.2, the transmission at a certain energy is equal to the number of conducting channels, corresponding to the number of bands crossing the energy level (note that the bands can be either degenerate or not).

3.5.2 Graphene stripes

Although graphite has been studied for decades, graphene was only isolated in 2004 [11]. The method which led to this important achievement seems to be as simple as the removal one by one of the weakly coupled layers of graphite with adhesive tape, until a single layer remains. The dimensions of these systems are though what make this achievement so astonishing. Since then several experiments [12, 13] have shown the remarkable properties of graphene, which proves to be a very good conductor, in which electrons move as massless relativistic particles. This is due to the linearity of the linear dispersion of conduction electrons around the Fermi points, as shown before in Sec. 3.2.2. Electrons in graphene are of course not massless and their typical speed is almost 400 times lower than the speed of light in vacuum, but because of the linear dispersion relation the effective mass is zero. The conclusions of these experiments are based on their observations of quantum Hall effect in graphene, which furtheron indicate the good quality of the samples. Since these results appeared an overwhelming amount papers have been published about the electronic properties of single and double layer graphene, see for instance Ref. [113, 114, 115, 116, 117, 86].

We present here some results for the band structure, density of states and transmission of several graphene ribbons or graphene stripes. The nomenclature used to define the stripes is that described before for characterizing

the nanotubes, taking leaving only unsaturated atoms with two sigma bonds, that is pending atoms are removed from the unit cell. Calculations are performed both within a π-orbital approach, as usually done for these systems, and in a more complete way, taking into account $2s$ and $2p$ orbitals within the Slater-Koster scheme. The parameters used are orthogonal sp^3 two-center parameters as given in Ref. [118], which are scaled by a distance-dependent factor.

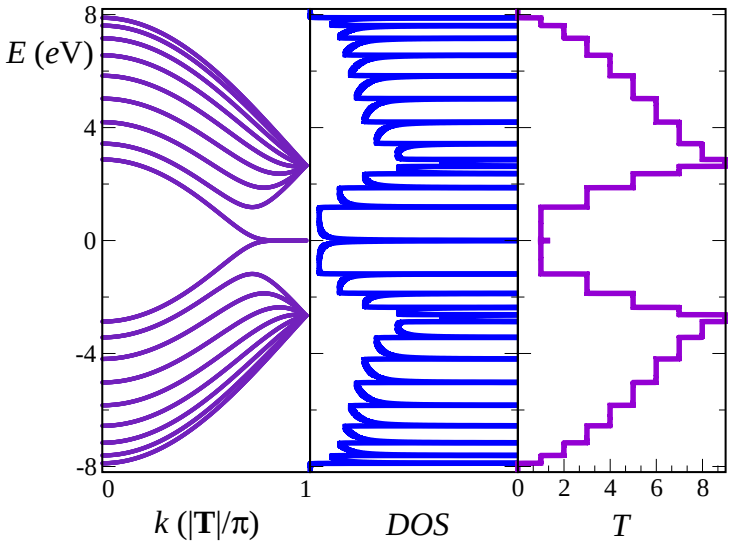

Figure 3.22: Band structure, density of states and transmission from left to right for an infinite graphene ribbon (5,5) for a one-orbital approximation.

Fig. 3.22 and Fig. 3.23 show results for a (5,5) graphene stripe for one-orbital and multi-orbital calculations respectively. The corresponding results for the (9,0) stripe, having armchair edges, are seen in Fig. 3.24 and Fig. 3.24. It is to notice that the stripes with zigzag edges are to be compared to armchair CNT and viceversa. Fig. 3.26 shows for these two types of graphene the change in transmission that takes place by introducing Anderson disorder in the system. The disorder is introduced in the diagonal terms of the Hamiltonian in a random way, changing their magnitude up to W. The transmission characteristic must be then averaged over different realizations of disorder. One can observed that graphene stripes, unlike CNTs [93], are much less protected to disorder. That is, elastic scattering is much more important in these systems.

Another feature to remark is the importance here of studying the differences that appear in these effects by going beyond the π-orbital approximation. In Fig. 3.27 can be observed how s orbitals have a not neglectable contribution in

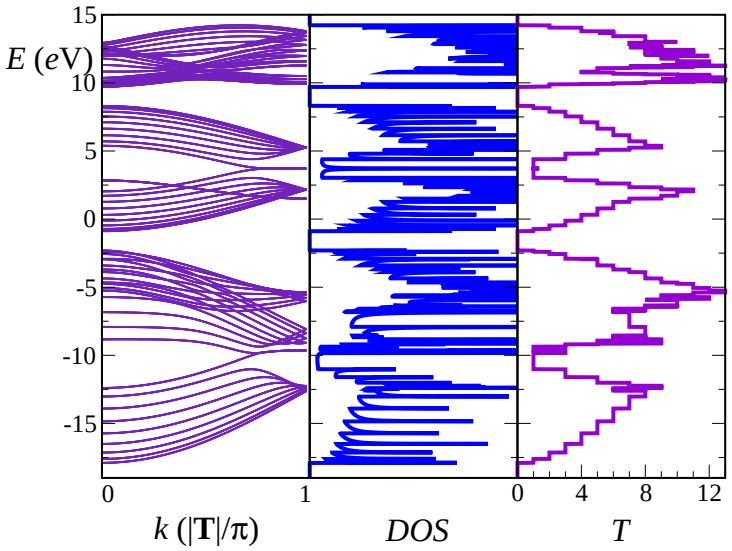

Figure 3.23: Band structure, density of states and transmission from left to right for an infinite graphene ribbon (5,5) with 2s and 2p orbitals considered.

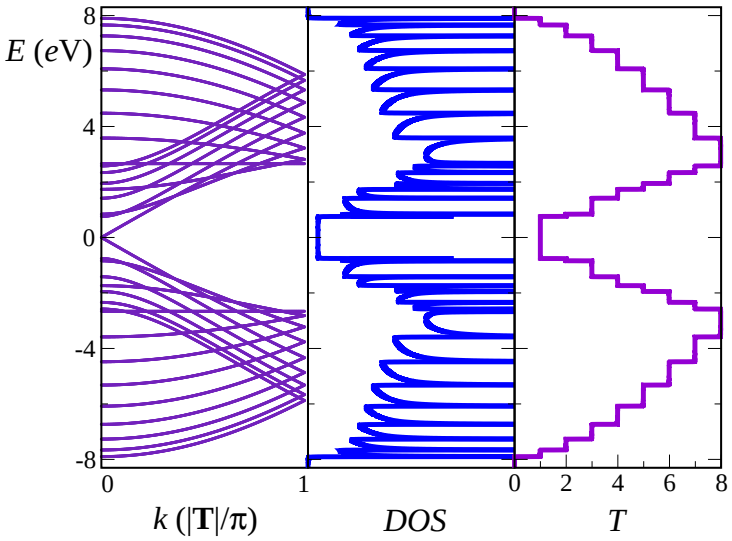

Figure 3.24: Band structure, density of states and transmission from left to right for an infinite graphene ribbon (9,0) for a one-orbital approximation.

a small energy window inside the π band. The Fermi energy is also shifted downwards in energy, changing the conductance value at this point. It is therefore of interest to follow the study of the influence of disorder in such systems considering all conduction electrons.

A further goal is also to go towards more realistic sizes for the stripes, and

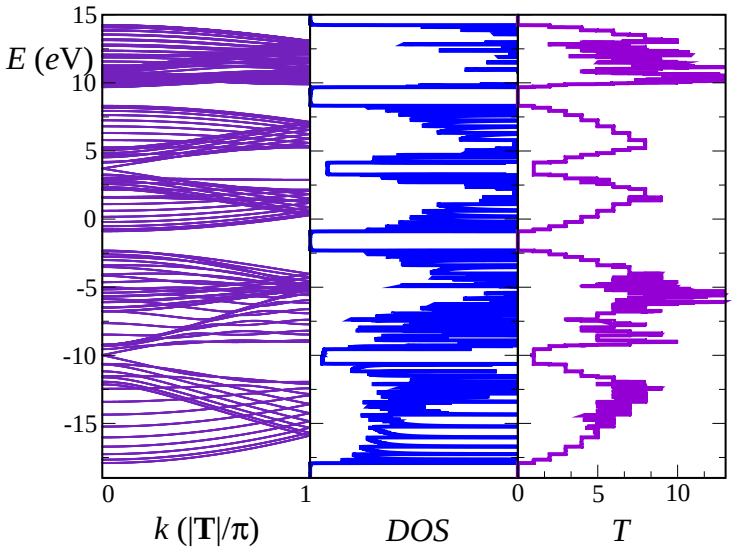

Figure 3.25: Band structure, density of states and transmission from left to right for an infinite graphene ribbon (9,0) with 2s and 2p orbitals considered.

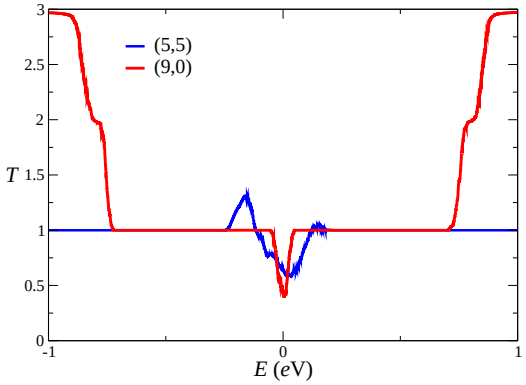

Figure 3.26: Transmission probability after averaging out 100 samples with Anderson disorder of $W = 0.5$ for two graphene stripes.

see the influence of disorder with length as in Fig. 3.28.

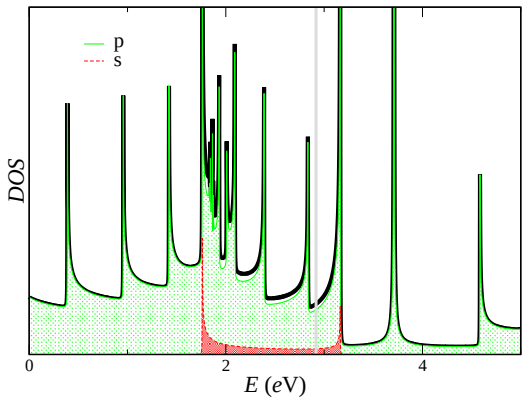

Figure 3.27: Density of states for the (5,5) graphene stripe, for a multiorbital calculation. The contributions of p and s orbitals are highlighted. The gray vertical line indicates the Fermi energy.

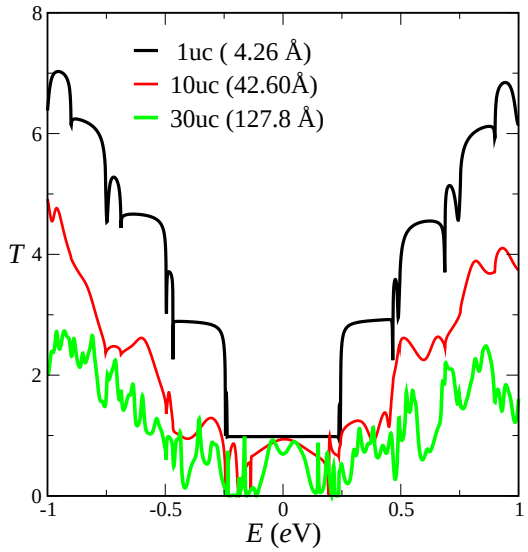

Figure 3.28: For the previous stripe (30,0) the transmission probability is presented in the present of Anderson disorder with $W = 3$ for different lengths of the disorder region.

Chapter 4

Multiterminal nanotubes junctions

Three-branch junctions are envisioned as potential three-terminal units likely functioning as a molecular transistor in the nanometer scale. We investigate the transport properties of three terminal carbon based nanojunctions within the scattering matrix approach. The stability of such junctions is subordinated to the presence of nonhexagonal arrangements in the molecular network. Such "defective" arrangements do influence the resulting quantum transport observables, as a consequence of the possibility of acting as pinning centers of the correspondent wavefunction. By investigating a fairly wide class of junctions we have found regular mutual dependencies between such localized states at the carbon network and a striking behavior of the conductance. In particular, we have shown that Fano resonances emerge as a natural result of the interference between defective states and the extended continuum background. As a consequence, the currents through the junctions hitting these resonant states might experience variations on a relevant scale with current modulations of up to 75%. Furthermore, we study the influence in transport of a time dependent electric field excitation on a carbon nanotube junction and for that we generalize, for molecular transport, one of the ways of tackling with a time-dependent problem, making use of the Floquet theory.

4.1 Introduction

CNTs have been proposed as leads and bridge molecules, since they possess a great versatility, allowing for metallic as well as semiconducting behavior, depending on their diameter and chirality, that is, their degree of helicity (see Sec. 3.3.1). Nanotubes can be easily modified by introducing pentagons, heptagons or octagons into their hexagonal network, as was already shown in the 90's [119, 120]. By joining a metallic nanotube with a semiconducting one, a heterojunction is formed showing a transport behavior corresponding to that of a rectifying diode, as already seen experimentally [121]; actually several applications of CNTs in nanoscale devices have been already described [122, 123, 124, 125, 126].

Yet, for making efficient molecular electronic circuits multi-probe junctions are also needed and their transport characteristics must be understood [127]. *Three-terminal junctions* are especially appropriate for these studies, as they can be taken as building blocks of multi-terminal junctions, where all three branches can be independently contacted by three leads. The understanding of the transport properties of these three-terminal systems is the goal of this work.

The first experimental observation of three-terminal CNTs were as branches in L-, T-, and Y-patterns occurring during the growth of carbon nanotubes produced in an arc-discharge method [128]. but the formation of these junctions was totally random. Since then, new growth methods have been developed to obtain these multi-terminal junctions in a more controlled and high-yield production way: a template-based pyrolytic technique which yields large numbers of well-aligned Y-junctions of multi-walled CNTs (MWCNTs, a coaxial arrangement of CNTs) [129, 130], a hot filament chemical vapor deposition (CVD) system where uniformly Y-shaped junctions are obtained as by-product, with structures that match those of topological models where only heptagons are included as defects in the hexagonal network [131], or pyrolysis of nickelocene in the presence of thiophene [132], or of ferrocene and cobaltocene [133]. Also a simple thermal catalyst CVD method without templates yields a production of H- and Y-junctions as well as 3D-CNT-webs [134, 135]. All these last methods are characterized by growth temperatures just moderately high (650 °C-1000 °C) or even quite low (room temperature). But also the high-temperature arc-discharge technique has been improved to produce Y-junctions in a reasonable proportion [136, 137]. Nearly at the same time, the first observations of three-terminal single-walled CNTs (SWCNTs) were made where the junctions were produced by thermal decomposition of fullerenes [138] or by more sophisticated methods including

electron irradiation on welded nanotubes to finally tailor the transformation of the junction geometry with the formation of heptagonal and octagonal defects [139].

By now, it has been made clear that Y-junctions are not any more a rare phenomenon. Actually taking into account all the different methods which yield similar CNT Y-junctions, these have to be accepted as regular members of the carbon nanostructure family. Although less experimental data is available, transport measurements have been carried out on nanotube junctions, by overlaying one individual SWCNT over another with four electrical contacts where a good tunnel contact at the junction is observed [140], or measuring the I-V characteristics of truly Y-junction MWCNTs which behave as intrinsic nonlinear and asymmetric devices, displaying a clear rectifying behavior [132, 141]. Moreover the transport properties of three-terminal junctions obtained by merging together SWNTs via molecular linkers have also been studied [142].

From the theoretical point of view, much work has been done to clarify the structure of these junctions as well as their intrinsic transport properties. To provide an accurate description of quantum transport in CNT-junctions one cannot neglect their electronic structure via an atomistic model. Theoretical predictions are then based on hypothesized atomic configurations, which try to match the experimental observations on branching angles and tube diameters. But especially the latter have always a wide uncertainty, (due to lack of knowledge of the tip in an STM device, etc). Most of the experiments on Y-junctions are nevertheless dealing with MWCNTs and even with a fish-bone like structure as some growth methods do not achieve a complete graphitization of the tubes. There is therefore still a need for a better experimental characterization of the junctions. Different approaches have been followed to come up with different proposed structures, like considering the junction as evolved from two bend tubes [143] or by considering that three carbon nanotubes join via two triangular central spacers [144]. But no matter how this structure is reached, non-hexagonal elements must be included in the honeycomb-like lattice, following the generalized Euler rule [145], which predicts a bond surplus of six for three-terminal junctions. These pentagons, heptagons or octagons are playing an important role in the transport properties characterizing these junctions, with an electronic structure which differs considerably from that of the nanotube "bulk" region. Thus several groups [146, 147, 148, 144, 149] have analyzed the geometry of multi-terminal junctions and its stability using topological arguments, molecular dynamics techniques or first-principle methods. The role of the symmetry of the junctions and of the chirality of the arms is also addressed by many

authors [150, 151, 152, 153] as well as the electronic interaction [154]. However, the controversy remains over the origin of the rectifying behavior, with some studies claiming it to be a characteristic intrinsic to the symmetry of the junction [151], and other works tracing it back to the interfaces with contacts [152].

Until now Fano resonances have not been exploited as an interesting feature in the transport through this kind of CNT junctions. This phenomenon emerges from the coherent interaction of a discrete state and a continuum and was first discovered by studying the asymmetric peaks of the helium spectrum [155]. Recently the occurrence of this effect and its applications have been studied in numerous mesoscopic devices, including MWCNTs [156, 157], and MWCNT bundles [158] or SWNT bundles [159], and most recently in multiply-connected CNTs [160]. As we will see the conductance through multi-terminal CNT junctions exhibits Fano resonances and these may be used in transport allowing for major changes of the current intensity in short intervals.

The aim of this work is the calculation of transmissions and conductances for different types of three-terminal CNTs, keeping in mind the properties of semi-infinite CNTs considered as partial components of our system analyzed before.

4.2 System and method

Fig. 4.1 shows four archetypical three-terminal CNT devices. These devices have a much greater versatility than two-terminal junctions as the third terminal can be used to apply a gate voltage and thus control the current flow in the channel built by the two other arms, using the gate as a current probe or as a voltage probe. Out of the many possibilities of building three-terminal junctions, we have chosen these four as to have within a few junctions different elements of comparison: different symmetries, different geometries, different chiralities. These junctions have nevertheless common properties, from which in conjunction with their disparities we may draw some general conclusions. As a model for nanoelectrodes, we will use semi-infinite carbon nanotubes and try to gain insight in the quantum transport through these junctions. We calculate the quantum conductance within the well-known Landauer-Büttiker formalism [161, 162] (see Chapter 2) by making use of equilibrium Green functions for tight-binding Hamiltonians [163]. Our structures have been optimized by a relaxation algorithm following a density-functional based nonorthogonal tight-binding scheme (DFTB) [164] (see Sec. 1.6) in order to

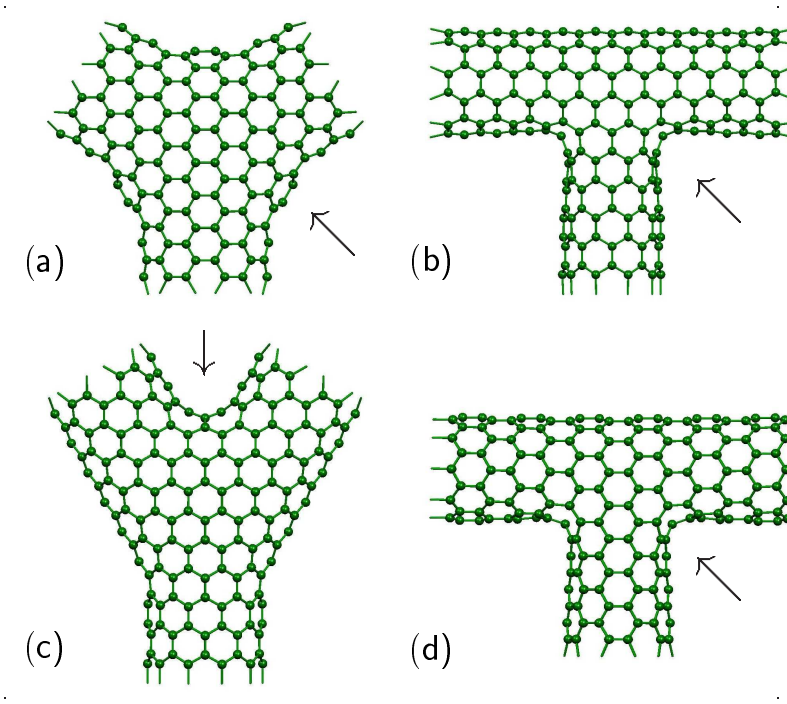

Figure 4.1: Four junctions entirely made out of semiconducting $(10, 0)$ and metallic $(6, 6)$ CNT leads. (a) Y-junction where three armchair tubes join at $120°$. (b) T-junction where two armchair nanotubes join with a semiconducting zigzag nanotube. (c) Y-junction where three armchair nanotubes join forming an angle of $72°$ between the upper arms. (d) T-junction where two semiconducting zigzag nanotubes join with an armchair nanotube. Both Y-junctions have heptagonal rings whereas the T-junctions achieved their relaxed structure by the introduction of four octagons and two pentagons. After relaxation, the average bond length of the heptagons is $2.02\,\%$ larger in (a) and $1.47\,\%$ larger in (c) than the bond length of the hexagonal network. In the case of the T-junctions the average bond length of the octagons is in (b) and (d) $1.35\,\%$ larger, the bond lengths in the pentagons not shared with the octagons are nonetheless smaller than that of the hexagons by $1.07\,\%$ in (b) and $1.31\,\%$ in (d). These values are reasonable for having stable configurations. The defects pointed by the arrows are shown in more detail in the next figures.

deal with stable structures. The basis set used is minimal but conveniently optimized for carbon atoms.

The semi-infinite leads are treated with a decimation technique, an application of the renormalization-group method which allows us to calculate the electronic properties of extended systems with a low computational cost. We follow the iterative procedure to decimate the individual layers (see App. A)

and operate in the space of localized orbitals. As principal layers for our system, we take slices of the CNT and for convenience we choose the CNT unit cell as unit slice. In this way, we renormalized out 2^n slices after n iteration steps, and this exponential behavior allows us to quickly achieve convergence.

The systems considered are all-carbon devices for which a π orbital description level has been proved to yield very satisfactory quantitative results [85], since the properties of carbon nanotubes are basically determined by sp^2 π orbitals.

The Hamiltonian describing our system can be written in a very compact form:

$$\mathcal{H} = \sum_{i,j} h_{ij} \left|i\right\rangle \left\langle j\right| \tag{4.1}$$

where h_{ij} is the coupling or hopping parameter. This transfer integral is only non-zero between nearest-neighbors and takes the value of 2.66 eV. We have also made this parameter distance-dependent, but no significant changes are observed. This can be seen in Fig. 4.2, where the DOS is plotted for one of the T-junctions for which another relaxation was available, making a comparison possible. The DOS calculated with distance-dependent hopping parameters for two differently relaxed structures show an almost identical behavior at low energies.

For calculating the conductance, we divide the system into a central region or scatterer (S) and the three leads (L_1, L_2, L_3). The Green function for our system, $\mathcal{G} = (E - \mathcal{H})^{-1}$, can be written in terms of block matrices

$$\begin{pmatrix} \mathcal{G}_{\mathrm{S}} & \mathcal{G}_{\mathrm{SL}_1} & \mathcal{G}_{\mathrm{SL}_2} & \mathcal{G}_{\mathrm{SL}_3} \\ \mathcal{G}_{\mathrm{L}_1\mathrm{S}} & \mathcal{G}_{\mathrm{L}_1} & \mathcal{G}_{\mathrm{L}_1\mathrm{L}_2} & \mathcal{G}_{\mathrm{L}_1\mathrm{L}_3} \\ \mathcal{G}_{\mathrm{L}_2\mathrm{S}} & \mathcal{G}_{\mathrm{L}_2\mathrm{L}_1} & \mathcal{G}_{\mathrm{L}_2} & \mathcal{G}_{\mathrm{L}_2\mathrm{L}_3} \\ \mathcal{G}_{\mathrm{L}_3\mathrm{S}} & \mathcal{G}_{\mathrm{L}_3\mathrm{L}_1} & \mathcal{G}_{\mathrm{L}_3\mathrm{L}_2} & \mathcal{G}_{\mathrm{L}_3} \end{pmatrix}$$
$$= \begin{pmatrix} E - \mathcal{H}_{\mathrm{S}} & -\mathcal{H}_{\mathrm{SL}_1} & -\mathcal{H}_{\mathrm{SL}_2} & -\mathcal{H}_{\mathrm{SL}_3} \\ -\mathcal{H}^{\dagger}_{\mathrm{SL}_1} & E - \mathcal{H}_{\mathrm{L}_1} & 0 & 0 \\ -\mathcal{H}^{\dagger}_{\mathrm{SL}_2} & 0 & E - \mathcal{H}_{\mathrm{L}_2} & 0 \\ -\mathcal{H}^{\dagger}_{\mathrm{SL}_3} & 0 & 0 & E - \mathcal{H}_{\mathrm{L}_3} \end{pmatrix}^{-1},$$

where the different leads are independent as we restrict our calculations to nearest-neighbor interaction throughout the whole system. Note that $\mathcal{H}_{\mathrm{L}}$ and $\mathcal{G}_{\mathrm{L}}$ are infinite-dimensional matrices. It is straightforward now to obtain

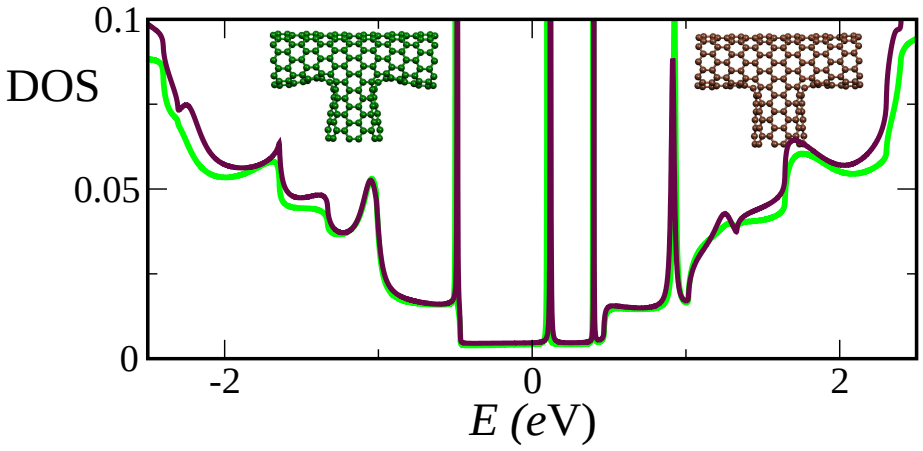

Figure 4.2: DOS for the T-junction (Fig. 4.1.d) for the structure as relaxed using a Tersoff-Brenner potential with molecular dynamics (lighter color) [149] and after relaxation with DFTB (Sec. 1.6) (darker line). Even if the different relaxation methods yield visibly different structures at the junction saddle zones, the DOS around the Fermi energy (with a distance-dependent hopping parameter) is nearly equal.

via a Dyson equation an explicit expression for $\mathcal{G}_{\mathrm{S}}$, which has now only finite matrices:

$$\mathcal{G}_{\mathrm{S}} = (E - \mathcal{H}_{\mathrm{S}} - \Sigma)^{-1} \tag{4.2}$$

where we define $\Sigma = \Sigma_{\mathrm{L}_1} + \Sigma_{\mathrm{L}_2} + \Sigma_{\mathrm{L}_3}$ as the self-energy terms containing the contribution of the semi-infinite leads $\Sigma_{\mathrm{L}_\alpha} = \mathcal{H}^{\dagger}_{\mathrm{L}_\alpha \mathrm{S}}\, g_{\mathrm{L}_\alpha}\, \mathcal{H}_{\mathrm{L}_\alpha \mathrm{S}}$, being $\alpha = 1$, 2 or 3 and $g_{\mathrm{L}_\alpha} = (E - \mathcal{H}_{\mathrm{L}_\alpha})^{-1}$ the lead Green functions. And these functions are calculated using the decimation technique explained in Sec. A.1.1.

With the lead Green functions we can easily calculate the strength of the coupling of the scatterer to the leads

$$\Gamma_{\mathrm{L}_\alpha}(E, \mu_\alpha) = \mathrm{i}\left(\Sigma_{\mathrm{L}_\alpha}(E, \mu_\alpha) - \Sigma^{\dagger}_{\mathrm{L}_\alpha}(E, \mu_\alpha)\right). \tag{4.3}$$

Using all these definitions, we can write the conductance function in a very compact form:

$$G^{\mathrm{el}}_{\alpha\beta} = \frac{2e^2}{h} \mathrm{Tr}\left\{\Gamma_{\mathrm{L}_\alpha} \mathcal{G}_{\mathrm{S}} \Gamma_{\mathrm{L}_\beta} \mathcal{G}^{\dagger}_{\mathrm{S}}\right\}, \tag{4.4}$$

where the factor two accounts for the spin degeneracy. The Landauer-Büttiker formula relates the conductance in a multi-terminal conductor to

its scattering properties. For the three terminal case, if we take one of the leads to be a voltage probe (say for instance lead L_3), we constrain the chemical potential in this arm to be [162]

$$\mu_3 = \frac{G_{31}^{el}\mu_1 + G_{32}^{el}\mu_2}{G_{31}^{el} + G_{32}^{el}}. \tag{4.5}$$

Although this constriction assures a zero current at terminal L_3, this probe is dissipative as the carriers in it loose their phase memory, accounting for a phase-incoherent contribution to the coherent current of carriers reaching directly probe L_1 from L_2. The total conductance can then be written as $G^{tot} = G^{el} + G^{inel}$, where

$$G_{12}^{inel} = \frac{G_{13}^{el}G_{32}^{el}}{G_{31}^{el} + G_{32}^{el}}. \tag{4.6}$$

For our systems the inelastic contribution to the conductance is very small at energies around the Fermi level.

The current measured in this way is then

$$I_{12} = \frac{2e}{h}\int_{-\infty}^{+\infty} \mathrm{d}E \left[f_{L_1}(E) - f_{L_2}(E)\right] \mathcal{T}_{12}(E, \mu_1, \mu_2), \tag{4.7}$$

where $f_{L_\alpha}(E) = \left(e^{(E-\mu_\alpha)/k_B T} + 1\right)^{-1}$ is the Fermi function in the lead L_α, $\mu_1 = eV/2$, $\mu_2 = -eV/2$, and $\mathcal{T}_{12}$ is the total transmission between lead L_2 and L_1 such that $G_{12}^{tot} = \left(2e^2/h\right)\mathcal{T}_{12}$. The voltage drop V is small enough to validate the linear-response regime, and we restrict our calculations to the zero temperature limit.

4.3 Transport properties

We have studied different types of SWCNT junctions, from which four are now presented in Fig. 4.1, chosen in such a way that a variety of heterojunction combinations and a variety of shapes are covered. In these junctions the following groups of three semiinfinite CNTs welded together: $(6,6)-(6,6)-(6,6)$ in a Y-shape, $(6,6)-(10,0)-(6,6)$, both Y- and T-shaped, and $(10,0)-(6,6)-(10,0)$ with a T shape. Two types of CNT leads have been adopted: $(6,6)$ armchair tubes and $(10,0)$ zigzag tubes. As

known (n, m) CNTs, where (n, m) are the indexes unambiguously determining the characteristics of the CNT, are metallic if $n - m$ is a multiple of three, neglecting the $\pi - \sigma$ hybridization. We thus have a metallic tube, the $(6, 6)$ CNT and a semiconducting one, the $(10, 0)$ exhibiting a gap of 0.82 eV. Then by using just these two different CNTs we are able to make M-M and M-S heterojunctions (where M stands for metallic and S for semiconducting).

In the chosen configurations, one of the terminals is taken to be either a voltage probe or a current probe. This gate voltage is controlled in our model by changing the onsite energies of this arm, which are fixed at a far end of the terminal and gradually change in the central region to meet the value set for the other two arms and the junction.

We will now proceed to describe the obtained results for the DOS and conductance of these junctions, which are given in Figs. 4.3, 4.4, 4.5 and 4.6.

Let us consider the electronic structure of the first Y-junction (Fig. 4.1.a), a highly symmetric junction where three metallic $(6, 6)$ armchair nanotubes intersect at $120°$. This structure has mirror symmetry with respect to four planes, being thus the most symmetrical of all four studied junctions, as the other three are characterized by two mirror planes. The necessary negative curvature is provided by the introduction of heptagonal defects, in a number of six to meet the topological constraints imposed by Euler theorem, and distributed symmetrically, two at each saddle region.

This junction shows a metallic behavior, but the transmission probability around the Fermi level is small as seen in the lower panel of Fig. 4.3. The localization of the states at the Fermi energy is schematically seen in the inset of this figure, showing that this is an extended state but also pinned by the defects. This is an effect we see along all the different junctions. It is known that heptagons and pentagons can induce additional electronic states close to the Fermi energy [148, 136], which are seen here (upper panel of Fig. 4.3) between the subbands.

The first T-junction (Fig. 4.1.b) is made up of two metallic $(6, 6)$ armchair nanotubes and a semiconducting $(10, 0)$ zigzag nanotube. This is achieved by introducing two octagons and one pentagon at each bending point. This junction also shows a metallic behavior (upper panel of Fig. 4.4) although one of its branches has a semiconducting character. Remarkable are the two sharp peaks located symmetrically around the Fermi level (approximately at 0.35 eV below and above it). The distribution of these states in the area of the non-hexagonal defects is seen in the upper insets of Fig. 4.4. These are states which do not extend at all to the upper part of the junction and are mainly localized at the defects. To corroborate this thesis, we have checked

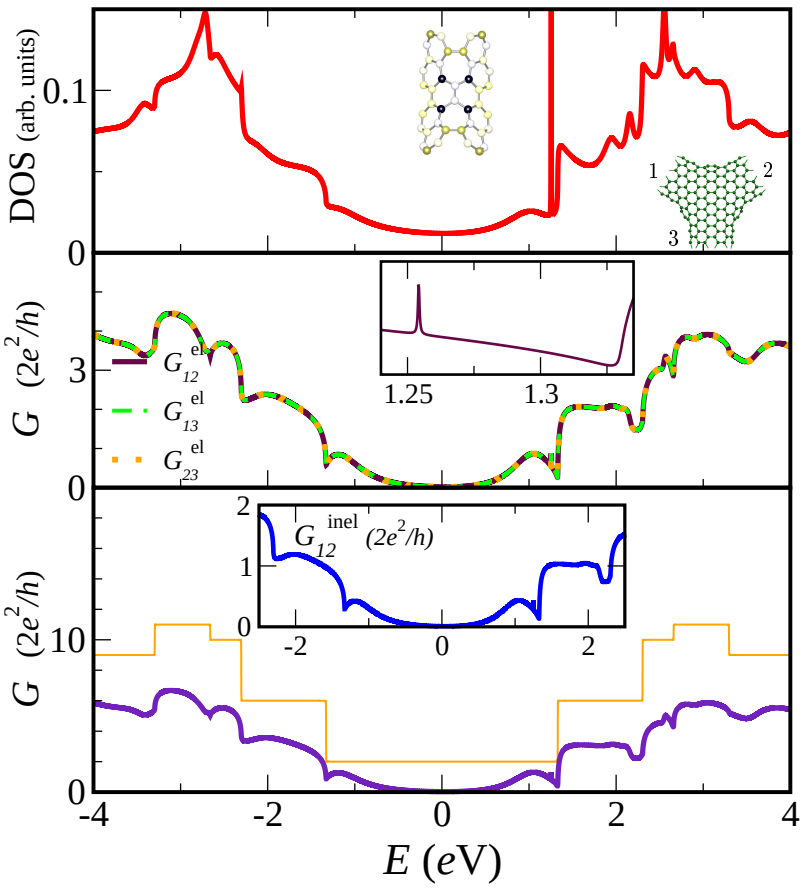

Figure 4.3: DOS (projected on the junction) and conductance of the Y-junction shown in Fig. 4.1.a as a function of the incident electron energy. The inset in the upper panel shows the defect region pointed by the arrow in Fig. 4.1.a with the atomic distribution of the LDOS at a localized state, whose conductance can be seen in the inset of the middle panel. The LDOS takes values from zero (white) to a its maximum value in dark-blue. The evolution of the atomic distribution of the LDOS at the junction have been followed up in an energy window around the Fermi level (see http://www-mcg.uni-r.de/downloads/CNTJunction/). In the inset of the middle panel we see a blow-up of $G_{12}^{\rm el}$ near the Fermi energy where resonant states are observed. The units of the conductance is the conductance quantum $2e^2/h$. In the lower panel the total conductance $G_{12}^{\rm tot}$ for the upper arms of the junction when making a voltage probe out of the third lead is presented (dark line) together with the conductance of the perfect infinite CNT of chirality matching that of the source-drain tubes, in this case the $(6,6)$ CNT (light line). In the inset here we plot the inelastic contribution to the conductance through the upper arms.

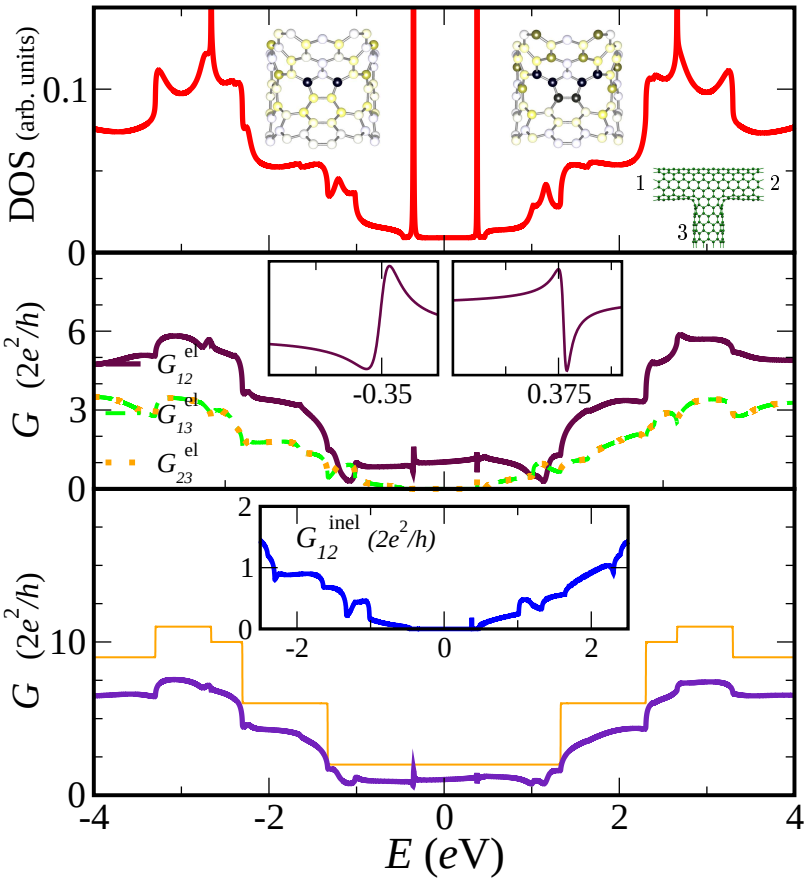

Figure 4.4: The same properties as in Fig. 4.3 are plotted here for the T-junction of Fig. 4.1.b. In the insets the asymmetric line shapes corresponding to a Fano resonance are clearly observed.

the behavior of the local density of states (LDOS) at the resonant energies. The presence of both extended states and localized defective states in the junction creates the conditions for the Fano resonance to be observed [155].

The resonance-like structure in the transmission exhibits indeed asymmetric line shapes resembling those of Fano resonances. These line shapes result from the interaction of a discrete state with a continuum of metallic states. The degree of asymmetry of these curves is determined by the so-called Fano parameter, which changes here its sign. Therefore at the resonances we have that $\mathcal{T} \propto (q+E)^2 \,/\, (1+E^2)$ where $q = \mathrm{Re}\,\mathcal{G}^0/\mathrm{Im}\,\mathcal{G}^0$ is the Fano parameter and $\mathcal{G}^0$ is the undressed Green function for the continuum. Due to the analyticity properties of the Green functions (causality), the real and imaginary

parts of $\mathcal{G}^0$ are related by a Kramers-Kronig (Hilbert) transformation:

$$\mathrm{Re}\ \mathcal{G}^0(E) = \frac{1}{\pi} P \int_{-\infty}^{+\infty} \frac{\mathrm{Im}\ \mathcal{G}^0(E')}{E' - E}\, \mathrm{d}E', \tag{4.8}$$

where P means principal value. From these equations, we see that for an asymmetric DOS with most of its weight situated at frequencies below the energy E_{Fano} in a small window around this energy, it is likely to obtain $q > 0$, whereas for asymmetric DOS with more weight at $E > E_{\mathsf{Fano}}$, q is likely negative. The shape of the DOS of the continuum of states of this metallic junction decreases rapidly before the left peak, and increases just after the one to the right. This accounts for the different signs of q as observed in the plot. Though the states around E_{Fano} are the most significant for determining the sign of q, it is necessary to take into account the whole range of energy of the band.

These characteristics are then observed in the I-V curves (Fig. 4.7.b), though its effect is not that of a switch-off of the current, as the transmission background of the continuum is too strong. Nevertheless differences in the current amplitude up to 30% are observed.

The second Y-junction, shown in Fig. 4.1.c, is made up with the same combination of leads as the previous T-junction, but forcing now the armchair tubes to bend, forming a Y-shape. In this case, we have a very different rearrangement of the defects. Four of the heptagons are situated on the upper saddle while the other two are shared by the obtuse angles. The junction is indeed metallic, as shown in Fig. 4.5, but as in the previous case quickly assumes the electronic character of the corresponding arms. Above the Fermi energy, the necessary conditions for a Fano resonance appear again. The sharp peak of a localized state is seen in the DOS and its corresponding Fano resonance in the conductance. Its behavior all in all resembles that of the junction in Fig. 4.1.b but anyhow presents remarkable differences, as a greater asymmetry, which are exclusively due to the junction shape and the situation of the defects.

The I-V characteristics of this junction shown in Fig. 4.7.c present an interesting profile, as the big change in current makes it interesting for its use as a circuit component.

The last of the presented junctions shown in Fig. 4.1.d is again a T-shaped one but built up of one metallic and two semiconducting tubes. Like in the other T junction the defects are octagons and pentagons, distributed symmetrically in both bending regions. The transport properties of this junction, given in Fig. 4.6, are dominated by the semiconducting behavior of

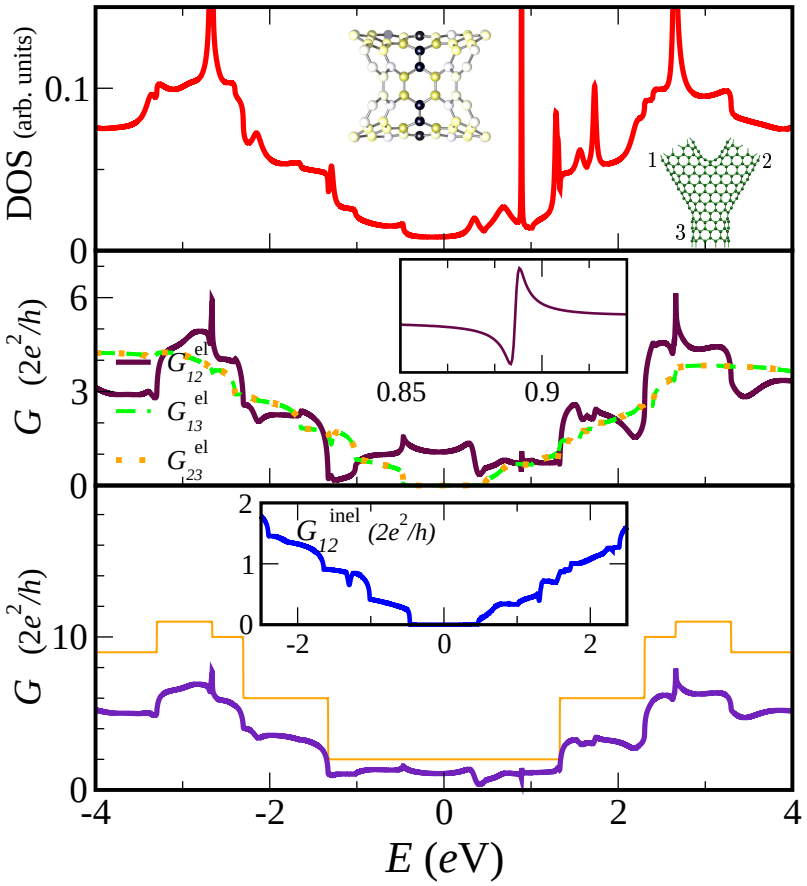

Figure 4.5: The same properties as in Fig. 4.3 are plotted here for the Y-junction of Fig. 4.1.c.

the upper branches, whose gap is reflected in the conductance of this junction. A non-equilibrium study of its properties would be necessary to fully explore its possible applications in electronics.

The influence of the gate voltage on the current is shown in Fig. 4.7. Here the current flowing between the upper branches is calculated under a small bias voltage of the order of a few tens of meV, while we smoothly change a gate voltage which shifts the levels of the orbitals at the third arm of the junction. We should stress at this point that the bias voltages used in this calculation allows us to remain within the linear response regime. As can be seen the current suffers a great modulation in some of the junctions, increasing its amplitude in up to 75%.

Despite the fact that our model is adequate for getting linear response, we

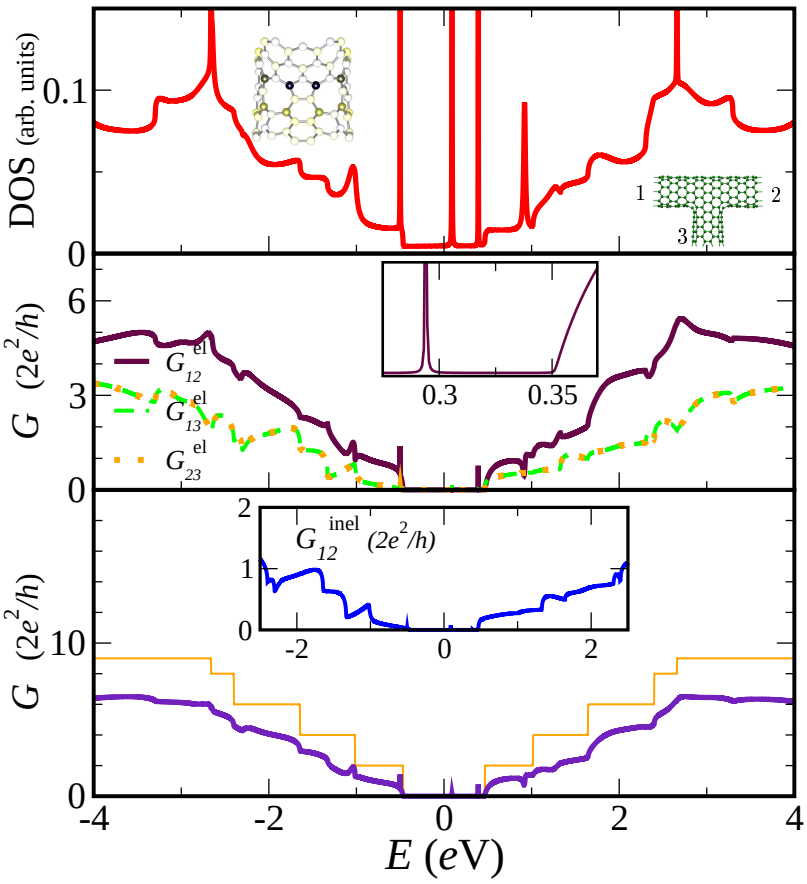

Figure 4.6: The same properties as in Fig. 4.3 are plotted here for the T-junction of Fig. 4.1.d.

apply it to a nonlinear situation for sheer comparison of our results to previous calculations [151]. We calculate the I-V characteristics of these junctions considering different possible experimental setups. In Fig. 4.8 we report the current through the third lead in two different situations: first the upper branches are grounded and the third lead is biased with a voltage V_{bias}. That is,

$$\mu_1 = \mu_2 = 0;\ \mu_3 = V_{\text{bias}}. \tag{4.9}$$

Under these conditions a certain degree of rectification power is present in the setup, but the rectification is not an inherent property of the junctions. This can be seen in a second case where the third lead is grounded while a bias is applied between the first and second lead, *i.e.* when plotting the current versus the bias voltage for the setup

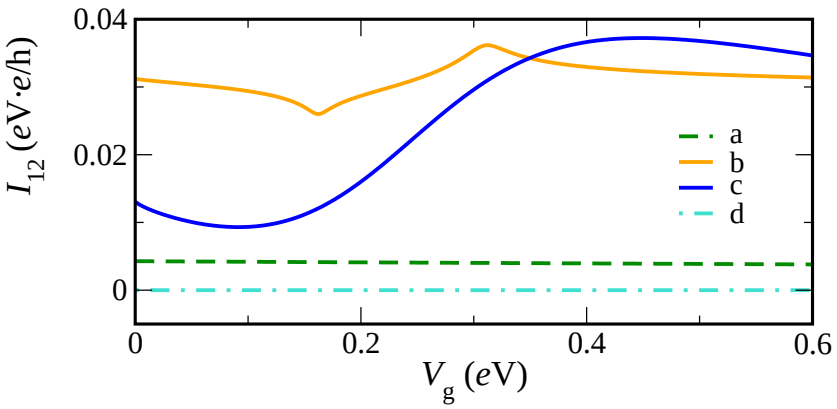

Figure 4.7: Current vs. gate voltage using one arm of the three-terminal junctions as gate electrode (L_3). The switch-on of the gate shows to be of interest for possible future applications of these junctions, and especially of the second of the Y-shaped ones. The labels a, b, c, d correspond to the notation given in Fig. 4.1 for the four junctions considered.

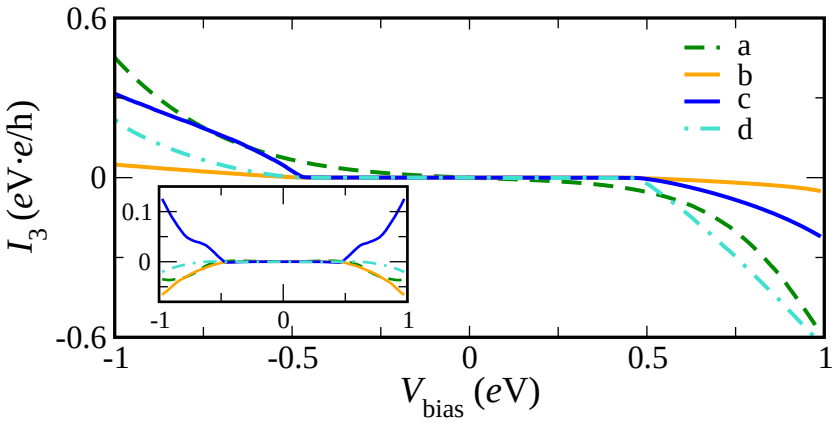

Figure 4.8: Current I_3 vs. bias voltage for the four junctions of Fig. 4.1. I_3 is the total current through lead L_3, that is $I_3 = I_{31} + I_{32}$. The current is calculated for the experimental setup described in Eq. (4.9) as well as for a different situation given by Eq. (4.10) and plotted in the inset. As in the previous figure the labels a, b, c, d correspond to the notation given in Fig. (4.1) for the four junctions we consider.

$$\mu_1 = -\mu_2 = -V_{\text{bias}}/2;\ \mu_3 = 0, \tag{4.10}$$

as shown in the inset of the same figure. The degree of asymmetry in view at the I-V curves when using the first of the experimental setups disappears for the second setup. In this case the current curves are symmetrical with respect to the bias voltage, both for I_3, plotted in the inset, as for the current

flow through the upper arms.

4.4 Discussion

By making use of the Landauer formalism and equilibrium Green functions techniques, we have studied the transport properties of different carbon nanotube junctions, at an atomistic description level, and paid especial attention to bound states. Our analysis of the conductance behavior of several three terminal carbon nanotube junctions allows us to identify common patterns and draw general conclusions. This can be done by sorting out different factors in the qualitative features of the conductance, namely (i) the role of structural defects in the molecular network, (ii) the resulting geometrical symmetry properties, and (iii) the electronic nature of the contacted leads (whether metallic or semiconducting tubes). By opening the energy of the electron incoming in the injecting lead one encounters typical resonant behaviors of the LDOS (see http://www-mcg.uni-r.de/downloads/CNTJunction/). For such energies most spectral power is associated to the defective atoms at the saddle regions. The presence of background states, mostly contributed by the attached leads, creates the conditions for an interference between localized and extended states, with the appearance of the so-called Fano resonance. Indeed resonant defective states in the DOS are paired by the typical Fano line shape of the form

$$\mathcal{T} \propto \frac{(q+E)^2}{1+E^2}. \tag{4.11}$$

This feature could be eventually detectable in experiments, as differences in current amplitude up to 75% are observed when using one arm of the three-terminal as a gate electrode. We have thus shown how through the localized states, we can control the current flow through the upper branches which is driven by a bias voltage applied across the first two terminals.

4.5 AC-response of a carbon nanotube Y-junction

The influence of an ac-field on carbon nanotube junctions could provide a useful way of tailoring the transport at the nanometer scale. Indeed, quantum systems exposed to strong time-dependent external fields show a variety of novel phenomena, which are otherwise not accesible within ordinary stationary quantum mechanics. Hence, the study of the effect of an external field in the charge transport through these systems described in the previous sections seems to promise interesting results which may show new control mechanisms of conductance.

The problem to deal with is described now by a time-dependent periodic Hamiltonian. One way of tackling such a problem is to apply the Floquet formalism which respects the time periodicity of the Hamiltonians at all levels.

Thanks to Floquet theorem our system is mapped into an equivalent one described by a time-independent Hamiltonian. This fact will allow us to apply Green function techniques to deal with the transport calculations, as already done to analyze time-independent transport problems. This method is explained in App. C and applied to a model system of a sandwiched molecular chain, so to illustrate more properly the implications of this technique.

The system under study swill be considered at the atomic level and will be described within a homogeneous tight-binding model in the limit of linear radiative response, zero temperature and low bias voltage. The radiation on the system is treated classically.

4.5.1 CNT Junction

The carbon nanotube junction is studied within a π-orbital tight-binding approach, which describes well the properties of these tubes as done before in this thesis work. The conduction properties are calculated using a one-electron model of the electron transfer (a scattering theory approach to the problem) in the absence of disorder, dissipation or any other environmental perturbation. For the leads we consider for the moment the wide-band limit. The IC approximation (see App. C) is not made here.

Current is induced by the application of dc voltages across the two electrodes through which the current flows, raising the Fermi level of one reservoir

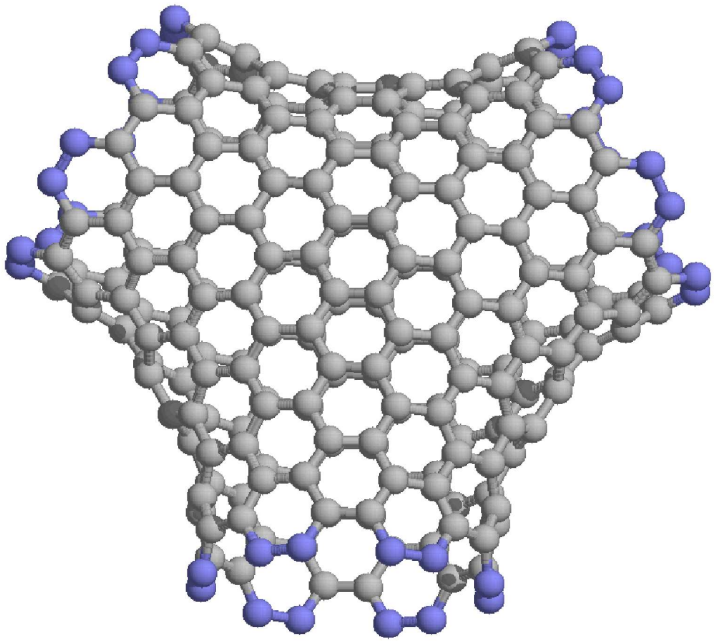

Figure 4.9: Symmetric carbon nanotube Y-junction as considered in this study. The central part shown here consists of 258 atoms. The branches of this junction are metallic (6,6) CNTs, joined together in this three-fold symmetric junction.

relative to the other. The third lead can be used as a gate electrode, as shown in Sec. 4.3.

The carbon junction Y-junction that we will study is a metallic junction composed of three merged armchair CNTs as described in Fig. 4.9. We will assume the metallicity of leads attached to each end of the junction.

In the absence of an external AC-field, the system is described by the following tight-binding Hamiltonian for the scatterer (S), leads (L_1, L_2, L_3) and the coupling between the scatterer and the leads:

$$\mathcal{H}^0 = \sum_{\alpha} \sum_{i_\alpha} \varepsilon_{i_\alpha} |i_\alpha\rangle \langle i_\alpha| + \sum_{\alpha,\beta} \sum_{i_\alpha, i'_\beta, i_\alpha \neq i'_\beta} V_{i_\alpha, i'_\beta} |i_\alpha\rangle \langle i'_\beta| \tag{4.12}$$

where the index α now runs over the different parts of the system S, L_1, L_2, and L_3, ε_{i_α} is the on-site energy of the state i of α and V_{i_α, i'_β} the hopping integral which is non zero up to nearest neighbor interactions. For simplicity

we will merge the index α into i:

$$\mathcal{H}^0 = \sum_{i,j} \left(\varepsilon_i \, \delta_{i,j} + V_{ij}\right) |i\rangle \, \langle j| \ , \tag{4.13}$$

so the indices i and j run over all the states of system: those of the scatterer and those of the leads. When taking the leads as semi-infinite tubes, all the hopping terms V_{ij} will be approximately the same as they couple equivalent orbitals. We will thus have $V_{ij} = -\gamma$ if i, j are nearest neighbors ($\langle i, j\rangle$), or $V_{ij} = 0$ otherwise.

We now switch on a monochromatic electric field $E(t) = \mathrm{E}_0 \cos(\Omega t)\, \hat{\mathcal{E}}$ of period $T = 2\pi/\Omega$. Again, the spatial dependence can be discarded as we are assuming that the wavelength of the laser is much longer than the dimensions of the junction. The total Hamiltonian will then include the effect of the field

$$\mathcal{H} = \mathcal{H}^0 + \mathcal{H}^1 \tag{4.14}$$

with

$$\mathcal{H}^1 \ = \ \sum_i e\mathrm{E}_0 \cos(\Omega t)\, \hat{\mathcal{E}} \cdot \mathbf{r}_i \, |i\rangle \, \langle i| \, . \tag{4.15}$$

$-e\mathbf{r}$ can be considered as the electric dipole operator in the molecule, assumed diagonal in the basis of atomic orbitals, as the spatial overlap between different orbitals is negligible, and to a good approximation is then given by taking $\mathbf{r}$ as the center of the orbital. We will once more assume that the leads are perfect conductors, so that the electric scalar potential is constant inside the reservoirs. For each lead we then assume $\mathbf{r}$ to take the same value for all its states, namely that of the position of the contact to the central region. It is important to notice that from now on we will need to consider the exact 3-dimensional structure, as we will make use of the position vectors of the orbitals and not just of their topological connections.

Before proceeding further, we move from the Schrödinger representation into an intermediate representation, as described in App. C.5. In this new frame the contribution of the laser field is removed from the diagonal terms of the Hamiltonian. We thus end with a Hamiltonian which has time-dependent driving terms just in the off-diagonal elements.

The Hamiltonian $\tilde{\mathcal{H}}$ in this representation is given by

$$\tilde{\mathcal{H}} = U\mathcal{H}^0 U^{-1}. \tag{4.16}$$

Specifically, the (ij)th element of the matrix form of the Hamiltonian can be written as

$$\tilde{\mathcal{H}}_{i,j}(t) = \mathcal{H}_{i,j}\exp\left(\frac{\mathrm{i}}{\hbar}e\mathrm{E}_0\frac{\sin(\Omega t)}{\Omega}\,\hat{\mathcal{E}}\cdot(\mathbf{r}_i-\mathbf{r}_j)\right)+eE_0\cos(\Omega t)\,\hat{\mathcal{E}}\cdot\mathbf{r}_i\,\delta_{i,j} \quad (4.17)$$

The wavefunction can be expanded as in Eq. (C.22) and Eq. (C.23)

$$\begin{aligned}\left|\Psi^{Int}(\mathbf{r},t)\right\rangle &= \exp\left(-\frac{\mathrm{i}}{\hbar}\epsilon t\right)\sum_{n=-\infty}^{+\infty}\exp\left(-\mathrm{i}n\Omega t\right)|\phi_{\epsilon,n}(\mathbf{r})\rangle = \\ &= \sum_{i\,n}\exp\left(-\frac{\mathrm{i}}{\hbar}\epsilon t-\mathrm{i}n\Omega t\right)b_{i,n}(\mathbf{r})\,|i\rangle\,.\end{aligned} \quad (4.18)$$

Substituting this equation into the Schrödinger equation, Eq. (C.17), simultaneously with the following Fourier expansion for the driving terms:

$$\exp\left(\mathrm{i}a\sin(\Omega t)\right) = \sum_{n=-\infty}^{+\infty}J_n(a)\exp\left(-\mathrm{i}n\Omega t\right). \quad (4.19)$$

after defining

$$a_{i\,j} \equiv \frac{e\mathrm{E}_0}{\hbar\Omega}\,\hat{\mathcal{E}}\cdot\left(\mathbf{r}_i-\mathbf{r}_j\right), \quad (4.20)$$

we can write the eigenvalue equation for the quasienergy as

$$\epsilon\phi_{\epsilon,n}(\mathbf{r}) = \sum_{i,j}\mathcal{H}^0_{i,j}\sum_{n'=-\infty}^{+\infty}J_{n-n'}\left(a_{ij}\right)|i\rangle\langle j|\,\phi_{\epsilon,n'}(\mathbf{r}) - n\hbar\Omega\phi_{\epsilon,n}(\mathbf{r}) \quad (4.21)$$

or for the coefficients

$$\epsilon b_{i,n}(\mathbf{r}) = \sum_{i,j}\mathcal{H}^0_{i,j}\sum_{n'=-\infty}^{+\infty}J_{n-n'}\left(a_{ij}\right)b_{j,n'}(\mathbf{r}) - n\hbar\Omega b_{i,n}(\mathbf{r}). \quad (4.22)$$

So we arrive at the following expression for the Floquet Hamiltonian:

$$\mathcal{H}^{Fl}_{in,jn'} = \mathcal{H}_{ij}J_{n-n'}\left(a_{ij}\right) - n\hbar\Omega\,\delta_{i,j}\,\delta_{n,n'}. \quad (4.23)$$

The Floquet states are naturally labeled by two indices i and n, where i runs over the different physical states and n over the number of Floquet replicas.

Green function techniques can be then applied to calculate transport properties of the system as explained in App. C, like the transmission probability given by

$$\mathcal{T} = Tr\left\{G^{Fl}\Delta^{Fl}_{L_i}G^{Fl^\dagger}\Delta^{Fl}_{L_f}\right\}. \tag{4.24}$$

Some results of the calculations of density of states can be seen in Fig. 4.11 and Fig. 4.12, for two different laser frequencies. The transmission in these cases is shown in Fig. 4.13 and Fig. 4.14. As a comparison the results for the nondriven case are given in Fig. 4.10.

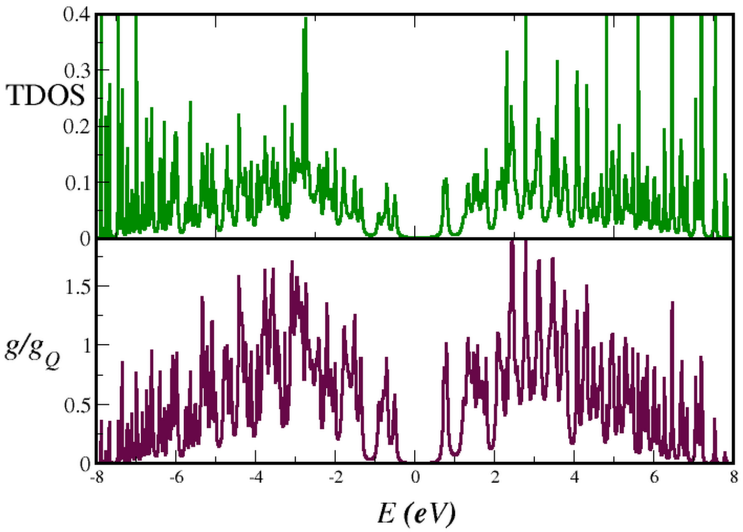

Figure 4.10: Density of states and transmission through two arms of the symmetric junction shown in Fig. 4.9.

We can observed the big influence the laser field can have on the transport through the system, being thus definitely an important additional control mechanism of current. The frequency of the field should be tuned according to the expected results, for which a much complete study should be made.

Nevertheless, by generalizing to 3D structures the work of Ref.[165], a general framework for AC transport at the molecular scale have been developed which

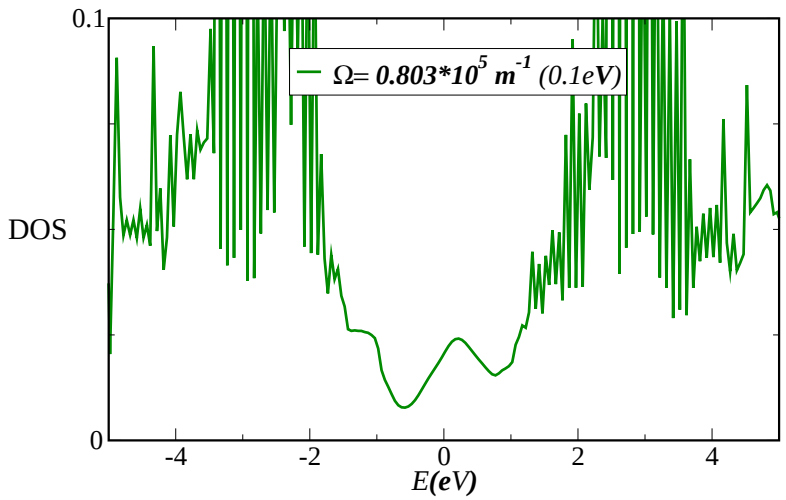

Figure 4.11: Density of states of the Y-junction studied under the influence of an AC-field of frequency Ω.

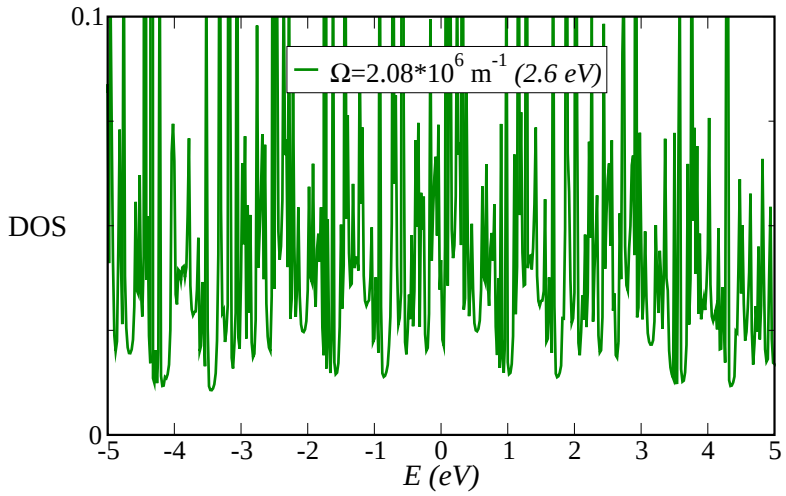

Figure 4.12: Density of states of the Y-junction studied under the influence of an AC-field of frequency Ω.

is easily extendable to other geometries or materials. AC transport in realistic molecular structures and tuning the field frequency will allow for different transport behaviors. Still much work remains to be done, including a detailed study of the orientational dependence of the junction relative to the laser field polarization and an atomic-level description of CNT leads.

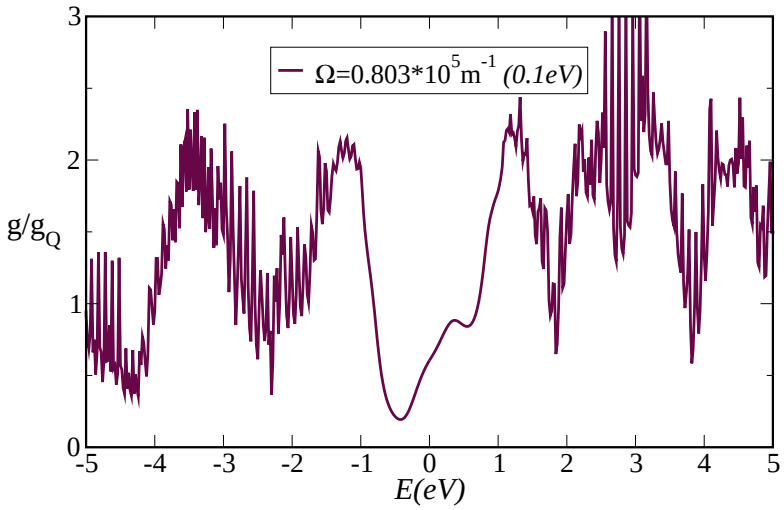

Figure 4.13: Transmission of the Y-junction studied under the influence of an AC-field of frequency Ω.

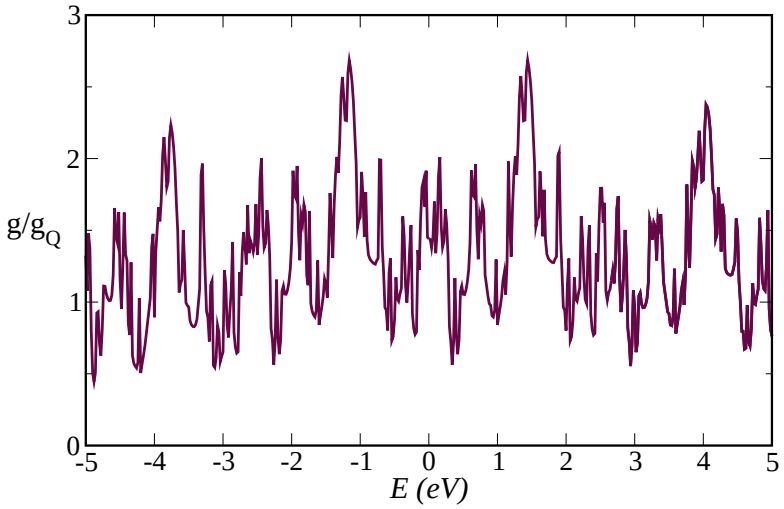

Figure 4.14: Transmission of the Y-junction studied under the influence of an AC-field of frequency Ω.

Chapter 5

Ab-initio study of the vibrational properties of fullerenes on a surface

5.1 Vibrational properties of C_{60} on graphene

After checking some of the properties of this molecule with ab-initio calculations, we place it onto graphene, in order to observe the effect of a substrate on its vibrational properties.

5.1.1 Method

We study the fullerene on a graphene substrate, using accurate *ab-initio* calculations [166] within the local density approximation to density functional theory, and replacing the core electrons by nonlocal pseudopotentials. We use a minimal basis set of 4 sp orbitals per carbon atom. Although this basis is not complete, it provides a sufficiently accurate description of the systems and effects that we intend to study.

5.1.2 Structure: the free molecule

As already mentioned C_{60} molecule has the soccer ball structure of a truncated icosahedron, which places each atom in an identical molecular environment. Pentagons and hexagons build this hollow sphere of carbon, being the C_{60} the smallest fullerene having all twelve pentagons separated. These

twelve pentagons are necessary for the closure of a surface with an arbitrary number of hexagons into a spheroid, as follows from Euler's theorem [145]. The fact that in C_{60} all pentagons are isolated contributes to its stability, as adjacent pentagons increase the strain energy. The response to the non-planarity achieved by the introduction of pentagons is a rehybridization from $sp^2 - \sigma$ and $p - \pi$ orbitals. Even though, the fullerene still maintains a high degree of π orbital alignment.

In the relaxed structure we observed that this molecule, with a calculated diameter of 7.07 Å, has two inequivalent bonds. And indeed we have found that the pentagonal edge ones with $d_{[5,6]} = 1.488$ Å are longer than the bonds shared with hexagonal rings with $d_{[6,6]} = 1.431$ Å as seen in Figure 5.1 (compare with *i.e.* [167]). This bond length alternation shows that in the lowest Kekulé structure, the double bonds are located at the junctions of hexagons ([6,6] bonds) and that there are no double bonds in pentagonal rings.

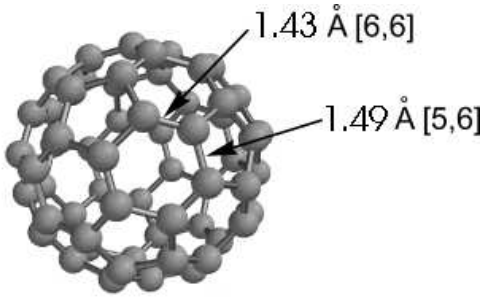

Figure 5.1: The icosahedral buckyball.

In order to check our method and its accuracy we have calculated further properties of this fullerene, verifying that it is indeed a very stable and strong molecule. By applying a finite-difference approach, described in Sec. 5.1.4, to simulate a hydrostatic pressure on the molecule, we calculate the bulk modulus for the C_{60} . The value obtained is $B_0 = 816\,GPa$, approaching that reported by other authors [168].

To understand the electronic structure of C_{60}, it is important to have a look at the molecular orbitals (MOs). The MO diagram (Fig. 5.2) shows low lying triply degenerated LUMOs (Lowest Unoccupied MOs) and a five-fold degenerated HOMO (Highest Occupied MO).

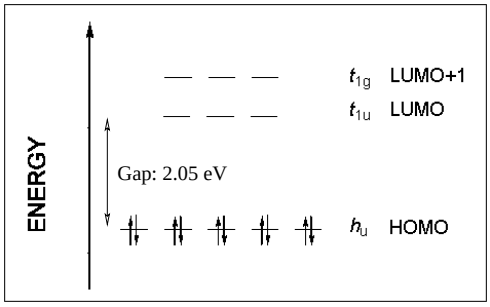

Figure 5.2: MO diagram.

5.1.3 Structure: C_{60} on graphene

Environment plays an important role in the transport properties of a molecule. In order to study the effect of a substrate we place the fullerene onto a graphene-like plane molecule with 24 carbon atoms and let the structure relax. *Two* minima were found for structures with distances to the substrate of 3.1 Å and 3.3 Å, the former being the one with lower energy.

5.1.4 Vibrational modes

The free C_{60} has 174 vibrational modes $(3N-6)$, which are also the dominant ones in solid C_{60}. Due to the high symmetry of C_{60}, from its 174 vibrational normal modes, only four are IR active (T_{1u}) and ten are Raman active (A_g, H_g). The normal modes T_{1u}'s are 3-fold degenerate and of odd-parity. A_g and H_g modes are 1-fold and 5-fold degenerate respectively. The A_g modes are the only two degrees of freedom, which conserve the I_h symmetry. The A_g mode with lowest frequency corresponds to a sphere breathing, a symmetric bond stretching. This mode is known as the Radial Breathing Mode. The highest A_g corresponds to an antisymmetric stretching of [6,6] bonds out of phase with [5,6] bonds. In general we can say for every kind of vibrational modes that the low-frequency modes involve radial motion, whereas the high-frequency modes are primarily tangential.

We calculate the frequencies for the A_g and H_g modes using the *Frozen Phonon Method* [169]. It consists of the computation of the total energy as a function of atomic displacements. A distorted crystal is treated as a crystal in a new structure with a lower symmetry than the undistorted one. The electronic energy of the crystal can be computed as a function of a suitably chosen phonon coordinate and used for dealing with both the undistorted and

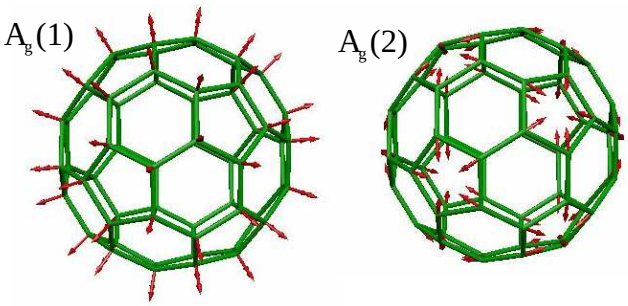

Figure 5.3: The two symmetry-conserving phonon modes.

the perturbed crystal. The interatomic force constants can be obtained by numerical differentiation of the calculated energy. Unfortunately, symmetry reduction due to perturbation increases drastically the computational effort. To retain partial symmetry one could use displacements corresponding to superstructures, which restricts the practical application of the method to phonons with high-symmetry wave vectors.

Therefore the frozen phonon method is a finite-difference approach for which we have used finite-atomic displacements of 0.02 Å, moving the bonds in the two directions of the phonon movement (*e.g.* for the Breathing Mode we both increase and decrease the molecular radius) in order to eliminate anharmonic effects. Then the total energy for each configuration is calculated.

The dimensionless electron-phonon coupling constant used in the theory of superconductivity is given by [170, 112]

$$\lambda = N(\epsilon_F)V \tag{5.1}$$

where N is the density of states at the Fermi level and V measures the electron-phonon scattering. As the value of V is dominated in C_{60} by the on-ball modes A_g and H_g [171], we also calculate its value for these modes for the LUMO orbital.

$$V = \sqrt{\frac{\hbar}{2M_{C_{60}}\omega}}\frac{\partial\epsilon}{\partial u} \tag{5.2}$$

where $M_{C_{60}}$ is the mass of C_{60} and $\frac{\partial\epsilon}{\partial u}$ represents the change of the energy levels with the displacements of the atoms.

From the values obtained for V for the diverse vibrational modes of wave number k, summarized in Table 5.1 and Table 5.2, we can conclude that the graphene plane is not affecting the electron-phonon coupling, and not

	Free C_{60}	Free C_{60}	On Graphene	On Graphene
	$k/2\pi(\mathrm{cm}^{-1})$	$V(\mathrm{eV})$	$k/2\pi(\mathrm{cm}^{-1})$	$V(\mathrm{eV})$
$A_g(1)$	507.6	0.002	497.2	0.006
$A_g(2)$	1533.7	0.051	1531.4	0.050
$H_g(1)$	285.25	0.006	282.3	0.007
$H_g(2)$	500.3	0.017	503.3	0.017
$H_g(3)$	819.6	0.011	821.4	0.011
$H_g(4)$	862.3	0.016	865.8	0.017
$H_g(5)$	1184.4	0.017	1185.78	0.017
$H_g(6)$	1373.23	0.020	1376.4	0.021
$H_g(7)$	1653.6	0.042	1650.8	0.017
$H_g(8)$	1793.3	0.041	1783.2	0.040

Table 5.1: k and V for the LUMO

	Free C_{60}	Free C_{60}	On Graphene	On Graphene
	$k/2\pi(\mathrm{cm}^{-1})$	$V(\mathrm{eV})$	$k/2\pi(\mathrm{cm}^{-1})$	$V(\mathrm{eV})$
$A_g(1)$	507.6	0.0073	497.2	0.0035
$A_g(2)$	1533.7	0.0216	1531.4	0.0240
$H_g(1)$	285.2	0.0216	282.3	-
$H_g(2)$	500.3	0.0131	503.3	-
$H_g(3)$	819.6	0.0174	821.4	-
$H_g(4)$	862.3	0.0154	865.8	-
$H_g(5)$	1184.4	0.0068	1185.8	-
$H_g(6)$	1373.2	0.0199	1376.4	0.0189
$H_g(7)$	1653.6	0.0413	1650.8	0.0385
$H_g(8) - nm172$	1793.3	0.0467	1810.2	0.0446

Table 5.2: k and V for the HOMO

changing much the phonon modes, when the LUMO is the driving orbital in the conduction. These results are nevertheless different for the HOMO, where a rehybridization occurs for some modes, when C_{60} is placed upon graphene.

5.2 Electromodulation of charge transfer and of the breathing-mode of C_{60} on surfaces

A study based on *ab-initio* density-functional calculations is presented on the modulation of charge transfer to a C_{60} molecule, placed onto a graphene substrate, due to an external applied electric field. Charge transfer results to be asymmetrical with respect to the field direction. The charged molecule adopts a slightly different structure, deviating from the perfect icosahedron of free buckyballs. These structural changes lead to modifications of the phonon properties. We focus our attention on the radial breathing mode and study the effect of the vibration on the electronic levels.

5.2.1 Introduction

C_{60} has been found to possess a great ability to adapt itself to different environments, as seen in many experiments. By an applied gate voltage in a field-effect transistor geometry (FET-device) a precise control of the charge per molecule is achieved, without changing the molecular arrangement through dopants. C_{60} can either act as an electron donor or as an electron acceptor, where a clear asymmetry between the properties of the hole-doped and the electron-doped fullerenes has been seen. There is a continuing effort to utilize transverse static electric fields in such devices to modulate properties of known superconductors.

By applying an electric field we compute the asymmetric transfer of charge to the fullerene. In these conditions we allow the geometry to relax, where the residual forces were kept smaller than $0.09\,e\mathrm{V}/\mathrm{\AA}$. The transferred charge induces a change in the ionic structure, which is going to alter its vibrational characteristics.

5.2.2 Results: charge transfer

By applying an electric field perpendicular to the graphene plane, we compute the transfer of charge to the molecule and the change in the ionic structure induced by the electric field.

In Figure 5.4 we can see an example of how the electronic properties are changed because of this charge transfer. The electronic energy levels of an electron-doped fullerene on a graphene plane can be seen in Fig. 5.4(a). By projecting these molecular orbitals onto the original atomic orbitals, we can

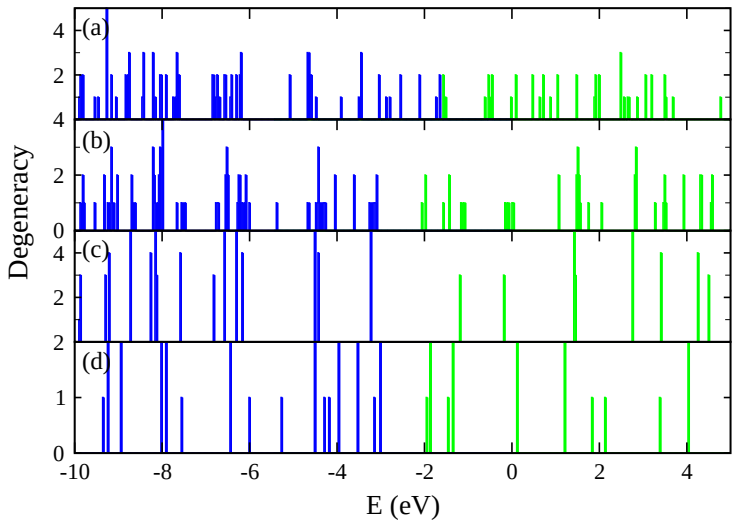

Figure 5.4: Electronic energy levels around the gap of the C_{60} for (a) a deformed C_{60} on a graphene plane in the presence of an applied field of 0.014 a.u. (1a.u.=51.4 eV/Å), which leaves the *buckyball* negatively charged; (b) a perfectly-shaped C_{60} on a graphene plane, (c) a free C_{60} , and (d) a graphene plane characterized at the atomic level with 24 carbon atoms. The darker color in the figure indicates occupied levels.

follow the evolution of the original HOMO and LUMO of the free C_{60} (see Fig. 5.4(c)). The degeneracy of these levels is broken as the structure loses its icosahedral symmetry.

On the graphene substrate the fullerene becomes negatively charged. Applying then an external electric field, we observe the charge transfer, which is highly asymmetric with respect to the direction of the field as seen in Fig. 5.5.

The distribution of the transferred charge within the molecule shows also a difference between electron-doped and hole-doped fullerenes in the presence of the applied field (see Figure 5.6).

5.2.3 Results: vibrational properties

Phonons and electron-phonon interactions are essential in the transport properties of C_{60}. Our interest is therefore in the effect of the applied electric field and of the substrate on the vibrational modes of the fullerene. We concentrate on the low frequency radial A_g mode or *"breathing mode"*, which is one of the two non-degenerate modes of the molecule. This mode is Raman active (with a Raman-scattering activity of 112.96 Å^4 amu^{-1}) and is totally

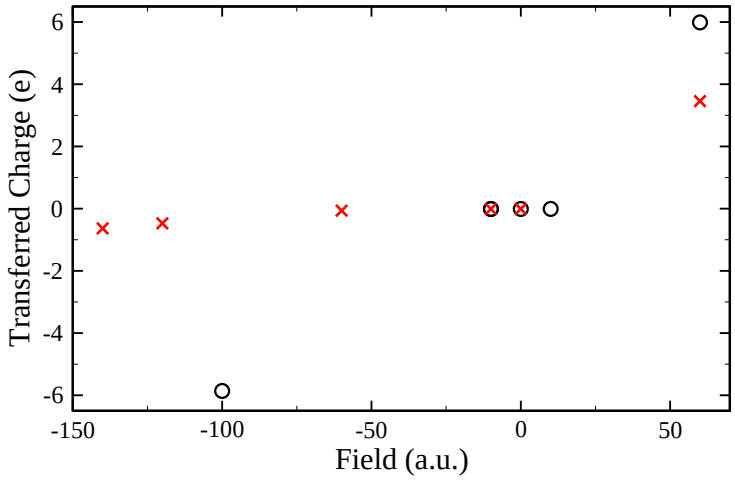

Figure 5.5: Charge transfer vs. applied field, both for a fixed geometry (open circles) and letting the structure relax with the different applied electric fields (X).

symmetric.

We first performed a test calculation, computing the frequencies of this mode for the free C_{60}, both by diagonalizing the Hessian (see *e.g.* Ref. [172]) and by applying the *Frozen Phonon Approximation* [169]. The results for these two approaches are as follows:

Ab-initio Dynamical Matrix Calculation: 550 cm^{-1}

Ab-initio Frozen Phonon Mode: 508 cm^{-1}
The deviation from the experiment [173, 174] is around 6%.

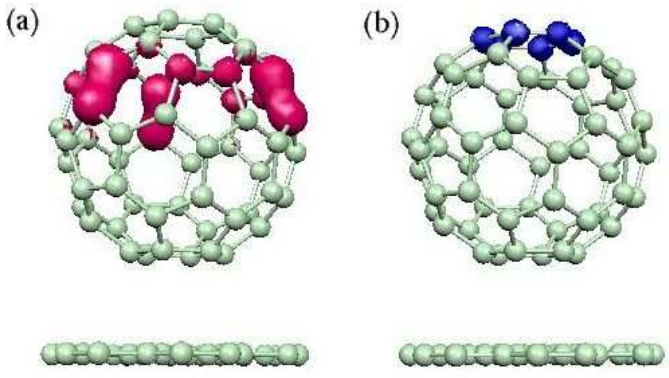

Figure 5.6: Distribution of the excess charge, for a hole-doped (a) and an electron-doped (b) fullerene.

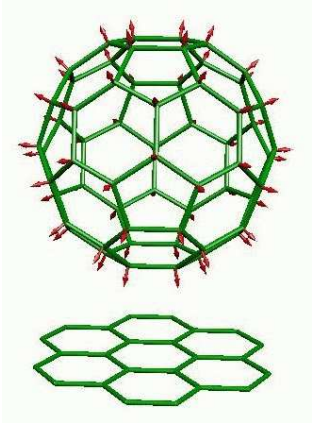

Figure 5.7: View of the computed displacement pattern (arrows) for the A_g mode with the lower frequency.

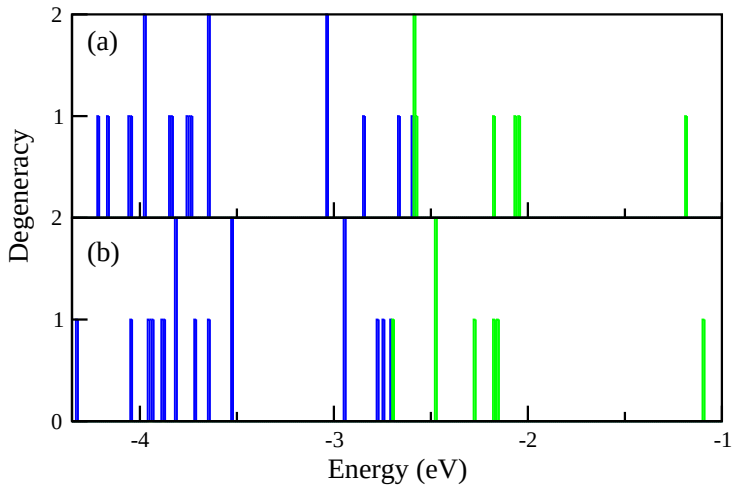

Figure 5.8: Change of HOMO and LUMO levels due to the breathing phonon mode. (Field: 60 a.u.) (a) Relaxed structure (b) Expanded fullerene through the phonon mode.

The influence of this radial phonon mode on the C_{60} on graphene in the presence of an electric field can be seen in the evolution of the HOMO and LUMO levels in Figure 5.8. The change of the levels is not linear with the displacement, and then can not assumed that the Frozen Phonon Mode is a good approach in this case.

Chapter 6

Conductance scaling in gold nanotubes

A new form of gold nanobridges has been recently observed in ultrahigh-vacuum experiments, where gold atoms rearrange to build helical nanotubes, akin in some respects to carbon nanotubes. The good reproducibility of these wires and their unexpected stability allow for conductance measurements and make them promising candidates for future applications. We present here a study of the transport properties of these nanotubes in order to understand the role of chirality and of the different orbitals in quantum transport observables. The conductance per atomic row shows a light decreasing trend as the diameter grows, which is also shown through an analytical formula based on a one-orbital model.

6.1 Introduction

Gold is known to be a good conductor for ages but its application to the electronics at a nanometer scale requires new approaches and an understanding of its physical properties at these small scales, as they will differ from the bulk properties. A great interest has been raised on the nature of electron transport through quasi one-dimensional channels, such as quantum wires, quantum point contacts and nanotubes. This is just a natural process as the scale of electronic devices continues to shrink.

Gold nanowires have been the focus of intense investigation efforts since decades. Especially gold nanocontacts have been extensively studied. These

contacts were normally obtained by dipping a STM (scanning tunnelling microscope) gold tip into a gold substrate and subsequently slowly withdrawing the tip, obtaining a "nanoneck" which is thinned and elongated until the contact breaks [175, 176, 81, 177]. Mechanically controlled breaking junctions [178, 179], or switching regular [180] are other techniques used for this purpose. Metal nanowires were found to show quantized conductance when the nanowires have diameters of the Fermi wave length's scale. Even at room temperature the conductance displays for these atomic contacts a quantization in units of a conductance quantum $G_0^{\text{tot}} = 2e^2/h$, where e is the electron charge and h is Planck's constant. Findings that triggered new interest on metallic contacts, so that a burst of theoretical and experimental work is under way.

A different approach for obtaining such nanowires has been followed in Japan in the group of Prof. Takayanagi and coworkers [181]. In this case a very thin gold film was bombarded with an electron beam working at high intensities, boring nanoholes in the gold. In this way freestanding nanobridges were formed between neighboring holes which were thinned by further irradiation. For some surface orientations the obtained bridges did no longer show a neck-shape, but a shape of straight and uniform nanowires with regular structures [181]. The formation of these bridges was followed up by using an ultrahigh vacuum transmission electron microscope, in which the electron gun was situated, allowing for an *in situ* device fabrication, eliminating effects of contamination on the structure. The obtained wires were stable under low beam intensities. The model fitting with the structure of these nanowires consists of a prism of a hexagonal close-packed lattice with a core showing a face-centered-cubic (fcc) structure. These wires have diameters greater than 1.5 nm, but continuing with the thinning technique new structures are formed spontaneously with smaller widths and lengths of 3 to 15 nm. Through a prolonged gentle irradiation a stepwise change of the diameter of the nanowires could be observed, being the smallest width reached of nearly 0.57 nm at room temperature [182] and of 0.4 nm at 150 K [183]. These new wires exhibit fascinating ordered structures that resemble those of the by now well-known carbon nanotubes (CNTs) [93]. High resolution microscope images, as seen in Fig. 6.1 indicate that these wires consist of coaxial nanotubes of helical atom rows coiled around the wire axis. These wires present therefore different possible chiralities as carbon nanotubes do, depending on the angle in which the atom rows rotate around the tube axis. Experimental evidence so far seems to support the fact that small chiral angles are preferred by the fabricated nanotubes. The multi-shell nanotubes keep the difference in the number of atom rows between adjacent shells con-

stant, leading to a kind of magic shell-closing number which is always seven. This fact can be understood as a new inner shell arises when the radii differ in approximately $a = 2.88$ Å, the neighboring distance of bulk gold, which implies a perimeter difference ($2\pi a \sim 7a$) corresponding to seven atom rows nearly parallel to each other. So single-walled nanotubes should exist with six or less atom rows, and actually one single-walled tube with five atom rows has been observed [183]. With seven or more atom rows a double-walled tube should be seen, which becomes a triple-walled nanotube when more than fourteen rows are present, and so on. The thinnest nanowire obtained is though a single strand of atoms exhibiting an anomalously large interatomic distance of up to $0.4\ nm$ [175]; similar values were also seen in experiments using other techniques (*i.e.* [179]). Different theoretical proposals have tried to find an explanation to these large spacings [184, 185] but no certainty of the mechanism behind these distances is still at hand.

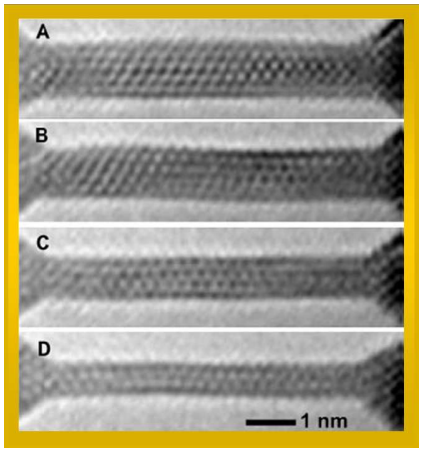

Figure 6.1: Transmission electron microscopy images of stable gold nanowires observed during one thinning process. The diameters of the wires in (A), (B), (C), and (D) are 1.3, 1.1, 0.8, and 0.6 nm, respectively. The dark dots represent positions of atoms projected on the image plane [image taken from Ref. [182]].

The good reproducibility of these wires, and their stability, [186, 187, 188, 189] which is better for those with outer tubes with an odd number of atom rows, makes them promising candidates for future applications. Though gold nanowires become harder to break at lower temperatures, they can be studied at room temperatures, where they can even reach longer dimensions due to diffusion. Generally, cylindrical structures are less stable than an icosahedral structure of metallic clusters would be, but these structures are induced and stabilized by the substrate. In this sense one should think of the observed nanowires as stable tip-suspended wires. The preferred radii

in experiments correspond to more favorable structures for which the wire tension is locally minimized [189]. These minima mean long-lived metastable states. The exchange of atoms between tips and wire plays a crucial role, leading to focus on string tension instead of free energy [189].

In order to observed such structures with other metals, these should have similar atomic mobility to gold, which is related to the ability to reconstruct surfaces. Gold surface reconstruction is related to s-d competition in bulk cohesion [190]; silver does not reconstruct and indeed no evidence of such nanotubes have been seen nor are expected [189].

Nearly parallel to this astonishing discovery of gold nanotubes, which represent a novel organization of matter, ultrathin metal wires (Al & Pb) were predicted to adopt noncrystalline stable atomic structures below a critical radius of the order of a few interatomic spacings of the bulk metal. These regular structures, among which coaxial helical cylindrical shells were found, result from the competition between optimal internal packing and minimal surface energy, displaying a single closed-packed surface with no edges at these small radii. That is, the surface atoms prefer a smooth well-packed low-surface energy structure optimizing the attractive cohesive forces [186]. Another molecular-dynamics simulation revealed a similar tubular multi-walled geometry for gold [187].

In these gold nanotubes conductance quantization has been detected and observed. Ballistic conductance measurements [191] help to confirm the proposed structural model through its derived electronic structure. Astonishingly enough several works hint at the fact that the conductance per atom row might decrease with the number of circumferential atoms and that the number of channels does not coincide with the number of atom rows coiling around these helical structures [192, 193].

6.2 Structural properties

Determining the structure of gold nanotubes is fundamental in order to understand their physical properties, such as conductance quantization. Experimental evidence points out that a structural transition from the thicker, internally crystalline wires into these thinner regular but noncrystalline ones takes place at a critical radius below 2 nm. Lattice spacing has been measured to be almost 2.88 Å, the neighboring distance of gold, for all the wires with diameters between 0.5 and 1.5 nm. We therefore take this distance as the interatomic spacing of the triangular lattice, as we can think of these

cylindrical tubes as rolled-up lattice planes of fcc Au (111), as depicted in Fig. 6.2. Atoms in successive shells appear to strain a bit to maintain commensurability between inner and outer shells. Ab-initio calculations show though that this shear strain should have just a very small effect on the electronic structure [194].

Despite the strong intershell interactions, these structures greatly resemble those of CNTs, where the honeycomb network of carbon atoms is replaced by the triangular lattice of gold atoms. These are actually complementary networks, and the gold nanotube structure can be obtained from the one of CNTs by putting gold atoms at the center of the honeycomb framework.

We use the indices (n, m) to classify the gold nanotubes (AuNTs), where n and m are integers defining the chiral vector, which is wrapped to form the tube. The chiral vector is then $(n\mathbf{a}_1 + m\mathbf{a}_2)$, perpendicular to the tube axis, where the vectors $\mathbf{a}_1$ and $\mathbf{a}_2$ span the 2D unit cell. The number of atom rows coiling around the tube axis is then $n + m$ while the nanotube translational vector reads $\mathbf{T}(n, m) = [(2m + n)/d_R]\,\mathbf{a}_1 - [(2n + m)/d_R]\,\mathbf{a}_2$, being d_R the greatest common divisor of $(2m + n)$ and $(2n + m)$, as $\mathbf{T}$ should

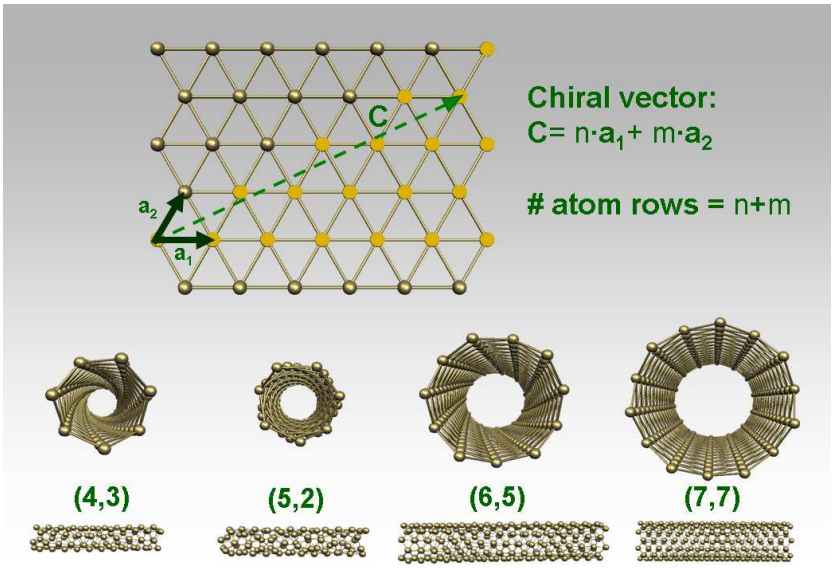

Figure 6.2: Some gold nanotubes are shown as well as the 2D triangular network, from which we can build these models. The coordinate system used is sketched on the lattice, the basis vectors being $\mathbf{a}_1$ and $\mathbf{a}_2$. The chiral vector $\mathbf{C}$ specifies the nanotube and corresponds to its circumference. The highlighted atoms on the lattice are those defining the region of inequivalent chiral vectors, which spans an angle of 30° as can be easily understood analyzing the symmetry of the lattice.

be the smallest lattice vector in its direction. Due to the symmetry of the triangular lattice the chiral vectors of all inequivalent tubes are comprised in a 30° angle, that is, in a one-twelfth irreducible wedge of the Bravais lattice. Consequently, without loosing generality we will restrict to indices with $n > 0$ and $0 < m < n$. Tubes of the form $(n, 0)$ and (n, n) are achiral, presenting thus no handedness. Only wires with an even number of strands may have the structure (n, n). Note that we can decoded our notation (n, m) into the one used in parallel with lattice vector spanning an angle of 120° like $(n + m, n)$, for an equivalent AuNT for transport.

For a fixed n, the radius is minimized for higher values of m (string tension decreases with shrinking radius), so as to fulfill simultaneously the tightest external packing and minimal wire radius [189]. The largest m for an odd number of atom rows is $n - 1$, leading always to a finite chirality and thus a helical structure in these cases. The outer tubes with an even number of atom rows seem to take nonhelical structures with shorter periods. The helicity of the tubes is observed experimentally through a wavy modulation of the STM images [182, 183].

This same structure of the triangular lattice is the one characterizing boron planar clusters and boron nanotubes when rolled up. In contrast to the perfectly round surfaces of CNTs or AuNTs, these tubes exhibit a puckered surface which is shown to be an important stabilizing factor [195] resulting from the nature of the chemical bonds built by this element. These related structures have also been shown to be stable and are predicted to have a metallic behavior [196, 197], as is also easily conjectured for gold nanotubes. The synthesis of such boron nanotubes have been recently achieved [198] though conductance measurements still seem to require a further development of the experimental techniques.

6.3 Method

We study the transport properties of several of these AuNTs using a multiorbital tight-binding Hamiltonian and Green function techniques. In particular, we adopt a Slater-Koster-type [23] tight-binding approach, with the parameters taken from the nonorthogonal parametrization of Papaconstantopoulos [22]. Our approach remains of a microscopic nature since the symmetries of the atomic $s, p,$ and d valence orbitals are taken into account. *Ab initio* studies including shell effects could be needed for greater quantitative accuracy.

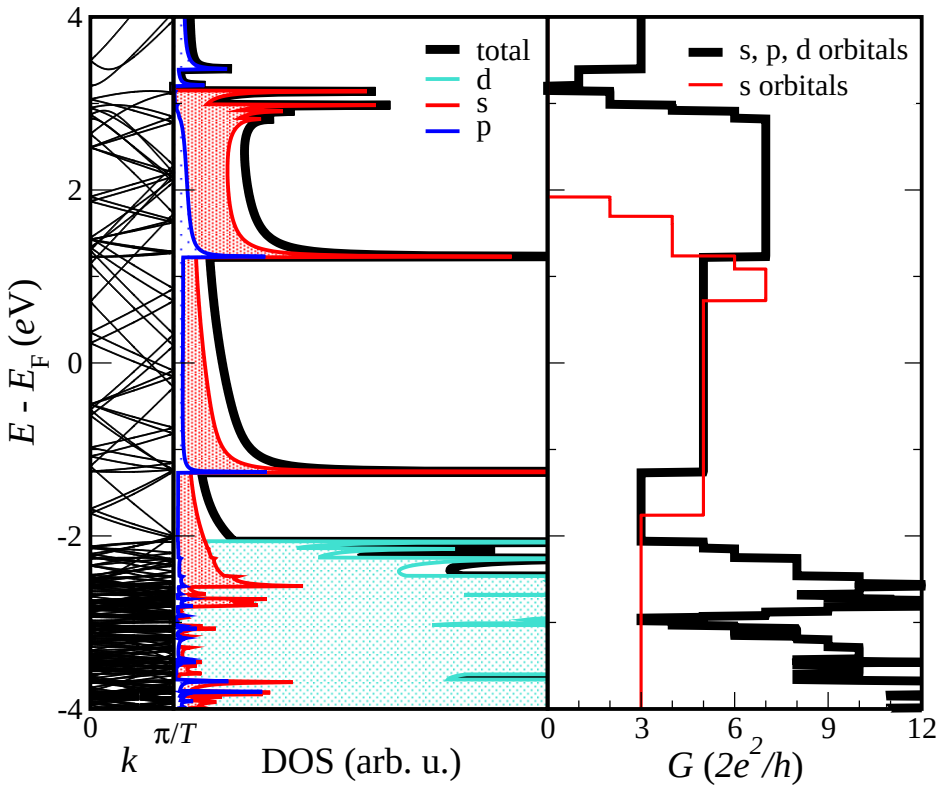

Figure 6.3: One-dimensional band structure, density of states and conductance for the $(4,3)$ gold nanotube. For this tube the translational vector is $T = |\mathbf{T}| = 3.03$ nm. The energies are shifted to set the origin at the Fermi energy, as in the next figures.

As a result, we analyze the differences in the transport calculations that raise from (i) the inclusion of all outer s, p, and d orbitals and from (ii) the simplified model of s orbitals, which is a tempting approximation for these kind of systems. In order to compare results, we will thus use both a one-orbital Hamiltonian describing just the s orbitals, and a nine-orbital Hamiltonian, containing s, p, and d orbitals including all conduction electrons.

The Hamiltonian describing our systems can be written as follows:

$$\mathcal{H} = \sum_{\langle i,j\rangle,\alpha,\beta} H_{i\alpha,j\beta} c^{\dagger}_{i\alpha} c_{j\beta} \tag{6.1}$$

where the indices $\langle i,j\rangle$ indicate nearest neighbor atom sites and the indices α,β mark the different orbitals. The transfer integrals $H_{i\alpha,j\beta}$ are the onsite energies or hopping parameters, dependent on whether i equals j or not.

The conductance is calculated from the transmission values applying the Landauer formula, using Green function techniques [163]. In particular, we derive the elastic linear response conductance via the Fisher-Lee formula for the quantum mechanical transmission [82] : $G = \frac{2e^2}{h}\mathrm{Tr}\left\{\mathbf{\Gamma}_\mathrm{L}\,\mathcal{G}\,\mathbf{\Gamma}_\mathrm{R}\,\mathcal{G}^\dagger\right\}$, where $\mathbf{\Gamma}_{\mathrm{L/R}} = \mathrm{i}(\mathbf{\Sigma}_{\mathrm{L/R}} - \mathbf{\Sigma}^\dagger_{\mathrm{L/R}})$, $\mathbf{\Sigma}_{\mathrm{L/R}}$ is the self energy of the left or right lead respectively, and $\mathcal{G}$ is the Green function of the central region dressed by the electrodes. The wave functions of the nanotubes are assumed to extend to the leads, allowing us to remain in a phase-coherent regime.

We consider semi-infinite single-walled nanotubes (SWNTs) as leads. To deal with such semi-infinite leads, we adopt the recursive renormalization procedure described in Sec. A.1.1. Considering the leads as bulk gold will yield an increased imaginary part of the lead self energies, which will slightly decrease the conductance values. For multiwalled nanotubes (MWNTs), it has been suggested that the conductance G is mainly determined by the outer shell which is also responsible for the structural stability [199]. A slight reduction of the conductance is expected from finite size effects.

To include temperature effects a generalization of the Landauer approach is followed as introduced earlier by Bagwell and Orlando [200], giving the finite temperature elastic coherent conductance as a convolution of the zero temperature conductance and the thermal smearing function $-\frac{\partial f(E)}{\partial E} = \frac{1}{4k_\mathrm{B}T}\mathrm{sech}^2(\frac{E}{2k_\mathrm{B}T})$, f being the Fermi distribution. This convolution is a natural way to incorporate finite temperature effects leading to a broadening of the energy levels, as it averages the conductance over an energy range $k_\mathrm{B}T$ near the Fermi level.

6.4 Results and discussion

The calculated density of states and the conductance for the gold nanotube $(4,3)$ are shown in Fig. 6.3. This tube is one of the simplest possible candidates with seven atom rows around its circumference (Fig. 6.2). The colored areas show the contribution of the different orbitals to the total density of states, indicating a dominance of s orbitals around the Fermi level. Considering only s orbitals around the Fermi energy is thus a good approximation, but when applying a bias it can be critical to include all s, p, d outer orbitals, as they play an important role in the opening of new conduction channels.

A comparison of the conductance of nanotubes of the same diameter but different chiralities, as shown in Fig. 6.4, suggests that no significant difference is expected in their conductance values at the Fermi energy. For applied bias

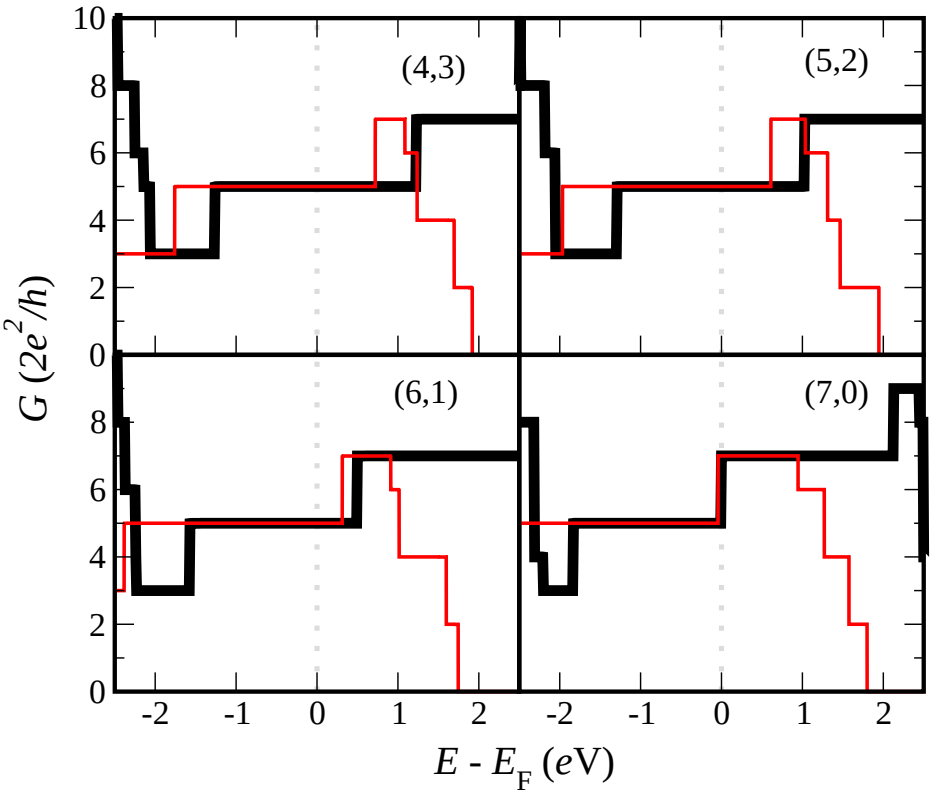

Figure 6.4: Conductance of AuNTs with seven atom rows but different chiralities. Thin lines indicate results including s orbitals only, whereas the thicker ones are showing the calculations with all nine outer orbitals.

voltages the current will show a chirality dependence, reflecting the different energies at which scattering states open.

In Fig. 6.5 the conductance is plotted for nanotubes of different radii, chosen as to have the smallest chirality possible for a given radius. The number of atom rows around the nanotube axis in each of them is $6, 7, 9, 11, 13,$ and 14 respectively. We see that, though the conductance increases for thicker nanotubes, this is not the general trend if divided by the number of atom rows. We can observe again how the expansion of the orbital basis to include all conduction electrons changes the energies at which new channels open, being critical to obtain correct current values.

By analyzing the Brillouin zone of the two-dimensional gold lattice taking into account only s orbitals, one can easily demonstrate after studying its dispersion relation as seen in Fig. 6.7 that the Fermi surface is with great accuracy approximated by a circle with a radius close to $k_F = 2\sqrt{\pi}/(\sqrt[4]{3}\,a)$,

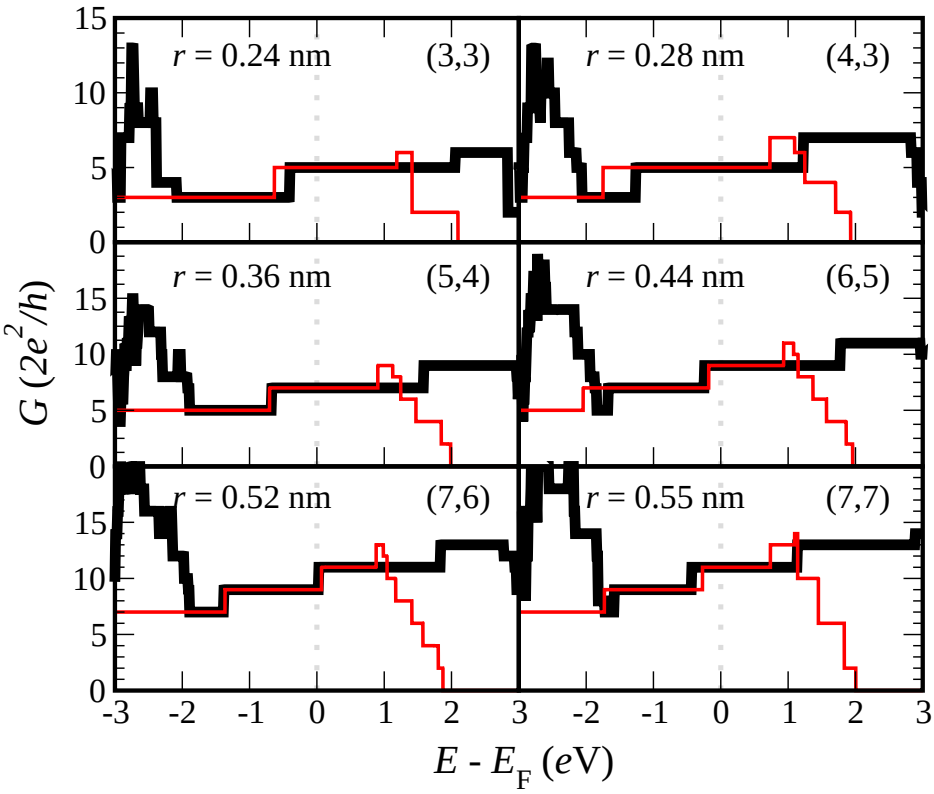

Figure 6.5: Conductance of AuNTs with different radii r. Thin lines indicate results including s orbitals only, whereas the thicker ones are showing the calculations with all nine outer orbitals.

where $a = 2.88$ Å. This simple model allows us to have an analytical approach to the conductance, as the number of energy bands crossing the Fermi surface, since the Brillouin zone of the gold nanotubes consist of parallel line segments due to the quantization of the wave vector along the circumferential direction. For simplicity we can restrict this counting to the first Brillouin zone by folding back to this area the segments lying outside it, which will elongate the lines inside it, as pictured in Fig. 6.6 (Ref. [201]). The conductance can then be written as follows:

$$G^{\mathrm{tot}} = \frac{2e^2}{h}\left[2\,\mathrm{Int}\left(\sqrt{\frac{n^2+m^2+nm}{\pi\sqrt{3}}}\right)+1\right] \tag{6.2}$$

and is only dependent of the nanotube indices and not on hopping parameters or onsite energies. This model yields a perfect matching with the numeri-

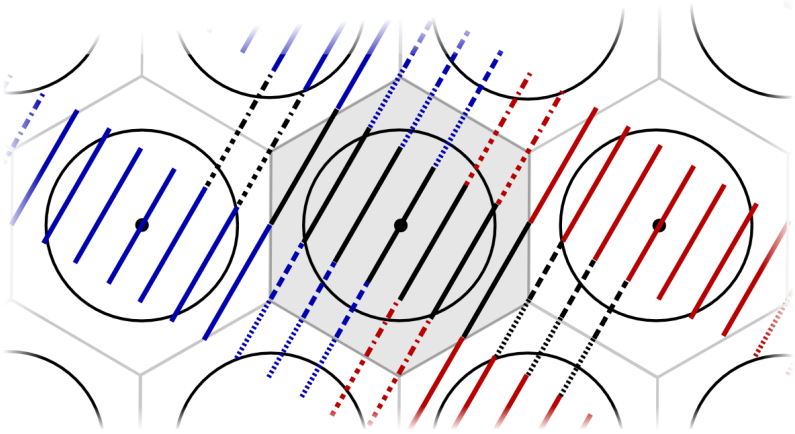

Figure 6.6: Schematic illustration of the reciprocal lattice of the 2D hexagonal Bravais lattice of Au (111) where the first Brillouin zone is highlighted through a darker background. The **k**-vectors lying at the Fermi surface give rise to a nearly perfect circle in this 2D structure. The thicker cutting lines represent the Brillouin zone of a nanotube in an extended zone scheme which allows the use of the dispersion relation calculated for the 2D gold layer to get the bands of a folded nanotube. In this example we show the wave vectors giving the bands in a (6,0) AuNT, a good candidate for this visualization as it has a small number of bands. These lines are plotted as solid bands inside the first Brillouin zone, and are plotted thinner when folded back into it through the reciprocal lattice vectors of the gold layer.

cal calculations described before. The result of this approximation of the conductance at the Fermi level is plotted in Fig. B.7 for nanotubes of different radii and chiralities, presenting the conductance per atom row. The solid line in this figure marks the results of AuNTs with the smallest helicity as characterized in Fig. 6.5. All these tubes present a number of channels smaller than the number of coiling atom rows, which is thus a characteristic of the geometry and electronic states of the nanotubes. We can observe how the upper envelope of all these points slowly decreases with an increasing number of coiling atom rows, or likewise with an increasing diameter. The conductance values will nevertheless be reduced by considering more realistic gold leads. This has also been confirmed in first-principles calculations [193].

Gold nanotubes have been observed as short ($L \sim 4$ nm) conductors between bulk gold electrodes. This calls for an extension of our theory to account for finite size effects. We did this by parametrically introducing into the nanotube two tunneling barriers at a distance L. Figure 6.9 shows

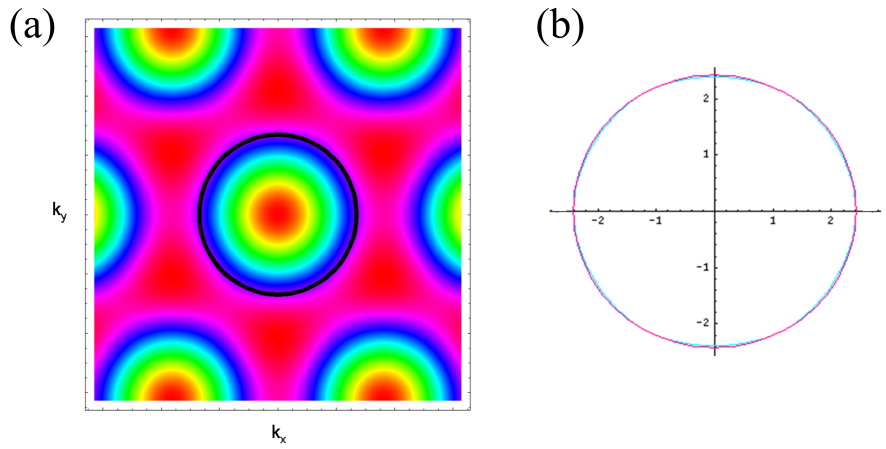

Figure 6.7: The Brillouin zone of the two-dimensional gold lattice is plotted in a color plot in (a), where the Fermi surface is highlighted in black. In (b) one can observe that there are just minimal differences between the actual Fermi surface and a circle of the appropriate diameter.

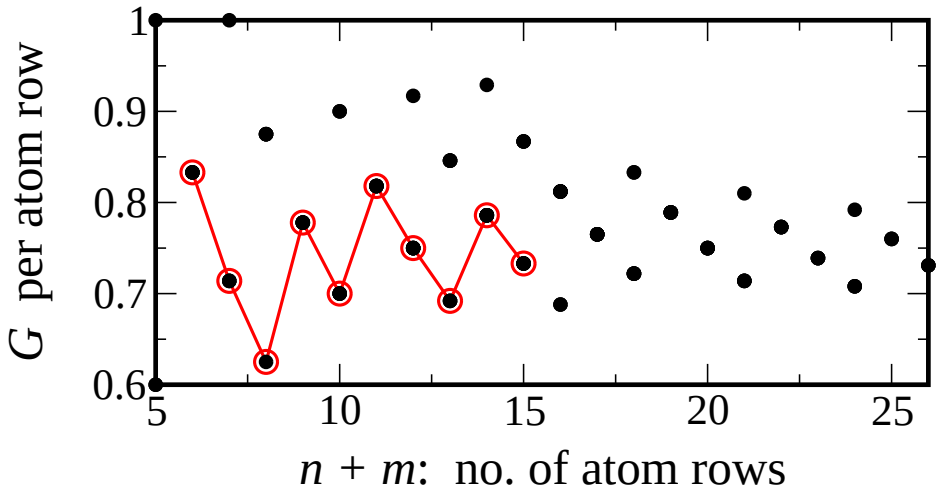

Figure 6.8: The conductance per atom row at the Fermi energy based on the analytical model accounting only for *s*-orbitals described in the text is shown for all possible (n,m) NTs, reproducing exactly the values of the numerical calculations. The solid line highlights the AuNTs with the smallest chiralities seen in the experiments.

the conductance between two homologous semi-infinite electrodes which are taken into account through modified self-energies. This modification is introduced by a multiplicative factor α, which simulates the barriers. Finite size effects can be made equally apparent by considering wide band leads,

i.e. $\mathbf{\Sigma}_{WB}(E) \cong -\mathrm{i}\,\mathbf{Im\Sigma}(E = E_\mathrm{F})$ to simulate bulk gold electrodes. As we can see in Fig. 6.9, we obtain the same kind of oscillating behavior with both approximations. This shows that the results of our model provide an upper limit for the conductance.

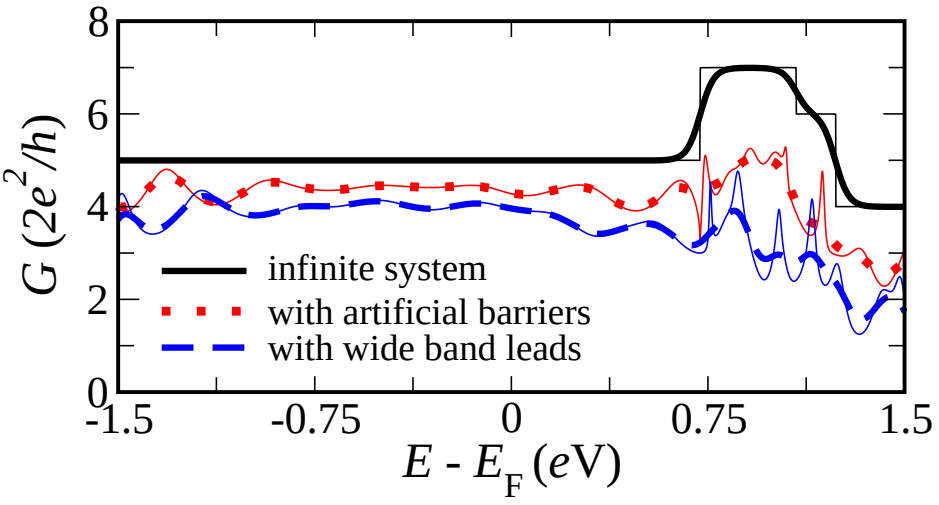

Figure 6.9: Conductance of the (4,3)-AuNT for a perfect infinite NT, for a finite tube with barriers in the connecting regions to the electrodes (where the constant α introduced in the text equals 0.6) and for a finite tube like in the previous case but in the wide band limit approximation taken at the Fermi energy. The lines corresponding to the last two cases show oscillations due to scattering at the ends of the finite size tube. The thicker lines correspond to room temperature conductance [200] while the thin lines underlying them correspond to zero temperature conductance.

6.5 Conclusions

In conclusion, we investigated the electronic properties of several gold nanotubes. We built the Hamiltonians of the systems by applying a tight-binding model for s orbitals as well as for all outer orbitals. All AuNTs are equally metallic independent of their chirality or diameter in contrast to the results obtained for their carbon counterparts [99], but expected from gold electronic nature. In the case of gold the quantization of electron waves along the circumference of the tube results in a Brillouin zone composed of line segments that always cut the Fermi surface of the Au [111] layer due to the continuity of this surface.

The *s*-orbital calculations demonstrate that a one-orbital approach to the problem of gold nanotubes is an excellent approximation for energies around the Fermi level, but should be avoided when applying a finite bias voltage to the system.

An analytical formula for the conductance of the *s*-orbital calculations, matching the numerical results perfectly, shows that the number of conduction channels is smaller than the number of atom rows and that there is a slight decrease of the conductance per atom row as the radius increases, though remains rather constant for the tubes of smallest helicity.

Chapter 7

Molecular switch

Azobenzene offers a paradigmatic example to realize light-driven switches at the molecular scale and thus has exciting potential applications in molecular electronics. Hence, it is crucial to clarify the transport characteristics of this molecule in both *cis* and *trans* isomeric states. Here, we address this issue by analyzing charge transport in a molecular junction consisting of carbon nanotubes (CNTs) acting as electrodes which are bridged by *cis*/*trans* azobenzene. In clear contrast to the conventionally used gold electrodes, the similarities of the energy scales on the nanotubes and the molecule may lead to the emergence of strongly hybridized states *within* the band gap of the isolated molecule. The low energy conduction properties of the junction can thus be dramatically modified by changes of the molecule-electrode contact topology as well as by changes of the tube chiralities. The $I-V$ characteristics are studied in the linear response regime using first principle based methods and Green function techniques. We further show that the *trans* state proves to be a better conducting element than its metastable *cis* configuration, although the absolute values of the calculated currents can be tuned by the choice of the tube chirality. We propose some possible experimental ways to realize the *trans-cis* transition for this kind of constrained geometries.

7.1 Introduction

In the past years, electrical transport at the single-molecule level has been widely explored in view of a variety of possible applications in molecular

electronics [202, 203, 204, 205, 206, 108, 207, 208, 209, 210, 211, 212]. As already mentioned, using molecules as device components may allow for future high-density logic circuits, as organic molecules are typically several orders of magnitude smaller than present feature sizes. Biologists, chemists, physicists, and material scientists face an amazing challenge: to design structures, tailor the molecules in their chemical synthesis and build them in into electronic devices, constituting switches, storage elements or other functions they were designed for. The dream of realizing electronic functions at the molecular scale has thus triggered cooperations among scientists of different fields [4]. This idea has its origin in the ground-breaking study of Aviram and Ratner in 1974 [213] where they suggested, just based on theoretical assumptions, that a molecule with a donor-spacer-acceptor structure would have a diode-like $I - V$ characteristics as those of traditional semiconductor pn-diodes, where the spacer is given by the depletion region at the interface.

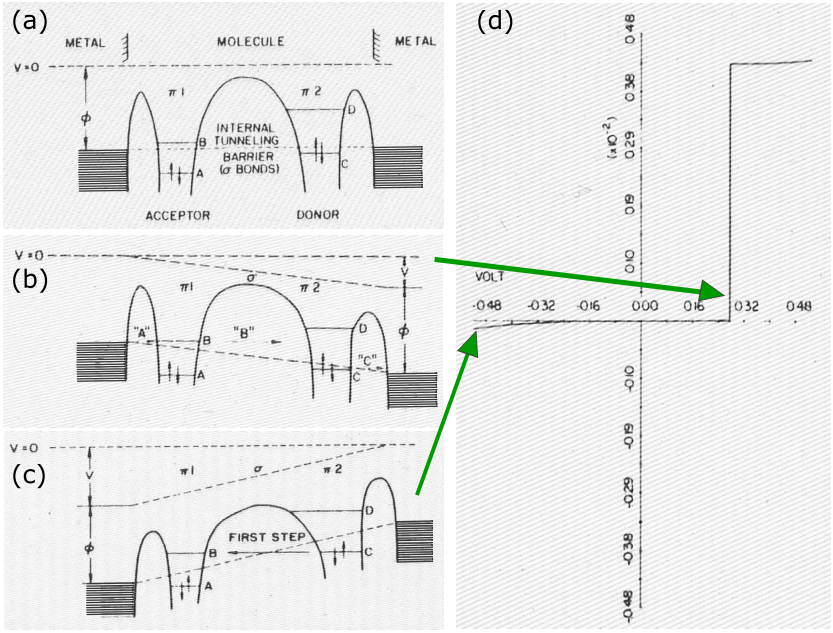

Figure 7.1: Proposed rectifying electronic device based on the use of a single organic molecule consisting of a donor π system and an acceptor π system separated by a sigma-bonded tunneling bridge, as described by Aviram and Ratner in their seminal paper. Figure (a) shows the structure with no bias voltage. In (b) a positive voltage is applied, lowering the potential on the right lead, and allowing current to flow from the cathode to the acceptor to the donor and finally to the anode. With the opposite bias (c) current can only flow at much higher voltages, giving thus an overall rectifying behavior (c) [images taken from Ref. [213]].

The rectifying molecule proposed in this work is built of a donor and accep-

tor delocalized π systems, separated by a linker, which must be insulating enough to preserve the energy difference between these two π systems but still allowing transport through the system. It must also fulfill the condition of being rigid to prevent short circuiting of the two units. The different energies of the frontier orbitals (HOMO and LUMO) of the two separated π systems set a preferential direction for transport, the one going from the acceptor to the donor as shown in Fig. 7.1.

This idea was at first far from being feasible to realize, but presently, experimental groups have come considerably closer to it [214, 209] by demonstrating rectifying behavior at the single-molecule level due to the advances in scanning probe techniques, nanolithography and other techniques for gaining control at the nanoscale. First successful experiments to immobilize a single molecule between two electrodes were reported by the groups of Reed and Tour [215], where using a mechanically controlled break junction a gold wire is broken into two electrodes which are quickly covered with strongly adhering self-assembled monolayers of a dithiol compound. The tips are then moved again close together until the onset of conductance is achieved.

One key element to realize electronics at the nanoscale is to manipulate in a *controlled* way the conduction properties of individual molecules [108, 216, 217]. Still, contacting a single molecule is a challenge for experimental physicists, though the advances in nanotechnology have allowed for manipulation of even single molecules. At least four different ways can be identified: mechanical means by *e.g.* acting with a STM-tip (*i.e.* [217]), electrical means by applying a gate electrode which controls the position of the molecular levels and thus can bring them in and out of resonance with the electrode continuum (*i.e.* [108, 105]), chemical manipulation by introducing radicals with pre-established electrical properties (*i.e.* [218]). Closely related to the latter is the use of photochrome radicals inserted at selected places in a molecular wire. Via the introduction of photochrome groups a structural modification can be induced by irradiation with light. As a result the π-conjugation of the molecular frame can be modified. Some typical examples are stilbene [219] and azobenzene [220] which undergo a *cis-trans* transition under irradiation.

7.2 Azobenzene: a bistable system

Bistable molecules are characterized by having two different metastable states. The physical properties of these molecules may differ for these two states, in particular differences in conductance and thus in their current transport properties make these systems of special interest for molecular electron-

ics. To use them as switches and possibly as molecular storage elements a good control of the addressing and switching of the molecules must be achieved.

Systems providing molecular switches can be based on different kinds of bistabilities: for example a reduction-oxidation process which changes between a neutral and ionized state of its units, a configuration change through a reversible re-arrangement reaction, a change to a long-living electronically excited state, or a conformation change controlled in such a way that both conformations are sufficiently stable at the operation temperatures. It is the latter we are going to address in this study.

We will study the switching mechanism of azobenzene which offers an archetypal example to realize light-triggered switches. A drawback of using light as the external stimulus to control the switch is the difficulties to integrate it in a circuit. However there are successful experiments proving light-driven switching behavior as that of M. Irie [221]. In fact, the motivation to start this work has come from the interaction with Dr. U. Beierlein and Dr. A. Holleitner from the Center for NanoScience (CeNS), who have started to perform ongoing transport experiments on azobenzene contacted by carbon nanotubes in the group of Prof. J. Kotthaus at the Ludwig Maximilian University of Munich.

Azobenzene is an organic molecule composed by two phenyl rings connected by a nitrogen bridge. As shown in Fig. 7.2, it has two metastable configuration, the *trans* and *cis* isomers and can reversibly change its conformation between these two states by stimulus with light in the proper wavelength range. The *cis* configuration in bulk measurements on azobenzene containing peptides shows thermal relaxation times of several hours at room temperature [222].

Some experiments with azobenzene applied as a mechano-optical device have been successfully performed [220], but more recently, the capability of azobenzene as an electronic switch has been the center of renewed interest. The theoretical studies of Zhang *et al.* [223, 224] explore this potential application as a molecular electronic device for the case of azobenzene attached to gold leads (see Fig. 7.3), finding promising results as a significant change in conductance is seen between both conformations. Though a mechanism is proposed to allow for a certain movement of the gold leads, azobenzene and similar molecules undergoing isomerization transitions require more versatile nanocontacts which suitably adjust to the change of length in going from one configuration to the other. Moreover, in view of the different energy scales associated with gold and with organic systems, a strong modification

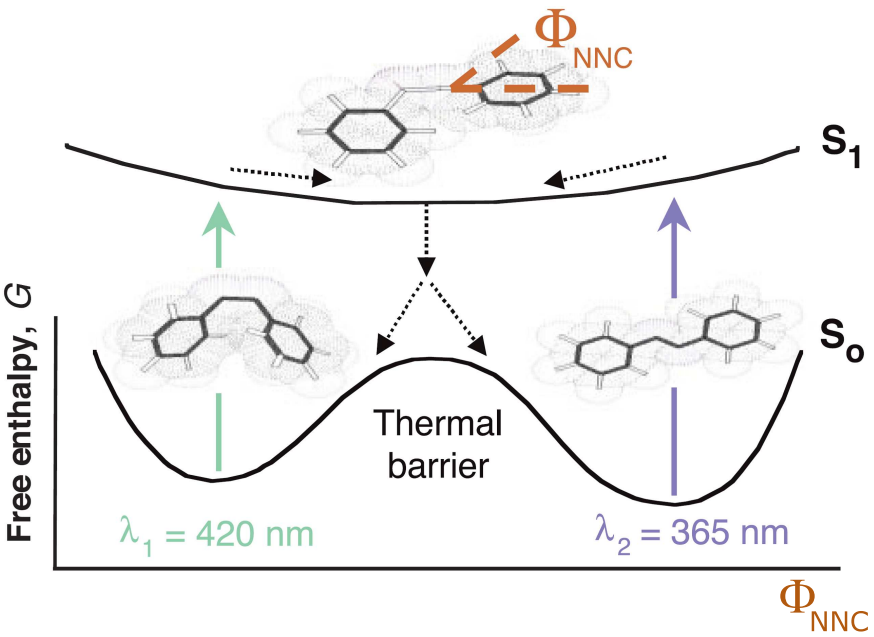

Figure 7.2: As a typical case of bistability, azobenzene shows double well potentials concerning its energy. The reversible azobenzene *cis/trans* transition along the inversion pathway on its potential energy landscape is sketched here. The relevant conformational coordinate is the bond angle Φ_{NNC}. The transition can be induced by optical excitation from the electronic ground state S_0 to the first excited state S_1 [image taken from Ref. [220]].

of the molecule electronic spectrum is not expected. Indeed, the coupling to Au-electrodes only leads to a broadening of the molecular orbitals, without essentially perturbing the molecular electronic structure. More exciting is the possibility of having *nanoscale* electrodes with similar intrinsic energy scales as those of the molecule, which may –in strong contrast to Au-electrodes– eventually lead to a strong renormalization of the low energy molecular electronic structure and hence to dramatic changes in the conductance (mixed states arising from a strong hybridization of electrode electronic states with molecular states may emerge within an energy window lying inside the HOMO-LUMO gap of the isolated molecules). The most attractive candidates are CNTs [225], which are essentially 1D systems and whose conduction character (metallic or semiconducting) can be tuned by changing their chirality. Changing their chirality is not such an easy task for experimentalists as for theoreticians but at least the different conduction behavior can be exploited.

We will thus study the transport characteristics of single *trans* and *cis*

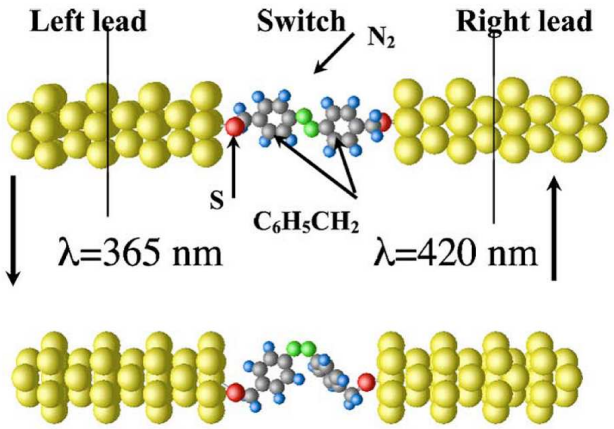

Figure 7.3: Device structure of the molecular switch that consists of two gold leads and an azobenzene molecule as proposed in Ref. [223, 224] [image taken from Ref. [224]].

azobenzene molecules contacted by metallic carbon nanotubes with two typical chiralities: armchair and zigzag CNTs. The system constitutes thus a mono-molecular electronic device, as the connecting wires are full nanoscale devices. Our scope is to highlight the dependence of charge transport on the electronic structure of the electrodes and the differences between the isomers, in view of their possible identification by electrical measurements as well as their potential application as molecular switches.

7.3 The isolated molecule

The *trans* isomer is characterized by a planar structure while in the *cis* isomer the phenyl aromatic rings are tilted with respect to each other, as can be seen in Fig. 7.6. Total energy calculations yield an energy difference between the isomers of ~ 0.4 eV (SIESTA) and ~ 0.5 eV (DFTB); the *trans* state being always the one with the lowest energy, and thus the true ground state of the molecule. The HOMO (Highest Occupied Molecular Orbital)-LUMO (Lowest Unoccupied Molecular Orbital) gap for the azobenzene molecule is of about ~ 1.98 eV.

Both, the density-functional (DFT) code SIESTA [44, 45] as well as DFT-based tight-binding (DFTB) [63] methodologies (see Sec. 1.6) have been used for geometry optimization of the isolated molecules. Relaxation of the molecular junctions and the corresponding charge transport calculations were car-

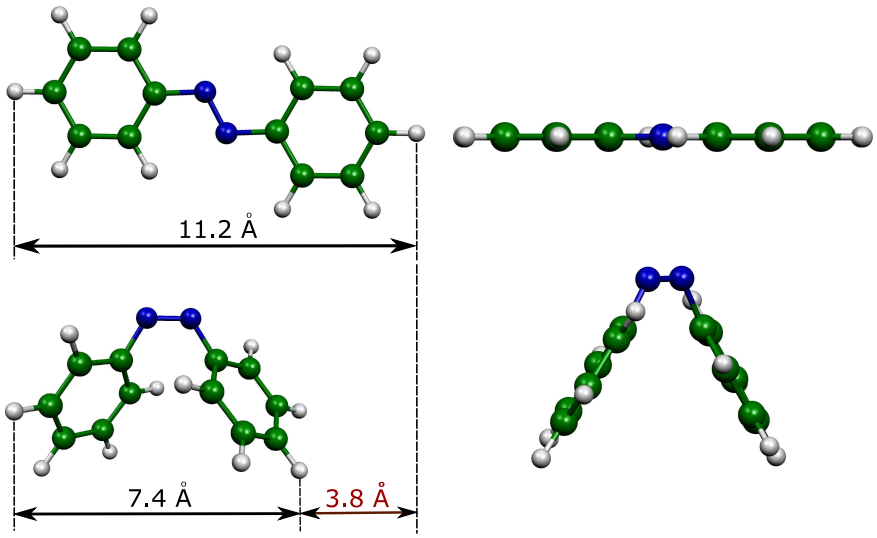

Figure 7.4: The *trans* (up) and *cis*(down) isomer of the isolated azobenzene are shown here. On the left the length difference between the two is highlighted whereas on the right the lateral view of the molecules is given where one can better observed the planarity of the *trans* configuration and the tilted angle of the *cis*.

ried out by a combination of the DFTB method with Green function techniques in the frame of the Landauer approach for transport [65].

7.4 Azobenzol

In order to improve the molecule-electrode coupling, the hydrogen atoms at the para-positions on the molecules are substituted by NCOH-groups, which have been used as linkers to CNT electrodes in recent transport experiments [226]. As we will see, it turns out that the oxygen atom plays a critical role in determining the conductance near the Fermi level.

The use of these linkers comes from the chemical process followed in the group of CeNS to attach the azobenzene molecules to the CNTs. The first step in this functionalization process is the treatment with an acid solution which produces nanotubes with open ends and carboxyl end-groups as seen in Fig. 7.5. These carboxyl end-groups are the starting point for chemical modifications. They are then converted to the corresponding acid chloride by refluxing in thionyl chloride:

$$(CNT) - COOH + SOCl_2 \longrightarrow (CNT) - COCl + SO_2 + HCl \qquad (7.1)$$

The chlorine group then attached to the nanotubes is very reactive and allows versatile modification. The chloride is replaced by an amino group, which is then attached to the azobenzene molecule, resulting thus in the previously mentioned linkers. The experimental process being performed continues after the chemical procedure with the deposition of a droplet of solution with functionalized tubes on a Si chip where the interesting structures are located with Atomic Force Microscopy (AFM) and then contacts are made using optical and e-beam lithography.

Upon addition of the linkers, the gap slightly increases to 2.03 eV. Conversely, the gap for the *cis* isomer decreases from 2.55 eV to 2.34 eV. However, the isomer geometries are not appreciably modified after relaxation. In Figure 7.6 we show the energetic position of the frontier orbitals of the isomers as well as the optimized geometries.

Remarkable is that after including the linkers, the length difference between the two isomers is slightly reduced. An further effect of the inclusion of chemical linkers is the increase of flexibility.

7.5 Azobenzene connected to CNT electrodes

Let us consider the CNT-azobenzene-CNT molecular junction. The complexity of the system leads to a very structured potential energy hypersurface with

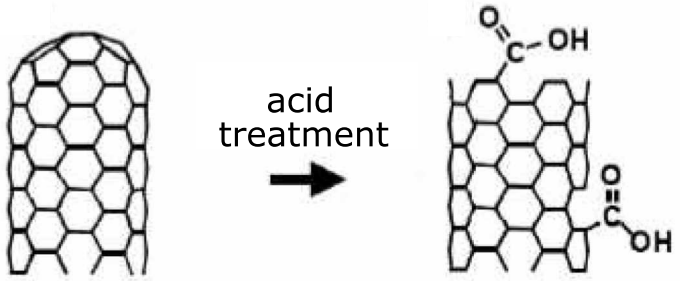

Figure 7.5: A necessary previous step towards the functionalization of carbon nanotubes for the self-assembly of hybrid structures is the acid treatment, leading to carboxyl end-groups [image from Udo Beierlein].

many metastable states. This nontrivial energy hypersurface makes the procedure of detection of a global minimum rather tedious. For the relaxation of the structure we first let all atoms move freely, without any constrictions, to obtain the optimized distance between left and right leads. For the sake of simplicity we only consider co-axial arrangements of the left and right CNTs, taking the optimized distance between the tubes from the previous relaxation. More general transport configuration set-ups may also be considered, though the conclusions about the differences in transport of the two isomers are not expected to change. Different junction geometries differing by the way the molecule is attached to the CNT surfaces were optimized using conjugated-gradient techniques (see some results of these relaxations in Fig. 7.7). The lowest-energy configurations were then used for the transport calculations, as no other experimental information about the contact topology is known. We remark at this point that the energy differences between the investigated metastable states are roughly of the order of a few meV/atom, so that our transport calculations can be considered as giving expected trends. Other energetically closer configurations may lead to slightly quantitative different results. However, our basic conclusions are not expected to be affected.

The electrical transport properties of the CNT-azobenzene-CNT junction are calculated using the "extended-molecule" concept. That is, to compute

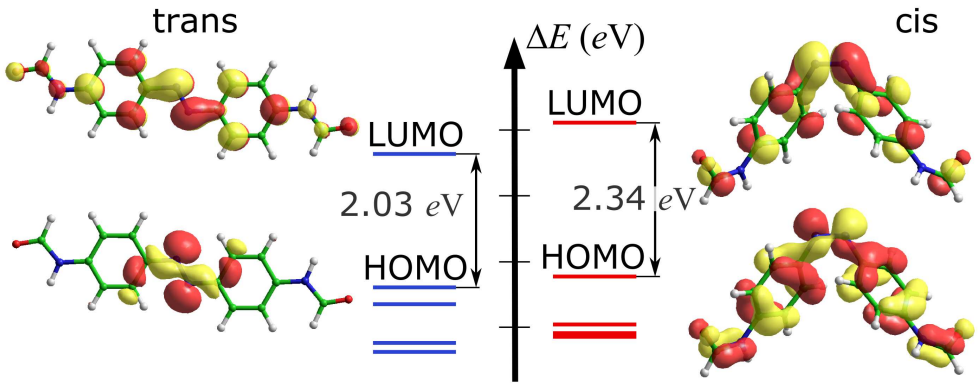

Figure 7.6: The positions of the frontier molecular orbitals of *trans* (left) and *cis* (right) azobenzene including the NCOH-linkers are shown. The HOMO-LUMO gap is slightly smaller in the *trans* state, which is also the lowest-energy configuration. The presence of the linkers does not appreciably modify the geometric structure of the isomers. Also shown is an isosurface plot of the electron density for the HOMO and LUMO orbitals. The *trans*-HOMO is mainly localized around the N-N dimer with almost no weight on the linker groups.

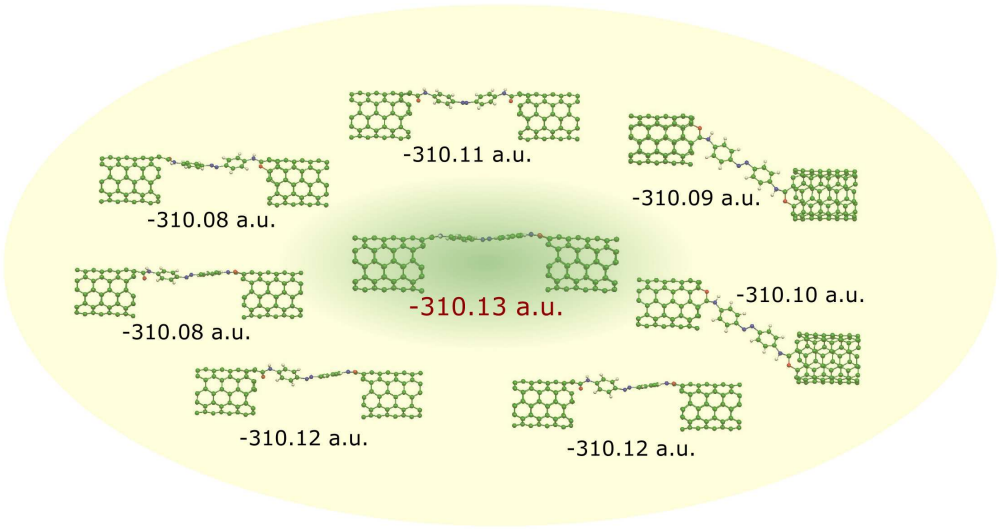

Figure 7.7: As already mentioned, for each configuration local minima are obtained very close in energy. Here we show some of these local minima for one of the cases studied corresponding to the *trans* isomer attached to armchair CNTs on both sides. The configuration with lowest minimum is the one shown in the center of the figure, and coincides with that of the most planar configuration for the azobenzene. Large series of simulation runs were always performed as the danger of falling into local minima is rather high. The energies are given in atomic units (1 a.u. $\simeq 27.211eV$.

not only the organic molecule but also the interaction with the electrodes, one considers a "super-molecule" including parts of the metallic contacts (see *e.g.* Ref. [227]). The structures are then relaxed, being now only movable those atoms of the extended molecule, around 100 atoms, that is, the azobenzene with the linkers and the first one (or two for the case of armchair nanotubes) unit cells of the leads.

Let's first consider some relevant structural details of the relaxed molecular junctions. Fig. 7.8 shows the density of states of the *trans* configuration for armchair and zigzag nanotubes and Fig. 7.9 and Fig. 7.10 show the conductance of the two azobenzene isomers for the cases of armchair and zigzag nanotubes respectively. In the *trans* configuration attached to armchair leads one of the benzene rings slightly rotates out of plane by about $8°$, so that the relaxed state deviates from the perfect planar geometry found in the isolated molecule. This structural distortion becomes even stronger when attaching the *trans* molecule to zigzag tubes ($14°$). On the contrary, for the *cis* isomer

geometrical modifications upon attachment to the leads do not depend so much on the chirality of the CNTs, and consist basically of a slight reduction of the tilt angle.

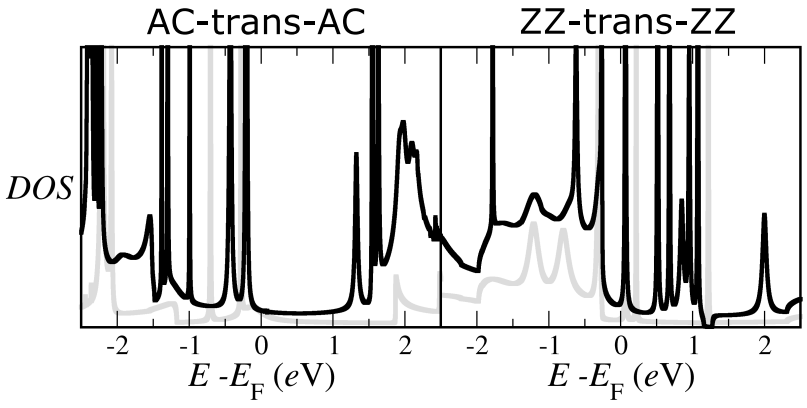

Figure 7.8: Density of states for the *trans* isomer for the cases of armchair(AC) nanotubes as leads (left) and zigzag(ZZ) nanotubes. The gray lines plot the density of states of the corresponding semi-infinite CNTs.

Concerning the CNT-molecule contact, two direct covalent bonds are formed between the azobenzene complex and the CNT leads, a C_{CNT}-C_1 bond and a C_{CNT}-O bond. The bond topology is however different for armchair and zigzag tubes, as shown in the insets of Fig. 7.9 and Fig. 7.10. In the former case a hexagon is formed, while in the latter case a pentagon is built. This appears to be a common feature of the bonding topology, since other initial configurations led to similar connectivities upon relaxation.

Once the geometries were optimized, we first focused on the dependence of the linear conductance on the charge injection energy (Fig. 7.9 and Fig. 7.10) for armchair and zigzag junctions, respectively. We calculate the energy-dependent transmission function $T(E)$ at zero voltage which is equivalent to the Landauer conductance $G = (2e^2/h)T(E, V = 0)$. Charge transport properties were investigated by a combination of the DFTB method with Green function techniques (see Sec. 1.6) in the frame of the Landauer approach to transport, where the linear conductance G can be obtained from the quantum mechanical transmission probability at zero voltage. We stress that when calculating the current $I(V)$ the full voltage dependent $T(E, V)$ is used: $I(V) = (2e/h) \int \mathrm{d}E \, [f_L(E) - f_R(E)] \, T(E, V)$. In the last expression $f_{L/R}(E)$ are the Fermi functions of the left and right electrodes. We remark that $T(E, V)$ is calculated for the so called extended molecule, which contains not only the azobenzene and the linkers, but also part of the electrodes. This

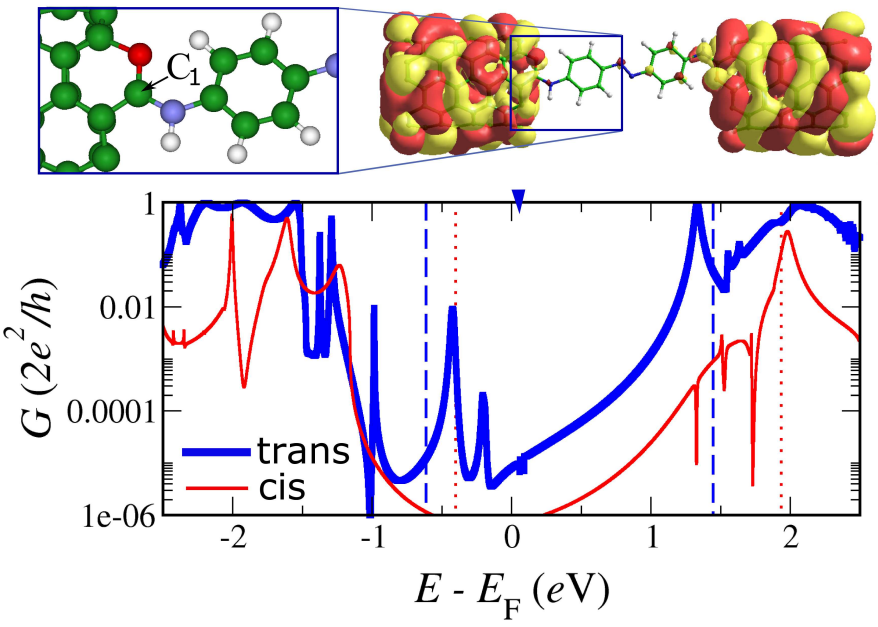

Figure 7.9: Linear conductance at zero bias for a (5,5) armchair-*trans*(*cis*)-armchair junction.
As a reference we indicate by vertical lines the energetic positions of the HOMO and LUMO orbitals of the isolated *trans* (dashed lines) and *cis* (dotted lines) molecules. Despite the fact that the isolated molecule has a HOMO-LUMO gap of about 2 eV, no clear signatures of it can be seen in the conductance. This is related to the presence of CNT states inside the gap, which strongly hybridized with molecular states. Top panel: density isosurface plot of a selected molecular orbital (at an energy indicated by the arrow near the Fermi level in the conductance plot) of the extended *trans* molecule. The low weight on the molecule reflects the rather low conductance at this energy. The inset is a zoom of the CNT-molecule interface showing the formation of a carbon hexagon with an oxygen defect upon relaxation. This configuration is the same for both isomers. Notice that the "bottleneck" of the junction is built by a single carbon atom, denoted by C_1. It is just the spectral weight on this atom which will strongly determined the effectivity of charge transport.

allows to treat the molecule-electrode coupling and the molecule electronic structure on the same footing [227, 65].

First of all, it turns out that the *trans* configuration shows an overall better "transparency" (higher conductance) than the *cis* state, *independent* of the CNT chirality, thus suggesting that the switching behavior may be already expected at low bias. The conductance of the armchair-*cis* junction displays

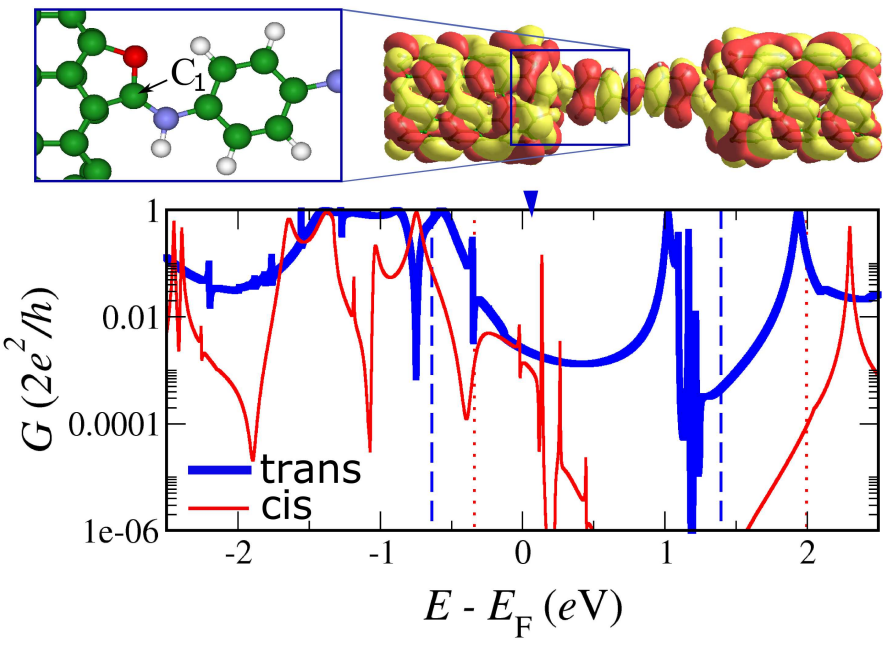

Figure 7.10: Linear conductance at zero bias for a (9,0) zigzag-*trans*(*cis*)-zigzag junction.

As in Fig. 7.9, the vertical dashed (dotted) lines indicate the positions of the frontier orbitals of the isolated *trans*(*cis*) isomers. Notice the increased conductance around the Fermi energy for both isomers as well as the more complex structure of the spectrum in this energy region. This is related to the quasi-singular behavior of the surface density of states of zigzag tubes, which displays a strongly localized edge state at the Fermi level. Top panel: for illustration, we also show the density isosurface plot of a selected orbital of the extended *trans* molecule (at an energy indicated by an arrow in the conductance plot). Notice the much higher weight on the molecule when comparing with the armchair junction in Fig. 7.9, which explains the higher transmission at this energy for the present case. The inset shows the local atomic structure at the CNT-molecule interface, where a pentagon is formed upon relaxation. As for armchair junctions, this local bonding topology is the same for both isomers.

a parabola-like gap around the Fermi level indicating that transport can only take place via virtual tunneling and thus very low currents are expected. On the contrary, several resonances are seen for the *trans* state around the Fermi energy, which despite their relative low intensity may give rise to resonant transport. These mixed states have a non-negligible overlap with the CNT extended bulk states and thus can contribute to transport. The fact that

such states lie within a low-energy window around E_F is a consequence of the similar energy scales on the molecule and the electrodes, hence the advantage of using carbon-based leads instead of the conventional Au-electrodes. As a result, conductance manipulation may become more feasible, since these states will sensitively depend on the molecule-CNT contact topology, as can be seen from our calculations. The low transmission of the *cis*-state is related to its distorted geometry which considerably breaks the π-conjugation along the molecular frame.

Turning now to the zigzag-azobenzene junctions, the conductance appears to be considerably larger for both isomers than for armchair junctions, see Fig. 7.10. One should notice at this point that for both chiralities there is essentially a single pathway from the CNT to the azobenzene molecule going through a carbon atom belonging to the linker and denoted as C_1 in Fig. 7.9 and 7.10. Thus, the local density of states (spectral weight) $A(E)$ on this atom completely determines the effectivity of charge transport through the junction. A major factor influencing $A(E)$ is related to the presence of the oxygen atom in the NCOH linker as can be seen in Fig. 7.11. Due to its higher electroaffinity, the oxygen tends to deplete the spectral weight on the C_1 atom. This mechanism is very effective for armchair junctions but fails to have a dominant effect for zigzag junctions. The reason is that the surface density of states of a zigzag tube has, as is well-known, a large spectral weight close to the Fermi energy (corresponding to a localized state at the zigzag edge –see Sec. B and for instance [228]–). Our DFT-based calculations as well as a minimal π-orbital model Hamiltonian (see Fig. B.7)for the junction show that -contrary to the armchair system- in zigzag junctions a much larger spectral weight on the C_1-atom persists for energies around the Fermi level. Moreover, the strong zero-energy edge resonance leads to a quasi-singular behavior of the electrode self-energies $\Sigma_{L/R}(E)$ and, as a result, to a rather complex renormalization of the molecular electronic states which is absent for armchair junctions. Thus, the conductance difference for both junctions is a result of the interplay between local (interface) chemistry and electrode surface electronic structure.

Moreover, calculations have been also performed upon saturating the CNT surface dangling bonds not in contact with the molecule with hydrogen, but no appreciable qualitative changes in the conclusions of this work were found.

To round off our discussion, we have calculated the I-V characteristics of the junctions to confirm the possible switching behavior already suggested by the analysis of the linear conductance. For the sake of completeness, a hybrid armchair-azobenzene-zigzag system was also investigated. The results for the three cases are displayed in Fig. 7.13. Charge transport for the *cis*

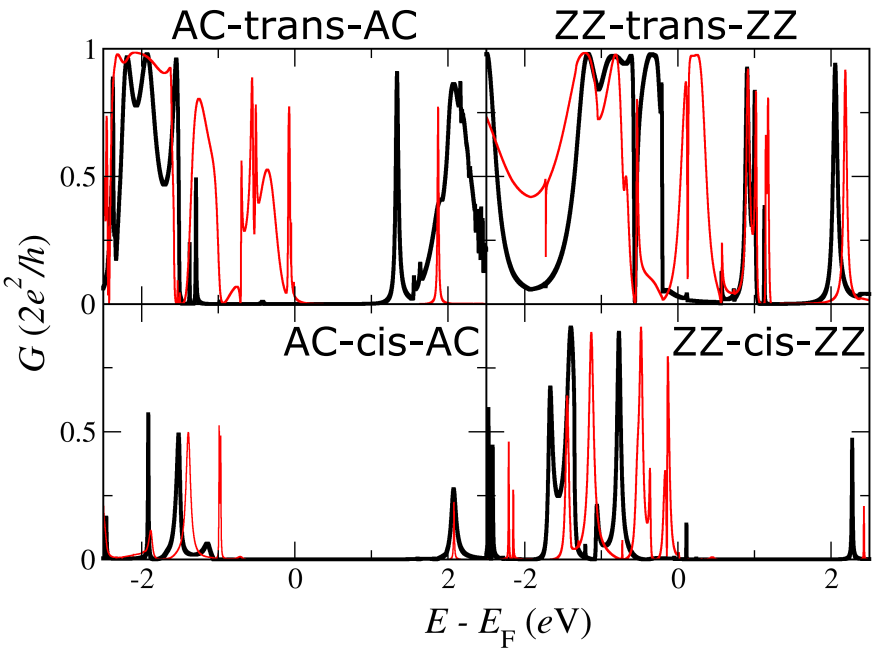

Figure 7.11: Change in conductance upon substitution of the oxygen atoms by carbon atoms on the same positions. The change is significant for all configurations indicating the key role of the linker oxygen atom in transport. The black thicker lines show the result with the NCOH linkers whereas for the red thinner lines the oxygen atom has been substituted by carbon atoms.

state is strongly suppressed already at low bias for *all* junctions, indicating a switching behavior. Note that the zigzag-*trans*-zigzag junction shows one up to three orders of magnitude larger currents than the other two junctions, where armchair tubes were used. This is even more dramatically seen in Fig. 7.14 where the average conductance I/V is shown. These results further support the conclusion that the electronic structure of *both* molecule and electrodes is crucial in determining the low-voltage transport when nanoscale electrodes are used. We would like to mention, that our equilibrium treatment of transport is validated by recent non-equilibrium calculations [224] using Au-electrodes which showed a similar qualitative behavior for the two isomers, i.e., $I_{trans}(V) \gg I_{cis}(V)$. Finally, we would like to comment on possible experimental realizations of the conformational switching when using CNT electrodes. One precondition to achieve it, is to increase the flexibility of the junction, either by using longer linkers, e.g., NCOH-$(CH_2)_n$ or by incorporating movable electrodes which would allow for a change in their relative orientation. We might expect that for a kinematically constrained molecule

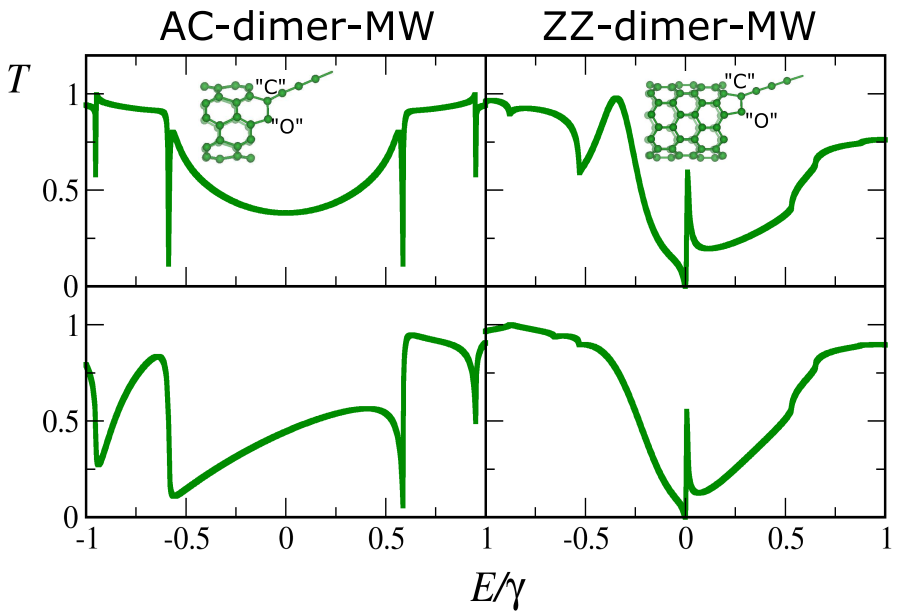

Figure 7.12: A π orbital Hamiltonian is used to describe the model system composed of a CNT, a C-O dimer (joined as sketched in the insets of Fig. 7.9 and Fig. 7.10) and a molecular wire (MW) attached to the C atom of the dimer. The plots on the left are for armchair CNTs and on the right for zigzag CNTs. The top panels correspond to setting equal onsite energies for the "C" and "O" atoms of the dimer, whereas in the bottom panels the onsite energy of the "O" atom is lowered approximately in the value of the hopping parameter γ. It can be observed that the effect of introducing differences in energy in the oxygen π orbital has a much more important effect in the configuration joining to armchair CNTs.

as the one studied here, the "standard" isomerization pathway upon laser excitation would in principle be of difficult realization. While this is true for Au-electrodes, the 1D nature of CNTs can considerably increase the mechanical flexibility of the junction. Additionally, alternative pathways through other metastable states compatible with the constrains can also become effective. Indeed, we have structurally optimized several molecular junctions and found out that the relaxed conformations have geometric characteristics lying between those of the *trans* and *cis* isomers. Light irradiation or mechanical actions may then trigger the transition from these metastable configurations to the final *cis* state. Another advantage of using CNT electrodes lies in the fact that they may posses a *negative* thermal expansion factor [229], so that a combination with other metallic electrodes may lead to thermally more stable junctions. This can be very important e.g., upon irradiation of the molecular junction with a laser pulse in order to trigger

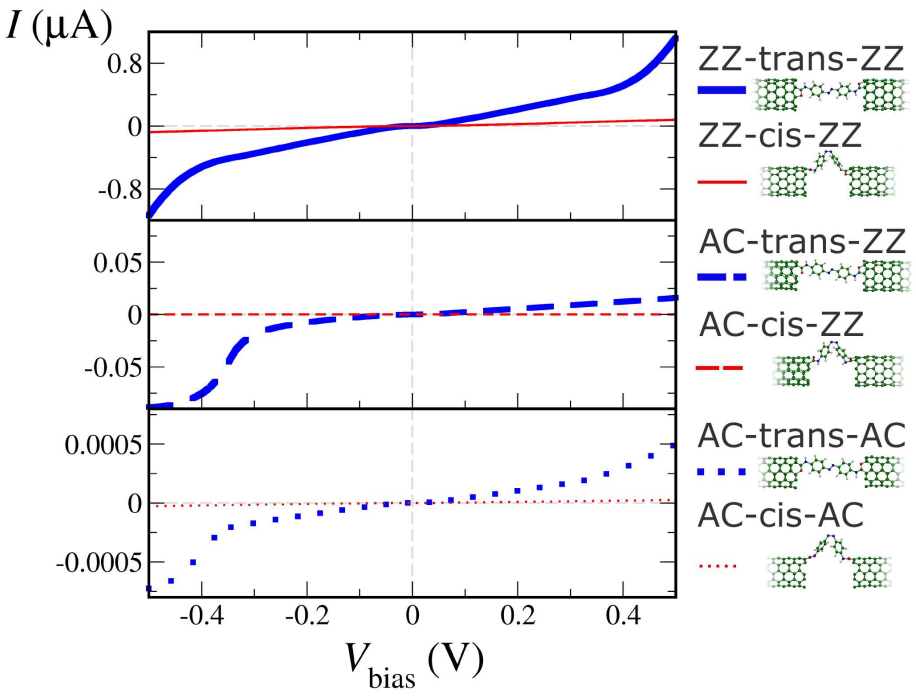

Figure 7.13: $I-V$ characteristics for the two isomeric configurations of the azobenzene molecule attached to armchair (upper plot) and zigzag (lower plot) CNTs and to both an armchair and a zigzag CNT (middle plot). The results for the *trans* isomer are shown by the thick lines whereas for the *cis* isomer thin lines are used. In the case of the *trans* isomer as well as for the *cis* isomer, higher current values are obtained for zigzag electrodes and decrease in the mixed case and are lowest for armchair electrodes.

the $trans-cis$ transition, since normal metal electrodes would expand upon heating, thus reducing the junction flexibility.

In conclusion, we have presented a study of the transport properties of different CNT/NCOH-linker/azobenzene/NCOH-linker/CNT systems under low bias using a first-principle based method that combines DFTB and Green function techniques. Our calculations show that the HOMO-LUMO gap for the *trans* configuration is always smaller than for the *cis* configuration, resulting in higher current values for the *trans* configuration for bias voltage below one volt. This suggests that light-driven switching behavior for this molecule is stable under small bias voltages. Different chiralities of CNTs used as leads seem to have a big influence in the absolute current values, putting forward the possibility of recognizing the CNT chirality through the

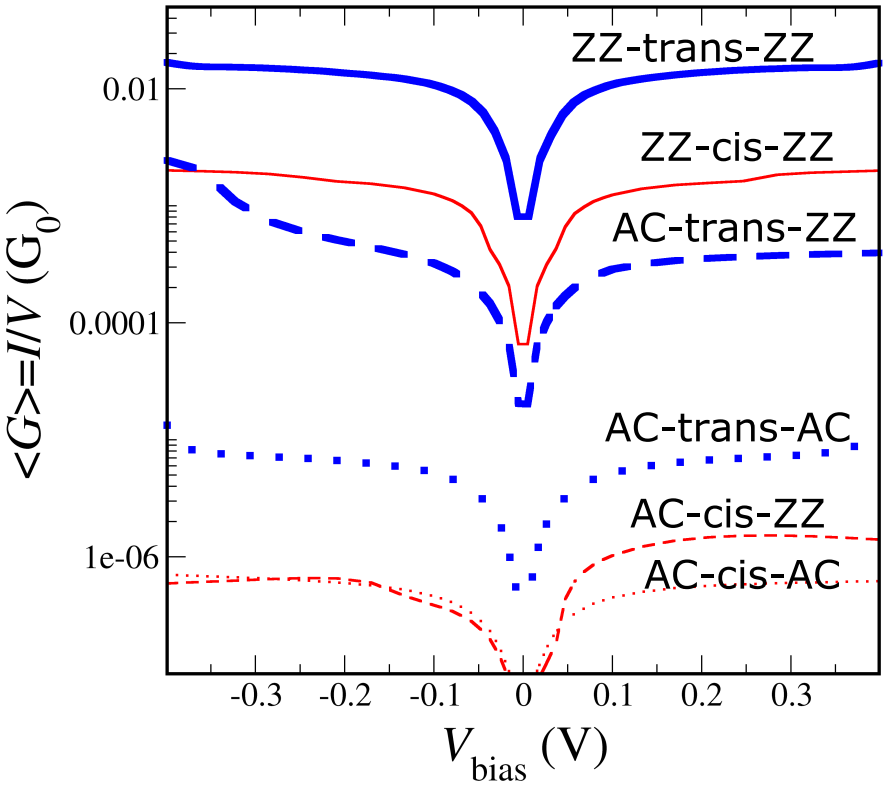

Figure 7.14: Average conductance I/V of the CNT-azobenzene junctions allowing for a direct comparison of the current amplitudes. Three possible CNT-molecule junctions are shown: zigzag-*trans/cis*-zigzag, armchair-*trans/cis*-zigzag, and armchair-*trans/cis*-armchair. A systematic hierarchy can be seen, showing (i) that the *trans* state is always better conducting that the *cis* one and that (ii) the inclusion of armchair CNTs acts always as to deteriorate the conductivity of the junction. The logarithmic divergence at zero voltage has been explicitly removed.

current intensity.

Conclusions and perspectives

Carbon is an essential element in life sciences. Organic chemistry in its variety and complexity relies after all on the characteristic and fascinating properties of this element. Consequently, it does not surprise so much to realize how large the effort has been to investigate its properties; but nevertheless, mainly from the chemists community. For the physicists the interest had mostly been lain on carbon solids as graphite and diamond, and these systems seemed to have exhausted their appeal. This picture was though completely changed some decades ago, when the family of carbon materials officially grew to include new members in the nanoscale: fullerenes and carbon nanotubes. They were discovered and characterized thanks to the advances in experimental techniques for studying systems at these nanoscopic scales. Moreover, most recently graphite has been synthesized as a monolayer and bilayer graphene, unfolding a rich realm of unknown properties. Carbon has thus found lately an outstanding role in the emerging field of new materials for electronics. It is accordingly of great interest and importance to study the transport properties of these materials, which better reveal, due to their dimensions, the laws of quantum mechanics and allow the possible discovery of new phenomena which are still missing a deep understanding. Theoretical studies play here an important role in identifying the conduction mechanisms, in clarifying the new physics underlying the experiments or even in the discovery of new quantum phenomena.

Small organic molecules, fullerenes, nanotubes and graphene are hence at the focus of current research of quantum transport. The possibility of using such molecular (molecular in a broader sense) systems for electronic applications, that is to realize *molecular electronics* [230, 231, 232], is an encouraging and promising aim for researchers. Employing molecules as active electronic devices requires to bring together the know-how from the solid-state and semiconductor research as well as from chemistry, chemical physics, and biology. The combination of these expertises would allow in the long run to go from *hybrid* molecular electronics, where the molecules are directly con-

tacted by inorganic electrodes, to *pure* molecular electronics, where all major functions of logic circuits are integrated into molecules which are connected to each other and where the non-molecular electrodes just accomplish the exchange of data and energy. On the other hand, gaining understanding in transport through molecules and their dynamics may even bring important breakthroughs in electronics of nanodevices, where bottom-up approaches have been up to now only poorly explored, in the more conservative attempt of translating well-known concepts of more conventional electronics.

Nearly all carbon-based materials have attracted the research activity exposed in this thesis: fullerenes, carbon nanotubes and junctions of these tubes, graphene, the organic molecule of azobenzene, and the gold variation of the nanotubes. To describe accurately quantum transport in realistic molecular systems one needs a reliable method to characterize the underlying electronic structure. For this reason, different methods have been applied during this thesis. The combination of density functional theory and the tight-binding approach and the merging of various calculation techniques such as Green function and decimation and Landauer transport approach, have allowed to tackle a manifold of transport problems. These tools permit the study of the aforementioned molecular scale systems in the whole energy spectrum, in contrast to other field-theoretical models valid only at low energies.

Well-established DFT codes have been used, like GAUSSIAN or SIESTA, as well as DFT-based codes such as DFTB. Implementations for transport of Green function techniques for systems with charge transfer as gDFTB have also proved of great help. Independently of these codes, well-known for the scientific community, an own code have been developed in this thesis which implements a combination of Slater-Koster tight-binding and Green functions techniques. It allows fast conductance and current calculations of large systems of several hundreds of atoms, such as helical nanotubes or multi-walled nanotubes, and implements multi-orbital calculations via the Slater-Koster scheme.

In three-terminal branched carbon nanotube junctions, an essential component for high-density integrated-circuit devices, we have been able to show, as explained in **Chapter** 4, that gating one of the arms of these junctions can have a big influence in the current flowing through the other two arms. We were able to show that these changes are due to Fano resonances in the junction arising from the interference between defective states and the extended continuum background. These defective states are associated to the non-hexagonal "defects" that are needed to obtain such junctions by wrapping up the honeycomb lattice of graphene. Through a thorough examination

of the projected density of states on the whole junction structure we could determine the degree of localization/extension of these states. A systematic study of the transport properties of different junctions allows us to propose an optimized combination of carbon nanotubes and symmetries to obtain a controlled change in current of up to 75 %, which is a remarkable result and suggests the importance of further future work in these systems [1].

In the problem of transport in gold nanotubes, exposed in **Chapter 6**, we have been able to apply the knowledge gained through the investigation of carbon nanotube systems to these recently synthesized structures. As a result, we could provide an analytical formula for the conductance through these tubes. This formula yielded results matching perfectly those obtained numerically for more complex calculations, including all conduction electrons. Thanks to this analytical expression, a fast overview can be acquired over the trends of the conductance versus growing tube diameter or versus helicity. The use of two different approaches, one considering just a one-orbital tight-binding scheme and another regarding all conduction electrons, allowed us to discriminate the different contributions of the physics underlying this problem [2]. In these transport calculations, we had to deal with systems of very large sizes. This is due to the fact that gold nanotubes appeared with a finite chirality, so that the unit cells are correspondingly large, comprising several hundreds of atoms. We proved, though, that a good combination of different decimation techniques (see Sec. A.1.1 and Sec. A.2) can result in a very efficient computational tool.

The work on transport on the azobenzene molecules is presented in **Chapter 7**. Though the *trans-cis* isomerization of this molecule has been extensively investigated both theoretically and experimentally, these studies are basically related to the investigation of the isomerization properties of free azobenzene molecules but not directly to role of the molecule isomeric state and/or the molecule-electrode contact topology and chemistry in transport. Only recently Zhang *et al.* [223, 224] addressed the differences in transport of the two isomers of azobenzene but only for a fixed contact geometry. In our study, on the other hand, the use of nanotube-based electrodes, which induce a much stronger renormalization of molecular electronic states around the Fermi energy, allows for wider possibilities of conductance manipulation [3]. We have shown through a study of the $I-V$ characteristics in the linear response regime, that the *trans* state is better conducting than the metastable *cis* configuration, supporting the idea of considering the different conductances as an universal feature of the molecule independent of the contacts. This work provides evidence of the possibility of realization of a molecular rectifier with this system setup. Moreover, we have put forward

in this study the relevant role of the interface chemistry related to the linker groups, which turns out to have dramatic consequences. The oxygen charge states, associated to the NCOH linker group, can *e.g.* influence the spectral weight on the C-atom, which forms the bottleneck of the junction, and thus change the "transparency" of the contact. Furthermore, a new way to tailor the conductance of the device is suggested via the use chiralities of the tubes used as electrodes.

The work of this thesis opens further questions for the investigation of these systems and materials. For much of this work a further analysis on a higher voltage regime would be undoubtedly of interest and could show new interesting phenomena. An extension to non-equilibrium techniques through the Keldysh formalism is therefore planned and underway. In the specific case of transport through azobenzene, this could lead to the study of a possible switching mechanism driven by current, of undisputed experimental interest (private communication of José Ignacio Pascual). Moreover, since molecules are typically very flexible objects, to be able to operate molecular devices at room temperature and at finite voltage it is extremely important to understand the role of molecular vibrations on quantum transport. Thus investigation of interplay of correlation and vibration effects is a main theoretical challenge here, towards which the work of this thesis will continue.

Another key issue which demands still much investigation effort is the role of contacts. For studies of transport through a single molecule, where the importance of the linker and the electrodes have been shown, a systematic study of different linkers should be made to explore how the conductance of the junction can be chemically tuned. For the other systems under study the inclusion of more realistic contacts and their effects is a next goal ahead. Depending on the quality of the molecule/leads contacts one could observe a whole range of physical effects ranging from coherent transport to sequential tunneling (the Coulomb blockade effect).

Another challenge ahead in the azobenzene problem (of great importance for understanding the experiments being currently performed) is how to realize the *trans-cis* isomerization for a constrained geometry, which can feasible by using carbon nanotubes, in strong contrast to Au electrodes.

In the study of transport through gold nanotubes, an extension of the work to include the effects of inter-shell interaction in multi-walled nanotubes was initiated and should proceed, as interesting results are expected from it, and describes in a more realistic way the experimental observations.

Of special interest is the prosecution of the work started on the effect of a laser field on carbon nanotube junction, which still requires more detailed

analysis and further investigation. It is nevertheless a promising way of have external additional control in transport, and some experimental groups are also putting an effort in realizing such molecular setups.

Also still open is the investigation of transport in defective graphene stripes. The works in these systems have experienced an incredible boost in the last months since the experimental results in mono- and bi-layers of graphene appeared. Still most results referred to one-orbital approximations, which, we have seen, do not capture all the physics of these rich systems.

Conclusiones

En esta tesis prácticamente la totalidad de los miembros de la llamada familia de carbono han sido objeto de estudio: fulerenos, nanotubos incluyendo uniones de éstos, grafenos, moléculas orgánicas como el azobenceno. También han sido estudiados sistemas de nanotubos de oro. Para describir de forma apropiada el transporte cuántico en sistemas moleculares realistas se necesitan métodos fiables para caracterizar la estructura electrónica. Por este motivo se han empleado diversos métodos a lo largo de esta tesis, combinando la teoría del funcional de la densidad y aproximaciones de ligaduras fuertes con técnicas de funciones de Green y de decimación y el formalismo de transporte de Landauer. Estas herramientas permiten estudiar los sistemas moleculares anteriormente mencionados en todo el espectro energético, a diferencia de otros métodos de teoría de campos válidos sólo a bajas energías.

Se han empleado códigos de teoría del functional de la densidad (DFT) bien establecidos como GAUSSIAN o SIESTA, y otros basados en esta teoría como DFTB. También han sido de gran ayuda implementaciones de las técnicas de transporte basadas en funciones de Green para sistemas con transferencia de carga como gDFTB. A parte, he desarrollado un código propio que combina el uso de la aproximación de ligaduras fuertes incluyendo varios orbitales por átomo mediante el esquema propuesto por Slater-Koster con técnicas de funciones de Green. Este programa permite cálculos de conductancia y corriente para sistemas de varios cientos de átomos, como nanotubos con cierta quiralidad o de varias capas.

En uniones de nanotubos de carbono de tres terminales, que suponen un elemento indispensable a la hora de componer sistemas de alta densidad de circuitos, hemos demostrado, como se expone en el capítulo 4, que al utilizar uno de los brazos de la union para aplicar un voltaje puerta se puede controlar la corriente que circula por los otros dos brazos. Estos cambios en la corriente se deben a resonancias de tipo Fano que aparecen al interaccionar estados extendidos con estados asociados a los defectos estructurales que aparecen es estas uniones. A través de un examen completo de la densidad de estados

proyectada en la estructura de la unión se ha podido determinar el grado de localización/extensión de estos estados. Un estudio sistemático de las propiedades de transporte de diferentes uniones nos a permitido proponer una combinación óptima de los tipos de nanotubos empleados y de las simetrías de la unión para obtener un cambio controlado en la corriente de hasta el 75 % [1].

En el problema de transporte en nanotubos de oro tratado en el capítulo 6, hemos podido aplicar los conocimientos obtenidos de los estudios de nanotubos de carbono a estas estructuras recientemente descubiertas. Como resultado de este estudio hemos podido aportar una fórmula analítica para la conductancia en estos sistemas que permite evaluar de forma rápida esta propiedad y obtener una visión global de la dependencia de la conductancia a la energía de Fermi con el diámetro o la quiralidad de los tubos [2]. Los resultados de esta fórmula coinciden con los resultados numéricos de cálculos de ligaduras fuertes incluyendo todos los electrones de conducción. Para estos cálculos que implican matrices de grandes dimensiones, por el alto número de átomos en la celda unidad y por el número de orbitales que han de ser considerados por átomo, se han tenido que combinar diversas técnicas de decimación, explicadas en las secciones A.1.1 y A.2, que resultan de gran eficacia.

El trabajo sobre transporte en moléculas de azobenceno se presenta en el capítulo 7. Aunque la isomerización de esta molécula ha sido ampliamente estudiada tanto de forma experimental como teórica, estos estudios se refieren principalmente a las propiedades de esta molécula aislada pero no tanto su papel en transporte ni los efectos en éste de la topología de los contactos. Recientemente se han publicado estudios de transporte en esta molécula de Zhang *et al.* [223, 224] que investigan las propiedades en transporte de los dos isomeros de azobenceno pero en una geometría fija con electrodos de oro. En nuestros estudios se utilizan nanotubos de carbono como electrodos. Estos inducen una renormalización mucho más acentuada de los estados electrónicos en torno a la energía de Fermi, permitiendo una mayor manipulación de la conductancia [3]. A través de un estudio de las características $I-V$ en el régimen de respuesta lineal, se ha podido demostrar que el isomero *trans* es mejor conductor que el isomero metaestable *cis*, permitiendo el uso de esta estructura como interruptor eléctrico. Además se ha puesto de manifiesto la importancia de la química relacionada con los grupos que forman el contacto con los electrodos.

Este trabajo abre también muchas preguntas y está previsto la continuación de estos estudios ampliando las técnicas para poder incluir efectos como los correspondientes a sistemas fuera de equilibrio, así como el papel de las

vibraciones en el transporte, por nombrar algunos.

Appendix A

Decimation techniques

In order to deal with systems composed of a large number of atoms and keep efficiency in the computational calculations we make use of different *decimation* techniques. These are different implementations of renormalization-group methods [233] and provide a very computationally efficient tool to deal with such systems.

A.1 Dealing with semi-infinite leads

One task to face when calculating the transport properties of a system connected to semi-infinite periodic leads is the description of these leads without taking a huge amount of atoms into account, calculating the self-energies (see Eq. (2.62)) accounting for the effects of the semi-infinite leads which couple propagating electrons states to the heterostructure conductor. In a self-energy term, the semi-infinite matrix describing one lead has to be collapsed into a finite one.

One way to tackle this problem is to realize that the semi-infinite nature of the lead allows us to describe the self-energy term using the very self-energy in a self-consistent way. As depicted in Fig. A.1, the shaded portion of the matrix is equivalent to the whole matrix itself. The self-energy as in Eq. (2.62) is given by $\Sigma = \mathcal{H}^{\dagger}_{\text{Lead}-\text{Conductor}}\, g\, \mathcal{H}_{\text{Lead}-\text{Conductor}}$ where g is the Green function corresponding to the isolated lead. Due to the semi-infinity of the system one can absorb the self-energy into the first element of the lead described by $\mathcal{H}_{\text{surf}}$, and write

$$\Sigma = \mathcal{H}^{\dagger}_{\text{Lead}-\text{Conductor}}\, (E - \mathcal{H}_{\text{surf}} - \Sigma)^{-1}\, \mathcal{H}_{\text{Lead}-\text{Conductor}} \tag{A.1}$$

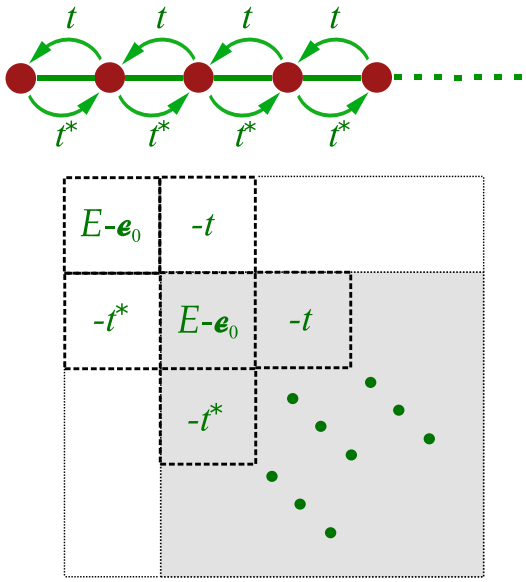

Figure A.1: Semi-infinite matrix $(E - \mathcal{H})$ of a lead consisting of an atomic one-dimensional chain in the space-basis nearest-neighbor approximation.

which is a self-consistent equation. For the trivial case of a one-dimensional lead with a constant potential ϵ_0 and only nearest-neighbor interactions given by t as illustrated in Fig. A.1, the self-energy is $\Sigma = |t|^2 \, g$, and from Eq. (A.1) one obtains the following self-consistent equation for g:

$$g = (E - \mathcal{H}_{\text{surf}} - \Sigma)^{-1} \tag{A.2}$$

that is,

$$g = \left(E - \epsilon_0 - |t|^2 \, g\right)^{-1} \tag{A.3}$$

or

$$-|t|^2 g^2 + (E - \epsilon_0)\, g - 1 = 0 \tag{A.4}$$

which of course can easily be solved exactly, given the expression for g:

$$g = \frac{E - \epsilon_0 \pm \sqrt{(E - \epsilon_0)^2 - 4\,|t|^2}}{2\,|t|^2}. \tag{A.5}$$

For more general cases, Eq. (A.1) is not exactly solvable and numerical procedures as iteration must be used [234]. It is then convenient to use other techniques such as decimation methods.

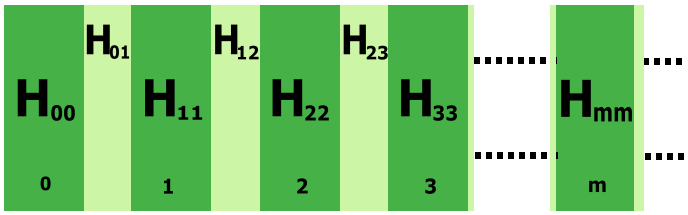

Figure A.2: Schematic setup of a semi-infinite system divided in an infinite set of slices or so-called principal layers, being the 0^{th} principal layer the surface layer. Each layer may contain any number of atoms and orbitals per atom and must be identical to the others, to which it connects only via nearest neighbor interactions.

We will apply different decimation techniques in order to obtain an effective Hamiltonian of an isolated surface without loosing the information of the original periodic semi-infinite system. The first technique corresponds to the one explained in the work of Guinea *et al.* (Ref. [235]), while the second one was proposed later by López-Sancho *et al.* (Ref. [236]). We will also discuss the differences between these techniques.

A.1.1 Following the technique proposed by Guinea *et al.*

The Green function $\mathcal{G}$ describing a periodic semi-infinite system of lattice electrons is defined by the following matrix equation:

$$(E\mathbb{1} - \mathcal{H})\,\mathcal{G} = \mathbb{1} \tag{A.6}$$

where E is the energy, $\mathcal{H}$ the Hamiltonian in a given basis. Since our system is periodic (necessary condition for the application of this method) we can always consider it as a set of a semi-infinite number of subsystems connected as shown in Fig. A.2. We can then define a so-called principal layer as one of these subsystems which may be built up by several crystal layers. We will firstly define these principal layers in such a way that interactions are only present between nearest neighbor layers. We can rewrite the previous matrix Eq. (A.6) in terms of block matrices as

$$\begin{pmatrix} E\mathbb{1}_{00}-\mathcal{H}_{00} & -\mathcal{H}_{01} & 0 & 0 & \dots \\ -\mathcal{H}_{10} & E\mathbb{1}_{11}-\mathcal{H}_{11} & -\mathcal{H}_{12} & 0 & \\ 0 & -\mathcal{H}_{21} & E\mathbb{1}_{22}-\mathcal{H}_{22} & -\mathcal{H}_{23} & \\ 0 & 0 & -\mathcal{H}_{32} & E\mathbb{1}_{33}-\mathcal{H}_{33} & \\ \vdots & & & & \ddots \end{pmatrix} \cdot \begin{pmatrix} \mathcal{G}_{00} & \mathcal{G}_{01} & \mathcal{G}_{02} & \mathcal{G}_{03} & \dots \\ \mathcal{G}_{10} & \mathcal{G}_{11} & \mathcal{G}_{12} & \mathcal{G}_{13} & \\ \mathcal{G}_{20} & \mathcal{G}_{21} & \mathcal{G}_{22} & \mathcal{G}_{23} & \\ \mathcal{G}_{30} & \mathcal{G}_{31} & \mathcal{G}_{32} & \mathcal{G}_{33} & \\ \vdots & & & & \ddots \end{pmatrix} = \mathbb{1} \tag{A.7}$$

where the subindices label the different principal layers, that is, $\mathcal{G}_{mn}$ is the Green function connecting the mth and nth layer of the system. We can separate the Dyson equations connecting the surface layer or 0th layer with the rest, obtaining

$$\begin{aligned} &(E\mathbb{1}-\mathcal{H}_{00})\,\mathcal{G}_{00}-\mathcal{H}_{01}\mathcal{G}_{10}=\mathbb{1},\\ &(E\mathbb{1}-\mathcal{H}_{11})\,\mathcal{G}_{10}-\mathcal{H}_{12}\mathcal{G}_{20}-\mathcal{H}_{10}\mathcal{G}_{00}=0,\\ &(E\mathbb{1}-\mathcal{H}_{22})\,\mathcal{G}_{20}-\mathcal{H}_{23}\mathcal{G}_{30}-\mathcal{H}_{21}\mathcal{G}_{10}=0,\\ &\dots\\ &(E\mathbb{1}-\mathcal{H}_{mm})\,\mathcal{G}_{m0}-\mathcal{H}_{m\,m+1}\mathcal{G}_{m+1\,0}-\mathcal{H}_{m\,m-1}\mathcal{G}_{m-1\,0}=0,\\ &\dots \end{aligned} \tag{A.8}$$

For an ideal structure, we can assume the Hamiltonians of the principal layers to be equal, that is $\mathcal{H}_{00}=\mathcal{H}_{11}=\mathcal{H}_{22}=\ldots=\mathcal{H}_{mm}\equiv\mathcal{H}_{\mathrm{PL}}$, which is the intra-slice matrix, and the assumption can be extended to the Hamiltonians for the coupling between the layers: $\mathcal{H}_{01}=\mathcal{H}_{12}=\ldots=\mathcal{H}_{m,m+1}\equiv\mathcal{H}_{\mathrm{coupl}}$ for the inter-slice matrix and $\mathcal{H}_{10}=\mathcal{H}_{21}=\ldots=\mathcal{H}_{m,m-1}\equiv\mathcal{H}^{\dagger}_{\mathrm{coupl}}$ as actually $\mathcal{H}_{10}=\mathcal{H}^{\dagger}_{01}$.

Thus we can rewrite the set of equations (A.8) as

$$\begin{aligned} &(E\mathbb{1}-\mathcal{H}_{\mathrm{PL}})\,\mathcal{G}_{00}-\mathcal{H}_{\mathrm{coupl}}\mathcal{G}_{10}=\mathbb{1}, && \nwarrow\\ &(E\mathbb{1}-\mathcal{H}_{\mathrm{PL}})\,\mathcal{G}_{10}-\mathcal{H}_{\mathrm{coupl}}\mathcal{G}_{20}-\mathcal{H}^{\dagger}_{\mathrm{coupl}}\mathcal{G}_{00}=0, && \rightarrow\ \mathcal{G}_{10}\\ &(E\mathbb{1}-\mathcal{H}_{\mathrm{PL}})\,\mathcal{G}_{20}-\mathcal{H}_{\mathrm{coupl}}\mathcal{G}_{30}-\mathcal{H}^{\dagger}_{\mathrm{coupl}}\mathcal{G}_{10}=0, && \swarrow\\ &(E\mathbb{1}-\mathcal{H}_{\mathrm{PL}})\,\mathcal{G}_{30}-\mathcal{H}_{\mathrm{coupl}}\mathcal{G}_{40}-\mathcal{H}^{\dagger}_{\mathrm{coupl}}\mathcal{G}_{20}=0, && \rightarrow\ \mathcal{G}_{30}\\ &(E\mathbb{1}-\mathcal{H}_{\mathrm{PL}})\,\mathcal{G}_{40}-\mathcal{H}_{\mathrm{coupl}}\mathcal{G}_{50}-\mathcal{H}^{\dagger}_{\mathrm{coupl}}\mathcal{G}_{30}=0, && \nwarrow\\ &\dots\\ &(E\mathbb{1}-\mathcal{H}_{\mathrm{PL}})\,\mathcal{G}_{m0}-\mathcal{H}_{\mathrm{coupl}}\mathcal{G}_{m+1\,0}-\mathcal{H}^{\dagger}_{\mathrm{coupl}}\mathcal{G}_{m-1,0}=0,\\ &\dots \end{aligned} \tag{A.9}$$

$$\text{with} \qquad \mathcal{G}_{10} = (E\mathbb{1} - \mathcal{H}_{\text{PL}})^{-1} \left(\mathcal{H}_{\text{coupl}} \mathcal{G}_{20} + \mathcal{H}_{\text{coupl}}^{\dagger} \mathcal{G}_{00} \right)$$
$$\mathcal{G}_{30} = (E\mathbb{1} - \mathcal{H}_{\text{PL}})^{-1} \left(\mathcal{H}_{\text{coupl}} \mathcal{G}_{40} + \mathcal{H}_{\text{coupl}}^{\dagger} \mathcal{G}_{20} \right)$$

where we resolve the explicit expression of the Green functions $\mathcal{G}_{m0}$ for odd m and substitute it into the neighbor equations for even m as schematically depicted in Eq. (A.9), getting rid of the odd layers. The resulting set of equations is therefore

$$\begin{aligned}
&W_s^{(1)} \mathcal{G}_{00} + \tau_1^{(1)} \mathcal{G}_{20} = \mathbb{1}, \\
&W_b^{(1)} \mathcal{G}_{20} + \tau_1^{(1)} \mathcal{G}_{40} + \tau_2^{(1)} \mathcal{G}_{00} = 0, \\
&W_b^{(1)} \mathcal{G}_{40} + \tau_1^{(1)} \mathcal{G}_{60} + \tau_2^{(1)} \mathcal{G}_{20} = 0, \\
&W_b^{(1)} \mathcal{G}_{60} + \tau_1^{(1)} \mathcal{G}_{80} + \tau_2^{(1)} \mathcal{G}_{40} = 0, \\
&\cdots \\
&W_b^{(1)} \mathcal{G}_{m0} + \tau_1^{(1)} \mathcal{G}_{m+2\,0} + \tau_2^{(1)} \mathcal{G}_{m-2,0} = 0, \\
&\cdots
\end{aligned} \tag{A.10}$$

where we have defined

$$\begin{aligned}
W_s^{(1)} &= (E\mathbb{1} - \mathcal{H}_{\text{PL}}) - \mathcal{H}_{\text{coupl}} (E\mathbb{1} - \mathcal{H}_{\text{PL}})^{-1} \mathcal{H}_{\text{coupl}}^{\dagger}, \\
W_b^{(1)} &= (E\mathbb{1} - \mathcal{H}_{\text{PL}}) - \mathcal{H}_{\text{coupl}} (E\mathbb{1} - \mathcal{H}_{\text{PL}})^{-1} \mathcal{H}_{\text{coupl}}^{\dagger} \\
&\quad - \mathcal{H}_{\text{coupl}}^{\dagger} (E\mathbb{1} - \mathcal{H}_{\text{PL}})^{-1} \mathcal{H}_{\text{coupl}}, \\
\tau_1^{(1)} &= -\mathcal{H}_{\text{coupl}} (E\mathbb{1} - \mathcal{H}_{\text{PL}})^{-1} \mathcal{H}_{\text{coupl}}, \\
\tau_2^{(1)} &= -\mathcal{H}_{\text{coupl}}^{\dagger} (E\mathbb{1} - \mathcal{H}_{\text{PL}})^{-1} \mathcal{H}_{\text{coupl}}^{\dagger}.
\end{aligned} \tag{A.11}$$

We have actually recovered Eq. (A.9) with new renormalized parameters. The first equation in A.10 connects now the renormalized 0th and 2nd layers and τ_1 and τ_2 are giving the effective interaction between them, while W_s is the effective matrix of $(E\mathbb{1} - \mathcal{H})$ for layer 0. We proceed in successive steps by eliminating the Green functions of the next alternating layers, which will now be $\mathcal{G}_{2n\,0}$ for odd n. One can easily see that this procedure can be iterated, obtaining at each step the corresponding renormalized W_b, W_b, τ_1, τ_2 matrices relating to the those of the previous step in the following way:

$$\begin{aligned}
W_s^{(i)} &= W_s^{(i-1)} - \tau_1^{(i-1)} \left(W_b^{(i-1)} \right)^{-1} \tau_2^{(i-1)}, \\
W_b^{(i)} &= W_b^{(i-1)} - \tau_1^{(i-1)} \left(W_b^{(i-1)} \right)^{-1} \tau_2^{(i-1)} \\
&\quad - \tau_2^{(i-1)} \left(W_b^{(i-1)} \right)^{-1} \tau_1^{(i-1)} \\
\tau_1^{(i)} &= -\tau_1^{(i-1)} \left(W_b^{(i-1)} \right)^{-1} \tau_1^{(i-1)} \\
\tau_2^{(i)} &= -\tau_2^{(i-1)} \left(W_b^{(i-1)} \right)^{-1} \tau_2^{(i-1)}
\end{aligned} \tag{A.12}$$

and the corresponding equations describing our system take the form

$$\begin{aligned} &W_s^{(i)}\mathcal{G}_{00} + \tau_1^{(i)}\mathcal{G}_{2^i 0} = \mathbb{1}, \\ &\cdots \\ &W_b^{(i)}\mathcal{G}_{2^i n\,0} + \tau_1^{(i)}\mathcal{G}_{2^i(n+1)\,0} + \tau_2^{(i)}\mathcal{G}_{2^i(n-1),0} = 0, \\ &\cdots \end{aligned} \tag{A.13}$$

for positive integer values of n.

After the ith step τ_1 and τ_2 gives the effective interaction between layers 0 and 2^i having renormalized out those in between. We can thus expect both τ_1 and τ_2 to decrease for any energy value with increasing number of steps, becoming quickly negligible as the layers they effectively connect are just too far apart. The surface and bulk layers are then practically decoupled, and we are left with the equations:

$$\begin{aligned} &W_s^{(N)}\mathcal{G}_{00} = \mathbb{1}, \\ &W_b^{(N)}\mathcal{G}_{2^N n\,0} = 0, \end{aligned} \tag{A.14}$$

where N is the number of steps necessary to achieve convergence in the iteration process. The criterium for reaching convergence is set with an arbitrarily small parameter δ which determines the required precision, imposing $\tau_1^N, \tau_2^N < \delta$. The Green function for the surface is therefore well described by

$$\mathcal{G}_{00} = \left(W_s^{(N)}\right)^{-1}. \tag{A.15}$$

It is straightforward to see that the Green function for the dual surface, *i.e.*, for the 0th layer of the complementary chain, is obtained by exchanging τ_1 with τ_2. The Green function of a bulk layer is given by

$$\mathcal{G}_{\text{bulk}} = \left(W_b^{(N)}\right)^{-1} \tag{A.16}$$

result that can be also obtained repeating the same decimation process but starting from an infinite system:

$$\begin{aligned} &\cdots \\ &(E\mathbb{1} - \mathcal{H}_{\text{PL}})\,\mathcal{G}_{-10} - \mathcal{H}_{\text{coupl}}\mathcal{G}_{00} - \mathcal{H}_{\text{coupl}}^{\dagger}\mathcal{G}_{-20} = 0, \\ &(E\mathbb{1} - \mathcal{H}_{\text{PL}})\,\mathcal{G}_{00} - \mathcal{H}_{\text{coupl}}\mathcal{G}_{10} - \mathcal{H}_{\text{coupl}}^{\dagger}\mathcal{G}_{-10} = \mathbb{1}, \\ &(E\mathbb{1} - \mathcal{H}_{\text{PL}})\,\mathcal{G}_{10} - \mathcal{H}_{\text{coupl}}\mathcal{G}_{20} - \mathcal{H}_{\text{coupl}}^{\dagger}\mathcal{G}_{00} = 0, \\ &\cdots \end{aligned} \tag{A.17}$$

As the number of renormalized layers grows exponentially with the number of steps the convergence of this decimation process is very quick and can save precious computer time.

If instead of semi-infinite nanotubes we have to deal with systems infinite in the direction(s) parallel to the surface (the bulk periodicity parallel to the surface is preserved by all atomic planes right up to the surface), the same decimation technique is still valid. We just have to do as a first step a change of basis, in order to work with a fixed momentum $\mathbf{k}$. Due to the symmetry in the parallel directions, the Hamiltonian commutes with translational operators in these directions and the eigenstates $\Psi(\mathbf{k}_{\parallel}, E)$ will have a well-defined energy and momentum, which allows us to treat the problem as a sum of decoupled problems for each $\mathbf{k}_{\parallel}$. We will thus start the iteration process from the Green function matrix equation:

$$\left[E\mathbb{1} - \mathcal{H}\left(\mathbf{k}_{\parallel}\right)\right] \mathcal{G}\left(\mathbf{k}_{\parallel}\right) = \mathbb{1} \tag{A.18}$$

instead of with Eq. (A.6) in a localized basis. In a last step the effective surface Hamiltonian in the real space is obtained by an appropriate Fourier analysis.

As is well known, in all the matrix-transfer methods a finite broadening must be introduced in the energy in order to get meaningful results. This amounts to substituting E by $E + i\eta$ where η is related to the degree of accuracy requested in the calculation. The value of η we usually assumed throughout the different problems studied during this thesis is 10^{-5}.

At last it is convenient to remark that this decimation method has no restriction to the extension of the interactions as long as they extend throughout a finite range. If, for instance, we want to consider interactions up to second-neighbor slices, we can just redefine our principal layer as composed of two of these slices instead of one, returning to the definition described above of nearest-neighbor interactions. Another alternative would be to derive again the decimation procedure including second nearest-neighbor interactions as actually described in the original paper [235].

Decimation with the overlap matrix

If the tight-binding approach includes overlap matrix elements between the localized orbitals, we can easily extend the previous method by starting from the corrected equation:

$$(E\mathcal{S} - \mathcal{H})\,\mathcal{G} = \mathbb{1} \tag{A.19}$$

If we define our principal layers again as being identical to each other and interacting and overlapping only at the nearest-neighbor level, we obtain the following set of equations:

$$\begin{aligned}
&(E\mathcal{S}_{\mathrm{PL}} - \mathcal{H}_{\mathrm{PL}})\,\mathcal{G}_{00} + (E\mathcal{S}_{\mathrm{coupl}} - \mathcal{H}_{\mathrm{coupl}})\,\mathcal{G}_{10} = \mathbb{1},\\
&(E\mathcal{S}_{\mathrm{PL}} - \mathcal{H}_{\mathrm{PL}})\,\mathcal{G}_{10} + (E\mathcal{S}_{\mathrm{coupl}} - \mathcal{H}_{\mathrm{coupl}})\,\mathcal{G}_{20} + \left(E\mathcal{S}^{\dagger}_{\mathrm{coupl}} - \mathcal{H}^{\dagger}_{\mathrm{coupl}}\right)\mathcal{G}_{00} = 0,\\
&(E\mathcal{S}_{\mathrm{PL}} - \mathcal{H}_{\mathrm{PL}})\,\mathcal{G}_{20} + (E\mathcal{S}_{\mathrm{coupl}} - \mathcal{H}_{\mathrm{coupl}})\,\mathcal{G}_{30} + \left(E\mathcal{S}^{\dagger}_{\mathrm{coupl}} - \mathcal{H}^{\dagger}_{\mathrm{coupl}}\right)\mathcal{G}_{10} = 0,\\
&\dots
\end{aligned} \tag{A.20}$$

Going through the same elimination procedure as before, we will arrive to the same recursive set of equations described by A.13 with the same definitions given by A.12, differing just at the moment of setting the initial values for the iteration:

$$\begin{aligned}
W_s^{(1)} &= (E\mathcal{S}_{\mathrm{PL}} - \mathcal{H}_{\mathrm{PL}})\\
&\quad + (E\mathcal{S}_{\mathrm{coupl}} - \mathcal{H}_{\mathrm{coupl}})\,(E\mathcal{S}_{\mathrm{PL}} - \mathcal{H}_{\mathrm{PL}})^{-1}\left(E\mathcal{S}^{\dagger}_{\mathrm{coupl}} - \mathcal{H}^{\dagger}_{\mathrm{coupl}}\right),\\
W_b^{(1)} &= (E\mathcal{S}_{\mathrm{PL}} - \mathcal{H}_{\mathrm{PL}})\\
&\quad + (E\mathcal{S}_{\mathrm{coupl}} - \mathcal{H}_{\mathrm{coupl}})\,(E\mathcal{S}_{\mathrm{PL}} - \mathcal{H}_{\mathrm{PL}})^{-1}\left(E\mathcal{S}^{\dagger}_{\mathrm{coupl}} - \mathcal{H}^{\dagger}_{\mathrm{coupl}}\right)\\
&\quad + \left(E\mathcal{S}^{\dagger}_{\mathrm{coupl}} - \mathcal{H}^{\dagger}_{\mathrm{coupl}}\right)(E\mathcal{S}_{\mathrm{PL}} - \mathcal{H}_{\mathrm{PL}})^{-1}\,(E\mathcal{S}_{\mathrm{coupl}} - \mathcal{H}_{\mathrm{coupl}}),\\
\tau_1^{(1)} &= (E\mathcal{S}_{\mathrm{coupl}} - \mathcal{H}_{\mathrm{coupl}})\,(E\mathcal{S}_{\mathrm{PL}} - \mathcal{H}_{\mathrm{PL}})^{-1}\,(E\mathcal{S}_{\mathrm{coupl}} - \mathcal{H}_{\mathrm{coupl}}),\\
\tau_2^{(1)} &= \left(E\mathcal{S}^{\dagger}_{\mathrm{coupl}} - \mathcal{H}^{\dagger}_{\mathrm{coupl}}\right)(E\mathcal{S}_{\mathrm{PL}} - \mathcal{H}_{\mathrm{PL}})^{-1}\left(E\mathcal{S}^{\dagger}_{\mathrm{coupl}} - \mathcal{H}^{\dagger}_{\mathrm{coupl}}\right).
\end{aligned} \tag{A.21}$$

A.1.2 Following the technique proposed by López-Sancho *et al.*

We will now see another equally valid approach to the problem of a semi-infinite crystal which is actually a *transfer-matrix* approach. We describe the system in the same way as before as a stack of identical principal layers with nearest neighbor interaction. Taking the matrix elements of $(E\mathbb{1} - \mathcal{H})\,\mathcal{G} = \mathbb{1}$ coupling to the surface layer, we obtain the usual chain of equations given by A.8. We make again the assumption (which is simplifying the equations though not being essential) that the surface layer is identical to the rest, *i.e.*,

an ideal surface and we can rewrite this chain of equations as in Eq. (A.9) like

$$\begin{aligned}
(E\mathbb{1} - \mathcal{H}_{\mathrm{PL}})\,\mathcal{G}_{00} &= \mathbb{1} + \mathcal{H}_{\mathrm{coupl}}\mathcal{G}_{10}, \\
(E\mathbb{1} - \mathcal{H}_{\mathrm{PL}})\,\mathcal{G}_{10} &= \mathcal{H}^{\dagger}_{\mathrm{coupl}}\mathcal{G}_{00} + \mathcal{H}_{\mathrm{coupl}}\mathcal{G}_{20}, \\
(E\mathbb{1} - \mathcal{H}_{\mathrm{PL}})\,\mathcal{G}_{20} &= \mathcal{H}^{\dagger}_{\mathrm{coupl}}\mathcal{G}_{10} + \mathcal{H}_{\mathrm{coupl}}\mathcal{G}_{30}, \\
&\dots \\
(E\mathbb{1} - \mathcal{H}_{\mathrm{PL}})\,\mathcal{G}_{m0} &= \mathcal{H}^{\dagger}_{\mathrm{coupl}}\mathcal{G}_{m-1,0} + \mathcal{H}_{\mathrm{coupl}}\mathcal{G}_{m+10}, \\
&\dots
\end{aligned} \tag{A.22}$$

The general term is then

$$\begin{aligned}
\mathcal{G}_{m0} &= (E\mathbb{1} - \mathcal{H}_{\mathrm{PL}})^{-1}\left(\mathcal{H}^{\dagger}_{\mathrm{coupl}}\mathcal{G}_{m-10} + \mathcal{H}_{\mathrm{coupl}}\mathcal{G}_{m+10}\right) \\
&= t_0\mathcal{G}_{m-10} + \tilde{t}_0\mathcal{G}_{m+10}
\end{aligned} \tag{A.23}$$

with $t_0 = (E\mathbb{1} - \mathcal{H}_{\mathrm{PL}})^{-1}\,\mathcal{H}^{\dagger}_{\mathrm{coupl}}$ and $\tilde{t}_0 = (E\mathbb{1} - \mathcal{H}_{\mathrm{PL}})^{-1}\,\mathcal{H}_{\mathrm{coupl}}$.

Applying Eq. (A.23) again to $\mathcal{G}_{m-10}$ and $\mathcal{G}_{m+10}$, we obtain

$$\begin{aligned}
\mathcal{G}_{m0} &= t_0\left(t_0\mathcal{G}_{m-20} + \tilde{t}_0\mathcal{G}_{m0}\right) + \tilde{t}_0\left(t_0\mathcal{G}_{m0} + \tilde{t}_0\mathcal{G}_{m+20}\right) \\
&= t_1\mathcal{G}_{m-20} + \tilde{t}_1\mathcal{G}_{m+20}
\end{aligned} \tag{A.24}$$

with $m \geq 2$ and where we define $t_1 = (\mathbb{1} - t_0\tilde{t}_0 - \tilde{t}_0 t_0)^{-1}\,t_0^2$ and $\tilde{t}_1 = (\mathbb{1} - t_0\tilde{t}_0 - \tilde{t}_0 t_0)^{-1}\,\tilde{t}_0^2$.

Since both equations, Eq. (A.23) and Eq. (A.24), are isomorphic, the process can be repeated iteratively. After i iterations we get

$$\mathcal{G}_{m0} = t_i\mathcal{G}_{m-2^i 0} + \tilde{t}_i\mathcal{G}_{n+2^i 0}, \quad m \geq 2^i \tag{A.25}$$

with

$$\begin{aligned}
t_i &= (\mathbb{1} - t_{i-1}\tilde{t}_{i-1} - \tilde{t}_{i-1}t_{i-1})^{-1}\,t_{i-1}^2, \\
\tilde{t}_i &= (\mathbb{1} - t_{i-1}\tilde{t}_{i-1} - \tilde{t}_{i-1}t_{i-1})^{-1}\,\tilde{t}_{i-1}^2
\end{aligned}$$

By replacing m in the general equation of the iteration step N with 2^N, we obtain the following system of equations

$$\begin{aligned}
\mathcal{G}_{10} &= t_0\mathcal{G}_{00} + \tilde{t}_0\mathcal{G}_{20}, \\
\mathcal{G}_{20} &= t_1\mathcal{G}_{00} + \tilde{t}_1\mathcal{G}_{40}, \\
&\dots \\
\mathcal{G}_{2^N 0} &= t_N\mathcal{G}_{00} + \tilde{t}_N\mathcal{G}_{2(N+1)\,0},
\end{aligned} \tag{A.26}$$

and by successive substitution from the last equation up to the first we obtain

$$\begin{aligned}\mathcal{G}_{10} &= t_0\mathcal{G}_{00} + \tilde{t}_0\left(t_1\mathcal{G}_{00} + \tilde{t}_1\mathcal{G}_{40}\right)\\ &= \left(t_0 + \tilde{t}_0 t_1\right)\mathcal{G}_{00} + \tilde{t}_0\tilde{t}_1\left(t_2\mathcal{G}_{00} + \tilde{t}_2\mathcal{G}_{80}\right)\\ &= \ldots\\ &= \left(t_0 + \tilde{t}_0 t_1 + \tilde{t}_0\tilde{t}_1 t_2 + \ldots + \tilde{t}_0\tilde{t}_1\tilde{t}_2\ldots\tilde{t}_{N-1}t_N\right)\mathcal{G}_{00} + \tilde{t}_0\ldots\tilde{t}_N\mathcal{G}_{2^{N+1}0}.\end{aligned} \tag{A.27}$$

N is the iteration step after which convergence is reached, which means that the number of iterations is such that $t_{N+1}, \tilde{t}_{N-1} < \delta$ is fulfilled, that is, the required precision is achieved, where the cut-off δ may be in principle chosen arbitrarily small. In this case, in the next iteration step we would have $\mathcal{G}_{2^{N+1}0} \simeq 0$, which is the reason of obtaining a finite number of equations in the set of Eq. (A.26).

We are left then with only the first term in Eq. (A.27), and we can define the coefficient relating the Green functions as the transfer matrix T, which incorporates the effects of 2^N layers:

$$T = t_0 + \tilde{t}_0 t_1 + \tilde{t}_0\tilde{t}_1 t_2 + \ldots + \tilde{t}_0\tilde{t}_1\tilde{t}_2\ldots\tilde{t}_{N-1}t_N, \tag{A.28}$$

where the Nth term is of order 2^{N+1} in $\mathcal{H}_{\text{coupl}}$ and should get vanishingly small rapidly.

In an analogous way,

$$\tilde{T} = \tilde{t}_0 + t_0\tilde{t}_1 + t_0 t_1\tilde{t}_2 + \ldots + t_0 t_1 t_2\ldots t_{N-1}\tilde{t}_N. \tag{A.29}$$

We can now write the Green function of a certain layer in terms of the Green function of the preceding (or following) layer, through the introduced transfer matrices T, $\tilde{T}$:

$$\mathcal{G}_{10} = T\mathcal{G}_{00} \tag{A.30}$$

$$\mathcal{G}_{00} = \tilde{T}\mathcal{G}_{10} \tag{A.31}$$

One can easily see that T is indeed a transfer matrix by substituting Eq. (A.30) in the first line of Eq. (A.22):

$$\left(E\mathbb{1} - \mathcal{H}_{\text{PL}}\right)\mathcal{G}_{00} = \mathbb{1} + \mathcal{H}_{\text{coupl}}T\mathcal{G}_{00}, \tag{A.32}$$

so that

$$\mathcal{G}_{00} = \left(E\mathbb{1} - \mathcal{H}_{\text{PL}} - \mathcal{H}_{\text{coupl}}T\right)^{-1}. \tag{A.33}$$

In particular, it can be concluded from Eq. (A.33), and considering Eq. (A.1), that the expression of the self-energy of the semi-infinite lead is given by:

$$\Sigma = \mathcal{H}_{\text{coupl}} T. \tag{A.34}$$

Thus the general formula of the Green function for a system consisting of a conductor composed of one principal layer between two identical semi-infinite leads is

$$\mathcal{G}(E) = \left(E - \mathcal{H}_{\text{PL}} - \Sigma_{\text{R}} - \Sigma_{\text{L}}\right)^{-1}, \tag{A.35}$$

with

$$\Sigma_{\text{R}} = \mathcal{H}_{\text{coupl}} T, \quad \Sigma_{\text{L}} = \mathcal{H}^{\dagger}_{\text{coupl}} \tilde{T}. \tag{A.36}$$

Decimation with the overlap matrix

If again we are dealing with non-negligible overlap matrix elements, we have to rewrite the equations of this decimation technique, starting once more from Eq. (A.19). Eq. (A.23) will be now

$$\begin{aligned} \mathcal{G}_{m0} &= \left(E\mathcal{S}_{\text{PL}} - \mathcal{H}_{\text{PL}}\right)^{-1} \\ &\quad \cdot \left[- \left(E\mathcal{S}^{\dagger}_{\text{coupl}} - \mathcal{H}^{\dagger}_{\text{coupl}}\right) \mathcal{G}_{m-1\,0} - \left(E\mathcal{S}_{\text{coupl}} - \mathcal{H}_{\text{coupl}}\right) \mathcal{G}_{m+1\,0} \right] \\ &= t_0 \mathcal{G}_{m-1\,0} + \tilde{t}_0 \mathcal{G}_{m+1\,0} \end{aligned} \tag{A.37}$$

with

$$\begin{aligned} t_0 &= -\left(E\mathcal{S}_{\text{PL}} - \mathcal{H}_{\text{PL}}\right)^{-1} \left(E\mathcal{S}^{\dagger}_{\text{coupl}} - \mathcal{H}^{\dagger}_{\text{coupl}}\right) \\ \tilde{t}_0 &= -\left(E\mathcal{S}_{\text{PL}} - \mathcal{H}_{\text{PL}}\right)^{-1} \left(E\mathcal{S}_{\text{coupl}} - \mathcal{H}_{\text{coupl}}\right). \end{aligned}$$

We substitute this equation in Eq. (A.37) for $\mathcal{G}_{m-1\,0}$ and $\mathcal{G}_{m+1\,0}$, obtaining an isomorphic one which allows us to iterate the process, having for the ith step the same expression as in Eq. (A.25), and thus

$$\begin{aligned} \mathcal{G}_{10} &\simeq \left(t_0 + \tilde{t}_0 t_1 + \tilde{t}_0 \tilde{t}_1 t_2 + \ldots + \tilde{t}_0 \tilde{t}_1 \ldots \tilde{t}_{N-1} t_N\right) \mathcal{G}_{00} \\ &= T \mathcal{G}_{00} \end{aligned} \tag{A.38}$$

Equivalently to Eq. (A.33), we have now the following expression for the surface Green function:

$$\mathcal{G}_{00} = \left[\left(E\mathcal{S}_{\text{PL}} - \mathcal{H}_{\text{PL}}\right) + \left(E\mathcal{S}_{\text{coupl}} - \mathcal{H}_{\text{coupl}}\right) T\right]^{-1}. \tag{A.39}$$

That is, the expressions for the Green functions of a system described by a general nonorthogonal localized-orbital Hamiltonian can be obtained from the expressions for the case of an orthogonal basis by making the substitutions:

$$\begin{aligned} &(E - \mathcal{H}_{\mathrm{PL}}) \longrightarrow (E\mathcal{S}_{\mathrm{PL}} - \mathcal{H}_{\mathrm{PL}})\,, \\ &\mathcal{H}_{\mathrm{coupl}} \longrightarrow -\left(E\mathcal{S}_{\mathrm{coupl}} - \mathcal{H}_{\mathrm{coupl}}\right) \end{aligned} \tag{A.40}$$

as also seen in Sec. A.1.1.

A.1.3 Differences between both techniques

Both methods presented above are valid and efficient approaches for the calculation of the Green function terms for an semi-infinite periodic system. These methods are applicable to any general Hamiltonian that can be described within a localized-orbital basis. Their formulations allow to fully consider the complete microscopic structure of the semi-infinite leads with a very limited computational cost. Other iterative methods for the computation of the Green function at the surface layer have to be applied with care in the neighborhood of singularities of $\mathcal{G}$ and require a big number of iterations before reaching convergence. That is the case of other "effective field" or transfer matrix approaches [237, 238, 239, 240] which, as such, give the surface Green function by the equation

$$\mathcal{G}_{00} = \left(E - \mathcal{H}_{\mathrm{PL}} - \mathcal{H}_{\mathrm{coupl}} T\left(E\right)\right)^{-1} \tag{A.41}$$

where the transfer matrix T is given by

$$T\left(E\right) = \left(E - \mathcal{H}_{\mathrm{PL}} - \mathcal{H}_{\mathrm{coupl}} T\left(E\right)\right)^{-1} \mathcal{H}_{\mathrm{coupl}}^{\dagger}\,, \tag{A.42}$$

which is then calculated via an iteration process until self-consistency is achieved. This involves many iteration cycles (an average of ~ 50), particulary near singularities. In contrast, the previous methods, as described in Sec. A.1.1 and Sec. A.1.2, require an average of ~ 20 cycles for much stronger requirements: a cutoff of 10^{-20} and an added imaginary part of $\eta = 10^{-5}$. Both allow for the inclusion of 2^N layers after N iterations (the effective interlayer interactions becoming vanishingly small after a few iterations), and for the simultaneous calculation of the Green functions for both the 'normal' and 'dual' surface and for the bulk layer, and in principle allow the use of an imaginary part η as small as one wishes. In practice though, making η very small can lead to numerical errors (of course depending on the computer). The occurrence of these errors is higher and for the López

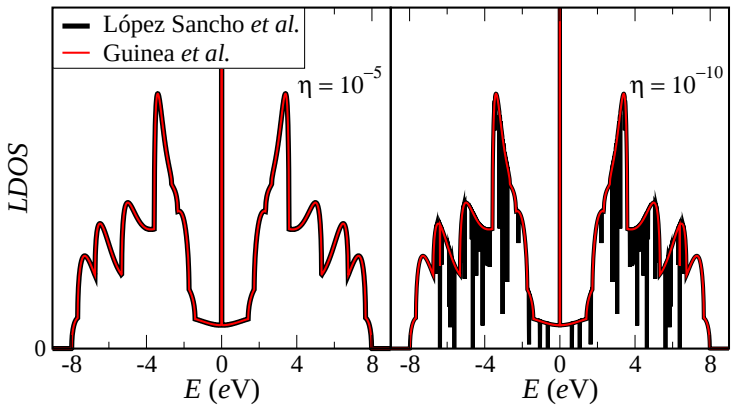

Figure A.3: Density of states of the semi-infinite (9,0) CNT projected on the surface unit cell, calculated both with the algorithm proposed by Guinea *et al.* (Sec. A.1.1) and with that proposed by López Sancho *et al.* (Sec. A.1.2). The calculation follows a one-electron tight-binding approximation with only nearest neighbor interactions. The parameters used are $2.66\,e$V for the hopping interactions and $0\,e$V for the on-site energies, lying thus the Fermi energy at $0\,e$V. The thin peak at the Fermi energy corresponds to the localized surface state discussed in Sec. B. The plot on the left is calculated adding an imaginary part to the energy $i\eta$ with $\eta = 10^{-5}$, while for the graph on the right a value of $\eta = 10^{-10}$ has been used.

Sancho *et al.* algorithm (Sec. A.1.2), as can be seen in the right-hand graph of Fig. A.3. It also is slightly more time-consuming.

We thus conclude that the decimation scheme outlined in Sec. A.1.1 proved to us to meet highest computational accuracy. The very similar algorithm exposed in Sec. A.1.2 is, due to the mathematical operations involved, a bit slower and more dependent on the computer accuracy. Nevertheless for values of $\eta = 10^{-3}$ or even $\eta = 10^{-5}$, both work perfectly well and the latter has indeed been extensively applied to CNT calculations, see for instance Ref. [241].

A.2 Dealing with large unit cells

As we have seen during this thesis, numerical methods have played an important role in these studies. In order to gain more efficiency performing the calculations and to make feasible the computation of transport properties through large systems, we employ yet another kind of decimation algorithm, which allows us to reduce the effective size of the central region of our sys-

tems. This method is especially useful for tight binding Hamiltonians $\mathcal{H}$ in which one has finite matrix elements between only a few neighboring sites and where the Green function is not required at every position in the system. This decimation method is an efficient way of performing Gaussian elimination in such systems. As in other decimation techniques one sublattice of a large (in principle, even infinite) system is removed with the definition of effective interactions on the remaining sublattice which is then subjected to the same process. This technique has been used in several works as for instance in Ref. [242, 243, 244]. This method is based on Löwdin's technique [245] (see also [246] in [247]) for the determination of eigenvalues of a secular matrix from the diagonalization of a smaller one. This method is exact if carried to all orders and, moreover, this does not have to be done by the summation of the Löwdin perturbation series but rather by simply folding back the matrix one row and column at a time, as describe below. Though this procedure has been referred to as truncation of the Hamiltonian matrix, it is more appropriate to apply the expression "folding down of the matrix", as the effects of the excluded parts of the Hamiltonian have been folded into the smaller remaining effective Hamiltonian.

Let us start again from the defining equation for the Green function $\mathcal{G}$, Eq. (A.6), but rewriting it as

$$\mathcal{A}(E)\,\mathcal{G}(E) = \mathbb{1} \tag{A.43}$$

by defining $\mathcal{A} = E\mathbb{1} - \mathcal{H}$. The element ik of this matrix equation is

$$[\mathcal{A}\cdot\mathcal{G}]_{ik} = \sum_{j=1}^{N} \mathcal{A}_{ij}\mathcal{G}_{jk} = \delta_{ik} \tag{A.44}$$

or equivalently

$$\sum_{j=1}^{N-1} \mathcal{A}_{ij}\mathcal{G}_{jk} + \mathcal{A}_{iN}\mathcal{G}_{Nk} = \delta_{ik} \tag{A.45}$$

where N is the dimension of the Hamiltonian $\mathcal{H}$. By choosing $i = N$ we obtain for the expression of $\mathcal{G}_{Nk}(E)$:

$$\mathcal{G}_{Nk} = \frac{1}{\mathcal{A}_{NN}}\delta_{Nk} - \sum_{j=1}^{N-1} \frac{\mathcal{A}_{Nj}\mathcal{G}_{jk}}{\mathcal{A}_{NN}} \tag{A.46}$$

which we can substitute in Eq. (A.45), eliminating thus $\mathcal{G}_{Nk}$:

$$\sum_{j=1}^{N-1} \mathcal{A}_{ij}\mathcal{G}_{jk} + \frac{\mathcal{A}_{iN}}{\mathcal{A}_{NN}}\delta_{Nk} - \sum_{j=1}^{N-1} \frac{\mathcal{A}_{iN}\mathcal{A}_{Nj}}{\mathcal{A}_{NN}}\mathcal{G}_{jk} = \delta_{ik}. \tag{A.47}$$

We are left with a system of equations of the variables $\mathcal{G}_{ik}$ with $i = 1, \ldots, N-1$ and $k = 1, \ldots, N-1$, and thus the second term of the left hand side of Eq. (A.47) vanishes. The variables $\mathcal{G}_{Nk}$ have been explicitly eliminated and thus the orbital or basis vector associated with N has been renormalized out. The remaining system of equations

$$\sum_{j=1}^{N-1} \left[\mathcal{A}_{ij} - \frac{\mathcal{A}_{iN}\mathcal{A}_{Nj}}{\mathcal{A}_{NN}} \right] \mathcal{G}_{jk} = \delta_{ik} \tag{A.48}$$

is equivalent to Eq. (A.44) with an effective matrix $\mathcal{A}^{(1)}$, instead of $\mathcal{A}$, describing a system of $N-1$ sites,

$$\sum_{j=1}^{N-1} \mathcal{A}^{(1)}_{ij} \mathcal{G}_{jk} = \delta_{ik} \tag{A.49}$$

where

$$\mathcal{A}^{(1)}_{ij} = \mathcal{A}_{ij} - \frac{\mathcal{A}_{iN}\mathcal{A}_{Nj}}{\mathcal{A}_{NN}}. \tag{A.50}$$

In this way, by substituting the definition of $\mathcal{A}$, it is straightforward to obtain the expression of the effective Hamiltonian $\mathcal{H}(E)$ with matrix elements

$$\mathcal{H}^{(1)}_{ij} = \mathcal{H}_{ij} + \frac{\mathcal{H}_{iN}\mathcal{H}_{Nj}}{E - \mathcal{H}_{NN}}. \tag{A.51}$$

where we have again used the fact that $\delta_{iN} = \delta_{Nj} = 0$, as i and j are not reaching the value N in this effective system.

The Green function corresponding to this effective Hamiltonian is identical to that of the full Hamiltonian on all non-decimated sites. Moreover, the eigenvalues of the reduced matrix give the eigenvalues of the original matrix (see for instance Ref. [242]). We can repeat this process, eliminating successively and one by one different sites, until we just remain with the "relevant" sites. If we next eliminate site or basis vector M we may write

$$\mathcal{H}^{(2)}_{ij} = \mathcal{H}^{(1)}_{ij} + \frac{\mathcal{H}^{(1)}_{iM}\mathcal{H}^{(1)}_{Mj}}{E - \mathcal{H}^{(1)}_{MM}}. \tag{A.52}$$

where $i, j \neq N, M$. We can thus reduce the scattering region, using this decimation technique, to a Hamiltonian for only those sites with finite matrix elements between themselves and the leads. This process can make our

system Hamiltonian much smaller, hence resulting in an important amount of saved computational time. Even if starting from a Hamiltonian with only nearest neighbor interactions, it is clear from Eq. (A.52) that after decimation the renormalized Hamiltonians will in general contain long-range interactions and hence, not only interactions between nearest neighbor pairs of sites must be stored. One further advantage of this method is that, when applied to very large systems, by studying the asymptotic behavior of the renormalized interactions one can discriminate between localized and extended states. This is due to the fact that the off-diagonal matrix elements of the renormalized Hamiltonians are expected to scale to zero in the localized regime.

Appendix B

Surface states in Carbon nanotubes

To use semi-infinite carbon nanotubes as a model for nanoelectrodes, it is important to gain insight into their properties as semi-infinite systems. For the quantum conductivity calculations we use the well-known Landauer expression and for the transmissions the Green function techniques as explained in Chap. 2, with tight-binding Hamiltonians for the systems. This has become a common choice in many theoretical investigation works, as it provides a good description, keeping its simplicity.

We will first deal with the semi-infinite leads alone (Fig. B.1 (a) and (b)), and follow up addressing the influence of surface and defect states of these leads on the transport across a molecular wire sandwiched between two of these semi-infinite CNTs (Fig. B.1 (c) and (d)). We will limit ourselves to the case of a single contact between the molecular bridge and the electrode, that is, the case where one single atom of the outer surface of the lead contacts the molecular wire. For this situation it has been shown that the conductance spectra exhibit quantum features of both the molecule and the electrode, whereas for the multiple contact case the quantum features of the CNT, in which we are interested, disappear [248, 249]. Experimental attempts to build nanotube-molecule-nanotube hybrids have been recently performed successfully, opening new applications for CNTs (*e.g.* [250]) and producing also three-terminal junctions through this chemical interlinking. A related setup where carbon nanotubes can be directly connected to a molecular structure is achieved when using them as scanning probe tips (*e.g.* [251]).

The semi-infinite leads are treated with a decimation technique, operating in the space of localized orbitals and not in the momentum-space. After

n iteration steps we have in this way renormalized out 2^n slices, and this exponential behavior allows us to quickly achieve convergence. This method is thoroughly explained in Sec. A.1.1.

The systems we considered are all-carbon devices for which a π orbital description level has been proved to yield a very good approximation [85], since the properties of carbon nanotubes are basically determined by these sp^2 π orbitals. Just for (n,m) tubes with $(n+m) < 5$, this π orbital approximation must be reconsidered, as for these cases the p_π are more strongly mixed with the σ states owing to the reduction in the bond angle. Such thin tubes have atomic configurations with hybridization closer to sp^3 than to sp^2.

The Hamiltonian for our system takes then the form:

$$\mathcal{H} = \sum_{i,j} \left(\varepsilon_i \, \delta_{i,j} + V_{ij}\right) |i\rangle \, \langle j| \tag{B.1}$$

where ε_i is the on-site energy and V_{ij} is the coupling or hopping parameter which we estimate as being $2.66\,eV$, taking only nearest neighbors pairs of ij.

For calculating the conductance in the two-terminal case, we partition the system considered in three parts: the central region or scatterer and the left and right lead ($\mathcal{H} = \mathcal{H}_\mathrm{L} + \mathcal{H}_\mathrm{S} + \mathcal{H}_\mathrm{R}$). The Green function for our system is $\mathcal{G} = (E + \mathrm{i}0^+ - \mathcal{H})^{-1}$ and can be written in terms of these submatrices

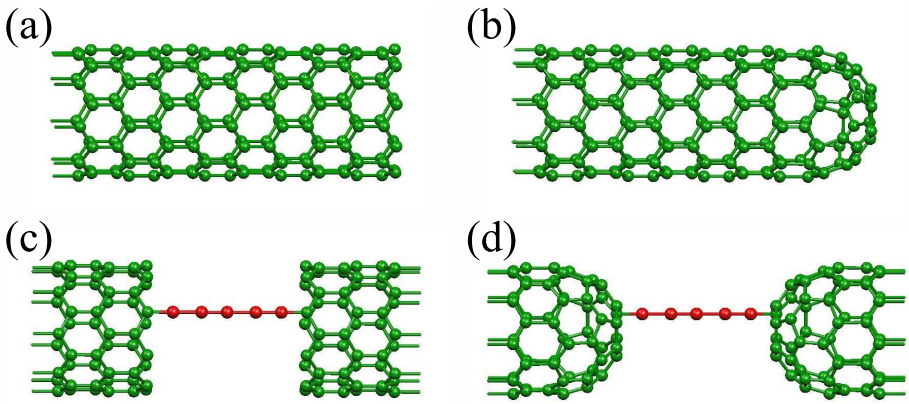

Figure B.1: The structure of a (9,0) zigzag CNT is illustrated here, which is going to the left to infinite, and (a) has an open end on the right, or (b) is capped by half a bucky-ball. Infinite systems of molecule-CNT hybrids are built when a molecular wires bridges two of these semi-infinite CNTs: (c) a molecular wire bridging two open-ended zigzag nanotubes, (d) a molecular wire bridging two cap-ended zigzag nanotubes.

as

$$\mathcal{G}_S = \left(E + \mathrm{i}0^+ - \mathcal{H}_S - \Sigma\right)^{-1}, \tag{B.2}$$

that is, including only finite matrices. $\Sigma = \Sigma_L + \Sigma_R$ is the self-energy term as introduced in Sec. 2.3.3.

B.0.1 Carbon nanotube leads

Localized states at the Fermi level are found at the cut end of zigzag nanotubes, a fact which is already seen at zigzag edges of semi-infinite graphite sheets (see for instance [252] and references therein). Similarly a quasi-bound state is observed at the end of a capped nanotube, where the pentagonal defects pin the level. Here we choose the zigzag CNT (9,0) which is a metallic nanotube to which later a voltage difference at its far ends can be applied, and it can be capped with half a C_{60} fullerene. The diameter of this tube is of about 6.8 Å. The observed localized states appear nevertheless also in semiconducting zigzag tube edges.

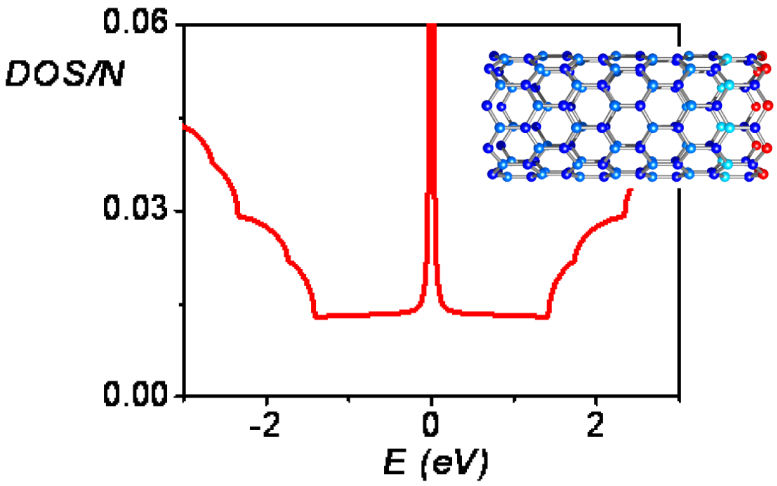

Figure B.2: LDOS of a semi-infinite open-ended (9,0) zigzag nanotube at one of its outermost atoms and distribution of this edge state onto the first unit cells. The color scale goes from red for highest density values to blue for the lowest.

In Fig. B.2, the localized nature of this state at the equilibrium Fermi level is shown, whose wave function decays rapidly when going inside the tube

and disappears when it is far enough. This can be seen in the color plot of the inset where red denotes the higher localized density of states (LDOS) or projected density of states.

For the cap-ended CNT a defect state opens in the gap above the Fermi energy. The wave function corresponding to this state is mainly located around the ring of pentagons introduced to close one of the ends of the CNT, as seen in Fig. B.3.

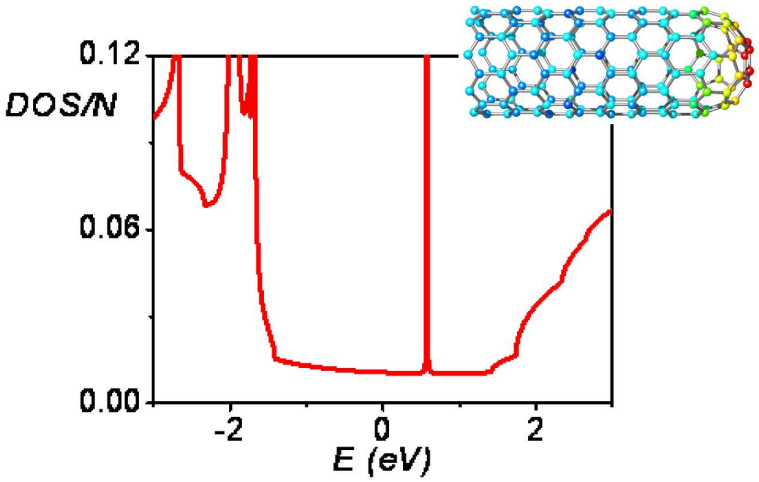

Figure B.3: LDOS of a semi-infinite cap-end zigzag nanotube at the cap with the distribution of the LDOS of the defect state plotted with a color scale as in Fig. B.2.

B.0.2 Two-terminal hybrid configurations

In order to investigate the effect of these localized states in transport we calculate the conductance of a homogeneous tight-binding chain (black lines) and of a dimerized one (red and blue lines), sandwiched between two semi-infinite nanotubes, both with a functionalized end or with a capped end. This is one of the simplest systems we can use to see the interference effects of the previous analyzed surface states (see Fig. B.4 and Fig. B.6).

A sandwiched chain between two nanotubes shows quantum features of both the molecular wire and the carbon nanotubes, with resonances of quantum unit height at energies close to those of the energy spectrum of the isolated

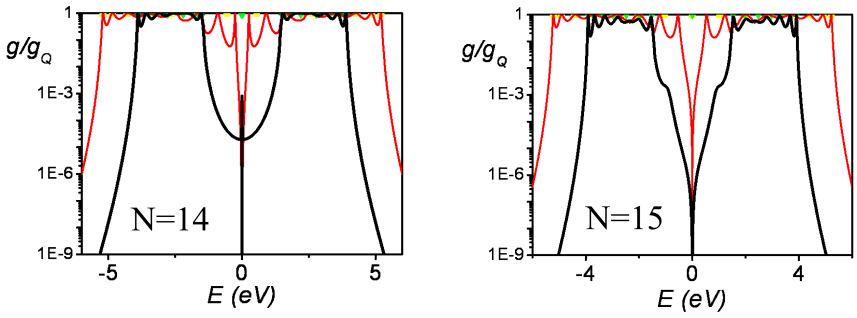

Figure B.4: Conductance of a molecular chain of 14 and 15 atoms sandwich between two cut-end CNTs.

chain (squares and triangles). Calculations with cut end nanotubes have already been performed (see for instance Ref. [248, 253]).

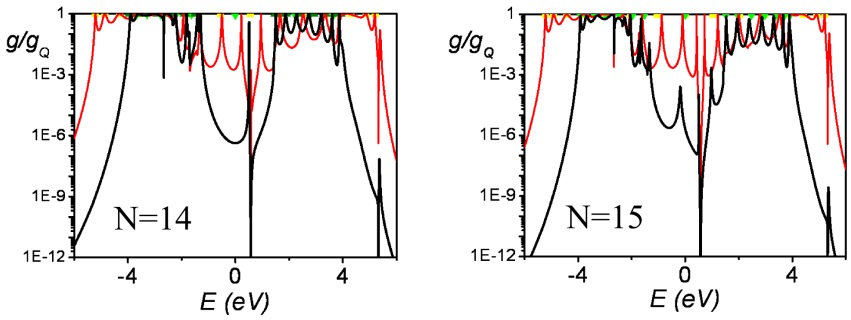

Figure B.5: Conductance of a molecular chain of 14 and 15 atoms sandwich between two capped-end CNTs. The dashed line shows the LDOS of the capped CNT.

We only see the manifestation of the resonant states of the cap or of the cut end when these states are supported by the molecular bridge. In these cases a peak is found when looking closely, but normally it shows a small transmission probability and just a slight broadening. Nevertheless the influence of the localized states is not likely to be overlooked as a anti-resonance dip shows up as a result of the interference of these surface states.

We can understand it with a very simple model, calculating the transport through a one-atom chain, which has an onsite energy ε_0, energy of its single

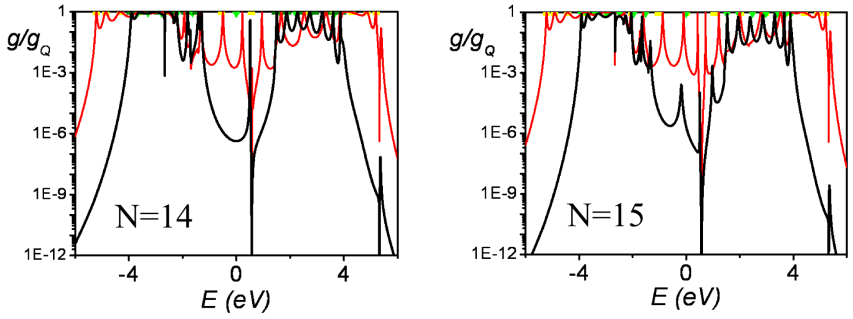

Figure B.6: Conductance of a molecular chain of 14 and 15 atoms sandwich between two capped-end CNTs. The dashed line shows the LDOS of the capped CNT.

eigenvalue. The transmission probability along this chain is given by:

$$\mathcal{T}(E) = \frac{4\Delta^2}{(E - \varepsilon_0 - 2\Lambda)^2 + 4\Delta^2} \tag{B.3}$$

where Λ and Δ are the real and imaginary part of the selfenergy of the leads, which we take to be identical on both sides:

$$\Sigma_{\text{left}} = \Sigma_{\text{right}} = \Lambda - \mathrm{i}\Delta \tag{B.4}$$

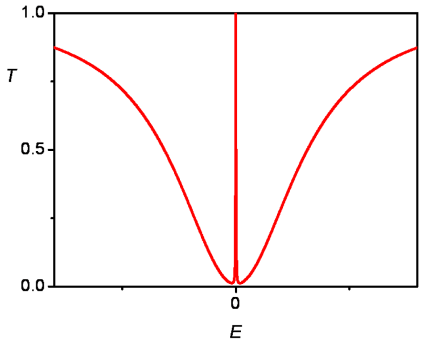

Figure B.7: Model transmission for $\varepsilon_0 = 0\,eV$, $B = 1$ and $\Gamma = 2.66\,eV$

We model now our leads as having a constant density of states (like the "wide-band" limit) and a Lorentzian peak centered at $E = 0$ as the surface state. This leads us to the following approximation for Δ:

$$\Delta = \pi B \Gamma^2 + \frac{2\delta\Gamma^2}{\delta^2 + 4E^2}. \tag{B.5}$$

where Γ is the hopping parameter between the chain atom and the leads, δ is the width at half-maximum of the peak and B is the background density of states. As the selfenergy is built from the Green function of the lead, we can reconstruct Σ taking into account the causality of the Green function. Thus we choose Λ as the Hilbert transform of Δ:

$$\Lambda = \frac{4\Gamma^2 E}{\delta^2 + 4E^2} \tag{B.6}$$

The result we obtain resembles the one we obtain for the CNT-leads at energies around the surface state, where a broad dip is the main signal.

Appendix C

Floquet theory

C.1 Periodic time-dependent Hamiltonians

A way of solving problems described by time-dependent Hamiltonians with driving terms periodic in time is to apply Floquet formalism, a method that respects the time periodicity of the Hamiltonians at all levels. Via the Floquet theorem we map our system into an equivalent one described by a time-independent Hamiltonian with an additional degree of freedom.

We can summarize the essence of this process in the following way:

Field-driven transport problem
(*time-dependent Hamiltonian*)

⇓ **Floquet Theory**

Effective quantum system
(*time-independent Hamiltonian*)

In this way, we go from our original state system to a modified and augmented Hilbert space, where we have an infinite number of replicas for the scatterer and the leads, as we will see in the following sections. This would not be a great gain if it was not for the fact that when expanding the driving terms of the Hamiltonian in their harmonics, these terms are weighted with Bessel functions, which will allow us to retain just a small amount of terms. The new Hamiltonian characterizing the effective quantum system has the

same essential structure as the one corresponding to the nondriven system. This will allow us to apply Green function techniques to deal with the transport calculations, as has been done to analyze nondriven scattering problems throughout this work.

C.2 Transport through a molecular wire

To illustrate this approach, we will next consider a simple model system: a molecular wire attached to two reservoirs as illustrated in Fig. C.1.

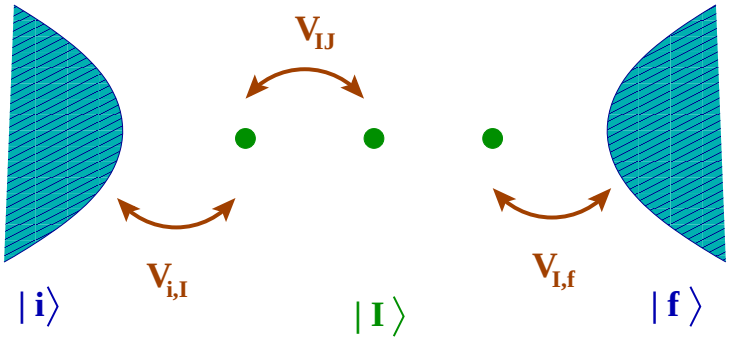

Figure C.1: Sketch of a molecular wire sandwiched between two electrodes with a schematic description of the hopping integrals. We consider the wire to extend along the x axis.

C.2.1 The nondriven system

The Hamiltonian describing this model system within a one-electron tight-binding model can be written as

$$\mathcal{H}^0 = \mathcal{H}_S + \mathcal{H}_L + \mathcal{H}_{LS}, \tag{C.1}$$

that is, results from the contributions of the scatterer $\mathcal{H}_S$, in this case a molecular wire, of the leads $\mathcal{H}_L$, and of the coupling Hamiltonian of conductor and leads $\mathcal{H}_{LS}$. It can be expressed as

$$\mathcal{H}^0 = \sum_{\alpha,\beta} \left(\varepsilon_\alpha \, \delta_{\alpha,\beta} + V_{\alpha\beta}\right) |\alpha\rangle \langle\beta| \,, \tag{C.2}$$

where the indices α and β run over the different sites of the system. We will designate the states in the left lead L_i as $|i\rangle$, those belonging to the molecular

wire as $|I\rangle$, and those of the right lead R_i, the final states of the transferring electrons, as $|f\rangle$. The onsite energies are ε_α, whereas the hopping parameters are characterized by the integrals $V_{\alpha\beta}$. The left and right leads, L_i and R_i, do not couple directly to each other.

To get current to flow, the application of a static field V_{DC} is required. The effect of this field can be seen as a shift of the onsite energies: $\varepsilon \rightarrow \varepsilon'$. Assuming a linear drop between the leads, one obtains that

$$\varepsilon'_\alpha = \begin{cases} \varepsilon_\alpha & \text{if } \alpha \in L_i \\ \varepsilon_\alpha - e\phi^{\mathrm{DC}}_{\alpha\alpha} & \text{if } \alpha \in I \text{ (wire)} \\ \varepsilon_\alpha - eV_{\mathrm{DC}} & \text{if } \alpha \in R_i \end{cases} \tag{C.3}$$

The electrostatic potential ϕ^{DC} is assumed to be constant in the reservoirs. In the wire, $\phi^{\mathrm{DC}}_{\alpha\alpha} = \langle\alpha|\,\phi^{\mathrm{DC}}(x)\,|\alpha\rangle$, where $\phi^{\mathrm{DC}}(x)$ changes linearly with x. On the following, we will nevertheless work in the limit of bias voltage close to zero, $V_{\mathrm{DC}} \rightarrow 0$.

The Schrödinger time-dependent equation, Eq. (1.2), describing the system is written as

$$\mathrm{i}\hbar\left|\dot{\Psi}(t)\right\rangle = \mathcal{H}^0\,|\Psi(t)\rangle \tag{C.4}$$

which can be expressed in terms of the expansion coefficients c_α of the wavefunction $\Psi(t)$ in the basis of the states $\{|\alpha\rangle\} = \{\{|i\rangle\},\{|I\rangle\},\{|f\rangle\}\}$, that is, $|\Psi(t)\rangle = \sum_\alpha c_\alpha(t)\,|\alpha\rangle$, in the following way:

$$\mathrm{i}\hbar\dot{c}_\alpha = \sum_\beta \mathcal{H}^0{}_{\alpha,\beta}c_\beta. \tag{C.5}$$

Since the Hamiltonian is time-independent, we can the eigenvalue equation,

$$\epsilon c_\alpha = \sum_\beta \mathcal{H}^0{}_{\alpha,\beta}c_\beta. \tag{C.6}$$

The transport properties can be calculated by applying Green function techniques, as described in Chapter 2. Namely, we calculate the Green function as

$$\mathcal{G} = \left[E - \mathrm{i}\eta - \mathcal{H}_{\mathrm{S}} - \Sigma\right]^{-1}, \tag{C.7}$$

where $\Sigma = \Sigma^{L_i} + \Sigma^{L_f}$ is the self-energy, taking into account the effects of the two leads. The transmission function is calculated using the expression

$$\mathcal{T}_{R_iL_i} = \mathrm{Tr}\left\{\Gamma_{R_i}\mathcal{G}\Gamma_{L_i}\mathcal{G}^\dagger\right\}. \tag{C.8}$$

as defined in Eq. (2.64) with the therein defined coupling matrices Γ.

C.2.2 The driven system

Our interest is to investigate the influence of an external AC field in a nanoscopic system, and in particular, as a first step, in this model system of a molecular wire. We will therefore consider the same system as before in Sec. C.2.1, now under the presence of a monochromatic electric field, E, as schematically illustrated in Fig. C.2.

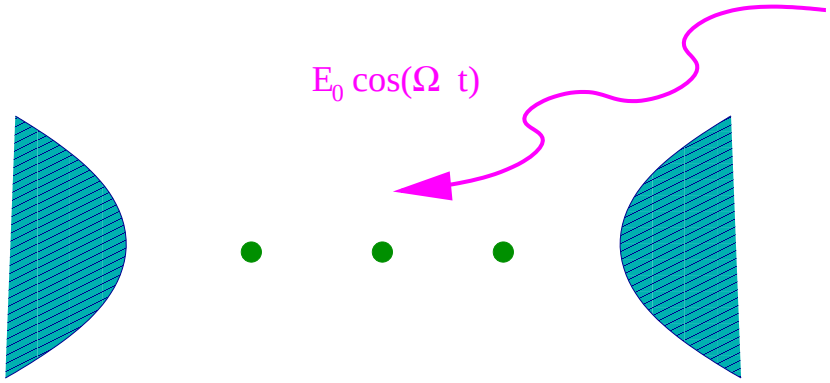

Figure C.2: Model of a laser-driven molecular wire. The molecular wire attached on both ends to perfect conducting leads in set under a monochromatic electric field.

A monochromatic electric field along the axis of the bridge molecule is thus switched on. The field is treated within the dipole approximation as a monochromatic infinite plane wave linearly polarized along the direction of the incident electron. Usually the wavelength of the radiation field is far larger than the size of the quantum system. We will work with this assumption known as the long wavelength approximation. It implies that the spatial dependence of the electric field can be neglected in the region of the molecule, and we can write for the electric field:

$$\mathrm{E}(t) = \mathrm{E}_0 \cos(\Omega t)\, \hat{\mathcal{E}}, \quad \text{of period} \quad T = 2\pi/\Omega\,, \tag{C.9}$$

and of direction given by the unitary vector $\hat{\mathcal{E}}$, along the wire axis.

The Hamiltonian of the whole system has to be extended now to include the effects of this external field,

$$\mathcal{H}^0 \;\rightarrow\; \mathcal{H} = \mathcal{H}^0 + \mathcal{H}^1 \tag{C.10}$$

that is, the external perturbation $\mathcal{H}^1$ adds to the non-driven system Hamiltonian $\mathcal{H}^0$, to obtain the total Hamiltonian $\mathcal{H}$ describing the system. $\mathcal{H}^1$

represents the interaction energy between the quantum system and the classical electric field, and it can be written as $\mathcal{H}^1 = -\mu(x) \cdot \mathrm{E}(t)$, where μ is the electric dipole operator. We consider the leads to be perfect conductors so that the field is zero inside them, *i.e.*, the electrical potential ϕ (defined by $\mathrm{E} = -\nabla\phi$) takes a constant value in the leads. The electric dipole operator is diagonal in the basis of the site orbitals $\{\alpha\}$ due to the small overlap between different orbitals, and the diagonal elements are assumed to be given to a good approximation by the position of the site orbital. That is,

$$\begin{cases} \text{if } \alpha \in L_i\text{:} & \mu_\alpha = -ex_{L_i} \equiv 0, & \phi\text{: constant} \\ \text{if } \alpha \in I \text{ (wire):} & \mu_\alpha = \langle I | \mu | I \rangle = -ex_I, & \phi\text{: varies linearly} \\ \text{if } \alpha \in R_i\text{:} & \mu_\alpha = -ex_{R_i}, & \phi\text{: constant} \end{cases} \tag{C.11}$$

where e is the magnitude of the electron charge. $\mathcal{H}^1$ is therefore time-dependent:

$$\mathcal{H}^1 = \sum_\alpha ex_\alpha \mathrm{E}_0 \cos(\Omega t) \, |\alpha\rangle \langle\alpha| \ . \tag{C.12}$$

The total Hamiltonian $\mathcal{H}$ can be then written in the same form as in Eq. (C.2) with

$$\varepsilon''_\alpha = \begin{cases} \varepsilon'_\alpha - \mu_{L_i} \mathrm{E}_0 \cos(\Omega t) & \text{if } \alpha \in L_i \\ \varepsilon'_\alpha - \mu_I \mathrm{E}_0 \cos(\Omega t) & \text{if } \alpha \in I \text{ (wire)} \\ \varepsilon'_\alpha - \mu_{R_i} \mathrm{E}_0 \cos(\Omega t) & \text{if } \alpha \in R_i \end{cases} \tag{C.13}$$

with the terms with a explicit dependence on time on the diagonal matrix elements.

The problem has thus the same form as the non-driven one with a Schrödinger equation like Eq. (C.5):

$$\mathrm{i}\hbar \dot{c}_\alpha(t) = \sum_\beta \mathcal{H}_{\alpha,\beta}(t) c_\beta(t), \tag{C.14}$$

but with a time-dependent Hamiltonian.

It is convenient to go over to another representation (see Sec. C.5), to remove the driving terms from the diagonal elements.

The unitary matrix for the transformation is given by

$$U = \exp\left(\frac{\mathrm{i}}{\hbar} \int^t \mathcal{H}^1 \left(t'\right) \, dt'\right), \tag{C.15}$$

and the wave function Ψ in this new frame is defined as

$$\Psi^{Int}(x,t) = U\Psi(x,t). \tag{C.16}$$

It satisfies the following evolution equation:

$$i\hbar\partial_t \Psi^{Int}(x,t) = \tilde{\mathcal{H}}\Psi^{Int}(x,t) \tag{C.17}$$

where $\tilde{\mathcal{H}}$ is the time-independent Hamiltonian in this representation as seen in Sec. C.5 below, given by

$$\tilde{\mathcal{H}} = U\mathcal{H}^0 U^{-1}\,. \tag{C.18}$$

Specifically,

$$\tilde{\mathcal{H}}_{\alpha,\beta}(t) = \exp\left(\frac{i}{\hbar}\left(\mu_\beta - \mu_\alpha\right)E_0\frac{\sin(\Omega t)}{\Omega}\right)\mathcal{H}^0_{\alpha,\beta}\,, \tag{C.19}$$

or

$$\tilde{\mathcal{H}}_{\alpha,\beta}(t) = \exp\left(i a_{\alpha\beta}\sin(\Omega t)\right)\mathcal{H}^0_{\alpha,\beta}\,, \tag{C.20}$$

where we have defined the dimensionless field amplitudes $a_{\alpha\beta} = E_0\left(\mu_\beta - \mu_\alpha\right)/\hbar\Omega$. It can be observed that this transformation has put the driving terms into the off-diagonal terms, as $a_{\alpha\alpha} = 0$.

Making use of the Floquet Ansatz to solve problems with a periodic time dependence as described in Sec. C.3 of this appendix, we postulate solutions of the wavefunction such that

$$\Psi^{Int}(x,t) = \exp\left(-\frac{i}{\hbar}\epsilon t\right)\psi_\epsilon(x,t), \tag{C.21}$$

where ϵ is the Floquet energy or quasienergy and $\psi_\epsilon(x,t) = \psi_\epsilon(x,\, t+T)$. $\psi_\epsilon(x,t)$ can be thus be expanded in a Fourier series based on the periodicity of the driving field:

$$\Psi^{Int}(x,t) = \exp\left(-\frac{i}{\hbar}\epsilon t\right)\sum_{n=-\infty}^{+\infty}\exp\left(-in\Omega t\right)\phi_{\epsilon,n}(x), \tag{C.22}$$

and moreover in the basis of the states of the system,

$$\left|\Psi^{Int}\right\rangle = \sum_{\alpha\, n}\exp\left(-\frac{i}{\hbar}\epsilon t - in\Omega t\right)b_{\alpha,n}(x)\left|\alpha\right\rangle. \tag{C.23}$$

Substituted into Eq. (C.17) yields

$$\begin{aligned}&\sum_{\alpha\, n}\exp\left(-i\frac{\epsilon t}{\hbar} - in\Omega t\right)\left(\epsilon + n\hbar\Omega\right)b_{\alpha,n}\left|\alpha\right\rangle = \\ &= \sum_{\beta,\gamma}\sum_{m,m'}\mathcal{H}^0_{\gamma,\beta}J'_m\left(a_{\gamma\beta}\right)\exp\left(-i\frac{\epsilon t}{\hbar} - i(m+m')\Omega t\right)b_{\beta,m}\left|\gamma\right\rangle\end{aligned} \tag{C.24}$$

where the driving term in Eq. (C.20) has been Fourier expanded, with the Bessel functions of order n, J_n, entering as expansion coefficients:

$$\exp\left(\mathrm{i}a\sin(\Omega t)\right) = \sum_{n=-\infty}^{+\infty} J_n\left(a\right)\exp\left(-\mathrm{i}n\Omega t\right). \tag{C.25}$$

After projection on a state $\langle\alpha|$ and keeping the nth expansion coefficients, one obtains:

$$\epsilon b_{\alpha,n} = \sum_{\beta,m} \mathcal{H}^0_{\alpha,\beta} J_{n-m}\left(a_{\alpha\beta}\right) b_{\beta,m} - n\hbar\Omega b_{\alpha,n}\,, \tag{C.26}$$

equation isomorphic to the eigenvalue Eq. (C.6), by defining the Floquet Hamiltonian, which is *time-independent*:

$$\mathcal{H}^{Fl}_{\alpha n,\beta m} = \mathcal{H}^0_{\alpha\beta} J_{n-m}\left(a_{\alpha\beta}\right) - n\hbar\Omega\,\delta_{\alpha,\beta}\,\delta_{n,m}\,. \tag{C.27}$$

The Floquet Hamiltonian $\mathcal{H}^{Fl}$ is associated with an *augmented state space*, described by the basis states $|\alpha\rangle$ and the label n for the replica. So our system is no longer described merely by physical states $|\alpha\rangle$, but each of these states has a formally infinite number sidebands associated to it. It consists of a formally infinite electronic state space, with appropriately renormalized interstate couplings. We make now an approximation by truncating this state, keeping only the minimal number of Floquet channels needed in order to obtain convergence. For each state in the physical system there is a finite-dimensional discrete manifold of states in the Floquet system. Due to the decay of the Bessel functions with n just a small number of replicas is required for convergence to be met (see Sec. C.3). If a sufficiently large amount of Floquet replica states are included in the calculations, a numerically exact solution of the field-driven dynamics can be obtained.

A further approximation that can be made in some cases is the independent channel approximation (IC), where off-diagonal terms coupling different Floquet replicas (with a different index n), are neglected. The inter-channel coupling comes from off-diagonal elements of $\mathcal{H}^{Fl}$ on the bridge, and from coupling terms to the leads. Both contributions are suppressed if the laser intensity tends to zero, the electronic coupling elements are small enough or the gap between the quasienergies of different bridge replicas is large enough, *i.e.*, the photon frequency is high. All these conditions lead to a poor mixing of the different replicas and may make of the IC approximation a reasonably good way to treat the problem. This simplification, which leaves a block diagonal Hamiltonian, when justified, may lead to a better insight of

the physics of the problem. The validity of such approximation should be checked by coupling several bridge replicas and verifying the small influence of these coupling in the results.

As the new Hamiltonian has the same essential structure as the one corresponding to the non-driven system we can again apply Green function techniques to study transport properties.

The Green function for the system has now the form

$$\mathcal{G}^{Fl} = \left[E - \mathcal{H}_S^{Fl} - \Sigma^{Fl}\right]^{-1} \tag{C.28}$$

The Floquet self-energy is given by

$$\Sigma^{L_i,Fl}_{Im,Jm'}(E) = \begin{cases} \sum_\nu J_{\nu-m}(-a_L)\, J_{\nu-m'}(-a_L)\, \Sigma^{L_i}_{1,1}(E_{i_0} - \nu\omega) & \text{if } I = J = 1 \\ \Sigma^{L_i}_{I,J} = 0 & \text{otherwise} \end{cases} \tag{C.29}$$

and

$$\Sigma^{L_f,Fl}_{Im,Jm'}(E) = \begin{cases} \sum_\nu J_{\nu-m}(a_R)\, J_{\nu-m'}(a_R)\, \Sigma^{L_f}_{N,N}(E_{i_0} - \nu\omega) & \text{if } I = J = N \\ \Sigma^{L_f}_{I,J} = 0 & \text{otherwise} \end{cases} \tag{C.30}$$

An electron from lead L_i starting with energy E_{i_0} can end up in a final state of energy $E_{f_0} = E_{i_0} + N_p\hbar\Omega$ with the absorption or emission of N_p photons. To compare our results with those of Ref. [165] we calculate the transition rate from a state of energy E_{i_0} with a net N_p-photon emission, given by

$$R_{i_0} = 2V^2 \left[\Delta(E_{i_0} - N_p\omega)\right]_{N,N} \left| \sum_{k,k'} J_k(a_{L_i}) \left[G^{Fl}(E_{i_0})\right]_{1k,Nk'} J_{N_p-k'}(a_{R_i}) \right|^2 \tag{C.31}$$

where

$$G^{Fl} = \left[E_{i_0} - \mathcal{H}_M^{Fl} - \Sigma^{L_i,Fl} - \Sigma^{L_f,Fl}\right]^{-1} \tag{C.32}$$

and $a_{L_i} = a_{1\,L_i}$, $a_{R_i} = a_{R_i\,N}$ (leads only couple to one state in the molecular bridge). Δ is the Newns-Anderson spectral density taken to be

$$\Delta(E) = \begin{cases} \frac{V^2}{\gamma}\sqrt{1 - \left(\frac{E}{2\gamma}\right)^2} & \text{if } \left|\frac{E}{2\gamma}\right| < 1 \\ 0 & \text{otherwise} \end{cases} \tag{C.33}$$

The actual rate is

$$rate = \sum_{N_p} \left[R^2_{i_0} \right]^2 \tag{C.34}$$

V is the coupling between reservoirs and bridge and γ is the coupling element inside the leads. We used the values $\frac{V^2}{\gamma} = 0.12$ and $\gamma = 0.5$ as in Ref. [165]. The sum over k runs over the bridge replicas and the one over N_p over the number of photons interchanged with the field. It seems that taking a maximum for N_p of 4 is more than enough as it already shows all the features appearing for higher ones.

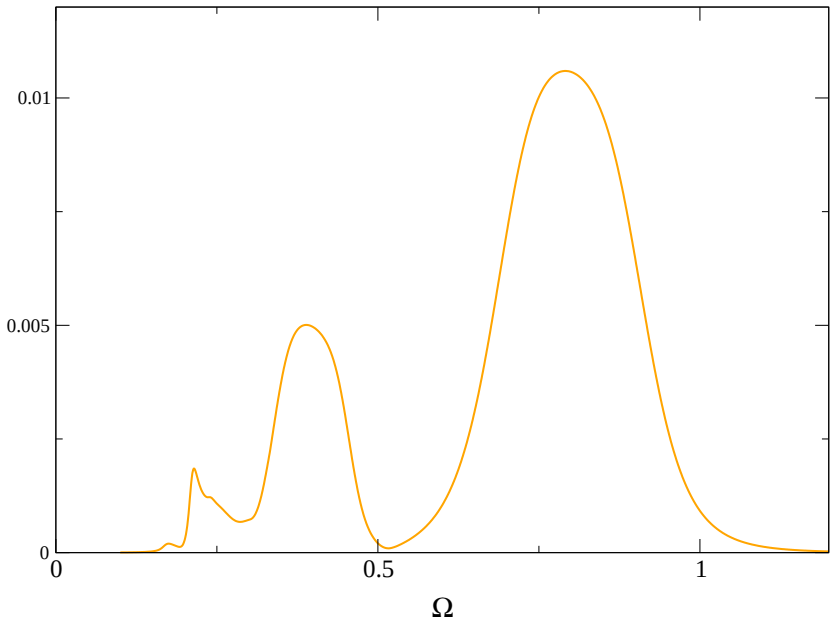

Figure C.3: Transmission rate from a state of energy E_{i_0} with a net N_p-photon emission through a three-atom chain. The values taken for this calculation are: $a_B = a_{21} = a_{32} = 0.2$, $a_L = a_{1L} = 2$, $a_R = a_{RN} = 2$, $V_B = 0.1, E_B = 0.8$ and $E_{i_0} = 0.0$.

C.3 The Floquet theorem

The fact of dealing with a Hamiltonian periodic in time, *i.e.* symmetric under time translations $t \to t + T$, allows us to apply the *Floquet theorem* [254, 255,

256, 257], according to which there exists a set of fundamental solutions to the time-dependent Schrödinger equation, which can be written in the form

$$\Psi(\mathbf{r},t) = \exp\left(-\frac{\mathrm{i}}{\hbar}\epsilon t\right)\psi_\epsilon(\mathbf{r},t) \tag{C.35}$$

which are the so-called Floquet-state solutions, where $\psi_\epsilon(\mathbf{r},t)$ is a periodic function of time, $\psi_\epsilon(\mathbf{r},t) = \psi_\epsilon(\mathbf{r},t+T)$, and ϵ is the Floquet energy or quasienergy. A general solution to the Schrödinger equation is given by a superposition of many Floquet states. The quasienergy shows through its name the analogy to the quasimomentum characterizing the Bloch eigenstates in a spatial periodic potential [16]. The quasienergy ϵ is unique up to multiples of $\hbar\Omega$, with $\Omega = \frac{2\pi}{T}$. Two Floquet states

$$|\psi_\epsilon\rangle \quad \text{and} \quad |\psi'_\epsilon\rangle = \mathrm{e}^{\mathrm{i}n\Omega t}|\psi_\epsilon\rangle \tag{C.36}$$

yield the identical solution to Eq. (C.35) but have quasienergies differing in $n\hbar\Omega$, ϵ and $\epsilon' = \epsilon + n\hbar\Omega$ respectively, for an integer n. It is therefore sufficient to know the quasienergies and their corresponding Floquet states in the interval $-\hbar\Omega/2 < \epsilon < \hbar\Omega/2$, as all others can be mapped back to this part of the spectrum.

The Floquet decomposition, Eq. (C.35) arises from the fact that the eigenstates of a periodic Hamiltonian can change at most by a phase factor upon action of a symmetry operator $\mathcal{S}_T$ on them (it has to conserve the norm) [258]

$$\mathcal{S}_T : \; t \longrightarrow t+T, \tag{C.37}$$

where $\mathcal{S}_T$ is a discrete time translation by one period of the driving.

By substituting Floquet Ansatz, Eq. (C.35), into the time-dependent Schrödinger equation, Eq. (1.2), one obtains the eigenvalue equation for the quasienergy ϵ:

$$\left[\mathcal{H}(\mathbf{r},t) - \mathrm{i}\hbar\frac{\partial}{\partial t}\right]\psi_\epsilon(\mathbf{r},t) = \epsilon\psi_\epsilon(\mathbf{r},t), \tag{C.38}$$

which has the form of the time-independent Schrödinger equation, Eq. (1.1), if $\mathcal{H}^{Fl} = \left[\mathcal{H}(\mathbf{r},t) - \mathrm{i}\hbar\frac{\partial}{\partial t}\right]$ is redefined as the hermitian Floquet operator. That is, the Floquet states are stationary states of this Hamiltonian.

We can take advantage of the periodicity of $\psi_\epsilon(\mathbf{r},t)$ by Fourier analyzing it:

$$\psi_\epsilon(\mathbf{r},t) = \sum_{n=-\infty}^{+\infty} \exp\left(-\mathrm{i}n\Omega t\right)\phi_{\epsilon,n}(\mathbf{r}). \tag{C.39}$$

The wave function can be written in the basis of the states of the system, assumed to be orthogonal and unit normalized $\{|\alpha\rangle\}$:

$$\begin{aligned} |\Psi\rangle &= \sum_\alpha c_\alpha(\mathbf{r},t)\,|\alpha\rangle = \exp\left(-\frac{\mathrm{i}}{\hbar}\epsilon t\right)\sum_\alpha b_\alpha(\mathbf{r},t)\,|\alpha\rangle \\ &= \exp\left(-\frac{\mathrm{i}}{\hbar}\epsilon t\right)\sum_\alpha\sum_{n=-\infty}^{+\infty}\exp\left(-\mathrm{i}n\Omega t\right)b_{\alpha,n}(\mathbf{r})\,|\alpha,n\rangle\,. \end{aligned} \tag{C.40}$$

From Eq. (C.40), we obtain the corresponding equation for $\phi_{\epsilon,n}$ by substituting this into the Schrödinger equation, Eq. (1.2), simultaneously with the corresponding Fourier expansions for the driving terms of the Hamiltonian.

C.4 The augmented space

The Floquet Hamiltonian $\mathcal{H}^{Fl}$ is associated with an *augmented state space*, described by the basis states $|\alpha,n\rangle$. The label n indicates that there are sidebands (formally an infinite number of them) associated to each state.

We can schematically see our system as described by multiple reproductions or "replicas" of our original system, shifted by multiples of the energy quantum $\hbar\Omega$, as represented in Fig. C.4.

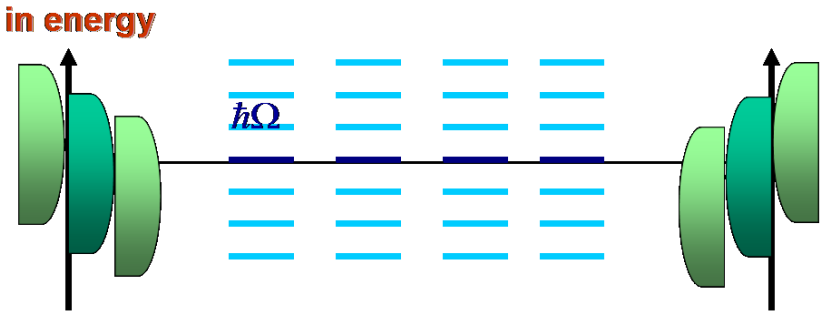

Figure C.4: A naïve representation of the multiplicity of states in the Floquet state space, where replicas differ by integer multiples of $\hbar\Omega$.

As in a time-dependent system energy is not a conserved quantity, it is of interest to defined a mean energy in a Floquet state Ψ, averaged over one

driving period T:

$$\begin{aligned}\bar{\mathcal{H}} &= \frac{1}{T}\int_0^T \mathrm{d}t\, \langle \Psi(t)\, |\mathcal{H}(t)|\, \Psi(t)\rangle = \\ &= \epsilon + \mathrm{i}\hbar\frac{1}{T}\int_0^T \mathrm{d}t \int_{-\infty}^{+\infty} \mathrm{d}\,\mathbf{r}\psi_\epsilon^*(\mathbf{r},t)\frac{\partial}{\partial t}\psi_\epsilon(\mathbf{r},t)\,.\end{aligned} \tag{C.41}$$

Invoking the Fourier expansion of ψ_ϵ, one obtains

$$\bar{\mathcal{H}} = \sum_{n=-\infty}^{+\infty} (\epsilon + n\hbar\Omega)\, \langle \phi_{\epsilon,n} \,|\, \phi_{\epsilon,n}\rangle\,, \tag{C.42}$$

which can be seen as the energy accumulated in each harmonic mode of Ψ and averaged with respect to the weight of each of these harmonics. One can understand the states at energies $E + n\hbar\Omega$ as inelastic scattering channels by which the electrons exchange energy with the driving field, and they can be referred to as photonic sidebands. They can be interpreted as new transport channels mediated by the emission or absorption of photon quanta. It must be though kept in mind that the Floquet state is a particular way to described a single, coherent wave function, with a wave vector $\mathbf{k}$.

As the Fourier expansion of driving terms of the Hamiltonian involves Bessel function as weighting factors of order n. The number of Floquet replicas or sidebands is formally infinite but the fast decay of the Bessel functions as seen in Fig. C.5 allows us to described the system by just retaining a moderate number of them. For each state in the physical system there is then just a finite-dimensional discrete manifold of states.

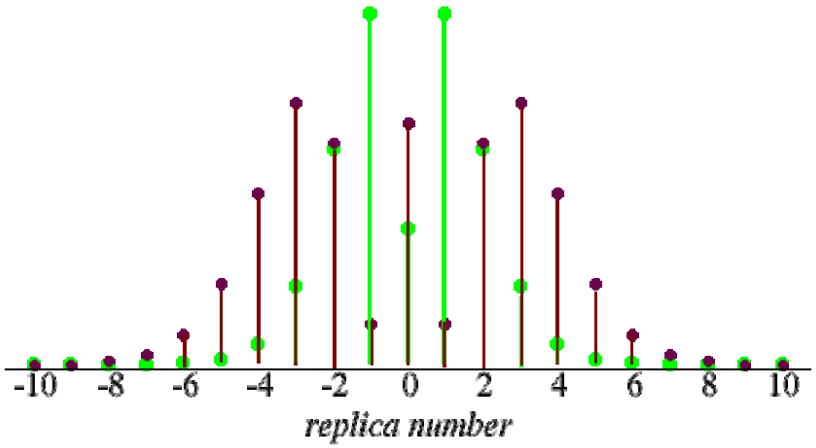

Figure C.5: Schematic representation of the decay of the weighting factor of the Bessel function as a function of their order number n.

C.5 Derivation of the intermediate picture

Between the Schrödinger picture and the Heisenberg picture one can define the interaction picture or Dirac picture [259], in which both the wavefunctions and the operators evolve with time. The evolution of the wavefunctions is determined by the time-dependent part of the Hamiltonian, whereas the evolution of an observable is set by the unperturbed part of the Hamiltonian (time-independent part). Instead, we will define here another intermediate picture which leads to opposite evolution dependences.

Given that the Hamiltonian of the system can be separated into a time-independent part $\mathcal{H}^0$ and a time-dependent perturbation $\mathcal{H}^1$:

$$\mathcal{H} = \mathcal{H}^0 + \mathcal{H}^1(t), \tag{C.43}$$

we define a state in this intermediate representation as

$$|\phi(t)\rangle_{Int} = \exp\left(\frac{\mathrm{i}}{\hbar}\int^t \mathcal{H}^1(t')\mathrm{d}t'\right)|\phi(t)\rangle_S \tag{C.44}$$

where Int refers to this picture while S labels elements in the Schrödinger picture, which is in general omitted. An operator A in the interaction picture is then defined as

$$A_{Int} \equiv \exp\left(\frac{\mathrm{i}}{\hbar}\int^t \mathcal{H}^1(t')\mathrm{d}t'\right) A_S \exp\left(\frac{-\mathrm{i}}{\hbar}\int^t \mathcal{H}^1(t')\mathrm{d}t'\right), \tag{C.45}$$

in particular,

$$\mathcal{H}^0_{Int} \equiv \exp\left(\frac{\mathrm{i}}{\hbar}\int^t \mathcal{H}^1(t')\mathrm{d}t'\right) \mathcal{H}^0_S \exp\left(\frac{-\mathrm{i}}{\hbar}\int^t \mathcal{H}^1(t')\mathrm{d}t'\right). \tag{C.46}$$

The time evolution of the ket state in this picture $|\phi(t)\rangle_{Int}$ is therefore:

$$\begin{aligned} \mathrm{i}\hbar\frac{\partial}{\partial t}|\phi(t)\rangle_{Int} &= \mathrm{i}\hbar\frac{\partial}{\partial t}\left[\exp\left(\frac{\mathrm{i}}{\hbar}\int^t \mathcal{H}^1(t')\mathrm{d}t'\right)|\phi(t)\rangle_S\right] = \\ &= \exp\left(\frac{\mathrm{i}}{\hbar}\int^t \mathcal{H}^1(t')\mathrm{d}t'\right)\mathcal{H}^0|\phi(t)\rangle_S, \end{aligned} \tag{C.47}$$

where we have made use of the Schrödinger equation, Eq. (1.2). One can see that this equation is equivalent to

$$\mathrm{i}\hbar\frac{\partial}{\partial t}|\phi(t)\rangle_{Int} = \mathcal{H}^0_{Int}|\phi(t)\rangle_{Int} \tag{C.48}$$

which express the time evolution completely in this intermediate picture. In the same way, one can show that the time evolution of an operator in this picture is given by

$$\mathrm{i}\hbar\frac{\mathrm{d}A_{Int}}{\mathrm{d}t} = \left[A_{Int}, \mathcal{H}^1\right]. \tag{C.49}$$

Bibliography

[1] M. del Valle, C. Tejedor, and G. Cuniberti, *Defective transport properties of three-terminal carbon nanotube junctions*, Phys. Rev. B **71**, 125306 (2005), doi:10.1103/PhysRevB.71.125306,

[2] M. del Valle, C. Tejedor, and G. Cuniberti, *Scaling of the conductance in gold nanotubes*, Phys. Rev. B **74**, 045408 (2006), doi:10.1103/PhysRevB.74.045408,

[3] M. del Valle, R. Gutiérrez, C. Tejedor, and G. Cuniberti, *Tuning the conductance of a molecular switch*, (2006), submitted,

[4] G. Cuniberti, G. Fagas, and K. Richter, eds., *Introducing Molecular Electronics*, Springer, Berlin and Heidelberg, 2005, doi:10.1007/b101525,

[5] K. von Klitzing, *The quantized Hall effect*, Rev. Mod. Phys. **58**, 519 (1986), doi:10.1103/RevModPhys.58.519,

[6] H. L. Störmer, *Nobel Lecture: The fractional quantum Hall effect*, Rev. Mod. Phys. **71**, 875 (1999), doi:10.1103/RevModPhys.71.875,

[7] D. C. Tsui, *Nobel Lecture: Interplay of disorder and interaction in two-dimensional electron gas in intense magnetic fields*, Rev. Mod. Phys. **71**, 891 (1999), doi:10.1103/RevModPhys.71.891,

[8] R. B. Laughlin, *Nobel Lecture: Fractional quantization*, Rev. Mod. Phys. **71**, 863 (1999), doi:10.1103/RevModPhys.71.863,

[9] R. E. Smalley, *Discovering the fullerenes*, Rev. Mod. Phys. **69**, 723 (1997), doi:10.1103/RevModPhys.69.723,

[10] S. Iijima, *Helical microtubules of graphitic carbon*, Nature **354**, 56 (1991), doi:10.1038/354056a0,

[11] K. S. Novoselov, A. K. Geim, S. V. Morozov, D. Jiang, Y. Zhang, S. V. Dubonos, I. V. Grigorieva, and A. A. Firsov, *Electric Field Effect in Atomically Thin Carbon Films*, Science **306**, 666 (2004), doi:10.1126/science.1102896,

[12] K. S. Novoselov, A. K. Geim, S. V. Morozov, D. Jiang, M. I. Katsnelson, I. V. Grigorieva, S. V. Dubonos, and A. A. Firsov, *Two-dimensional gas of massless Dirac fermions in graphene*, Nature **438**, 197 (2005), doi:doi:10.1038/nature04233,

[13] Y. Zhang, Y.-W. Tan, H. L. Stormer, and P. Kim, *Experimental observation of the quantum Hall effect and Berry's phase in graphene*, Nature **438**, 201 (2005), doi:10.1038/nature04235,

[14] R. Landauer, *Spatial Variation of Currents and Fields Due to Localized Scatterers in Metallic Conduction*, IBM J. Rev. Dev. **1**, 223 (1957), doi:,

[15] A. Szabo and N. S. Ostlund, *Modern Quantum Chemistry*, McGraw-Hill, Toronto, 1989,

[16] N. W. Ashcroft and N. D. Mermin, *Solid State Physics*, Saunders College, New York, 1976,

[17] G. Czycholl, *Theoretische Festkörperphysik*, Springer, Heidelberg, 2004,

[18] E. Hückel, *Quantentheoretische Beiträge zum Benzolproblem: I. Die Elektronenkonfiguration des Benzols und verwandter Verbindungen*, Zeitschrift Für Physik **70**, 204 (1931), doi:10.1007/BF01339530,

[19] E. Hückel, *Quantentheoretische Beiträge zum Benzolproblem: II. Quantentheorie der induzierten Polaritäten*, Zeitschrift Für Physik **72**, 310 (1931), doi:10.1007/BF01341953,

[20] E. Hückel, Zeitschrift Für Physik **76**, 628 (1932), doi:,

[21] E. Hückel, Zeitschrift Für Physik **83**, 632 (1933), doi:,

[22] D. A. Papaconstantopoulos, *Handbook of the Band Structure of Elemental Solids*, Plenum, New York, 1986,

[23] J. C. Slater and G. F. Koster, *Simplified LCAO Method for the Periodic Potential Problem*, Phys. Rev. **94**, 1498 (1954), doi:10.1103/PhysRev.94.1498,

[24] A. V. Podolskiy and P. Vogl, *Compact expression for the angular dependence of tight-binding Hamiltonian matrix elements*, Phys. Rev. B **69**, 233101 (2004), doi:10.1103/PhysRevB.69.233101,

[25] R. O. Jones and O. Gunnarsson, *The density functional formalism, its applications and prospects*, Rev. Mod. Phys. **61**, 689 (1989), doi:10.1103/RevModPhys.61.689,

[26] S. Lundqvist and N. H. March, *Theory of the inhomogeneous electron gas*, Plenum, New York, 1983,

[27] M. C. Payne, M. P. Teter, D. C. Allan, T. A. Arias, and J. D. Joannopoulos, *Iterative minimization techniques for ab initio total-energy calculations: molecular dynamics and conjugate gradients*, Rev. Mod. Phys. **64**, 1045 (1992), doi:10.1103/RevModPhys.64.1045,

[28] R. G. Parr and W. Yang, *Density functional theory of atoms and molecules*, Oxford University Press, New York, 1989,

[29] H. Eschrig, *The fundamentals of density functional theory*, Teubner, Stuttgart, Leipzig, 1996,

[30] R. M. Martin, *Electronic structure: Basis theory and practical methods*, Cambridge University Press, Cambridge, UK, 2004,

[31] C. Fiolhais, F. Nogueira, and M. Marques, eds., *A primer in density functional theory*, Springer, Berlin and Heidelberg, 2003,

[32] L. H. Thomas, *The calculation of atomic fields*, Proc. Cambridge Phil. Roy. Soc. **23**, 542 (1927),

[33] E. Fermi, *Un metodo statistico per la determinazione di alcune priorieta dell'atome*, Rend. Accad. Naz. Lincei **6**, 602 (1927),

[34] P. A. M. Dirac, *Note on exchange phenomena in the Thomas-Fermi atom*, Proc. Cambridge Phil. Roy. Soc. **26**, 376 (1930),

[35] P. Hohenberg and W. Kohn, *Inhomogeneous Electron Gas*, Phys. Rev. **136**, B864 (1964), doi:10.1103/PhysRev.136.B864,

[36] N. D. Mermin, *Thermal properties of the inhomogeneous electron gas*, Phys. Rev. **137**, A1441 (1965), doi:10.1103/PhysRev.137.A1441,

[37] M. Levy, *Universal variational functionals of electron densities, first-order density matrices, and natural spin-orbitals and solution of the n-representability problem*, Proc. Natl. Acad. Sci. USA **76**, 6062 (1979),

[38] M. Levy, *Electron densities in search of hamiltonians*, Phys. Rev. A **26**, 1200 (1982), doi:10.1103/PhysRevA.26.1200,

[39] E. Lieb, *Density functionals for coulom systems*, Int. J. Quant. Chem. **24**, 243 (1983), doi:10.1002/qua.560240302,

[40] W. Kohn and L. J. Sham, *Self-Consistent Equations Including Exchange and Correlation Effects*, Phys. Rev. **140**, A1133 (1965), doi:10.1103/PhysRev.140.A1133,

[41] J. F. Janak, *Proof that* $\partial E/\partial n_i = \epsilon$ *in density-functional theory*, Phys. Rev. B **18**, 7165 (1978), doi:10.1103/PhysRevB.18.7165,

[42] T. L. Beck, *Real-space mesh techniques in density-functional theory*, Rev. Mod. Phys. **72**, 1041 (2000), doi:10.1103/RevModPhys.72.1041,

[43] J. P. Perdew and K. Burke, *Comparison shopping for a gradient-corrected density functional*, Int. J. Quant. Chem. **57**, 309 (1996), doi:10.1002/(SICI)1097-461X(1996)57:3<309::AID-QUA4>3.0.CO;2-1,

[44] P. Ordejón, E. Artacho, and J. M. Soler, *Self-consistent order-N density-functional calculations for very large systems*, Phys. Rev. B **53**, R10441 (1996), doi:10.1103/PhysRevB.53.R10441,

[45] J. M. Soler, E. Artacho, J. D. Gale, A. García, J. Junquera, P. Ordejón, and D. Sánchez-Portal, *The Siesta method for ab initio order-N materials simulation*, J. Phys.-Condens. Matter **14**, 2745 (2002), doi:10.1088/0953-8984/14/11/302,

[46] G. B. Bachelet, D. R. Hamann, and M. Schlüter, *Pseudopotentials that work: From H to Pu*, Phys. Rev. B **26**, 4199 (1982), doi:10.1103/PhysRevB.26.4199,

[47] L. Kleinman and D. M. Bylander, *Efficacious Form for Model Pseudopotentials*, Phys. Rev. Lett. **48**, 1425 (1982), doi:10.1103/PhysRevLett.48.1425,

[48] N. Troullier and J. L. Martins, *Efficient pseudopotentials for plane-wave calculations*, Phys. Rev. B **43**, 1993 (1991),

[49] O. F. Sankey and D. J. Niklewski, *Ab initio multicenter tight-binding model for molecular dynamics simulations and other applications in covalent systems*, Phys. Rev. B **40**, 3979 (1989),

[50] J. P. Lewis, K. R. Glaesemann, G. A. Voth, J. Fritsch, A. A. Demkov, J. Ortega, and O. F. Sankey, *Further developments in the local-orbital densityfunctional- theory tight-binding method*, Phys. Rev. B **64**, 195103 (2001),

[51] J. Junquera, O. Paz, D. Sánchez-Portal, and E. Artacho, *Numerical atomic orbitals for linear-scaling calculations*, Phys. Rev. B **64**, 235111 (2001),

[52] J. Kim, F. Mauri, and G. Galli, *Total-energy global optimizations using nonorthogonal localized orbitals*, Phys. Rev. B **52**, 1640 (1995),

[53] P. Ordejon, *Order-N tight-binding methods for electronic-structure and molecular dynamics*, Comput. Mater. Sci. **12**, 157 (1998),

[54] D. Porezag, T. Frauenheim, T. Köhler, G. Seifert, and R. Kaschner, *Construction of tight-binding-like potentials on the basis of density-functional theory: Application to carbon*, Phys. Rev. B **51**, 12947 (1995), doi:10.1103/PhysRevB.51.12947,

[55] J. Tersoff, *Empirical Interatomic Potential for Carbon, with Applications to Amorphous Carbon*, Phys. Rev. Lett. **61**, 2879 (1988), doi:10.1103/PhysRevLett.61.2879,

[56] G. Seifert and H. Eschrig, *LCAO-Xα calculations of transition metal clusters*, Phys. Stat. Sol. b **127**, 573 (1985), doi:10.1002/pssb.2221270218,

[57] G. Seifert, H. Eschrig, and W. Bieger, Z. Phys. Chem. (Leipzig) **267**, 529 (1986),

[58] H. Eschrig and I. Bergert, *An optimized LCAO version for band structure calculations application to copper*, Phys. Stat. Sol. b **90**, 621 (1978), doi:10.1002/pssb.2220900221,

[59] P. Blaudeck, T. Frauenheim, D. Porezag, G. Seifert, and E. Fromm, *A method and results for realistic molecular dynamic simulation of*

hydrogenated amorphous carbon structures using a scheme consisting of a linear combination of atomic orbitals with the local-density approximation, J. Phys.-Condens. Matter **4**, 6389 (1992), doi:10.1088/0953-8984/4/30/006,

[60] W. M. C. Foulkes and R. Haydock, *Tight-binding models and density-functional theory*, Phys. Rev. B **39**, 12520 (1989), doi:10.1103/PhysRevB.39.12520,

[61] D. Tománek and A. Schluter, *Structure and bonding of small semiconductor clusters*, Phys. Rev. B **36**, 1208 (1987), doi:10.1103/PhysRevB.36.1208,

[62] J. P. Perdew and A. Zunger, *Self-interaction correction to density-functional approximations for many-electron systems*, Phys. Rev. B **23**, 5048 (1981), doi:10.1103/PhysRevB.23.5048,

[63] T. Frauenheim, G. Seifert, M. Elstner, Z. Hajnal, G. Jungnickel, D. Porezag, S. Suhai, and R. Scholz, *A Self-Consistent Charge Density-Functional Based Tight-Binding Method for Predictive Materials Simulations in Physics, Chemistry and Biology*, Phys. Stat. Sol. b **217**, 41 (2000), online,

[64] A. D. Carlo, A. Pecchia, L. Latessa, T. Frauenheim, and G. Seifert, *Introducing Molecular Electronics*, ch. 6, Springer, Berlin and Heidelberg, 2006,

[65] A. Pecchia and A. D. Carlo, *Atomistic theory of transport in organic and inorganic nanostructures*, Reports on Progress in Physics **67**, 1497 (2004), doi:10.1088/0034-4885/67/8/R04,

[66] S. Datta, *Electronic Transport in Mesoscopic Systems*, Cambridge University Press, Cambridge, UK, 1995,

[67] S. Sanvito, *Ab-initio methods for spin-transport at the nanoscale level*, cond-mat/0503445 (2005), cond-mat/0503445,

[68] T. Heinzel, *Mesoscopic electronics in solid state nanostructures*, WILEY-VCH Verlag, Weinheim, 2003,

[69] P. B. Allen, *New method for solving Boltzmann's equation for electrons in metals*, Phys. Rev. B **17**, 3725 (1978), doi:10.1103/PhysRevB.17.3725,

[70] C. T. White and T. N. Todorov, *Carbon nanotubes as long ballistic conductors*, Nature **393**, 240 (1998), doi:10.1038/30420,

[71] P. L. McEuen, M. Bockrath, D. H. Cobden, Y.-G. Yoon, and S. G. Louie, *Disorder, pseudospins, and backscattering in carbon nanotubes*, Phys. Rev. Lett. **83**, 5098 (1999), doi:10.1103/PhysRevLett.83.5098,

[72] S. Frank, P. Poncharal, Z. L. Wang, and W. A. de Heer, *Carbon Nanotube Quantum Resistors*, Science **280**, 1744 (1998),

[73] S. J. Tans, M. H. Devoret, H. Dai, A. Thess, R. E. Smalley, L. J. Geerligs, and C. Dekker, *Individual single-wall carbon nanotubes as quantum wires*, Nature **386**, 474 (1997), doi:10.1038/386474a0,

[74] W. Liang, M. Bockrath, D. Bozovic, J. H. Hafner, M. Tinkham, and H. Park, *Fabry - Perot interference in a nanotube electron waveguide*, Nature **411**, 665 (2001), doi:10.1038/35079517,

[75] J. Appenzeller, R. Martel, P. Avouris, H. Stahl, U. T. Hunger, and B. Lengeler, *Phase-coherent transport in ropes of single-wall carbon nanotubes*, Phys. Rev. B **64**, 121404 (2001), doi:10.1103/PhysRevB.64.121404,

[76] A. Bachtold, M. S. Fuhrer, S. Plyasunov, M. Forero, E. H. Anderson, A. Zettl, and P. L. McEuen, *Scanned probe microscopy of electronic transport in carbon nanotubes*, Phys. Rev. Lett. **84**, 6082 (2000), doi:10.1103/PhysRevLett.84.6082,

[77] N. Nemec, D. Tománek, and G. Cuniberti, *Contact Dependence of Carrier Injection in Carbon Nanotubes: An Ab Initio Study*, Phys. Rev. Lett. **96**, 076802 (2006), doi:10.1103/PhysRevLett.96.076802,

[78] M. Büttiker, Y. Imry, R. Landauer, and S. Pinhas, *Generalized many-channel conductance formula with application to small rings*, Phys. Rev. B **31**, 6207 (1985), doi:10.1103/PhysRevB.31.6207,

[79] Y. V. Sharvin, *A Possible Method for Studying Fermi Surfaces*, Soviet Physics JETP **21**, 655 (1965),

[80] B. J. van Wees, H. van Houten, C. W. J. Beenakker, J. G. Williamson, L. P. Kouwenhoven, D. van der Marel, and C. T. Foxon, *Quantized conductance of point contacts in a two-dimensional electron gas*, Phys. Rev. Lett. **60**, 848 (1988), doi:10.1103/PhysRevLett.60.848,

[81] N. Agraït, J. G. Rodrigo, and S. Vieira, *Conductance steps and quantization in atomic-size contacts*, Phys. Rev. B **47**, 12345 (1993), doi:,

[82] D. S. Fisher and P. A. Lee, *Relation between conductivity and transmission matrix*, Phys. Rev. B **23**, 6851 (1981), doi:10.1103/PhysRevB.23.6851,

[83] L. Pauling, *The nature of the chemical bond. application of results obtained from the quantum mechanics and from a theory of paramagnetic susceptibility to the structure of molecules*, J. Am. Chem. Soc. **53**, 1367 (1931), doi:10.1021/ja01355a027,

[84] P. R. Wallace, *The band theory of graphite*, Phys. Rev. **71**, 622 (1947), doi:10.1103/PhysRev.71.622,

[85] R. Saito, G. Dresselhaus, and M. S. Dresselhaus, *Physical Properties of Carbon Nanotubes*, Imperial College Press, London, 1998,

[86] N. M. R. Peres, F. Guinea, and A. H. Castro Neto, *Electronic properties of disordered two-dimensional carbon*, Phys. Rev. B **73**, 125411 (2006), doi:10.1103/PhysRevB.73.125411,

[87] M. S. Dresselhaus, G. Dresselhaus, and R. Saito, *Carbon fibers based on C_60 and their symmetry*, Phys. Rev. B **45**, 6234 (1992), doi:10.1103/PhysRevB.45.6234,

[88] M. Monthioux and V. L. Kuznetsov, *Who should be given the credit for the discovery of carbon nanotubes?*, Carbon **44**, 1621 (2006), doi:10.1016/j.carbon.2006.03.019,

[89] L. V. Radushkevich and V. M. Lukyanovich, *O strukture ugleroda, obrazujucegosja pri termiceskom razlozenii okisi ugleroda na zeleznom kontakte (in russian)*, Zurn. Fisic. Chim. **26**, 88 (1952),

[90] A. Oberlin, M. Endo, and T. Koyama, *Filamentous growth of carbon through benzene decomposition*, J. Cryst. Growth **32**, 335 (1976),

[91] S. Iijima and T. Ichihashi, *Single-shell carbon nanotubes of 1-nm diameter*, Nature **363**, 603 (1993), doi:10.1038/363603a0,

[92] D. S. Bethune, C. H. Klang, M. S. de Vries, G. Gorman, R. Savoy, J. Vazquez, and R. Beyers, *Cobalt-catalysed growth of carbon nanotubes with single-atomic-layer walls*, Nature **363**, 605 (1993), doi:10.1038/363605a0,

[93] S. Reich, C. Thomsen, and J. Maultzsch, *Carbon Nanotubes*, Wiley-VCH, Berlin, 2004,

[94] M. S. Dresselhaus, G. Dresselhaus, and P. Avouris, eds., *Carbon nanotubes*, vol. 80 of *Topics in Applied Physics*, Springer-Verlag, Berlin Heidelberg, 2001,

[95] M. Dresselhaus, G. Dresselhaus, P. Eklund, and R. Saito, *Carbon nanotubes*, Phys. World **11**, 33 (1998), online,

[96] C. Dekker, *Carbon Nanotubes as molecular wires*, Physics Today **52**, 22 (1999), online,

[97] T. W. Odom, J.-L. Huang, P. Kim, , and C. M. Lieber, *Structure and Electronic Properties of Carbon Nanotubes*, J. Phys. Chem. B **104**, 2794 (2000), doi:10.1021/jp993592k,

[98] Saito Laboratory Homepage: www.surf.nuqe.nagoya-u.ac.jp,

[99] R. Saito, M. Fujita, G. Dresselhaus, and M. Dresselhaus, *Electronic structure of chiral graphene tubules*, Appl. Phys. Lett. **60**, 2204 (1992), doi:10.1063/1.107080,

[100] N. Hamada, S. Sawada, and A. Oshiyama, *New one-dimensional conductors: Graphitic microtubules*, Phys. Rev. Lett. **68**, 1579 (1992), doi:10.1103/PhysRevLett.68.1579,

[101] J. Yi, M. Porto, and G. Cuniberti, *Encyclopedia of Nanoscience and Nanotechnology*, vol. 5, American Scientific Publishers, California, 2004,

[102] M. Armano, G. A. Bongiorno, A. Donarini, M. Romiti, E. Bellotti, and P. Milani, Nuovo Cimento **XLI**, 219 (1996),

[103] H. W. Kroto, J. R. Heath, S. C. O'Brien, R. F. Curl, and R. E. Smalley, C_{60}*: Buckminsterfullerene*, Nature **318**, 162 (1985), doi:10.1038/318162a0,

[104] C. Joachim and J. K. Gimzewski, *An electromechanical amplifier using a single molecule*, Chem. Phys. Lett. **265**, 353 (1997), doi:10.1016/S0009-2614(97)00014-6,

[105] H. Park, J. Park, A. K. L. Lim, E. H. Anderson, A. P. Alivisatos, and P. L. McEuen, *Nanomechanical oscillations in a single-C60 transistor*, Nature **407**, 57 (2000),

[106] S. Alavi, B. Larade, J. Taylor, H. Guo, and T. Seideman, *Current-triggered vibrational excitation in single-molecule transistors*, Chem. Phys. **281**, 293 (2002), doi:10.1016/S0301-0104(02)00567-0,

[107] J. Park, A. N. Pasupathy, J. I. Goldsmith, C. Chang, Y. Yaish, J. R. Petta, M. Rinkoski, J. P. Sethna, H. D. A. na, P. L. McEuen, and D. C. Ralph, *Coulomb blockade and the Kondo effect in single-atom transistors*, Nature **417**, 722 (2002), doi:10.1038/nature00791,

[108] A. R. Champagne, A. N. Pasupathy, and D. C. Ralph, *Mechanically adjustable and electrically gated single-molecule transistors*, Nano Letters **5**, 305 (2005), doi:10.1021/nl0480619,

[109] W. Krätschmer, L. Lamb, K. Fostiropoulos, and D. R. Huffman, *Solid C_{60}: a new form of carbon*, Nature **347**, 354 (1990), doi:10.1038/347354a0,

[110] R. Taylor, J. P. Hare, A. K. Abdul-Sada, and H. W. Kroto, *Isolation, separation and characterisation of the fullerenes C_{60} and C_{70}: the third form of carbon*, J. Chem. Soc.: Chem. Comm. **20**, 1423 (1990), doi:10.1039/C39900001423,

[111] H. Ajie, M. M. Alvarez, S. J. Anz, R. D. Beck, F. Diederich, K. Fostiropoulos, D. R. Huffman, W. Kraetschmer, Y. Rubin, K. E. Schriver, D. Sensharma, and R. L. Whetten, *Characterization of the soluble all-carbon molecules C_{60} and C_{70}*, J. Phys. Chem. **94**, 8630 (1990), doi:10.1021/j100387a005,

[112] O. Gunnarsson, *Superconductivity in fullerides*, Rev. Mod. Phys. **69**, 575 (1997), doi:10.1103/RevModPhys.69.575,

[113] D. A. Abanin, P. A. Lee, and L. S. Levitov, *Spin-Filtered Edge States and Quantum Hall Effect in Graphene*, Phys. Rev. Lett. **96**, 176803 (2006), doi:10.1103/PhysRevLett.96.176803,

[114] N. M. R. Peres, A. H. C. Neto, and F. Guinea, *Conductance quantization in mesoscopic graphene*, Phys. Rev. B **73**, 195411 (2006), doi:10.1103/PhysRevB.73.195411,

[115] A. H. C. Neto, F. Guinea, and N. M. R. Peres, *Edge and surface states in the quantum Hall effect in graphene*, Phys. Rev. B **73**, 205408 (2006), doi:10.1103/PhysRevB.73.205408,

[116] L. Brey and H. A. Fertig, *Edge states and the quantized Hall effect in graphene*, Phys. Rev. B **73**, 195408 (2006), doi:10.1103/PhysRevB.73.195408,

[117] T. Ohta, A. Bostwick, T. Seyller, K. Horn, and E. Rotenberg, *Controlling the Electronic Structure of Bilayer Graphene*, Science **313**, 951 (2006), doi:10.1126/science.113068,

[118] C. H. Xu, C. Z. Wang, C. T. Chan, and K. M. Ho, *A transferable tight-binding potential for carbon*, J. Phys.-Condens. Matter **4**, 6047 (1992), doi:10.1088/0953-8984/4/28/006,

[119] S. lijima, T. Ichihashi, and Y. Ando, *Pentagons, heptagons and negative curvature in graphite microtubule growth*, Nature **356**, 776 (1992), doi:10.1038/356776a0,

[120] S. Ihara, S. Itoh, and J. Kitakami, *Helically coiled cage forms of graphitic carbon*, Phys. Rev. B **48**, 5643 (1993), doi:10.1103/PhysRevB.48.5643,

[121] Z. Yao, H. W. C. Postma, L. Balents, and C. Dekker, *Carbon nanotube intramolecular junctions*, Nature **402**, 273 (1999), doi:10.1038/46241,

[122] H. W. C. Postma, T. Teepen, Z. Yao, M. Grifoni, and C. Dekker, *Carbon Nanotube Single-Electron Transistors at Room Temperature*, Science **293**, 76 (2001),

[123] A. Javey, J. Guo, Q. Wang, M. Lundstrom, and H. Dai, *Ballistic carbon nanotube field-effect transistors*, Nature **424**, 654 (2003),

[124] J. A. Misewich, R. Martel, P. Avouris, J. C. Tsang, S. Heinze, and J. Tersoff, *Electrically Induced Optical Emission from a Carbon Nanotube FET*, Science **300**, 783 (2003),

[125] T. Rueckes, K. Kim, E. Joselevich, G. Y. Tseng, C.-L. Cheung, and C. M. Lieber, *Carbon Nanotube-Based Nonvolatile Random Access Memory for Molecular Computing*, Science **289**, 94 (2000),

[126] S. Heinze, J. Tersoff, and P. Avouris, *Carbon nanotube electronics and optoelectronics*, in Cuniberti *et. al.* [4], doi:10.1007/b101525,

[127] J. Yi and G. Cuniberti, *A three terminal ring interferometer logic gate*, Annals of the New York Academy of Sciences **1006**, 306 (2003), doi:10.1196/annals.1292.021,

[128] D. Zhou and S. Seraphin, *Complex branching phenomena in the growth of carbon nanotubes*, Chem. Phys. Lett. **238**, 286 (1995),

[129] J. Li, C. Papadopoulos, and J. Xu, *Nanoelectronics: Growing Y-junction carbon nanotubes*, Nature **402**, 253 (1999),

[130] Y. C. Sui, J. A. González-León, A. Bermúdez, and J. M. Saniger, *Synthesis of multi branched carbon nanotubes in porous anodic aluminum oxide template*, Carbon **39**, 1709 (2001),

[131] B. Gan, J. Ahn, Q. Zhang, S. F. Yoon, Rusli, Q. F. Huang, H. Yang, M. B. Yu, and W. Z. Li, *Branching carbon nanotubes deposited in HFCVD system*, Diamond and Related Materials **9**, 897 (2000),

[132] B. C. Satishkumar, P. J. Thomas, A. Govindaraj, and C. N. R. Rao, *Y-junction carbon nanotubes*, Appl. Phys. Lett. **77**, 2530 (2000),

[133] F. L. Deepak, A. Govindaraj, and C. N. R. Rao, *Synthetic strategies for Y-junction carbon nanotubes*, Chem. Phys. Lett. **345**, 5 (2001),

[134] J.-M. Ting and C.-C. Chang, *Multijunction carbon nanotube network*, Appl. Phys. Lett. **80**, 324 (2002),

[135] H. Zhu, L. Ci, C. Xu, J. Liang, and D. Wu, *Growth mechanism of Y-junction carbon nanotubes*, Diamond and Related Materials **11**, 1349 (2002),

[136] Z. Klusek, S. Datta, P. Byszewski, P. Kowalczyk, and W. Kozlowski, *Scanning tunneling microscopy and spectroscopy of Y-junction in carbon nanotubes*, Surface Science **507-510**, 577 (2002),

[137] Z. Osváth, A. Koós, Z. Horváth, J. Gyulai, A. Benito, M. Martínez, W. Maser, and L. Biró, *Arc-grown Y-branched carbon nanotubes observed by scanning tunneling microscopy (STM)*, Chem. Phys. Lett. **365**, 338 (2002),

[138] P. Nagy, R. Ehlich, L. Biró, and J. Gyulai, *Y-branching of single walled carbon nanotubes*, Appl. Phys. A **70**, 481 (2000),

[139] M. Terrones, F. Banhart, N. Grobert, J.-C. Charlier, H. Terrones, and P. M. Ajayan, *Molecular Junctions by Joining Single-Walled Carbon Nanotubes*, Phys. Rev. Lett. **89**, 075505 (2002),

[140] M. S. Fuhrer, J. Nygård, L. Shih, M. Forero, Y.-G. Yoon, M. S. C. Mazzoni, H. J. Choi, J. Ihm, S. G. Louie, A. Zettl, and P. L. McEuen, *Crossed Nanotube Junctions*, Science **288**, 494 (2000),

[141] C. Papadopoulos, A. Rakitin, J. Li, A. S. Vedeneev, and J. M. Xu, *Electronic Transport in Y-Junction Carbon Nanotubes*, Phys. Rev. Lett. **85**, 3476 (2000),

[142] P.-W. Chiu, M. Kaempgen, and S. Roth, *Band-Structure Modulation in Carbon Nanotube T Junctions*, Phys. Rev. Lett. **92**, 246802 (2004), doi:10.1103/PhysRevLett.92.246802,

[143] B. Gan, J. Ahn, Q. Zhang, Q. F. Huang, C. Kerlit, S. F. Yoon, Rusli, V. A. Ligachev, X.-B. Zhang, and W.-Z. Li, *Topological structure of Y-junction carbon nanotubes*, Materials Letters **45**, 315 (2000),

[144] G. Treboux, P. Lapstun, and K. Silverbrook, *Conductance in nanotube Y-junctions*, Chem. Phys. Lett. **306**, 402 (1999),

[145] V. H. Crespi, *Relations between global and local topology in multiple nanotube junctions*, Phys. Rev. B **58**, 12671 (1998), doi:10.1103/PhysRevB.58.12671,

[146] G. E. Scuseria, *Negative curvature and hyperfullerenes*, Chem. Phys. Lett. **195**, 534 (1992), doi:10.1016/0009-2614(92)85558-R,

[147] L. A. Chernozatonskii, *Carbon nanotube connectors and planar jungle gyms*, Physics Letters A **172**, 173 (1992),

[148] M. Menon and D. Srivastava, *Carbon Nanotube "T Junctions": Nanoscale Metal-Semiconductor-Metal Contact Devices*, Phys. Rev. Lett. **79**, 4453 (1997),

[149] A. Pérez-Garrido and A. Urbina, *Metal-semiconductor heterojunctions in T-shaped carbon nanotubes*, Carbon **40**, 1227 (2002),

[150] A. N. Andriotis, M. Menon, D. Srivastava, and L. Chernozatonskii, *Ballistic switching and rectification in single wall carbon nanotube Y junctions*, Appl. Phys. Lett. **79**, 266 (2001),

[151] A. N. Andriotis, M. Menon, D. Srivastava, and L. Chernozatonskii, *Transport properties of single-wall carbon nanotube Y junctions*, Phys. Rev. B **65**, 165416 (2002),

[152] V. Meunier, M. B. Nardelli, J. Bernholc, T. Zacharia, and J.-C. Charlier, *Intrinsic electron transport properties of carbon nanotube Y-junctions*, Appl. Phys. Lett. **81**, 5234 (2002),

[153] M. Menon, A. N. Andriotis, D. Srivastava, I. Ponomareva, and L. Chernozatonskii, *Carbon Nanotube "T Junctions": Formation Pathways and Conductivity*, Phys. Rev. Lett. **91**, 145501 (2003),

[154] S. Chen, B. Trauzettel, and R. Egger, *Landauer-Type Transport Theory for Interacting Quantum Wires: Application to Carbon Nanotube Y Junctions*, Phys. Rev. Lett. **89**, 226404 (2002),

[155] U. Fano, *Effects of Configuration Interaction on Intensities and Phase Shifts*, Phys. Rev. **124**, 1866 (1961),

[156] J. Kim, J.-R. Kim, J.-O. Lee, J. W. Park, H. M. So, N. Kim, K. Kang, K.-H. Yoo, and J.-J. Kim, *Fano Resonance in Crossed Carbon Nanotubes*, Phys. Rev. Lett. **90**, 166403 (2003),

[157] Z. Zhang, V. Chandrasekhar, D. A. Dikin, and R. S. Ruoff, *Conduction in Carbon Nanotubes Through Metastable Resonant States*, cond-mat/0311360 (2003),

[158] W. Yi, L. Lu, H. Hu, Z. W. Pan, and S. S. Xie, *Tunneling into Multiwalled Carbon Nanotubes: Coulomb Blockade and the Fano Resonance*, Phys. Rev. Lett. **91**, 076801 (2003),

[159] B. Babić and C. Schönenberger, *Observation of Fano-Resonances in Single-Wall Carbon Nanotubes*, Phys. Rev. B **70**, 195408 (2004), doi:10.1103/PhysRevB.70.195408,

[160] G. Kim, S. B. Lee, T.-S. Kim, and J. Ihm, *Fano resonance and orbital filtering in multiply connected carbon nanotubes*, Phys. Rev. B **71**, 205415 (2005),

[161] R. Landauer, *Electrical transport in open and closed systems*, Zeitschrift Für Physik B **68**, 217 (1987),

[162] M. Büttiker, *Symmetry of electrical conduction*, IBM J. Rev. Dev. **32**, 317 (1988), doi:,

[163] G. Cuniberti, F. Grossmann, and R. Gutiérrez, *The Role of Contacts in Molecular Electronics*, Adv. Solid State Phys. **42**, 133 (2002),

[164] M. Elstner, D. Porezag, G. Jungnickel, J. Elsner, M. Haugk, T. Frauenheim, S. Suhai, and G. Seifert, *Self-consistent-charge density-functional tight-binding method for simulations of complex materials properties*, Phys. Rev. B **58**, 7260 (1998), doi:10.1103/PhysRevB.58.7260,

[165] A. Tikhonov, R. D. Coalson, and Y. Dahnovsky, *Calculating electron transport in a tight binding model of a field-driven molecular wire: Floquet theory approach*, J. Chem. Phys. **116**, 10909 (2002), doi:10.1063/1.1448292,

[166] *Gaussian 98*, 1998,

[167] K. Hedberg, L. Hedberg, D. S. Bethune, C. A. Brown, H. C. Dorn, R. D. Johnson, and M. de Vries, *Bond Lengths in Free Molecules of Buckminsterfullerene, C_{60}, from Gas-Phase Electron Diffraction*, Science **254**, 410 (1991), doi:10.1126/science.254.5030.410,

[168] R. S. Ruoff and A. L. Ruoff, *Is C_{60} stiffer than diamond?*, Nature **350**, 663 (1991), doi:10.1038/350663b0,

[169] J. Kürti, G. Kresse, and H. Kuzmany, *First-principles calculations of the radial breathing mode of single-wall carbon nanotubes*, Phys. Rev. B **58**, R8869 (1998), doi:10.1103/PhysRevB.58.R8869,

[170] C. M. Varma, E. I. Blount, P. Vashista, and W. Weber, *Electron-phonon interactions in transition metals*, Phys. Rev. B **19**, 6130 (1979), doi:10.1103/PhysRevB.19.6130,

[171] M. Schluter, M. Lannoo, M. Needels, G. A. Baraff, and D. Tománek, *Electron-phonon coupling and superconductivity in alkali-intercalated C_{60} solid*, Phys. Rev. Lett. **68**, 526 (1992), doi:10.1103/PhysRevLett.68.526,

[172] M. T. Dove, *Structure and Dynamics: an atomic view of materials*, Oxford University Press, Oxfors, 2003,

[173] G. B. Adams, J. B. Page, O. F. Sankey, K. Sinha, J. Menendez, and D. R. Huffman, *First-principles quantum molecular-dynamics study of the vibrations of icosahedral C_{60}*, Phys. Rev. B **44**, 4052 (1991), doi:10.1103/PhysRevB.44.4052,

[174] H. Kuzmany, M. Matus, B. Burger, and J. Winter, *Raman Scattering in C_{60} fullerenes and fullerides*, Adv. Mater. **6**, 731 (1994), doi:10.1002/adma.19940061004,

[175] H. Ohnishi, Y. Kondo, and K. Takayanagi, *Quantized conductance through individual rows of suspended gold atoms*, Nature **395**, 780 (1998), doi:10.1038/27399,

[176] J. I. Pascual, J. Méndez, J. Gómez-Herrero, A. M. Baró, N. García, and V. T. Binh, *Quantum contact in gold nanostructures by scanning tunneling microscopy*, Phys. Rev. Lett. **71**, 1852 (1993), doi:,

[177] J. L. Costa-Krämer, N. García, P. García-Mochales, P. A. Serena, M. I. Marqués, and A. Correia, *Conductance quantization in nanowires formed between micro and macroscopic metallic electrodes*, Phys. Rev. B **55**, 5416 (1997), doi:,

[178] B. Ludoph, M. H. Devoret, D. Esteve, C. Urbina, and J. M. van Ruitenbeek, *Evidence for Saturation of Channel Transmission from Conductance Fluctuations in Atomic-Size Point Contacts.*, Phys. Rev. Lett. **82**, 1530 (1999), doi:,

[179] A. I. Yanson, G. R. Bollinger, H. E. van den Brom, N. Agraït, and J. M. van Ruitenbeek, *Formation and manipulation of a metallic wire of single gold atoms*, Nature **395**, 783 (1998), doi:10.1038/27405,

[180] H. Yasuda and A. Sakai, *Conductance of atomic-scale gold contacts under high-bias voltages*, Phys. Rev. B **56**, 1069 (1997), doi:,

[181] Y. Kondo and K. Takayanagi, *Gold Nanobridge Stabilized by Surface Structure*, Phys. Rev. Lett. **79**, 3455 (1997), doi:10.1103/PhysRevLett.79.3455,

[182] Y. Kondo and K. Takayanagi, *Synthesis and Characterization of Helical Multi-Shell Gold Nanowires*, Science **289**, 606 (2000), doi:10.1126/science.289.5479.606,

[183] Y. Oshima, A. Onga, and K. Takayanagi, *Helical gold nanotube synthesized at 150 K*, Phys. Rev. Lett. **91**, 205503 (2003), doi:10.1103/PhysRevLett.91.205503,

[184] D. Sánchez-Portal, E. Artacho, J. Junquera, P. Ordejón, A. García, and J. M. Soler, *Stiff Monatomic Gold Wires with a Spinning Zigzag Geometry*, Phys. Rev. Lett. **83**, 3884 (1999), doi:,

[185] H. Häkkinen, R. N. Barnett, A. G. Scherbakov, and U. Landman, *Nanowire Gold Chains: Formation Mechanisms and Conductance*, J. Phys. Chem. B **104**, 9063 (2000), doi:10.1021/jp002691r,

[186] O. Gülseren, F. Ercolessi, and E. Tosatti, *Noncrystalline Structure of Ultrathin Unsupported Nanowires*, Phys. Rev. Lett. **80**, 3775 (1998), doi:10.1103/PhysRevLett.80.3775,

[187] G. Bilalbegović, *Structure and stability of finite gold nanowires*, Phys. Rev. B **58**, 15412 (1998), doi:10.1103/PhysRevB.58.15412,

[188] E. Z. da Silva, A. J. R. da Silva, and A. Fazzio, *How Do Gold Nanowires Break?*, Phys. Rev. Lett. **87**, 256102 (2001), doi:10.1103/PhysRevLett.87.256102,

[189] E. Tosatti, S. Prestipino, S. Kostlmeier, A. dal Corso, and F. di Tolla, *String Tension and Stability of Magic Tip-Suspended Nanowires*, Science **291**, 288 (2001), doi:10.1126/science.291.5502.288,

[190] N. Takeuchi, C. T. Chan, and K. M. Ho, *Theoretical study of noble-metal (100) surface reconstructions using first-principles techniques*, Phys. Rev. Lett. **63**, 1273 (1989), doi:10.1103/PhysRevLett.63.1273,

[191] Y. Oshima, K. Mouri, H. Hirayama, and K. Takayanagi, *Quantized Electrical Conductance of Gold Helical Multishell Nanowires*, Journal of the Physical Society of Japan **75**, 053705 (2006), doi:10.1143/JPSJ.75.053705,

[192] R. T. Senger, S. Dag, and S. Ciraci, *Chiral Single-Wall Gold Nanotubes*, Phys. Rev. Lett. **93**, 196807 (2004), doi:10.1103/PhysRevLett.93.196807,

[193] T. Ono and K. Hirose, *First-Principles Study of Electron-Conduction Properties of Helical Gold Nanowires*, Phys. Rev. Lett. **94**, 206806 (2005), doi:10.1103/PhysRevLett.94.206806,

[194] X. Yang and J. Dong, *Geometrical and electronic structures of the (5, 3) single-walled gold nanotube from first-principles calculations*, Phys. Rev. B **71**, 233403 (2005), doi:10.1103/PhysRevB.71.233403,

[195] I. Boustani, A. Rubio, and J. A. Alonso, *Ab initio study of B_{32} clusters: competition between spherical, quasiplanar and tubular isomers*, Chem. Phys. Lett. **311**, 21 (1999), doi:10.1016/S0009-2614(99)00767-8,

[196] A. Quandt and I. Boustani, *Boron Nanotubes*, ChemPhysChem **6**, 2001 (2005), doi:10.1002/cphc.200500205,

[197] M. H. Evans, J. D. Joannopoulos, and S. T. Pantelides, *Electronic and mechanical properties of planar and tubular boron structures*, Phys. Rev. B **72**, 045434 (2005), doi:10.1103/PhysRevB.72.045434,

[198] D. Ciuparu, R. F. Klie, Y. Zhu, and L. Pfefferle, *Synthesis of Pure Boron Single-Wall Nanotubes*, J. Phys. Chem. B **108**, 3967 (2004), doi:10.1021/jp049301b S1089-5647(04)09301-0,

[199] A. Hasegawa, K. Yoshizawa, and K. Hirao, *Electronic structure of gold nanowires*, Chem. Phys. Lett. **345**, 367 (2001), doi:10.1016/S0009-2614(01)00900-9,

[200] P. F. Bagwell and T. P. Orlando, *Landauer's conductance formula and its generalization to finite voltages*, Phys. Rev. B **40**, 1456 (1989), doi:10.1103/PhysRevB.40.1456,

[201] W. A. Harrison, *Electronic Structure of Polyvalent Metals*, Phys. Rev. **118**, 1190 (1960), doi:10.1103/PhysRev.118.1190,

[202] M. Ivanov, D. Ilieva, G. Minchev, T. Petrova, V. Dragostinova, T. Todorov, and L. Nikolova, *Temperature-dependent light intensity controlled optical switching Iin azobenzene polymers*, Appl. Phys. Lett. **86**, 181902 (2005),

[203] X. Xiao, D. Brune, J. He, S. Lindsay, C. B. Gormand, and N. Tao, *Redox-gated electron transport in electrically wired ferrocene molecules*, Chem. Phys. **326**, 138 (2006), doi:10.1016/j.chemphys.2006.02.022,

[204] C. Joachim and M. A. Ratner, *Molecular electronics: Some views on transport junctions and beyond*, Proc. Natl. Acad. Sci. USA **102**, 8801 (2005),

[205] I. Visoly-Fisher, K. Daie, Y. Terazono, C. Herrero, F. Fungo, L. Otero, E. Durantini, J. J. Silber, L. Sereno, D. Gust, T. A. Moore, A. L. Moore, and S. M. Lindsay, *Conductance of a biomolecular wire*, Proc. Natl. Acad. Sci. USA **103**, 8686 (2006),

[206] T. Albrecht, A. Guckian, J. Ulstrup, and J. G. Vos, *Transistor-like behavior of transition metal complexes*, Nano Letters **5**, 1451 (2005), doi:10.1021/nl050818o,

[207] H. B. Weber, J. Reichert, F. Weigend, R. Ochs, D. Beckmann, M. Mayor, R. Ahlrichs, and H. v. Löhneysen, *Electronic transport*

through single conjugated molecules, Chem. Phys. **281**, 113 (2002), doi:10.1016/S0301-0104(02)00343-9,

[208] J. Reichert, R. Ochs, D. Beckmann, H. B. Weber, M. Mayor, and H. v. Löhneysen, *Driving Current through Single Organic Molecules*, Phys. Rev. Lett. **88**, 176804 (2002), doi:10.1103/PhysRevLett.88.176804,

[209] M. Elbing, R. Ochs, M. Koentopp, M. Fischer, C. von Hänisch, F. Weigend, F. Evers, H. B. Weber, and M. Mayor, *A single-molecule diode*, Proc. Natl. Acad. Sci. USA **102**, 8815 (2005), doi:10.1073/pnas.0408888102,

[210] Z. J. Donhauser, B. A. Mantooth, K. F. Kelly, L. A. Bumm, J. D. Monnell, J. J. Stapleton, D. W. Price, A. M. Rawlett, D. L. Allara, J. M. Tour, and P. S. Weiss, *Conductance Switching in Single Molecules Through Conformational Changes*, Science **292**, 2303 (2001), doi:10.1126/science.1060294,

[211] M. Lastapis, M. Martin, D. Riedel, L. Hellner, G. Comtet, and G. Dujardin, *Picometer-Scale Electronic Control of Molecular Dynamics Inside a Single Molecule*, Science **308**, 1000 (2005), doi:10.1126/science.1108048,

[212] S. W. Wu, G. V. Nazin, X. Chen, X. H. Qiu, and W. Ho, *Control of Relative Tunneling Rates in Single Molecule Bipolar Electron Transport*, Phys. Rev. Lett. **93**, 236802 (2004), doi:10.1103/PhysRevLett.93.236802,

[213] A. Aviram and M. A. Ratner, *Molecular rectifiers*, Chem. Phys. Lett. **29**, 277 (1974), doi:10.1016/0009-2614(74)85031-1,

[214] M. Mayor, C. von Hänisch, H. B. Weber, J. Reichert, and D. Beckmann, *A trans-Platinum(II) Complex as a Single-Molecule Insulator*, Angew. Chem. Int. Ed. Engl. **41**, 1183 (2002), doi:10.1002/1521-3773(20020402)41:7<1183::AID-ANIE1183>3.0.CO;2-Z,

[215] M. A. Reed, C. Zhou, C. J. Muller, T. P. Burgin, and J. M. Tour, *Conductance of a Molecular Junction*, Science **278**, 252 (1997), doi:10.1126/science.278.5336.252,

[216] V. V. Zhirnov and R. K. Cavin, *Molecular electronics: Chemistry of molecules or physics of contacts-*, Nature Materials **5**, 11 (2006), doi:10.1038/nmat1554,

[217] F. Moresco, G. Meyer, K.-H. Rieder, H. Tang, A. Gourdon, and C. Joachim, *Conformational Changes of Single Molecules Induced by Scanning Tunneling Microscopy Manipulation: A Route to Molecular Switching*, Phys. Rev. Lett. **86**, 672 (2001), doi:10.1103/PhysRevLett.86.672,

[218] J. Gu, B. Liang, L. Liu, Y. Tian, Y. Chen, B. Lu, and Z. Lu, *Photoinduced properties of liquid crystalline azobenzene polymer in Langmuir-Blodgett films investigated by surface plasmon resonance*, Thin Solid Films **327-329**, 427 (1998), doi:10.1016/S0040-6090(98)00678-6,

[219] R. Gutiérrez, F. Grossmann, and R. Schmidt, *Conductance Properties of Stilbenoid Molecules*, ChemPhysChem **4**, 1252 (2003), doi:10.1002/cphc.200300768,

[220] T. Hugel, N. B. Holland, A. Cattani, L. Moroder, M. Seitz, and H. E. Gaub, *Single-Molecule Optomechanical Cycle*, Science **296**, 1103 (2002), doi:10.1126/science.1069856,

[221] M. Irie, Mol. Cryst. Liq. Cryst. **227**, 263 (1993),

[222] C. Renner, J. Cramer, R. Behrendt, and L. Moroder, *Photomodulation of conformational states. II. Mono- and bicyclic peptides with (4-aminomethyl)phenylazobenzoic acid as backbone constituent*, Biological Polymers **54**, 501 (2000), doi:10.1002/1097-0282(200012)54:7<501::AID-BIP30>3.0.CO;2-8,

[223] C. Zhang, M.-H. Du, H.-P. Cheng, X.-G. Zhang, A. E. Roitberg, and J. L. Krause, *Coherent Electron Transport through an Azobenzene Molecule: A Light-Driven Molecular Switch*, Phys. Rev. Lett. **92**, 158301 (2004), doi:10.1103/PhysRevLett.92.158301,

[224] C. Zhang, Y. He, H.-P. Cheng, Y. Xue, M. A. Ratner, X.-G. Zhang, and P. Krstic, *Current-voltage characteristics through a single light-sensitive molecule*, Phys. Rev. B **73**, 125445 (2006), doi:10.1103/PhysRevB.73.125445,

[225] X. Guo, J. P. Small, J. E. Klare, Y. Wang, M. S. Purewal, I. W. Tam, B. H. Hong, R. Caldwell, L. Huang, S. O'Brien, J. Yan, R. Breslow, S. J. Wind, J. Hone, P. Kim, and C. Nuckolls, *Covalently Bridging Gaps in Single-Walled Carbon Nanotubes with Conducting Molecules*, Science **311**, 356 (2006), doi:10.1126/science.1120986,

[226] Alex Holleitner, private communication,

[227] F. Grossmann, R. Gutiérrez, and R. Schmidt, *Conductance Calculations for Real Systems on the Nanoscale*, ChemPhysChem **3**, 650 (2002), doi:10.1002/1439-7641(20020816)3,

[228] Y. Kobayashi, K. Fukui, T. Enoki, K. Kusakabe, and Y. Kaburagi, *Observation of zigzag and armchair edges of graphite using scanning tunneling microscopy and spectroscopy*, Phys. Rev. B **71**, 193406 (2005),

[229] Y.-K. Kwon, S. Berber, and D. Tománek, *Thermal Contraction of Carbon Fullerenes and Nanotubes*, Phys. Rev. Lett. **92**, 015901 (2004), doi:10.1103/PhysRevLett.92.015901,

[230] C. Joachim, J. K. Gimzewski, and A. Aviram, *Electronics using hybrid-molecular and mono-molecular devices*, Nature **408**, 541 (2000), doi:10.1038/35046000,

[231] M. A. Reed and J. M. Tour, *Computing With Molecules*, Scientific American **282**, 86 (2000),

[232] R. Waser, ed., *Nanoelectronics and Information Technology*, Wiley-VCH, Weinheim, 2003,

[233] C. E. T. Gonçalves da Silva and B. Koiller, *Local density of states in a disordered chain: A renormalization group approach*, Solid State Commun. **40**, 215 (1981), doi:10.1016/0038-1098(81)90743-2,

[234] I. Appelbaum, T. Wang, J. D. Joannopoulos, and V. Narayanamurti, *Ballistic hot-electron transport in nanoscale semiconductor heterostructures: Exact self-energy of a three-dimensional periodic tight-binding Hamiltonian*, Phys. Rev. B **69**, 165301 (2004), doi:10.1103/PhysRevB.69.165301,

[235] F. Guinea, C. Tejedor, F. Flores, and E. Louis, *Effective two-dimensional Hamiltonian at surfaces*, Phys. Rev. B **28**, 4397 (1983), doi:10.1103/PhysRevB.28.4397,

[236] M. P. López Sancho, J. M. López Sancho, and J. Rubio, *Quick iterative scheme for the calculation of transfer matrices: application to Mo(100)*, J. Phys. F: Met. Phys. **14**, 1205 (1984), doi:10.1088/0305-4608/14/5/016,

[237] L. M. Falicov and F. Yndurain, *Model calculation of the electronic structure of a (111) surface in a diamond-structure solid*, J. Phys. C **8**, 147 (1975), doi:10.1088/0022-3719/8/2/009,

[238] V. Anishchik, L. M. Falicov, and F. Yndurain, *Electronic surface properties of group V semimetals*, Surface Science **57**, 375 (1976), doi:10.1016/0039-6028(76)90189-8,

[239] E.-N. Foo, M. F. Thorpe, and D. Weaire, *Effective surface potential method for calculating surface states*, Surface Science **57**, 323 (1976), doi:10.1016/0039-6028(76)90186-2,

[240] E. J. Mele and J. D. Joannopoulos, *Electronic states at unrelaxed and relaxed GaAs (110) surfaces*, Phys. Rev. B **17**, 1816 (1978), doi:10.1103/PhysRevB.17.1816,

[241] M. B. Nardelli, *Electronic transport in extended systems: Application to carbon nanotubes*, Phys. Rev. B **60**, 7828 (1999), doi:10.1103/PhysRevB.60.7828,

[242] A. R. Williams and D. Weaire, *The Löwdin technique as an exact folding procedure in band-structure calculations*, J. Phys. C **9**, L47 (1976), doi:10.1088/0022-3719/9/2/005,

[243] C. J. Lambert and D. Weaire, *Decimation and Anderson Localization*, Phys. Stat. Sol. b **101**, 591 (1980), doi:10.1002/pssb.2221010218,

[244] M. Leadbeater and C. J. Lambert, *A decimation method for studying transport properties of disordered systems*, Ann. Phys. (Leipzig) **7**, 498 (1998), online,

[245] P.-O. Löwdin, *A note on the quantum-mechanical perturbation theory*, J. Chem. Phys. **19**, 1396 (1951), doi:10.1063/1.1748067,

[246] M. L. Cohen and V. Heine, *The fitting of pseudopotentials to experimental data and their subsequent application*, in Ehrenreich *et. al.* [247],

[247] H. Ehrenreich, F. Seitz, and D. Turnbull, eds., *Introducing Molecular Electronics*, Academic Press, New York, 1970,

[248] G. Fagas, G. Cuniberti, and K. Richter, *Electron transport in nanotube-molecular-wire hybrids*, Phys. Rev. B **63**, 045416 (2001),

[249] G. Cuniberti, G. Fagas, and K. Richter, *Fingerprints of mesoscopic leads in the conductance of a molecular wire*, Chem. Phys. **281**, 465 (2002), doi:10.1016/S0301-0104(02)00341-5,

[250] P. W. Chiu, G. S. Duesberg, U. Dettlaff-Weglikowska, and S. Roth, *Interconnection of carbon nanotubes by chemical functionalization*, Appl. Phys. Lett. **80**, 3811 (2002),

[251] S. S. Wong, E. Joselevich, A. T. Woolley, C. L. Cheung, and C. M. Lieber, *Covalently functionalized nanotubes as nanometre-sized probes in chemistry and biology*, Nature **394**, 52 (1998),

[252] G. Fagas, A. Kambilii, and M. Elstner, *Complex-band structure: a method to determine the off-resonant electron transport in oligomers*, Chem. Phys. Lett. **389**, 268 (2004),

[253] R. Gutiérrez, G. Fagas, K. Richter, F. Grossmann, and R. Schmidt, *Conductance of a molecular junction mediated by unconventional metal-induced gap states*, Europhys. Lett. **62**, 90 (2003), doi:10.1209/epl/i2003-00366-3,

[254] G. Floquet, *Sur les équations différentielles linéaries á coefficients périodiques*, Ann. École Norm. Sup. **12**, 47 (1883),

[255] J. H. Shirley, *Solution of the Schrödinger equation with a Hamiltonian periodic in time*, Phys. Rev. **138**, B979 (1965),

[256] M. Grifoni and P. Hänggi, *Driven quantum tunneling*, Physics Reports **304**, 229 (1998), doi:10.1016/S0370-1573(98)00022-2,

[257] G. Platero and R. Aguado, *Photon-assisted transport in semiconductor nanostructures*, Physics Reports **395**, 1 (2004), doi:10.1016/j.physrep.2004.01.004,

[258] S. Kohler, *The interplay of chaos and dissipation in driven quantum systems*, PhD thesis, University of Augsburg, Augsburg, Germany, 1999,

[259] J. Sakurai, *Modern Quantum Mechanics*, Addison-Wesley, New York, 1994,